Unquenched Lattice Upsilon Spectroscopy

Thesis submitted to the University of Glasgow
for the degree of Doctor of Philosophy

March 2001

Laurence Mark Marcantonio

Department of Physics and Astronomy
University of Glasgow

ProQuest LLC.
789 East Eisenhower Parkway
P.O. Box 1346
Ann Arbor, MI 48106 – 1346

For Mum, Dad and Marcello

Acknowledgements

I would like to thank my supervisor Christine Davies, for her help during my time as a PhD student. Similarly, outwith Glasgow I wish to acknowledge the assistance and advice I have received from Junko Shigemitsu, John Sloan, Alan Irving and Chris Maynard. The members of the UKQCD collaboration at Glasgow were most helpful, they include Gunnar Bali, Peter Boyle, Sara Collins, Paul McCallum, and, especially, Joachim Hein. The staff of the Particle Physics Theory Group at Glasgow also provided extremely useful lectures, tutorials and conversations, they are (were) Prof. G. Moorhouse and Dr.s M. Alford, I. M. Barbour, R. L. Crawford, A. T. Davies, C. D. Froggatt, D. Sutherland and A. Watt. Last, but not least, my fellow students were: Alan, Alessandro Tiesi, Alessandro Usai, Gordon, Joe, Mark Campbell, Mark Gibson, Mark Senechal, Nektarios, Peter and Susan.

The work was funded by the Particle Physics and Astronomy Research Council (PPARC).

Declaration

Apart from Chapters 1 and 2 and except where specific reference is made to the work of others, this thesis has been composed by the author.

Sections from this work will be published in:

L. Marcantonio, P. Boyle, C. T. H. Davies, J. Hein and J. Shigemitsu, *The unquenched* Υ *spectrum*, Nucl. Physics B (Proc. Suppl.) (Lattice 2000, Bangalore, India).

Abstract

A non-relativistic effective theory of QCD (NRQCD) is used in calculations of the upsilon spectrum. Simultaneous multi-correlation fitting routines are used to yield lattice channel energies and amplitudes. The lattice configurations used were both dynamical, with two flavours of sea quarks included in the action; and quenched, with no sea quarks. These configurations were generated by the UKQCD collaboration. The dynamical configurations used were "matched", having the same lattice spacing, but differing in the sea quark mass. Thus, it was possible to analyse trends of observables with sea quark mass, in the certainty that the trend isn't partially due to varying lattice spacing.

The lattice spacing used for spectroscopy was derived from the lattice $1^1P_1 - 1^3S_1$ splitting. On each set of configurations two lattice bare b quark masses were used, giving kinetic masses bracketing the physical Υ mass. The only quantity showing a strong dependence on these masses was the hyperfine splitting, so it was interpolated to the real Υ mass. The radial and orbital splittings gave good agreement with experiment. The hyperfine splitting results showed a clear signal for unquenching and the dynamical hyperfine splitting results were extrapolated to a physical sea quark mass. This result, combined with the quenched result yielded a value for the hyperfine splitting at $n_f = 3$, predicting an η_b mass of 9.517(4) GeV.

The NRQCD technique for obtaining a value of the strong coupling constant in the $\overline{\rm MS}$ scheme was followed. Using quenched and dynamical results a value was extrapolated to $n_f = 3$. Employing a three loop beta function to run the coupling, with suitable matching conditions at heavy quark thresholds, the final result was obtained for $n_f = 5$ at a scale equal to the Z boson mass. This result was $\alpha^{(5)}_{\overline{\rm MS}}(M_Z)$=0.110(4).

Two methods for finding the mass of the b quark in the $\overline{\rm MS}$ scheme were employed. The results of both methods agree within error but the errors were too large to see any clear signal of unquenching in $\overline{m}_b$. The best result obtained was 4.42(33) GeV.

Contents

List of Figures

List of Tables

Chapter 1

Introduction

1.1 Quantum Chromodynamics and the Strong Coupling Constant

Quantum Chromodynamics [1] (QCD) is a gauge theory of the strong interactions. The gauge group is the $SU(3)$ colour group, i.e. the group consisting of unitary 3×3 matrices with determinant $+1$. Colour is the name given to the gauge degree of freedom responsible for the dynamics of strong interactions. This theory suggests that strongly interacting fundamental fermions each have three possible colours, and that they interact via eight bi-coloured bosons called gluons.

For this gauge group the bosons are Yang-Mills vectors which can be written as a linear combination of Yang-Mills fields:

$$A^{\mu}(x) = T_a A^{\mu}_a. \tag{1.1}$$

The index, μ, is the usual spacetime Minkowski index running from 0 to 3. The index a runs over the basis of generators for the traceless 3×3 matrices and hence runs from 1 to 8. Usually, these are taken as $T_a = \lambda_a/2$; where the λ_a are the Gell-Mann matrices [2]. In that representation, they satisfy:

$$\mathrm{tr}(\lambda_b \lambda_c) = 2\delta_{bc}, \tag{1.2}$$

and

$$\left[\frac{\lambda_b}{2}, \frac{\lambda_c}{2}\right] = i f_{bcd} \frac{\lambda_d}{2}. \tag{1.3}$$

The f_{abc} are the structure constants of the group, satisfying:

$$f_{123} = 1, \tag{1.4}$$

$$f_{147} = -f_{156} = f_{246} = f_{257} = f_{345} = -f_{367} = \frac{1}{2}, \tag{1.5}$$

$$f_{458} = f_{678} = \frac{\sqrt{3}}{2}. \tag{1.6}$$

The 4×4 antisymmetric field tensor for QCD is given by:

$$G^{\mu\nu}(x) = \lambda_a G_a^{\mu\nu}(x)/2. \tag{1.7}$$

In order to find the appropriate form of $G_a^{\mu\nu}(x)$ for a gauge-invariant Lagrangian, fermions must be included via the QCD Dirac Lagrangian:

$$\mathcal{L}_q = \overline{\psi_f^i}(x)(i\gamma^\mu \partial_\mu^{i,j} - m_f \delta^{ij})\psi_f^j(x), \tag{1.8}$$

where

$$\partial_\mu^{i,j} = \delta^{ij}\partial_\mu. \tag{1.9}$$

The indices i, j here are colour indices and take the values $1, \ldots, 3$. However, this Lagrangian is non-invariant under the gauge transformation specified by the local function, $\alpha(x)$:

$$\psi_f^j(x) \longrightarrow \left(1 + i\alpha_a(x)\frac{\lambda_a}{2}\right)\psi_f^j(x). \tag{1.10}$$

For the transformation on $\overline{\psi}$ simply change the sign of the second term above. As with QED, gauge-invariance may be recovered by introducing gluons transforming as:

$$G_\mu^a \longrightarrow G_\mu^a - \frac{1}{g_0}\partial_\mu \alpha_a(x). \tag{1.11}$$

In order to cancel the additional instances of α, the covariant derivative is introduced:

$$D_\mu = \partial_\mu + ig_0\frac{\lambda_a}{2}G_\mu^a. \tag{1.12}$$

Since $SU(3)$ is a non-Abelian group, the gluon field transforms with dependence on another gluon field:

$$G_\mu^a \to G_\mu^a - \frac{1}{g_0}\partial_\mu \alpha_a - f_{abc}\alpha_b G_\mu^c. \tag{1.13}$$

In order to have a gauge-invariant kinetic term for the gluons, $G^{\mu\nu}$ must have a more complicated form than is the case with $F^{\mu\nu}$ in non-Abelian QED.

$$G_a^{\mu\nu}(x) = \partial^\mu A_a^\nu(x) - \partial^\nu A_a^\mu(x) + g_0 f_{abc} A_b^\mu(x) A_c^\nu(x) \tag{1.14}$$

Thus the final gauge-invariant Lagrangian for QCD is:

$$\mathcal{L}_{QCD} = \overline{\psi_f^i(x)}\left(i\gamma^\mu D_\mu^{i,j} - m_f\delta^{ij}\right)\psi_f^j(x) - \frac{1}{4}G_{\mu\nu}^a G_a^{\mu\nu}. \tag{1.15}$$

To summarise this theory of the strong interactions: it is a system of $n_f = 6$ flavours of quarks, each flavour providing 3 coloured quarks, with bare masses m_f, interacting with 8 massless gluons through a bare interaction coupling g_0. The non-Abelian nature of the theory also means that it predicts the existence of three and four gluon vertices, due to the extra term in 1.14. This term gives contributions such as $g_0 A^3$ and $g_0^2 A^4$, which are not present in Abelian theories.

Normally, calculations of expectation values in quantum field theories proceed via perturbation theory. This involves a series of terms ordered in ascending powers of the coupling constant, α, of the theory. Here α is defined (in natural units, $\hbar = c = 1$) as:

$$\alpha = \frac{g^2}{4\pi}. \tag{1.16}$$

In practice, a naïve calculation of all terms in the perturbation series at any order in α may yield infinite results. For gauge theories, one must redefine (or renormalise) the couplings and masses of the field theory to achieve finite results. Calculations of expectation values to any order in perturbation theory, for example, involve different phenomena from the previous order. So renormalisation must be carried out at each order calculated. In using field theories which possess gauge symmetries, it is at least certain that renormalisation is possible. Using renormalisation group equations, the renormalisation may then be carried out without affecting expectation values of physical quantities. In practice, several different ways of renormalising can be carried out. Thus, several different renormalisation schemes are available and the value of non-physical observables depends on the particular scheme used.

1.2 Quark bound states: Hadrons

Experimentally, objects possessing an overall colour charge have never been observed. This is thought to be due to the coloured quarks being confined within colourless objects known as hadrons, a phenomenon called *confinement*. The baryons are combinations of three quarks, each possessing one colour degree of freedom confined into an overall colourless "particle". For the mesons the picture is of two quarks: one possessing an anti-colour and the other a colour. The hadrons are bound together by virtual gluon exchange.

Due to this phenomenon of confinement, quarks are not seen individually, so the properties of individual quarks are inferred via the properties of the hadrons in which they reside. Some quark properties can still be determined fairly accurately. The electromagnetic charges of quarks can be calculated by comparing the quark contents of hadrons with the hadronic electromagnetic charges. However, the masses of individual quarks cannot be simply observed; all that can be done is to provide a theoretical model of the hadronic structure and adjust the quark masses in the theory until the theoretical prediction agrees with the experimental data.

Another noteable feature of QCD is *asymptotic freedom*. Due to the non-

Abelian nature of QCD, the coupling of coloured particles is stronger the larger the separation of the colour carriers. This effect is in strict contrast with QED, where the coupling diminishes with distance, as in the familiar *Coulomb potential* picture. Theoretically, this, combined with the strength of the strong coupling mean that the traditional perturbative methods of solving (weakly coupled) quantum field theories break down at low energies. Hence, QCD motivates the development of non-perturbative solutions to quantum field theories.

The subject of this thesis is the bound state (meson) of the $b\bar{b}$ system, usually known from the name of the lightest vector resonance, the 1^3S_1[1] state, as the Υ system.

1.3 The Bottomonium Mesons

The subject of this thesis is the bottomonium ($b\bar{b}$) system. It was discovered in 1977 [3][4] as three resonances at 9.4GeV, 10GeV and 10.4GeV. The lightest of these states is now identified as the Υ meson. Several of the other mesonic states for this flavour singlet meson have been discovered. The experimentally observed states can be grouped into two types: Υ, with quantum numbers of $^3S_1$, and $\chi_{b;0,1,2}$, with $^3P_{0,1,2}$. For Υ, n takes the values 1,...,6, and n_{χ_b}=1,2[2]. The Υ states are also commonly called $\Upsilon(1S)$ or Υ, $\Upsilon(2S)$ or Υ' etc... In this thesis $n_\Upsilon \geq 4$ are ignored, since these states are very wide, thereby not offering good opportunities for comparison with experiment. The reason for this is that the $\Upsilon(4S)$ is above the $B\overline{B}$ threshold and so it readily decays [5] [6], as illustrated in figure 1.1. Furthermore, the theory eventually used in this thesis doesn't include a mechanism for the decay to $B\overline{B}$, severely limiting the theory's prospects for getting the mass of $\Upsilon(4S)$ correct. For $n_\Upsilon \leq 3$ the decay of $\Upsilon(n_\Upsilon S)$ proceeds via the Zweig suppressed channels of figures 1.2 and 1.3. There is also the electroweak annihilation channel shown in figure 1.4. Transitions occur between the $\Upsilon(nS)$ states via the decay: $\Upsilon(2S) \rightarrow \Upsilon(1S)\pi^+\pi^-$. The 1^1S_0 or η_b state is included as a prediction in this study. It is included despite not having been observed for bottomonium, as it has been observed in charmonium, the $c\bar{c}$ system whose dynamics show several similarities to $b\bar{b}$..

1.3.1 Production of Currently Unobserved Bottomonium States

Of the bottomonium states measured on the lattice in this thesis, the η_b and $h_b(^1P_1)$ have yet to be observed experimentally. Their existence is inferred since there are η_c and h_c states in charmonium. There is also thought to be a $^3D_1$ charmonium state, although no attempt was made to measure the mass of a bottomonium equivalent in this thesis.

[1]The notation used here is $^{2S+1}L_J$, where S is the eigenvalue (expectation value) of the spin angular momentum operator, L the eigenvalue for the orbital angular momentum operator, and the total angular momentum number, $J = L + S$. The eigenvalue, L is denoted by spectroscopic notation, such that $L = 0$ is denoted by S, $L = 1$ by P, and $L = 2$ by D. Sometimes an additional n is included for the radial excitation value of the state. Thus, there are states $1^3S_1, 2^3S_1, \ldots$.

[2]There is no reason to stop an analysis at $n_{\chi_b} = 2$, but higher radial excitations haven't been observed.

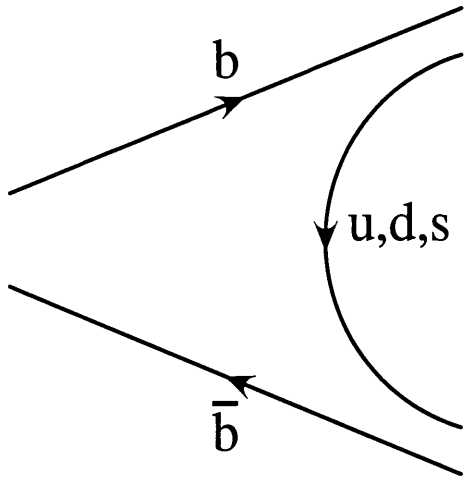

Figure 1.1: The decay of a $b\bar{b}$ meson to a $B\overline{B}$ pair.

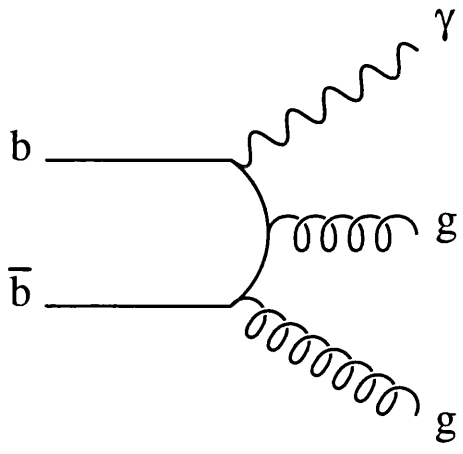

Figure 1.2: The Zweig suppressed decay of a $b\bar{b}$ meson to a photon and a pair of gluons.

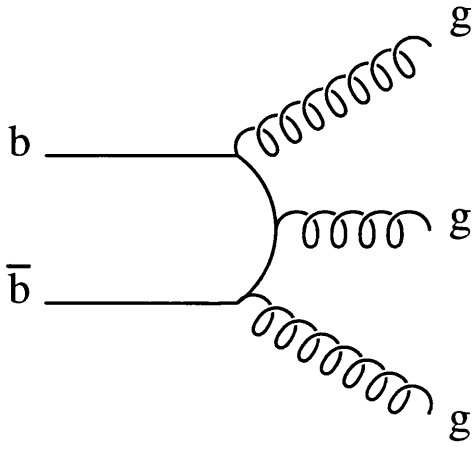

Figure 1.3: The Zweig suppressed decay of a $b\bar{b}$ meson into gluons.

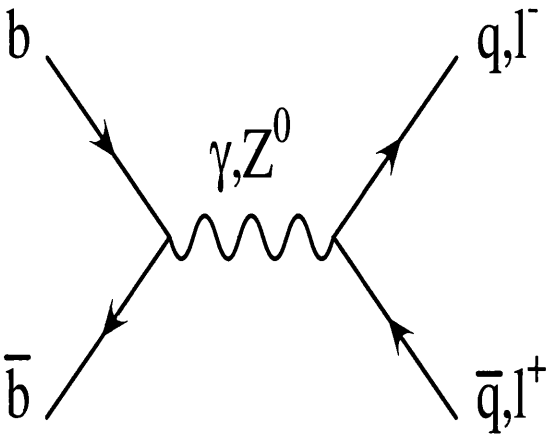

Figure 1.4: The electroweak decay of a $b\bar{b}$ meson into quarks or leptons.

Godfrey and Rosner [7] suggest that a mechanism for production of the $\eta_b(1S)$ could be via magnetic dipole transitions:

$$\Upsilon(nS) \rightarrow \eta_b(1S) + \gamma, \tag{1.17}$$
$$n = 2, 3. \tag{1.18}$$

There is another channel through the h_b:

$$\Upsilon(3S) \rightarrow h_b + \pi + \pi, \tag{1.19}$$
$$h_b \rightarrow \eta_b + \gamma. \tag{1.20}$$

Thus, with more channels from the $\Upsilon(3S)$, it is preferred to the $2S$ as a source.

One of the D-wave states, $^3D_1$ could be produced in direct scans of the center of mass in e^+e^- collisions. The 1^3D_J states have been sought in the electromagnetic cascades:

$$\Upsilon(3S) \rightarrow \gamma + \chi_b(2P) \rightarrow \gamma + \gamma +^3 D_J. \tag{1.21}$$

Tantalisingly, the number of $\Upsilon(3S)$ decays available is only slightly smaller than the estimated number required for a definitive observation of the 1^3D_J.

1.3.2 Energy Scales in Bottomonium

Typically, the radial and orbital splittings in the bottomonium spectrum have values around 500 MeV (see table A.1). The mass of the lightest vector resonance, the $\Upsilon(1S)$, is 9.46 GeV. Such splittings come from dynamics of the same order as kinetic scales indicating that the system had non-relativistic dynamics. Furthermore, the mass degeneracy of the b and $\bar{b}$ quarks implies that $1/2M_\Upsilon \sim M_b$, where M_b is the rest mass of the b quarks. This has motivated attempts to understand bottomonium dynamics using non-relativistic

models to cover the larger orbital and radial splittings, with relativistic corrections coming in for the finer spin split structure. In this thesis non-relativistic potential models are discussed and *Non-Relativistic QCD (NRQCD)* is used as the lattice heavy quark action. The potential models yield a value for the squared speed of the b quarks of $v^2 \sim 0.1$, in natural units. Typically, quark momenta (and so gluon momenta and energy) are of $\mathcal{O}(M_b v) \sim 1.4\text{GeV}$. At such an energy scale it is not true that $\alpha_s \ll 1$, preventing the use of perturbation theory. Hence, a non-perturbative approach is required. The method adopted here is to implement NRQCD on a lattice.

1.4 The Path Integral Method

Lattice gauge theory is a numerical solution to the path integral method [9] [10] [2] of quantum field theory. The starting point for a path integral is the theory action, defined from the Lagrangian of the theory by:

$$S = \int d^4x \mathcal{L}. \tag{1.22}$$

The inclusion of the measure d^4x serves to emphasize that the action is evaluated over all spacetime points. The partition function is defined as:

$$\mathcal{Z} = \int \mathcal{D}\overline{\psi}\mathcal{D}\psi\mathcal{D}A\mathrm{e}^{iS}. \tag{1.23}$$

For QCD, $\mathcal{D}\psi$, $\mathcal{D}\overline{\psi}$ and $\mathcal{D}A$ represent integration over all possible quark, antiquark and gluon fields in the theory. Overall, the summations cover all possible paths and all possible fields, weighted by the action. In practice, a field propagates along the classical path of least action whilst experiencing fluctuations around that path, and also with other fields of the theory.

The expectation value of some operator, $\mathcal{O}$, in the theory is given by:

$$\left\langle \mathcal{O}(\overline{\psi}, \psi, A) \right\rangle = \frac{1}{\mathcal{Z}} \int \mathcal{D}\overline{\psi}\mathcal{D}\psi\mathcal{D}A\mathcal{O}(\overline{\psi}, \psi, A)\mathrm{e}^{iS}. \tag{1.24}$$

Unfortunately the formulation shown above possesses an integrand which oscillates [11], so numerical techniques can't be applied. By carrying out an *analytic continuation* [9] the oscillation can be converted to a decaying exponential. Under an analytic continuation (a *Wick rotation* here) the following Minkowski spacetime quantities rotate into Euclidean quantities (marked with an E):

$$x^0 = -ix_E^4, \tag{1.25}$$
$$\gamma_0 = \gamma_4^E, \tag{1.26}$$
$$i\gamma_i = \gamma_i^E, \tag{1.27}$$
$$iA^0 = A_E^4. \tag{1.28}$$

The action and partition function then become:

$$S = iS^E, \tag{1.29}$$

$$\mathcal{Z}_E = \int \mathcal{D}\overline{\psi}\mathcal{D}\psi\mathcal{D}A\mathrm{e}^{-S^E}. \tag{1.30}$$

This new statistical-mechanics-like theory differs from the original version of quantum field theory. Nevertheless, by the analytic continuation, the Euclidean Green function, $G(x, it)$, uniquely defines the Minkowski spacetime version, $G(x, t)$. Thus, although the theories differ the solutions can be related.

1.5 Lattice QCD

Lattice QCD [11] [12] [13] [14] is a method of numerically solving Euclidean path integrals like equation 1.30.

In lattice gauge theory, spacetime is discretised into a grid of points with separation, a, the lattice spacing. Lattice spacetime coordinates then take the restricted set of values:

$$x^\nu = n^\nu a, \tag{1.31}$$

where n^ν is an integer valued "site-reference" vector in the νth dimension, and a is the lattice spacing. The components of n^ν are limited to a maximum value, N. For 4D Euclidean spacetime this gives a lattice with N^4 sites, and sides of length $L = Na$.[3] Fermion fields only exist at these discrete points, $\phi(n^\nu a)$. The discretisation also introduces a momentum cut-off of order a^{-1}. On the lattice derivatives become finite differences:

$$\partial_\nu\psi(x) \rightarrow \frac{1}{2a}(\psi(n+\hat{\nu}) - \psi(n-\hat{\nu})), \tag{1.32}$$

$$\Box\psi(x) \rightarrow \frac{1}{a^2}\sum_\nu(\psi(n+\hat{\nu}) - \psi(n-\hat{\nu}) - 2\psi(n)). \tag{1.33}$$

Integrals become sums over lattice sites:

$$\int d^4x \rightarrow a^4\sum_n. \tag{1.34}$$

1.5.1 Lattice Dirac Equation

Implementing the Wick Rotation from Minkowski spacetime to Euclidean spacetime (see equations 1.25, 1.26, 1.27, the Dirac equation for a free fermion becomes:

$$S^E = \int d^4x\overline{\psi}(x)(\gamma_\nu\partial_\nu + m)\psi(x). \tag{1.35}$$

[3] It is possible and sometimes desirable to use lattices where the temporal lattice spacing differs from the spatial value, such lattices are known as *anisotropic*. However, for this thesis the temporal lattice spacing is the same as the spatial, but with $N_{\text{temporal}} = 2N_{\text{spatial}}$.

A naïve discretisation of equation 1.35 can be carried out by implementing the discretisations of equations 1.32, 1.33, and 1.34. This gives:

$$S^E = \sum_{n,m} \overline{\psi}_L(n) K(n,m) \psi_L(m), \tag{1.36}$$

$$K(n,m) = \sum_{\nu} \frac{1}{2} \gamma_\nu (\delta_{n+\hat{\nu},m} - \delta_{n-\hat{\nu},m}) + m_L \delta_{n,m} I, \tag{1.37}$$

where the subscript L denotes lattice quantities and I is the identity matrix. The fermion propagator is defined as the inverse of the matrix K, $K^{-1}(m,n)$:

$$\sum_{l} K(n,l) K^{-1}(l,m) = \delta_{n,m}. \tag{1.38}$$

The lattice delta function and Fourier transform are:

$$\delta_{n,m} = \frac{1}{(2\pi)^4} \int_{-\pi}^{\pi} d^4 p_L \mathrm{e}^{i p_L (n-m)}, \tag{1.39}$$

$$K(n,m) = \frac{1}{(2\pi)^4} \int_{-\pi}^{\pi} d^4 p_L K(p_L) \mathrm{e}^{i p_L (n-m)}. \tag{1.40}$$

Under a Fourier transform K becomes:

$$K(p_L) = \sum_{\nu} \gamma_\nu i \sin p_\nu^L + m_L I. \tag{1.41}$$

The lattice energy-momentum dispersion relation is then:

$$E_L^2(p_L) = m_L^2 + \sum_{i=1}^{3} a^{-2} \sin^2 p_i^L. \tag{1.42}$$

The explicit a dependence has been re-introduced to illustrate the effect of taking the continuum limit. As the coordinate 4-vector x_ν in physical units is $a x_\nu^L$, the momentum 4-vector in physical units, q_ν, is equivalent to $a^{-1} p_\nu$. Taking the continuum limit:

$$E_L^2(p_L) = m^2 + q^2 + \mathcal{O}(a^2). \tag{1.43}$$

Although the propagator clearly reduces to the continuum limit satisfactorily, it contains lattice artifacts. In any one dimension there are two points in the first Brillouin zone which give the same energy-momentum dispersion relation as $\sin(\pi + p) = -\sin p$. Thus, for example, $E_L^2(p_L) = E_L^2(p_L + (0, 0, \pi/a, \pi/a))$. Overall the straightforward discretisation of the action for one particle produces 2^D (D is the spacetime dimension) particles, with the additional $2^D - 1$ particles purely lattice artefacts.

This difficulty, known as the *fermion doubling problem* was circumvented by Wilson [15]. His suggestion was to add a term $-\frac{ar}{2} \sum_n a^4 \overline{\psi}_L(n) \Box \psi_L(n)$ to the lattice

action. It is added to equation 1.36 to give the *Wilson fermion action.* It clearly vanishes in the continuum limit. The dispersion relation (equation 1.42) becomes (for $r = 1$):

$$E_L^2(p_L) = \Big(m_L + a^{-1}\Big(1 - \sum_i \cos p_i^L\Big)\Big)^2 + \sum_i a^{-2}\sin^2 p_i^L. \tag{1.44}$$

For $p_L = (0,0,0,0)$ this gives the desired relation, $E_L^2 = m_L^2$. However, now the offending high-momentum modes such as $p_L = (0,0,\pi/a,\pi/a)$ give $E_L^2 = m_L{+}2/a$. Taking the continuum limit gives the $2^D - 1$ extra lattice fermions infinite masses, decoupling them from the theory propagators.

The modern convention is to write the Wilson fermion action in terms of the *hopping parameter*, κ, defined as:

$$\kappa = \frac{1}{2m + 8r}. \tag{1.45}$$

1.5.2 Gauge Fields on the Lattice

The lattice gauge degrees of freedom are defined via the observation that for a charged particle interacting with a gauge field in the continuum the wavefunction of the particle picks up a phase factor from the interaction [14]:

$$\psi \to \psi \exp\left(ig\int_P A^\nu dx_\nu\right) = U(P)\psi. \tag{1.46}$$

The symbol P refers to path ordering. A familiar example of this phenomenon is the familiar process whereby the wavefunction of a static electron interacts with the scalar potential in standard QED to gain or lose energy, qV. In which case $U(P) = \exp(igA^0 t)$, with t the time length of the path. This extra oscillation is what we would expect as the electron energy changes due to the voltage.

For a path of length a, a lattice gauge field "link" can be defined as a function of the continuum gauge field at the centre of the link:

$$U_\nu(n) = \mathrm{e}^{igaA_\nu(n)}. \tag{1.47}$$

For QCD, the U links are $SU(3)$ matrices. One is illustrated in figure 1.5. It leads from site n to site $n + \hat{\mu}$. The opposite connection from $n + \hat{\mu}$ to n, $U_{-\mu}(n + \hat{\mu})$ is defined via the Hermitian conjugate of $U_\mu(n)$:

$$U_\mu^\dagger(n) = U_{-\mu}(n + a\hat{\mu}). \tag{1.48}$$

The lattice gauge link action is constructed to ensure gauge invariance. The behaviour of lattice fermions and gauge boson links under a gauge transformation are

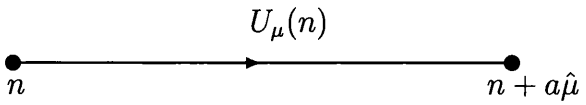

Figure 1.5: A lattice gauge link at site n in the μ direction.

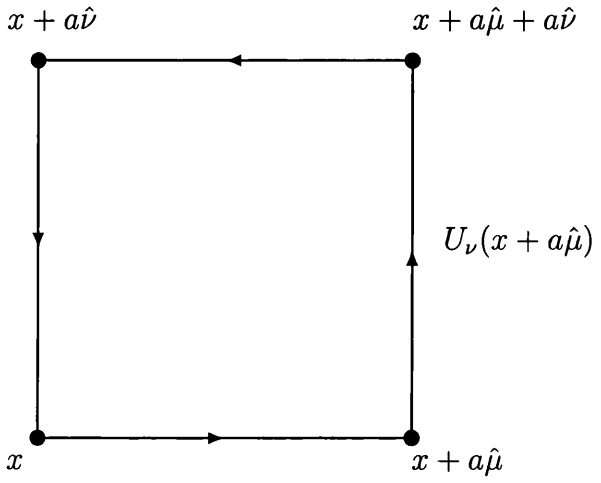

Figure 1.6: A plaquette in the $\mu\nu$ plane.

given by:

$$\psi_L(m) \rightarrow G(m)\psi_L(m), \tag{1.49}$$
$$\overline{\psi}_L(m) \rightarrow \overline{\psi}_L(m)G^{-1}(m), \tag{1.50}$$
$$U_\mu(m) \rightarrow G(m)U_\mu(m)G^{-1}(m + a\hat{\mu}), \tag{1.51}$$

where the local matrix $G \in SU(3)$. Thus, gauge-invariant (non-local) quantities on a lattice can be formed in two ways:

- Traced closed loops of gauge links, the simplest being the plaquette, illustrated in figure 1.6: $\mathrm{Tr}U^{\square}_{\mu\nu}(n) = \mathrm{Tr}U_\mu(n)U_\nu(n + a\hat{\mu})U^\dagger(n + a\hat{\nu})U^\dagger_\nu(n)$
- Non-local quark bilinears such as $\overline{\psi}_L(m)U_\mu(m)\psi(m + a\hat{\mu})$

That is, the lattice fermion action requires the insertion of gauge links between sites in order to make it gauge invariant. Expanding the plaquette to $\mathcal{O}(a^2)$, we find that $U^{\square}_{\mu\nu}(n) = \mathrm{e}^{iga^2F_{\mu\nu}(n)}$, so the lattice version of the Yang-Mills action, the Wilson gauge field

action, may be written:

$$S_G^{(W)} = \beta \sum_{\mu\nu} \sum_{\square} \left(1 - \frac{\mathrm{ReTr}}{6}\left(U_{\mu\nu}^{\square} + \left(U_{\mu\nu}^{\square}\right)^{\dagger}\right)\right), \tag{1.52}$$

where $\beta = \frac{2N}{g_0^2}$ for an $SU(N)$ group, *i.e.*:

$$\beta_{\mathrm{QCD}} = \frac{6}{g_{0,\mathrm{QCD}}^2}. \tag{1.53}$$

1.5.3 The Continuum Limit of the Lattice Action

Ideally, in the continuum limit, full QCD should re-emerge from the lattice action. However, in practice, at non-zero lattice spacing, lattice actions contain discretisation errors. The correspondence between the lattice and the continuum may be improved, by adding lattice counter terms to the action at the appropriate order of the lattice spacing. Such counterterms should disappear in the continuum limit, and cancel or reduce the leading order discretisation errors. This procedure is known as *improvement.*

For the gauge field action of equation 1.52, the plaquette action reproduces the Euclidean continuum action, with a quadratic discretisation error [14]:

$$S_G^{(W)} = \frac{1}{2}\int d^4x \mathrm{Tr}(F_{\mu\nu}F_{\mu\nu}) + \mathcal{O}(a^2), \tag{1.54}$$

where $F_{\mu\nu}F_{\mu\nu}$ is the continuum Euclidean space equivalent of $G_a^{\mu\nu}G_{\mu\nu}^a$, as defined in equation 1.14.

For the Wilson fermion action with the counterterm for "doubler" cancellation the corresponding relation is [16]:

$$S_F^{(W,r)} = \gamma_\mu^E D_\mu + m + \frac{arD^2}{2} + \mathcal{O}(a^2), \tag{1.55}$$

with the covariant derivative, D, as defined in equation 1.12.

The discretisation error is thus linear in the lattice spacing. In order to increase the rate of approach to the continuum, Symanzik introduced the *improvement programme* [17].

1.5.4 The Clover Action

Applying the Symanzik improvement programme, Sheikoleslami and Wohlert [16] added the *Clover term* to the action:

$$S_{SW}^F = -C_{SW}\frac{ar}{4}\overline{\psi}ig\sigma_{\mu\nu}F_{\mu\nu}\psi, \tag{1.56}$$

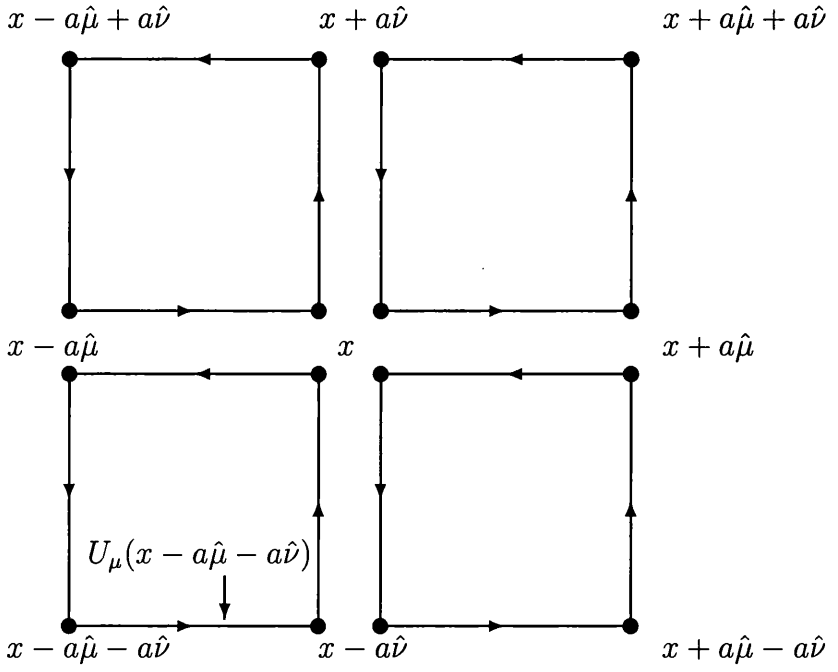

Figure 1.7: The Cloverleaf arrangement of lattice gauge field links.

where $\sigma_{\mu\nu}$ and the cloverleaf of plaquettes are defined as:

$$\sigma_{\mu\nu} = \frac{1}{2}[\gamma_\mu, \gamma_\nu], \tag{1.57}$$

$$F_{\mu\nu} = \frac{1}{8}(\mathcal{P}_{\mu\nu} - \mathcal{P}_{\mu\nu}^\dagger), \tag{1.58}$$

$$\begin{aligned}\mathcal{P}_{\mu\nu}(x) &= U_\mu(x)U_\nu(x + a\hat{\mu})U_\mu^\dagger(x + a\hat{\mu} + a\hat{\nu})U_\nu^\dagger(x + a\hat{\nu}) \\ &+ U_\nu^\dagger(x)U_\mu(x - a\hat{\nu})U_\nu(x + a\hat{\mu} - a\hat{\nu})U_\mu^\dagger(x + a\hat{\mu}) \\ &+ U_\nu(x)U_\mu^\dagger(x + a\hat{\nu})U_\nu^\dagger(x - a\hat{\mu} + a\hat{\nu})U_\mu(x - a\hat{\mu}) \\ &+ U_\mu^\dagger(x)U_\nu^\dagger(x - a\hat{\mu})U_\mu(x - a\hat{\mu} - a\hat{\nu})U_\nu(x - a\hat{\nu}).\end{aligned} \tag{1.59}$$

Cloverleaf improvement works because of the continuum Euclidean relation for on shell Green's functions (see Boyle [18]):

$$\not{D}^2 = D^2 - \frac{ig}{2}\sigma_{\mu\nu}F_{\mu\nu} = m^2. \tag{1.60}$$

Equation 1.55 undergoes the change:

$$\begin{aligned}m + \frac{ar}{2}D^2 &\rightarrow m + \frac{ar}{2}\not{D}^2, \\ &= m + \frac{ar}{2}m^2.\end{aligned} \tag{1.61}$$

The bare quark mass can then be redefined to $\mathcal{O}(am)$, giving the new mass parameter, $\tilde{m} = m(1 + \frac{ar}{2}m)$. The Wilson fermion action is now accurate to $\mathcal{O}(a^2)$.

1.5.5 Non-perturbative Improvement

With massive quarks, the *partially conserved axial current* (PCAC) relation between the isovector axial current, $A^i_\mu(x)$, and the pseudoscalar density, $P^i(x)$, in the continuum is:

$$\partial_\mu A^b_\mu(x) = 2m_{\mathrm{PCAC}} P^b(x), \tag{1.62}$$

$$A^b_\mu(x) = \overline{\psi(x)}\gamma_\mu\gamma_5\frac{\tau^b}{2}\psi(x), \tag{1.63}$$

$$P^b(x) = \overline{\psi(x)}\gamma_5\frac{\tau^b}{2}\psi(x). \tag{1.64}$$

Here τ^b denotes the Pauli spin matrices. Unfortunately, on the lattice the PCAC relation is violated by $\mathcal{O}(a)$ discretisation errors [19]. The Alpha collaboration studied such effects using lattice Schrödinger functionals. They found non-perturbative mixing of suitable dimension five operators (such as $\overline{\psi}\sigma_{\mu\nu}F_{\mu\nu}\psi$). They were then able to vary the mixing coefficients in such a way that the discretisation errors on the PCAC relation were minimised [20] [21] [22]. Most of the dimension five operators can be absorbed into others and into lattice mass and charge renormalisations, leaving only the term with the C_{SW} coefficient of equation 1.56. The improvement is then a question of finding the optimum value of C_{SW}. The most recent result, from which the UKQCD collaboration obtained the C_{SW} values used for the dynamical configurations of this thesis, is [23]:

$$C_{SW} = \frac{1 - 0.454g_0^2 - 0.175g_0^4 + 0.012g_0^6 + 0.045g_0^8}{1 - 0.720g_0^2}. \tag{1.65}$$

1.6 Monte Carlo methods

Given the improved lattice actions of the previous sections, some method is required to solve path integral equations with these actions included. On the lattice, the infinite products of integration measures such as $\mathcal{D}U$ and $\mathcal{D}\psi$, (see section 1.4) become finite products. For example, the continuum infinite product $\mathcal{D}\psi$, is $\prod_n d\psi(n)$ on the lattice.

Using the Euclidean partition function, of equation 1.30 (and dropping the E subscript), the expectation value of some operator on the lattice is:

$$\langle\mathcal{O}\rangle = \frac{1}{Z}\int \mathcal{D}U\mathcal{D}\psi\mathcal{D}\overline{\psi}\mathcal{O}\mathrm{e}^{-S^L_{QCD}}. \tag{1.66}$$

The L superscript on the action is introduced as a reminder that this is a lattice action, and not the ususal continuum QCD action. The lattice QCD action may be split into the exclusively gluonic part (S^L_G), and a fermionic part (S^L_F) (which carries gauge links

in order to preserve gauge invariance). The fermionic part has the form $S_F^L = \overline{\psi} M[U]\psi$. The integration over the quark-antiquark fields can be done analytically [11] through the Grassmann integral identity:

$$\int \mathcal{D}\overline{\psi}\mathcal{D}\psi \mathrm{e}^{-\overline{\psi}M[U]\psi} = \det M[U]. \tag{1.67}$$

This has the advantage of leaving the integral over bosonic variables only, avoiding obvious difficulties with trying to do Grassmann integration on a lattice:

$$\langle \mathcal{O}[U] \rangle = \frac{1}{Z} \int \mathcal{D}U \mathcal{O}[U] \det M[U] \mathrm{e}^{-S_G^L}. \tag{1.68}$$

The integral over $\mathcal{D}U$ is evaluated using *Monte Carlo* methods, whereby N_{cfg} different *configurations* of gauge fields are generated, and the expectation value, $\langle \mathcal{O} \rangle$, is approximated by a sum over these configurations:

$$\langle \mathcal{O} \rangle \sim \frac{1}{N_{\mathrm{cfg}}} \sum_{i=1}^{N_{\mathrm{cfg}}} \mathcal{O}[U^{(i)}]. \tag{1.69}$$

In practice, such an approximation might include many configurations where $\mathcal{O}[U^{(i)}]$ is relatively small and therefore unimportant. It is better to select important configurations only, so *importance sampling* techniques are utilised. In the current context this involves generating gauge fields with a probability, $p[U]$, proportional to the rest of the integrand in equation 1.68:

$$p[U] \propto \det M[U] \mathrm{e}^{-S_G^L}. \tag{1.70}$$

The Quenched Approximation

For lattice QCD the fermion matrix $M[U]$ has spinor, site, and colour indices, giving an overall rank $4VN_c$, with V the lattice volume and $N_c = 3$ colours. For large volumes, the calculation of the determinant of M is computationally very expensive.

In order to reduce this expense, past calculations simply set the determinant to a constant, in which case it simply cancels with the same value from the partition function, Z, of equation 1.68. This is the *quenched approximation.* It has been shown that this is equivalent to neglecting sea quark vacuum polarisation [11]. This appears to be a serious omission from the calculation, as for the Υ system there will clearly be $u\overline{u}$, $d\overline{d}$ and $s\overline{s}$ pairs in the meson due to vacuum polarisation. However, much of the character of QCD remains in the calculation: it is still, for example, a non-abelian theory, and still possesses three colour degrees of freedom. Thus, past lattice calculations gave good results despite quenching. Crudely, it is the running of the coupling constant that is affected. If the quantity being calculated doesn't depend on the coupling, then not much effect should be seen.

1.6.1 The Hybrid Monte Carlo Algorithm

Going beyond the quenched approximation, to get the configurations used to generate the results in this thesis, involved the use of a *Hybrid Monte Carlo* (HMC) algorithm. The fermion determinant comes from a Gaussian integral over bosonic variables, ϕ, called *pseudofermions*:

$$\det M^\dagger M = \int \mathcal{D}\phi^\dagger \mathcal{D}\phi \mathrm{e}^{-\phi^\dagger (M^\dagger M)^{-1}\phi}. \tag{1.71}$$

Unfortunately, there are two main problems with this approach:

- HMC only works for an even number of dynamical fermions, not the three that are believed to be present in the physical mesons.
- The dynamical quark masses in current HMC calculations are too large. Unfortunately it is too computationally expensive to achieve a light enough dynamical quark mass with HMC, and such quarks will also suffer from more severe finite volume effects.

The second of these problems will be addressed in this thesis by extrapolations of results for unnaturally heavy sea quarks to a physical pseudoscalar mass. Getting around the first is currently the focus of work in the design of new algorithms. In this thesis the $n_f = 3$ limit is reached by extrapolation of the quenched ($n_f = 0$) and dynamical ($n_f = 2$) configuration results.

1.6.2 Autocorrelations

The HMC algorithm works by finding configurations of "important" gauge fields. Once an important region of configuration space is reached, the next configuration is generated by continuing the process, reaching similar configurations in a series of "steps" from the initial good ones. This means that the generated configurations have some relation to each other, *i.e.* they are not statistically independent in the way that experimental results are. In other words, there is an extent to which such configurations are correlated with each other, they are said to be *autocorrelated.*

In working out the size of autocorrelations it is important to differentiate between *primary* and *secondary* quantities. Primary quantities are directly generated from the lattice, whilst secondary quantities are subsequently calculated as functions of the primary quantities. If X is a primary quantity measured N times, then the naïve way to calculate its variance is with the familiar result:

$$\sigma^2_{\langle X \rangle} = \frac{\langle X^2 \rangle - \langle X \rangle^2}{N-1}, \tag{1.72}$$

$$\left\langle X^2 \right\rangle = \frac{1}{N}\sum_{i=1}^{N} X_i^2, \tag{1.73}$$

$$\langle X \rangle = \frac{1}{N} \sum_{i=1}^{N} X_i. \tag{1.74}$$

In the presence of *autocorrelations* such measurements aren't statistically independent, and the error calculated above is too low. The autocorrelation is defined as:

$$\langle X_i X_{i+\tau} \rangle - \langle X_i \rangle \langle X_{i+\tau} \rangle . \tag{1.75}$$

The true error, σ_{true}, is then:

$$\sigma^2_{\text{true}} = \frac{\langle X^2 \rangle - \langle X \rangle^2}{N} 2\tau_{\text{int}}, \tag{1.76}$$

$$\tau_{\text{int}} \equiv \frac{1}{2} \sum_{\tau=-\infty}^{+\infty} \frac{\langle X_i X_{i+\tau} \rangle - \langle X_i \rangle \langle X_{i+\tau} \rangle}{\langle X_i X_i \rangle - \langle X_i \rangle \langle X_i \rangle}. \tag{1.77}$$

The parameter τ_{int} is called the integrated autocorrelation time, and differs for different types of primary quantities. It represents the time (in algorithm updating steps) over which the autocorrelation persists.

In this thesis two types of primary quantities were calculated on the lattice: plaquettes and various heavy quark correlators (see chapter 2 for these). In order to measure autocorrelation times a *jackknife* or *bootstrap* [24] [25] procedure can be used. For the results in this thesis Jackknifing was used.

Jacknifing involves taking the data set and "cutting out" (hence jackknifing) or "binning" one or more of the data values. The remaining values are averaged. The process is then repeated by the removal of other values. Overall when binning, say, n values (jackknifing with a *bin length* of n), the new jackknifed value is:

$$X_k^{(J)} \equiv \frac{1}{N-n} \sum_{\substack{i=1 \\ i \neq (n(k-1)+1), \ldots, nk}}^{N} X_i. \tag{1.78}$$

For a secondary quantity $Y(X)$ the values are:

$$\left\langle Y^{(J)} \right\rangle \equiv \frac{1}{N} \sum_{k=1}^{N} Y(X_k^{(J)}), \tag{1.79}$$

$$\sigma^2_{\left\langle Y^{(J)} \right\rangle} \equiv \frac{N-n}{N} \sum_{k=1}^{N} \left(Y(X_k^{(J)}) - \left\langle Y^{(J)} \right\rangle \right)^2. \tag{1.80}$$

This calculation, by varying the bin length, n, allows a measurement of the autocorrelation in the primary quantity. By increasing n, in the presence of autocorrelations, the jackknife error, $\sigma^{(J)}$ will increase. If increasing n produces no increase in $\sigma^{(J)}$ then this indicates that the X_i are uncorrelated. Otherwise, the largest value of n beyond

which $\sigma^{(J)}$ no longer increases is the autocorrelation length. Calling such a value $\tilde{n}$, we have:

$$\tilde{n} \simeq 2\tau_{\text{int}}. \tag{1.81}$$

In another context jackknifing actually reduces the naïve errors. Given two secondary quantities which depend on correlated primary quantities, the difference between them is overestimated by normal statistics.

Chapter 2

Effective Theories of Heavy Quarkonia

2.1 Introduction

Potential models were applied extensively in the development of QED, various efforts have been made to repeat the process for QCD. Of course, QCD differs from QED in that it exhibits asymptotic freedom and colour confinement. Perturbation theory can be used to reproduce the asymptotically free part of the potential. However, colour confinement is a non-perturbative effect, and requires other techniques. In this chapter some of this work is summarised. The actual theory used in the lattice calculations for this thesis is *Non-Relativistic QCD* (NRQCD). It is an effective theory of QCD in the heavy quark limit.

2.2 Potential models

The Standard Model contains 6 quarks. The three lightest (up, down, and strange) are lighter than the heavy three (charm, bottom, and top) by a mass gap which is much greater than the typical QCD scale, Λ_{QCD}. Assuming the momentum of quarks within hadronic bound states to be $\mathcal{O}(\Lambda_{QCD})$[1], then the three light quarks with masses $\mathcal{O}(\Lambda_{QCD})$ are relativistic as they have $v_l^2 \approx c^2$. For the heavy three with $m_h \gg \Lambda_{QCD}$, their typical speeds $v_h^2 \ll c^2$. Thus, in a system such as Υ with two heavy quarks, bound via gluons which propagate at speed, c, it seems reasonable to try potential models with their suggestion of static quarks interacting via instantaneous gluon propagators.

[1]This assumption is not necessarily true, however radial and orbital excitation energies are roughly this size.

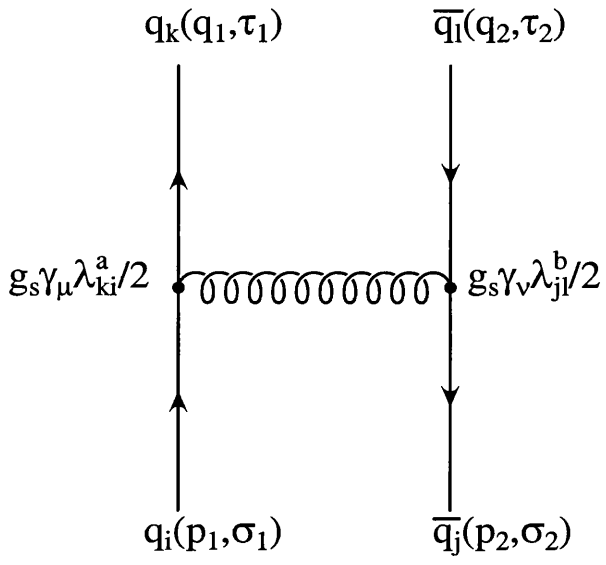

Figure 2.1: The one-gluon exchange process for quark-antiquark scattering.

2.2.1 Perturbative Potential Model

To obtain the perturbative part of the potential it is necessary to consider elastic scattering of the heavy quark and anti-quark via one gluon exchange. The S-matrix element for this interaction (at the lowest non-trivial order in perturbation theory) is [28]:

$$S_{fi} \equiv \langle f, \text{out}|i, \text{in}\rangle = \delta_{fi} + i(2\pi)^4\delta^{(4)}(P_f - P_i)\mathcal{M}_{fi}. \tag{2.1}$$

The potential, $V(\mathbf{r})$ is obtained through a Fourier transform of the lowest order scattering amplitude, $\mathcal{M}_{fi}(k)$. The scattering is:

$$q_i(p_1,\sigma_1) + \overline{q_j}(p_2,\sigma_2) \longrightarrow q_k(q_1,\tau_1) + \overline{q_l}(q_2,\tau_2), \tag{2.2}$$

. where i,j,k,l=1,2,3 are colour indices. The two channels through which this process occurs at tree-level are shown in figures 2.1 and 2.2. From those diagrams $\mathcal{M}_{fi}$ is given by:

$$\mathcal{M}_{fi} = -\frac{1}{(2\pi)^6}\frac{m^2}{E_{p1}E_{p2}E_{q1}E_{q2}}g_s^2\frac{1}{3^{1/2}}\delta_{ij}\frac{1}{3^{1/2}}\delta_{kl} \times (\mathcal{M}_{exch} + \mathcal{M}_{annh}), \tag{2.3}$$

where

$$\mathcal{M}_{exch} = \frac{1}{(p_1 - q_1)^2}\frac{\lambda^a_{ki}}{2}\frac{\lambda^a_{jl}}{2}\overline{u}(q_1,\tau_1)\gamma_\mu u(p_1,\sigma_1)\overline{v}(p_2,\sigma_2)\gamma^\mu v(q_2,\tau_2), \tag{2.4}$$

and

$$\mathcal{M}_{annh} = -\frac{1}{(p_1 + p_2)^2}\frac{\lambda^a_{ji}}{2}\frac{\lambda^a_{kl}}{2}\overline{u}(q_1,\tau_1)\gamma_\mu v(q_2,\tau_2)\overline{v}(p_2,\sigma_2)\gamma^\mu u(p_1,\sigma_1). \tag{2.5}$$

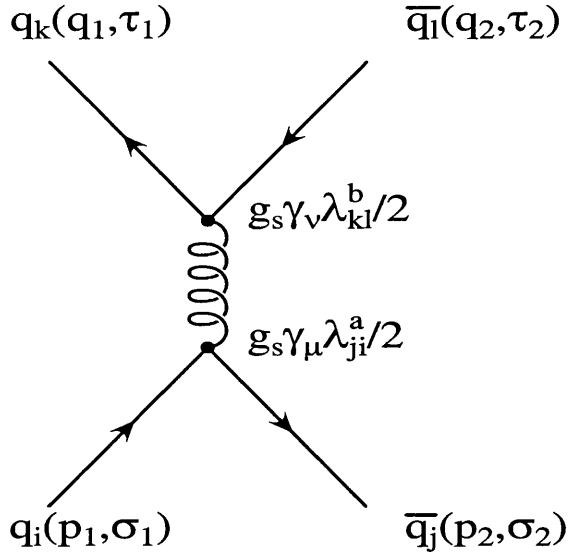

Figure 2.2: Pair annihilation for quark-antiquark scattering.

The factor of $\delta_{ab}g^{\mu\nu}$ [18] associated with the gluon propagator is responsible for the contraction of the spacetime indices on the γ matrices, and for the adjoint colour indices $a, b(= 1, \ldots, 8)$ on the Gell-Mann matrices [29], λ^a. The δ functions in the colour indices $i, j, k, l(= 1, \ldots, 3)$ arise because mesons are colour singlets. Thus, for example:

$$u_i(p_1, \sigma_1)\overline{v}_j(p_2, \sigma_2) = u(p_1, \sigma_1)\overline{v}(p_2, \sigma_2)\frac{1}{\sqrt{3}}\delta_{ij}. \tag{2.6}$$

The Gell-Mann matrices satisfy:

$$\mathrm{Tr}\left[(\lambda^a)^2\right] = 16, \tag{2.7}$$

so the colour factor for the one-gluon exchange graph is:

$$\frac{1}{\sqrt{3}}\delta_{ij}\frac{1}{\sqrt{3}}\delta_{kl}\frac{\lambda^a_{ki}}{2}\frac{\lambda^a_{jl}}{2} = \frac{1}{12}\mathrm{Tr}\left[(\lambda^a)^2\right] = \frac{4}{3}, \tag{2.8}$$

whereas the annihilation graph gives no contribution to the amplitude:

$$\frac{1}{\sqrt{3}}\delta_{ij}\frac{\lambda^a_{ij}}{2} = \frac{1}{2\sqrt{3}}\mathrm{Tr}\,(\lambda^a) = 0. \tag{2.9}$$

Defining the exchange gluon momentum as:

$$k = p_1 - q_1 = q_2 - p_2. \tag{2.10}$$

The scattering amplitude is:

$$\mathcal{M}_{fi} = \frac{1}{(2\pi)^6}\frac{4}{3}\frac{g_s^2}{k^2}. \tag{2.11}$$

Now taking the Fourier transform:

$$V(r) = -\frac{1}{(2\pi)^3}\int d^3k e^{-ik.x}\frac{4}{3}\frac{g_s^2}{k^2}. \tag{2.12}$$

Using equation 1.16 this is:

$$V(r) = -\frac{4}{3}\frac{g_s^2}{4\pi r} = -\frac{4}{3}\frac{\alpha_s}{r}. \tag{2.13}$$

So the short range potential is of a Coulombic form. To impose the constraint of asymptotic freedom on this potential, simply use the running coupling for α_s :

$$\lim_{-k^2 \gg \Lambda_{QCD}^2} \alpha_s(k^2) \sim \frac{12\pi}{(33-2n_f)}\frac{1}{\ln(-k^2/\Lambda_{QCD}^2)}. \tag{2.14}$$

In the context of Lattice QCD, this is a particularly important equation. It indicates that quenched ($n_f = 0$) Lattice QCD should have a lower strong coupling constant than unquenched QCD. Thus, signals for unquenching should be sought in quantities which depend on α_s. In particular, for the Υ spectroscopy reported in this thesis, the hyperfine splitting (see section 2.2.4) ought to differ between quenched and unquenched calculations. Indeed such an effect is found in Chapter 4.

The above result may be generalised to include other forms of potential. Ignoring the normalisation factors and (anti-)quark spins, the tree level scattering amplitudes are:

$$\overline{u}(q_1)\Gamma u(p_1)V_\Gamma(k)\overline{v}(p_2)\Gamma v(q_2). \tag{2.15}$$

The Γs are constructed from the familiar Dirac γ matrices. Their transformation properties classify the type of interaction. For example, in the case calculated above $\Gamma = \gamma_\mu$, and thus is considered to be a *vector* potential, labelled V_V. Other potentials which may be considered are [28]:

$$\Gamma_{\text{scalar}} = 1 \qquad V_s, \tag{2.16}$$

$$\Gamma_{\text{pseudoscalar}} = \gamma_5 \quad V_{ps} = 0, \tag{2.17}$$

$$\Gamma_{\text{axial-vector}} = \gamma_\mu\gamma_5 \quad \sigma_1 \cdot \sigma_2 V_a, \tag{2.18}$$

$$\Gamma_{\text{tensor}} = \sigma_{\mu\nu} \quad \sigma_1 \cdot \sigma_2 V_t, \tag{2.19}$$

where σ_1 and σ_2 are the spins of the quark and anti-quark respectively, and $\sigma_{\mu\nu}$ is defined as:

$$\sigma_{\mu\nu} \equiv \frac{i}{2}\left[\gamma_\mu, \gamma_\nu\right]. \tag{2.20}$$

There is no pseudoscalar static contribution at leading order, as it vanishes in the non-relativistic limit. The axial-vector and tensor contributions depend on the spin of the quark and anti-quark and hence imply that that spin-dependent splittings are of the same order as spin-independent splittings [30]. The experimental spectrum of the Υ

rules this possibility out. Ergo, at leading order the potential consists of only scalar and vector components:

$$V_0(r) = V_{\rm v}(r) + V_{\rm s}(r). \tag{2.21}$$

The 0 subscript signifies that this potential is zeroth order with respect to relativistic corrections.

2.2.2 Inclusion of Non-Perturbative Aspects of the Potential

For the long-range potential a non-perturbative approach is necessary. The Coulomb potential alone would suggest degeneracy between the $2S$ and $1P$ levels [31]. Phenomenological potential models are required. One such additional potential is of the form [6]:

$$V \sim r^n \quad 2 > n > 0. \tag{2.22}$$

The harmonic oscillator r^2 type is ruled out because, whilst it gives $1P$ lower than $2S$, it suggests that for the J/ψ system the $1D$ and $2S$ are degenerate [31].

A popular form of this model is the *Cornell model* [32], which includes a term which grows linearly with interquark separation, *i.e.* a confining term:

$$V(r) = -\frac{4}{3}\frac{\alpha_s}{r} + \sigma r, \tag{2.23}$$

where σ is called the string tension. This successfully reproduces the zeroth order spectrum fairly well, with $1P$ lower than $2S$ and $1D$ higher than $2S$ (for the charmonium system only, as no Υ D state has yet been observed). Another form which is also successful is the Richardson potential [33]:

$$V(r) = \int d^3k e^{-ik\cdot r}\frac{\alpha_s(k^2)}{4\pi k^2}. \tag{2.24}$$

On substitution of $\alpha_s(k^2)$ from equation 2.14, this gives an integral of the form:

$$f(n_f)\int d^3k \frac{e^{-ik\cdot r}}{k^2 \ln(1 + k^2/\Lambda^2_{QCD})}, \tag{2.25}$$

where $f(n_f)$ simply represents the integral normalisation and running coupling coefficients. For large k this behaves as a Coulomb potential, and for small k as a linear potential. At intermediate k the potential is logarithmic.

2.2.3 Relativistic Corrections to Potential Models

The zeroth order potentials of the previous section give good results for the spin independent splittings, such as that between the $\Upsilon(1S)$ (or 1^3S_1) and $\Upsilon(2S)$ (2^3S_1). However

they don't account for the mass differences between states which differ in their spins such as the J/ψ ($c\bar{c}$ meson with quantum numbers 1^3S_1) and the η_c ($c\bar{c}$ with 1^1S_0). To distinguish between such states it is necessary to include relativistic corrections to the zeroth order potential.

A popular way of including relativistic corrections is to use the method of Eichten and Feinberg [34]. They give the spin-dependent potential up to $\mathcal{O}(1/m^2)$ as:

$$\begin{aligned} V_{sd}(r) &= \frac{\mathbf{L}_1 \cdot \mathbf{S}_1 - \mathbf{L}_2 \cdot \mathbf{S}_2}{m^2 r}\left(\frac{dV_0(r)}{2dr} + \frac{dV_1(r)}{dr}\right) \\ &+ \frac{\mathbf{L}_1 \cdot \mathbf{S}_2 - \mathbf{L}_2 \cdot \mathbf{S}_1}{m^2 r}\frac{dV_2(r)}{dr} \\ &+ \left(\frac{(\mathbf{r}\cdot\mathbf{S}_1)(\mathbf{r}\cdot\mathbf{S}_2)}{m^2 r^2} - \frac{\mathbf{S}_1 \cdot \mathbf{S}_2}{3m^2}\right) V_3(r) \\ &+ \frac{\mathbf{S}_1 \cdot \mathbf{S}_2}{3m^2} V_4(r), \end{aligned} \tag{2.26}$$

where the quark and antiquark spins are now written as $\mathbf{S}_i$ (for i=1,2), the quantum orbital angular momentum $\mathbf{L}$ is given by $\mathbf{L} = \mathbf{r} \times \mathbf{p}$. The central potential V_0 is just the heavy quark static potential, one of the candidates discussed in sections 2.2.1 and 2.2.2.

The potentials $V_1, \ldots, V_4$ come from the expectation values of correlations of components of the chromoelectric and chromomagnetic fields. Those fields can be treated non-perturbatively, *e.g.* by calculating them from the Wilson action of Lattice QCD [35]. Thus, to include a spin-dependent part to a potential of the type $\sigma \cdot \mathbf{B}/2m_Q$, the heavy quark propagator is modified via the insertion of two (from symmetry considerations) lattice $\mathbf{B}$ fields. The addition this makes to the potential can be calculated from the ratio of the Wilson loop with $\mathbf{B}$ fields to that without.

Another useful method is to use the generalised *Breit-Fermi Hamiltonian* [28]:

$$H_{BF} = 2m + \frac{\mathbf{p}^2}{m} - \frac{\mathbf{p}^4}{4m^3} + V_0(r) + V_{SI} + V_{LS} + V_{SS} + V_T, \tag{2.27}$$

The mass is given as 2m because in this case there are two equal mass particles. Similarly, the reduced mass μ which ought to occur in the term $\mathbf{p}^2/2\mu$ is replaced by $m/2$. Once again, $V_0(r)$ is the heavy quark static potential of sections 2.2.1 and 2.2.2. The spin-independent correction for this Hamiltonian is given in [28]. The potentials of interest for this thesis are given by:

$$V_{LS}(r) = \frac{1}{2m^2 r}\left(3\frac{dV_V(r)}{dr} - \frac{dV_S(r)}{dr}\right)\mathbf{L}\cdot\mathbf{S}, \tag{2.28}$$

$$V_{SS}(r) = \frac{2}{3m^2}\mathbf{S}_1 \cdot \mathbf{S}_2 \nabla^2 V_V(r), \tag{2.29}$$

$$V_T(r) = \frac{1}{12m^2}\left(\frac{1}{r}\frac{dV_V(r)}{dr} - \frac{d^2V_V(r)}{dr^2}\right)S_{12}, \tag{2.30}$$

with S_{12} given by:

$$S_{12} = 12\left(\frac{(\mathbf{S}_1 \cdot \mathbf{r})(\mathbf{S}_2 \cdot \mathbf{r})}{r^2} - \frac{\mathbf{S}_1 \cdot \mathbf{S}_2}{3}\right). \tag{2.31}$$

The unsubscripted operators are the operators for the total meson, thus the total mesonic spin $\mathbf{S}$ is just a sum of the individual quark spins, $\mathbf{S} = \mathbf{S}_1 + \mathbf{S}_2$. These contributions are trivial to calculate, with $\mathbf{J} = \mathbf{L}+\mathbf{S}$, and the eigenvalues of these operators written as J, L and S, we get:

$$\langle \mathbf{L} \cdot \mathbf{S} \rangle = \frac{1}{2}(J(J+1) - L(L+1) - S(S+1)), \tag{2.32}$$

$$\langle \mathbf{S}_1 \cdot \mathbf{S}_2 \rangle = \frac{1}{2}(S(S+1) - S_1(S_1+1) - S_2(S_2+1)). \tag{2.33}$$

Notice from the expression for $\langle \mathbf{L} \cdot \mathbf{S} \rangle$ that the spin orbit term has vanishing expectation values for L=0 or S=0. For the spectral states of interest in this thesis the only contribution from this term is thus with $L \neq 0$ and S=1.

For the tensor term V_T, the value of S_{12} in the case $S_1 = S_2 = 1/2$, can be re-written as:

$$S_{12} = 2\left(3\frac{(\mathbf{S} \cdot \mathbf{r})^2}{r^2} - \mathbf{S}^2\right). \tag{2.34}$$

The expectation value for S_{12} was calculated by Kwong and Rosner [36], and is given by:

$$\langle S_{12} \rangle = \frac{-12}{(2L-1)(2L+3)}\left(\langle \mathbf{S} \cdot \mathbf{L} \rangle^2 + \frac{1}{2}\langle \mathbf{S} \cdot \mathbf{L} \rangle - \frac{1}{3}S(S+1)L(L+1)\right). \tag{2.35}$$

Thus, like the spin orbit term, the tensor term has vanishing expectation values for either L or S equal to zero. It is now easy to calculate these expectation values for the various energy levels of the Υ system. They are listed in table 2.1. The numbers in parentheses after the usual $^{2S+1}L_J$ state labels are the J^{PC} numbers for the various states, where P is the parity quantum number and C the charge conjugation number for the states. They are calculated in the usual way for quark anti-quark states:

$$P = (-1)^{L+1} \quad C = (-1)^{L+S}. \tag{2.36}$$

2.2.4 Potential Models and the Fine Structure of Heavy Bottomonium

P-Wave Fine Structure in Bottomonium

So far it has been shown that the static potential is both scalar and vector in nature. Also that it has a short distance Coulombic component and a long distance potential rising as

	$^1S_0(0^{-+})$	$^3S_1(1^{--})$	$^1P_1(1^{+-})$	$^3P_0(0^{++})$	$^3P_1(1^{++})$	$^3P_2(2^{++})$
$\langle \mathbf{S}_1 \cdot \mathbf{S}_2 \rangle$	-3/4	1/4	-3/4	1/4	1/4	1/4
$\langle \mathbf{L} \cdot \mathbf{S} \rangle$	0	0	0	-2	-1	1
$\langle S_{12} \rangle$	0	0	0	-4	2	-2/5

Table 2.1: Expectation values of the orbital and spin angular momentum operators relevant to the spin splittings in the Υ system. The expressions in the parentheses after the states are the J^{PC} quantum numbers of the states.

a positive power (less than two) of the interquark spacing. Experimental results can be used to analyse how much of the vector type and how much the scalar contribute. One such is the *Peskin Ratio* [37]:

$$\rho = \frac{M(^3P_2) - M(^3P_1)}{M(^3P_1) - M(^3P_0)}. \tag{2.37}$$

Table 2.1 indicates that the spin-spin interaction will not contribute to this splitting as it cannot distinguish between the states used in the calculation of ρ. Where the spin-spin term does make a difference is for the $^3S_1$ and $^1S_0$ states, indeed it is the only one of the potentials considered which will give rise to this *hyperfine* splitting between them, as seen in the mass difference between the J/ψ and the η_c.

Considering the static potential as the Coulomb plus Cornell type, *i.e.* equation 2.23, and then making the further assumption that this potential is wholly vector in nature ($V_V = V_0$ and $V_S = 0$), gives:

$$\rho_V = \frac{1}{5}\frac{8\alpha_s \langle r^{-3} \rangle + 7\sigma \langle r^{-1} \rangle}{2\alpha_s \langle r^{-3} \rangle + \sigma \langle r^{-1} \rangle}, \tag{2.38}$$

This result has the bounds $4/5 \leq \rho_V \leq 7/5$, and so is inconsistent with the experimental result 0.66 for the $\chi_b(1P)$ states (see table A.1). The scalar alternative gives ρ_S=2. Thus, the static potential is thought to be made up of both scalar and vector components. Normally, the Cornell confining bit is identified as the scalar part, and the Coulomb as the vector. With this in place we get:

$$\rho_{SV} = \frac{1}{5}\frac{8\alpha_s \langle r^{-3} \rangle - \frac{5}{2}\sigma \langle r^{-1} \rangle}{2\alpha_s \langle r^{-3} \rangle - \frac{1}{4}\sigma \langle r^{-1} \rangle}. \tag{2.39}$$

In the pure vector-Coulomb limit ($\sigma = 0$), ρ_{SV}=0.8. Hence, some appropriate scalar-Cornell contribution on top of the dominant vector-Coulomb part will give agreement between this model and the experimental result.

S-wave Hyperfine Structure in Bottomonium

As mentioned earlier the part of the interquark potential which creates the hyperfine ($^3S_1 - ^1S_0$) splitting has to be the spin-spin term, as both the spin-orbit and tensor parts

don't distinguish between either of those states. Assuming 1-gluon exchange giving a vector potential $V_V = -\frac{4}{3}\frac{\alpha_s}{r}$, and noting from Poisson's equation [38] that:

$$\nabla^2\left(\frac{1}{r}\right) = -4\pi\delta^3(r), \tag{2.40}$$

these two equations used in equation 2.29 give the expectation value for the spin-spin splitting in heavy quarkonium as:

$$\langle V_{SS}\rangle = \frac{1}{m^2}\frac{32\pi}{9}\alpha_s\left|\psi(0)\right|^2\left[\langle \mathbf{S}_1\cdot\mathbf{S}_2\rangle\right]^{^3S_1}_{^1S_0}, \tag{2.41}$$

where $[]^x_y$ means subtract the expectation value for y from that at x. Using table 2.1, equation 2.41 evaluates to:

$$\langle V_{SS}\rangle = \frac{32\pi}{9m^2}\alpha_s(q)\left|\psi(0)\right|^2. \tag{2.42}$$

An alternative way of looking at the S-wave hyperfine splitting is to use the time-independent Schrödinger equation [28] for a two particle system:

$$\left[-\frac{\Delta}{2\mu}+V(\mathbf{x})\right]\psi(\mathbf{x}) = E\psi(\mathbf{x}), \tag{2.43}$$

$$\mu = \frac{m_1m_2}{(m_1+m_2)}, \tag{2.44}$$

$$\Delta = \frac{1}{r^2}\frac{\partial}{\partial r}r^2\frac{\partial}{\partial r}-\frac{\mathbf{L}^2}{r^2}. \tag{2.45}$$

For (flavour singlet) bottomonium this can be simplified as $\mu = m/2$. The wavefunction can then be factorised into a radial part and the usual spherical harmonics:

$$\psi(\mathbf{x}) = \frac{1}{r}y(r)\mathcal{Y}_{LM}(\theta,\phi). \tag{2.46}$$

They have normalisations:

$$\int_0^\infty dr|y(r)|^2 = 1, \tag{2.47}$$

$$\int d\Omega\mathcal{Y}^*_{LM}\mathcal{Y}_{L'M'} = \delta_{LL'}\delta_{MM'}. \tag{2.48}$$

The Laplacian of equation 2.45 changes under this factorisation and the reduced wavefunction $y(r)$ satisfies a new radial wavefunction:

$$\Delta\psi(\mathbf{x}) = \frac{1}{r}\left(\frac{d^2}{dr^2}-\frac{L(L+1)}{r^2}\right)y(r)\mathcal{Y}_{LM}(\theta,\phi), \tag{2.49}$$

$$y''(r) = \left(2\mu[V(r)-E]+\frac{L(L+1)}{r^2}\right)y(r). \tag{2.50}$$

For S-waves the spherical harmonic is $\mathcal{Y}_{00} = 1/\sqrt{4\pi}$, so we have:

$$\psi(\mathbf{x}) = \frac{1}{\sqrt{4\pi}}\frac{y(r)}{r}, \tag{2.51}$$

$$\Delta\psi(\mathbf{x}) = = \frac{1}{\sqrt{4\pi}}\frac{y''(r)}{r}. \tag{2.52}$$

Inserting equation 2.52 into the Schrödinger equation (equation 2.43), gives:

$$\begin{aligned} -\int d^3r \frac{y''y'}{4\pi r^2} &= -\frac{1}{2}\int_0^\infty dr(y'^2)' = -\frac{1}{2}(y'^2)|_0^\infty = -2\pi(\psi + r\psi')^2|_0^\infty = 2\pi\,|\psi(0)|^2\,, \quad (2.53)\\ &= 2\mu\int d^3r[E - V(r)]\frac{yy'}{4\pi r^2} = \mu\int_0^\infty dr[E - V(r)](y^2)' = \mu\int_0^\infty drV'(r)y^2,\\ &= \mu\,\langle V'\rangle\,. \end{aligned}$$

Using the Cornell potential this yields:

$$|\psi(0)|^2 = \frac{m}{4\pi}\left\langle \frac{4}{3}\frac{\alpha_s}{r^2} + \sigma \right\rangle. \tag{2.54}$$

Thus, for sufficiently light quarks (where the linear part of the potential dominates), equation 2.54 becomes:

$$|\psi(0)|^2 = \frac{m\sigma}{4\pi}, \tag{2.55}$$

which, in turn, leads to the conclusion that the hyperfine splitting will vary inversely with quark mass, m. How good this assertion is can be tested from the results for the hyperfine splittings in the next chapter. Unfortunately, as the η_b has not been seen, no experimental comparison is possible between the $J/\psi - \eta_c$ and $\Upsilon - \eta_b$ experimental splittings.

The Effect of Unquenching on the Hyperfine Splitting

Many phenomenological models use the running coupling constant (see equation 2.14). In the quenched approximation $n_f = 0$, and so the coupling should run faster than in the presence of sea quarks. Thus, the expected situation is that α_s is lower in the quenched approximation than in the full theory. Even from early attempts at unquenching on the lattice, such an effect was observed, for example, by the SESAM Collaboration [39]. Furthermore, in the absence of sea quarks, string breaking won't occur in the theory.

The wavefunction at the origin is another useful lattice observable through which the effect of unquenching on the interquark potential may be measured. Such a measurement is discussed in El Khadra *et al.* [40] [41]. They found that, with a Richardson potential model, the value of $|\psi(0)|^2$ was 30% less than in the full theory.

2.3 Non relativistic QCD (NRQCD)

2.3.1 The Motivation for NRQCD

The potential models which have been discussed previously in this chapter can be successful in predicting the spectra of the $c\bar{c}$ and $b\bar{b}$ systems. However, there are several disadvantages to potential model methods. The parameters α_s and the string tension, σ, have to be adjusted to reproduce the low-lying spectral states. Higher states are then estimated from the results of those fits. Thus, the process is very much one of modelling, rather than trying to extend first principle ideas in a rigorous fashion. Similarly, the exact nature of the potential (*i.e.* what are the relative importances of vector and scalar parts?) doesn't emerge as different models yield different conclusions on this problem.

Nevertheless, potential models do give some useful input towards the establishment of an effective theory from first principles. In particular, the *Virial Thoerem* [42], which relates the expectation value of the meson kinetic energy, $\langle K \rangle$, to the expectation of a derivative of the potential:

$$\langle K \rangle = \frac{1}{2} \left\langle r \frac{dV}{dr} \right\rangle . \tag{2.56}$$

Quigg *et al.* [42] used various potentials successfully, amongst them a logarithmic type $V(r) \sim \ln r$. Such a potential type yields a constant $\langle K \rangle$. Thus, with:

$$K = \frac{p^2}{2\mu}, \tag{2.57}$$

where μ is the meson reduced mass, which is $m_Q/2$ for quarkonium. Thus, the velocity of an individual quark within the meson is estimated as:

$$\left\langle v_Q^2 \right\rangle = \frac{\langle K \rangle}{m}. \tag{2.58}$$

From the fit of Quigg and Rosner [42] the results are:

$$\begin{aligned} c \ \text{ in } \ J/\psi &: v^2 \sim 0.24, \\ b \ \text{ in } \ \Upsilon &: v^2 \sim 0.07. \end{aligned} \tag{2.59}$$

Thus, potential models self consistently predict a non-relativistic speed for the quarks within the Υ meson, and, to a lesser extent, within the J/ψ system too.

Such a result implies that a non-relativistic approximation to the QCD action would work [43]. The experimental status of the spectra reinforces this view. Both Υ and ψ have spin-independent splittings of $\mathcal{O}(500MeV)$, whereas the spin-dependent splittings such as the hyperfine are of $\mathcal{O}(100MeV)$ for the ψ and of $\mathcal{O}(50MeV)$ for the Υ. Thus a

picture emerges of spin-independent splittings which are unaffected by quark masses (*i.e.* zeroth order in v), with a finer spin-dependent structure where the different constituent quark masses do have an effect on the splitting. Combining these observations with equation 2.59, a theory with finer structure arising out of $\mathcal{O}(v^2)$ corrections to the zeroth order case may be appropriate.

One major point in favour of NRQCD is the relative ease of implementation. The problem becomes an initial value problem and is therefore computationally inexpensive to implement.

However, there is a sense in which bottomonium systems are not suited to lattice QCD. This is due to the dependence of NRQCD on three different scales: the mass ($\mathcal{O}(M)$), the 3-momentum ($\mathcal{O}(Mv)$) and the kinetic energy ($\mathcal{O}(Mv^2)$). In a lattice computation one needs a space-time grid which is large relative to $1/Mv^2$, but with a lattice spacing that is small compared to $1/M$. Unfortunately for the Υ $M/Mv^2 \sim 10$, which suggests that to achieve sensible finite volume and discretisation error sizes a lattice of size $\approx 100^4$ should be used. Such lattice sizes are computationally expensive. Now the quark mass is the least important of the three scales for the dynamics of a heavy quark system. So, removing it from the theory coarser lattices with $a \sim 1/M$ can be used to study the dynamics of the Υ. The procedure followed is to introduce an ultraviolet cut-off $\Lambda \sim M$. Thus relativistic heavy quarks are excluded from the theory. The expected heavy quark momentum is of order $Mv \ll M$, and so the cut-off doesn't remove the typical 3 momenta from the theory. Hence NRQCD actually makes it computationally cheaper to make lattice calculations of the Υ or J/ψ spectra.

2.3.2 Deriving NRQCD

As shown in section 2.3.1, the Dirac theory can be regularised by the inclusion of an ultraviolet cut-off, Λ [44]. For a non-relativistic interaction, with relativistic intermediate states, those intermediate states are virtual and thus do not propagate very far, *i.e.* they are local. Hence, the exclusion of such states may be compensated through the addition of local interaction terms in the Lagrangian. Such terms are added in powers of $1/\Lambda$. In general, a required accuracy of order $(p/\Lambda)^n$ will involve keeping terms in the Lagrangian up to and including $\mathcal{O}(1/\Lambda)^n$. The couplings of the local interaction terms are then determined by requiring that the regularised theory agrees with the unregularised one to order $(p/\Lambda)^n$.

This procedure becomes even more useful if combined with a *Foldy-Wouthuysen-Tani (FWT)* transformation [45] [46] [47]. A FWT transformation makes the following change to the Dirac theory:

$$\begin{aligned}\overline{\Psi}(\gamma^\mu D_\mu - M)\Psi \;\rightarrow\; & \psi^\dagger \left(iD_t - M + \frac{\mathbf{D}^2}{2M} \right) \psi \\ & + \psi^\dagger \left(\frac{g}{2M}\sigma \cdot \mathbf{B} + \frac{g}{8M^2}\nabla \cdot \mathbf{E} + \frac{\mathbf{D}^4}{8M^3} + \cdots \right) \psi.\end{aligned} \tag{2.60}$$

Here, Ψ is the 4-component Dirac spinor, whilst ψ is a two component Pauli spinor, such that ψ represents the quark, and $\psi^\dagger$ the anti-quark. In QCD, the fields $\mathbf{B}$ and $\mathbf{E}$ are the chromomagnetic and chromoelectric fields respectively. Combining both the FWT transform and the regularisation of the Dirac theory gives the cut-off, $\Lambda \sim M$. Thus, the $1/M$ FWT transformation is a $1/\Lambda$ transformation. In order to obtain an accuracy of $(p/\Lambda)^n = v^n$, only terms up to and including $\mathcal{O}(1/\Lambda^n)$ have to be retained.

The modern way of deriving NRQCD is to follow the method of Lepage *et al.* [48]. Their method involves the use of power counting rules to determine the size of the correction terms and then to include only the terms required for a certain level of accuracy.

2.3.3 Power counting in NRQCD

The power counting rules may be constructed from the observation that the number operator for a heavy quark in a quarkonium meson is very nearly unity.

$$\int d^3x \psi^\dagger(x)\psi(x) \approx 1 \tag{2.61}$$

From Heisenberg's Uncertainty Principle the quark is localised in a region $\Delta x \sim 1/p$. Thus, the mesonic 3-volume has magnitude:

$$\int d^3x \sim \frac{1}{p^3}. \tag{2.62}$$

So, $\psi^\dagger\psi \sim p^3$, or $\psi \sim p^{3/2}$. Similarly the kinetic energy operator has an expectation value of Mv^2 and so:

$$\int d^3x \psi^\dagger(x)\frac{\mathbf{D}^2}{2M}\psi(x) \sim Mv^2, \tag{2.63}$$

which gives $\mathbf{D} \sim Mv$. Schrödinger's equation for the heavy quark field is:

$$\left(iD_t + \frac{\mathbf{D}^2}{2M}\right)\psi(x) = 0. \tag{2.64}$$

Thus $D_t \sim Mv^2$.

In NRQCD the "natural" gauge to use is the *Coulomb Gauge* in which $\nabla \cdot \mathbf{A} = 0$. One consequence of using this gauge is that the vector potential is small (as will be seen shortly). In this gauge, equation 2.64, becomes:

$$\left(i\partial_t - g\phi(x) + \frac{\nabla^2}{2M}\right)\psi \approx 0, \tag{2.65}$$

yielding $g\phi(x) \sim K$. The field, ϕ, is the temporal component of the field A^μ. This result indicates that the potential energy which balances the kinetic energy for this bound system comes from the operator $g\phi$.

Operator	ψ	χ	D_t	$\mathbf{D}$	$g\phi*$	$g\mathbf{A}*$	$g\mathbf{E}*$	$g\mathbf{B}*$
Estimate	$(Mv)^{3/2}$	$(Mv)^{3/2}$	Mv^2	Mv	Mv^2	Mv^3	M^2v^3	M^2v^4

Table 2.2: Estimates of the orders of magnitudes of the fields and operators needed in the NRQCD action. *These estimates are specific to the Coulomb gauge.

From the Euler-Lagrange equations, this result can be checked, and the magnitude of the previously neglected spatial components, $\mathbf{A}$, estimated, by calculating:

$$\frac{\partial \mathcal{L}}{\partial A^\mu} = \partial_\nu \left(\frac{\partial \mathcal{L}}{\partial(\partial_\nu A^\mu)} \right). \tag{2.66}$$

Here the Lagrangian is the lowest order NRQCD Lagrangian, $\mathcal{L}_{NRQCD}$, given by:

$$\mathcal{L}_{NRQCD} = \psi^\dagger(x) \left(iD_t + \frac{\mathbf{D}^2}{2M} \right) \psi(x). \tag{2.67}$$

The results are the field equations for ϕ and $\mathbf{A}$:

$$\nabla^2 g\phi(x) = -g^2 \psi^\dagger(x)\psi(x), \tag{2.68}$$

$$\begin{aligned} \left(\partial_t^2 - \nabla^2\right) g\mathbf{A}(x) = & \frac{ig^2 \nabla\psi^\dagger(x)\psi(x)}{2M} \\ & - \frac{ig^2 \psi^\dagger(x)\nabla\psi(x)}{2M} \\ & + \partial_t(\nabla g\phi(x)). \end{aligned} \tag{2.69}$$

Note that equation 2.68 is calculated with no vector potential $\mathbf{A}$. From equation 2.68 $g^2 \sim v$. Substituting this result in equation 2.69 gives $g\mathbf{A}(x) \sim Mv^3$, confirming that for the Coulomb gauge, the vector potential in heavy quarkonium is smaller than the scalar potential by a factor of v. Knowledge of the relative magnitudes of ϕ and $\mathbf{A}$, allows an estimate of the magnitudes of the chromoelectric and chromomagnetic fields. These follow from the usual definitions of the 4 vector $(\phi, \mathbf{A})$:

$$\begin{aligned} g\mathbf{E} &= -\nabla g\phi + \cdots \sim pK, \\ g\mathbf{B} &= \nabla \times g\mathbf{A} + \cdots \sim K^2. \end{aligned} \tag{2.70}$$

Appropriately for a non-relativistic system the (chromo)magnetic fields are smaller than the (chromo)electric fields by a factor of v.

The powers of the various quantities used in NRQCD are shown in table 2.2.

2.3.4 Relativistic Corrections

Relativistic corrections to equation 2.67 must respect the symmetries of the theory, such as gauge invariance, parity, rotational invariance *etc.* For example, a term such as $\psi^\dagger \mathbf{E} \cdot \sigma \psi$,

is not allowed, as it is odd under parity, whereas the $\sigma \cdot \mathbf{B}$ term is allowed. Charge conjugation invariance demands that the action is symmetric under the interchange of the quark and antiquark fields, $\psi \leftrightarrow \chi$. These terms must also be local, and only those terms of a sufficiently high magnitude need to be included in the heavy quark action. So, a term which satisfies the symmetries of the theory, such as $\psi^\dagger \mathbf{B}^2 \psi / M$, but which is of order v^6, isn't included. In order to increase the accuracy of equation 2.67 by a factor of $\mathcal{O}(v^2)$ (and to give accuracy to lowest order in α_s [43]), only four terms bilinear in the heavy quark field are needed:

$$\begin{aligned} \delta\mathcal{L}_{\text{bilinear}} &= c_1 \frac{1}{M^3} \psi^\dagger \mathbf{D}^4 \psi \\ &+ c_2 \frac{g}{M^2} \psi^\dagger (\mathbf{D} \cdot \mathbf{E} - \mathbf{E} \cdot \mathbf{D}) \psi \\ &+ c_3 \frac{ig}{M^2} \psi^\dagger \sigma \cdot (\mathbf{D} \times \mathbf{E} - \mathbf{E} \times \mathbf{D}) \psi \\ &+ c_4 \frac{g}{M} \psi^\dagger \sigma \cdot \mathbf{B} \psi. \end{aligned} \tag{2.71}$$

The dimensionless coefficients c_i are functions of the running coupling constant α_s and mass, M. The Schrödinger equation is used to redefine temporal derivatives as spatial, in order to simplify the time evolution of the wavefunctions.

In equation 2.71, the $\mathbf{D}^4$ term comes from the expansion of the relativistic energy-momentum dispersion relation ($E^2 = p^2 + M^2$) to order Mv^4. The second term is known as the *Darwin* term. The fourth term splits states with the same orbital angular momentum quantum number, L, but which differ in their spin number ($e.g.$ $^3S_1$ and $^1S_0$), S. The third term splits states with the same L and S numbers, but different values of J ($^3P_{0,1,2}$).

As well as the previous correction terms there are *contact* and *colour* terms. The contact terms come from four fermion interactions, and are given by:

$$\begin{aligned} \delta\mathcal{L}_{\text{contact}} &\equiv d_1 \frac{1}{M^2} \psi^\dagger \chi \chi^\dagger \psi \\ &+ d_2 \frac{1}{M^2} \psi^\dagger \sigma \chi \cdot \chi^\dagger \sigma \psi. \end{aligned} \tag{2.72}$$

They are only suppressed by a factor of v from the terms in equation 2.67. However, such terms do not occur in continuum QCD and so their coefficients are of order α_s^2, making them less important than the bilinear interactions of equation 2.71. The colour terms again involve four fermion operators, this time coupling to coloured states. They are given by:

$$\begin{aligned} \delta\mathcal{L}_{\text{colour}} &\equiv d_3 \frac{1}{M^2} \sum_a \psi^\dagger T^a \chi \chi^\dagger T^a \psi \\ &+ d_4 \frac{1}{M^2} \sum_a \psi^\dagger T^a \sigma \chi \cdot \chi^\dagger T^a \sigma \psi. \end{aligned} \tag{2.73}$$

They have coefficients of order α_s^2. Such coupling is equivalent to virtual gluon emission in the meson, giving rise to the colour singlet meson becoming coloured. However, virtual gluon emission is suppressed by a factor of v^2, so the colour terms are even less important than the contact terms.

The combined heavy quark action of equations 2.67 and 2.71 has spin dependence suppressed by order v^2. Thus, it is about 10% of the size of the lower order terms. In order to determine the resulting spin splittings of the theory to an order of 10% one must then include spin dependent corrections to the level of v^4 relative to the leading terms. These new terms are:

$$\begin{aligned}\delta\mathcal{L}_{\text{spin}} &= f_1\frac{g}{M^3}\psi^\dagger\left\{\mathbf{D}^2, \sigma\cdot\mathbf{B}\right\}\psi \\ &+f_2\frac{ig}{M^4}\psi^\dagger\left\{\mathbf{D}^2, \sigma\cdot(\mathbf{D}\times\mathbf{E}-\mathbf{E}\times\mathbf{D})\right\}\psi \\ &+f_3\frac{ig^2}{M^3}\psi^\dagger\sigma\cdot(\mathbf{E}\times\mathbf{E})\,\psi.\end{aligned} \tag{2.74}$$

The operator $(\mathbf{E}\times\mathbf{E})$ is non-zero since QCD is a non-Abelian theory. The inclusion of such terms was studied on a lattice by *e.g.* Manke *et al.* [49]. They found that the shifts in splittings were of the anticipated order $\sim 10\%$. With a higher value of v^2 for the charmonium system, these corrections are more important for accurate J/ψ spectroscopy.

2.3.5 The Coefficients of Relativistic Corrections

With a suitable NRQCD cut-off ($\Lambda \sim M$) in place, the tree-level c_i may be determined. For c_1 in equation 2.71, the energy-momentum dispersion relation for a relativistic quark is used:

$$(\mathbf{p}^2+M^2)^{1/2} \approx M + \frac{\mathbf{p}^2}{2M} - \frac{\mathbf{p}^4}{8M^3}, \tag{2.75}$$

suggesting that the appropriate correction term is:

$$\delta\mathcal{L}_{\text{bilinear},c_1} = \frac{1}{8M^3}\psi^\dagger\mathbf{D}^4\psi, \tag{2.76}$$

yielding $1/8$ for c_1. To obtain the coefficients $c_{2,3}$ of equation 2.71, and the coefficient f_2 of equation 2.74, the amplitude of quark scattering off of a static electric field in QCD is calculated:

$$T_{\mathbf{E}}(\mathbf{p},\mathbf{q}) = \overline{u}(\mathbf{q})\gamma^0 g\phi(\mathbf{q}-\mathbf{p})u(\mathbf{p}). \tag{2.77}$$

Matching this result to NRQCD at small v involves an expansion, in $\mathbf{p}/M$ and $\mathbf{q}/M$. The Dirac spinor with non-relativistic normalisation ($u^\dagger u = 1$) is:

$$u(\mathbf{p}) = \left(\frac{E_p+M}{2E_p}\right)^{1/2}\begin{bmatrix}\psi \\ \frac{\sigma\cdot\mathbf{p}}{E_p+M}\psi\end{bmatrix}. \tag{2.78}$$

Substituting this expression in equation 2.77 yields:

$$\begin{aligned} T_{\mathbf{E}} &= \sqrt{\frac{(E_p+M)(E_q+M)}{4E_pE_q}} \\ &\quad \times\psi^\dagger\left[1+\frac{\mathbf{p}\cdot\mathbf{q}+i\sigma\cdot\mathbf{q}\times\mathbf{p}}{(E_q+M)(E_p+M)}\right]g\phi(\mathbf{q}-\mathbf{p})\psi \\ &\equiv S_{\mathbf{E}}(\mathbf{p},\mathbf{q})+V_{\mathbf{E}}(\mathbf{p},\mathbf{q}), \end{aligned} \tag{2.79}$$

where S and V stand for the vector and scalar parts of the amplitude respectively. Use has been made of the structure constants of $SU(2)$ via the formula:

$$\sigma_i\sigma_j = \delta_{ij} + i\epsilon_{ijk}\sigma_k. \tag{2.80}$$

Expanding equation 2.79 to order $\mathbf{p}^2, \mathbf{q}^2$ (see equation 2.75) gives for $S_{\mathbf{E}}$:

$$S_{\mathbf{E}}(\mathbf{p},\mathbf{q}) = \left(1-\frac{(\mathbf{p}-\mathbf{q})^2}{8M^2}\right)\psi^\dagger g\phi(\mathbf{q}-\mathbf{p})\psi. \tag{2.81}$$

The first term in this equation corresponds to the NRQCD term involving D_t of equation 2.67. Thus the D_t term has a coefficient of 1 in the NRQCD action. The second term in equation 2.81 corresponds to the $\mathbf{D}\cdot\mathbf{E}-\mathbf{E}\cdot\mathbf{D}$ term in equation 2.71. Hence, $c_2 = 1/8$. A similar procedure on $V_{\mathbf{E}}$ yields $c_3 = 1/8$ and f_2 in 2.74 is 3/64.

Following a similar procedure for quark scattering in a static vector potential $\mathbf{A}$:

$$T_{\mathbf{B}}(\mathbf{p},\mathbf{q}) = -\overline{u}(\mathbf{q})\gamma\cdot g\mathbf{A}(\mathbf{q}-\mathbf{p})u(\mathbf{p}). \tag{2.82}$$

The result compared to NRQCD makes $c_4 = 1/2$ and $f_1 = 1/8$. For the $\sigma\cdot\mathbf{E}\times\mathbf{E}$ part double scattering of a quark of a static electric field has to be considered, and it turns out that $f_3 = -1/8$.

Overall, the various constants needed in the theory have to be evaluated. The QCD coupling g, becomes a function of the spacing ($g = g(a)$) on a lattice, and is used to prescribe the lattice. The spacing a is determined in the region of interest by matching lattice splittings to experimental values. The quark mass, M, is tuned to give a meson mass which matches the experimental Υ kinetic mass (coming from the energy-momentum dispersion relation). The couplings, c_i, are calculated by calculating a scattering amplitude alternately in full QCD and in NRQCD. They are then adjusted to give agreement between both theories. Unfortunately, beyond the previous tree-level discussion, the c_i are of the form $1+\alpha_s A$, with A a function of the lattice bare quark mass, aM. This makes NRQCD non-renormalizable.

2.4 NRQCD on a Lattice

On the lattice a Euclidean metric is used. With such a metric, the NRQCD Lagrangian developed in previous sections becomes:

$$\begin{aligned}
\mathcal{L}_E &= \psi^\dagger(x)\left(D_t - \frac{\mathbf{D}^2}{2M}\right)\psi(x) + \mathcal{L}_{SI} + \mathcal{L}_{SD}, \qquad (2.83)\\
\mathcal{L}_{SI} &= \psi^\dagger(x)\left(-\frac{1}{8M^3}\mathbf{D}^4 + \frac{ig}{8M^2}(\mathbf{D}\cdot\mathbf{E} - \mathbf{E}\cdot\mathbf{D})\right)\psi(x),\\
\mathcal{L}_{SD} &= \psi^\dagger\left(-\frac{g}{8M^2}(\sigma\cdot\mathbf{D}\times\mathbf{E} - \sigma\cdot\mathbf{E}\times\mathbf{D}) - \frac{g}{2M}\sigma\cdot\mathbf{B}\right)\psi(x).
\end{aligned}$$

2.4.1 Discrete NRQCD Operators

On the lattice, derivatives become difference equations, and so the following operator definitions become useful (dropping the E subscript of previous sections):

$$\begin{aligned}
a\Delta_\nu^{(+)}\psi(x) &= U_\nu(x)\psi(x+a\hat{\nu}) - \psi(x), \qquad (2.84)\\
a\Delta_\nu^{(-)}\psi(x) &= \psi(x) - U_\nu^\dagger(x-a\hat{\nu})\psi(x-a\hat{\nu}), \qquad (2.85)\\
\Delta_\nu^{(\pm)}\psi(x) &= \frac{1}{2}(\Delta_\nu + \Delta_{-\nu}). \qquad (2.86)
\end{aligned}$$

These operators are known as forward, backward and centred differences respectively. The inclusion of lattice gauge field matrices ensures the retention of gauge invariance. Similarly, the continuum operator, $\mathbf{D}^2$ becomes the lattice Laplacian operator $\Delta^{(2)}$ given by:

$$\Delta^{(2)} = \sum_i \Delta_i^{(+)}\Delta_i^{(-)} = \sum_i \Delta_i^{(-)}\Delta_i^{(+)}. \qquad (2.87)$$

Then the lattice kinetic energy operator is:

$$H_0 = -\frac{\Delta^{(2)}}{2M}. \qquad (2.88)$$

The lattice version of the continuum field, $F_{\mu\nu}$, involves the cloverleaf operator, $\mathcal{P}_{\mu\nu}$, introduced in section 1.5.4 (see equation 1.57). This field carries the superscript (c) as a reminder that it is in cloverleaf form and not a simpler type. It is defined as:

$$\begin{aligned}
gF_{\mu\nu}^{(c)}(x) &= -\frac{1}{4a^2}\sum_{\mathcal{P}_{\mu\nu}(x)} \mathcal{I}\left[\mathcal{P}_{\mu\nu}(x)\right], \qquad (2.89)\\
\mathcal{I}[M] &\equiv \frac{M - M^\dagger}{2i} - \frac{I_3}{3}\mathrm{Im}(\mathrm{Tr}(M)),
\end{aligned}$$

where I_3 is the 3×3 identity matrix. From this definition, lattice $\mathbf{E}$ and $\mathbf{B}$ fields may also be defined allowing the extension of lattice NRQCD to $\mathcal{O}(v^4)$.

$$\begin{aligned} E^i(x) &= F^{(c)}_{0i}(x) \\ B^i(x) &= \frac{1}{2}\epsilon_{ijk}F^{(c)}_{jk}(x) \end{aligned} \tag{2.90}$$

The covariant derivatives of $F_{\mu\nu}$ are:

$$\begin{aligned} a\Delta^{(+)}_\omega F^{(c)}_{\mu\nu}(x) &\equiv U_\omega(x)F^{(c)}_{\mu\nu}(x+a\hat{\omega})U^\dagger_\omega(x) - F^{(c)}_{\mu\nu}, \\ a\Delta^{(-)}_\omega F^{(c)}_{\mu\nu}(x) &\equiv F^{(c)}_{\mu\nu}(x) - U^\dagger_\omega(x-a\hat{\omega})F^{(c)}_{\mu\nu}(x-a\hat{\omega})U_\omega(x-a\hat{\omega}). \end{aligned} \tag{2.91}$$

2.4.2 The Lattice Heavy Quark Evolution Equation to $\mathcal{O}(v^2)$

Using only the terms up to and including $\mathcal{O}(v^2)$ in equation 2.83 gives the heavy quark action on a lattice to that order (dropping the Euclidean subscript E):

$$S^{\mathcal{O}(v^2)} = a^3\sum_x(\psi^\dagger(x)\psi(x) - \psi^\dagger(x+a\hat{t})U^\dagger_4(x)(1-aH_0)\psi(x)). \tag{2.92}$$

The Green's functions of the theory satisfy the following equation:

$$\sum_y K(x,y)G(y,0) = \delta_{\mathbf{x},\mathbf{x}_0}\delta_{t,t_0}. \tag{2.93}$$

In this equation, $K(x,y)$ is the bilinear term appearing in the action. The heavy quark Green's function $G(y,0)$ is equivalent to $G(\mathbf{y},t_y;\mathbf{0},0)$. This gives the evolution equation for the heavy quark propagator (Green's function) as:

$$G^{\mathcal{O}(v^2)}(\mathbf{x},t+a;\mathbf{x}_0,t_0) = U^\dagger_4(x)(1-aH_0)G(\mathbf{x},t;\mathbf{x}_0,t_0) + \delta_{\mathbf{x},\mathbf{x}_0}\delta_{t+a,t_0}. \tag{2.94}$$

Fourier transforming the spatial components of this equation removes the Δs from H_0:

$$aH_0G(\mathbf{x},t;\mathbf{x}_0,t_0) = \left(\sum_i \frac{4\sin^2(p_ia/2)}{2Ma}\right)G(\mathbf{p},t;\mathbf{p}_0,t_0). \tag{2.95}$$

Unfortunately, $\max(aH_0) = 6/Ma$ for $\mathbf{p} = (\pi/a,\pi/a,\pi/a)$, leaving $|1-aH_0| \not< 1$ if $Ma < 3$, and the evolution matrix with eigenvalues of magnitude greater than unity. In order to attain a stable evolution, the following change has been made [48] to equation 2.94:

$$G^{\mathcal{O}(v^2)}(\mathbf{x},t+a;\mathbf{x}_0,t_0) = \left(1-\frac{aH_0}{2n}\right)^n U^\dagger_4(x)\left(1-\frac{aH_0}{2n}\right)^n G(\mathbf{x},t;\mathbf{x}_0,t_0) + \delta_{\mathbf{x},\mathbf{x}_0}\delta_{t+a,0}. \tag{2.96}$$

This equation is stable for $Ma > 3/2n$. By choosing an appropriate value of n stability is assured. However, as a result of this stabilisation unwanted terms are created, these must be accounted for.

Spatial Derivatives

Lattice spatial derivatives were defined in equations 2.84, 2.85, and 2.86. Expanding the gauge field, $U_j(x) = e^{igaA_j(x)}$ as an exponential and Taylor expanding $\psi(x + a\hat{j})$ gives:

$$a\Delta_j^{(+)} \equiv aD_j + \frac{a^2}{2}D_j^2 + \cdots, \tag{2.97}$$

$$a\Delta_j^{(-)} \equiv aD_j - \frac{a^2}{2}D_j^2 + \cdots, \tag{2.98}$$

$$a\Delta_j^{(\pm)} \equiv aD_j + \frac{a^3}{6}D_j^3 + \cdots. \tag{2.99}$$

They are accurate to $\mathcal{O}(a^2)$. The accuracy is extended to $\mathcal{O}(a^4)$ via the replacement of the Δs by new operators, the $\tilde{\Delta}$s. As an example, consider:

$$\tilde{\Delta}_j^{(+)} = \Delta_j^{(+)} - \frac{a}{2}(\Delta_j^{(+)})^2. \tag{2.100}$$

The new operators, $\Delta_j^{(-)}$ and $\Delta_j^{(\pm)}$, are similarly defined. By the same method, the lattice Laplacian operator, $\Delta^{(2)}$, is replaced by:

$$\tilde{\Delta}^{(2)} = \Delta^{(2)} - \frac{a^2}{12}\sum_j \left[\Delta_j^{(+)}\Delta_j^{(-)}\right]^2. \tag{2.101}$$

Temporal Derivatives

The status of temporal derivatives in NRQCD is different from that of spatial derivatives, as the theory is now non relativistic. This is useful as it makes the evolution of the Green's functions an initial value problem, rather than a boundary value problem like full QCD. A naïve reduction of temporal discretization errors, analogous to that for spatial errors, would introduce higher order temporal derivatives into the evolution, thereby ruining this simplicity.

As an alternative, we consider the evolution equation 2.96, neglecting the lattice gauge field link $U_t^\dagger(x)$[2], for $t > 0$ this is:

$$\begin{aligned} G(\mathbf{x}, t+a) &= \left(1 - \frac{aH_0}{2n}\right)^{2n} G(\mathbf{x}, t) \\ &= \mathrm{e}^{-aH_{\text{eff}}} G(\mathbf{x}, t), \end{aligned} \tag{2.102}$$

with the effective Hamiltonian, H_{eff} given by:

$$\begin{aligned} H_{\text{eff}} &\equiv -\frac{2n}{a}\ln\left(1 - \frac{aH_0}{2n}\right), \\ &= H_0 + \frac{a}{4n}H_0^2 + \cdots. \end{aligned} \tag{2.103}$$

[2]The gauge field part is automatically exponentiated anyway.

This motivates the introduction of a new Hamiltonian:

$$\tilde{H}_0 \equiv H_0 - \frac{a}{4n}H_0^2. \tag{2.104}$$

2.4.3 Reduction of Discretization Errors in the Lattice Chromoelectric and Chromomagnetic Fields

The lattice cloverleaf field, $F_{\mu\nu}^{(c)}$ only differs from the continuum field, $F_{\mu\nu}$, at the level of a^2. Lepage *et al.* [48] calculated a corrected clover-leaf operator accurate to $\mathcal{O}(a^4)$. It is:

$$\begin{aligned} g\tilde{F}_{\mu\nu}^{(c)}(x) &= \frac{5}{3}gF_{\mu\nu}^{(c)}(x) - \frac{1}{6}\left[U_\mu(x)gF_{\mu\nu}^{(c)}(x+a\hat{\mu})U_\mu^\dagger(x)\right. \\ &+ U_\mu^\dagger(x-a\hat{\mu})gF_{\mu\nu}^{(c)}(x-a\hat{\mu})U_\mu(x-a\hat{\mu}) \\ &- \left.(\mu \leftrightarrow \nu)\right]. \end{aligned} \tag{2.105}$$

However, this correction requires further modification when *tadpole improvement* is applied (see section 2.4.5).

2.4.4 The Heavy Quark Evolution Equation to $\mathcal{O}(v^4)$.

Using the power counting rules of section 2.3.3, summarised in table 2.2; it can be shown that the last 4 terms appearing in the Lagrangian 2.71 are of $\mathcal{O}(Mv^4)$. Thus, any discretization errors of magnitude $\geq Mv^4$ must be removed from a Lagrangian seeking accuracy of that order. This means that the correction terms to the lattice temporal derivative and Laplacian must be included. Hence, for the temporal derivative correction of equation 2.104, we have:

$$-\frac{a}{4n}H_0^2 \sim a(Mv^2)^2 \sim Mv^4. \tag{2.106}$$

Similarly, from equations 2.88 and 2.101:

$$\frac{a^2}{24M}\sum_i(\Delta_j^{(+)}\Delta_j^{(-)})^2 \sim \frac{a^2}{M}(M^2v^2)^2 \sim Mv^4. \tag{2.107}$$

These terms are then included in the final evolution equation. The status of the corrected clover-leaf field, $\tilde{F}_{\mu\nu}^{(c)}$, is more ambiguous. They are a factor $\mathcal{O}(a^2M^2v^2) \sim \mathcal{O}(v^2)$ (since $a \sim 1/M$) smaller. Likewise from equation 2.99 the corrected $\tilde{\Delta}^{(\pm)}$ is smaller by the same factor, relative to $\Delta^{(\pm)}$. Consequently their inclusion is not necessary to achieve accuracy to $\mathcal{O}(Mv^4)$.

However, Davies *et al.* [50] found that when they used a Lagrangian without the $\mathcal{O}(a^2M^2v^2)$ corrections, the bottomonium hyperfine splittings had fairly severe $\mathcal{O}(a^2)$ variation with lattice spacing. Bearing in mind the non-renormalisability of NRQCD it

is hoped that lattice results will have sufficiently reduced a dependence that they will be essentially independent of a, and so the unreachable continuum limit is not a major handicap. In order to reduce (or remove) the scaling behaviour, the terms in the $\mathcal{O}(Mv^4)$ Lagrangian responsible for the hyperfine splitting (*i.e.* those involving σ) ought to be corrected. Thus, there is a motivation for the corrections $\tilde{F}^{(c)}_{\mu\nu}$ and $\tilde{\Delta}^{(\pm)}$. The same effects turned up in the related charmonium calculation of Davies *et al.* [51].

Overall, the $\mathcal{O}(Mv^4)$ accurate evolution equation is (using the shorthand $G(\mathbf{x},t)$ instead of $G(\mathbf{x},t;\mathbf{x}_0,t_0)$) for a heavy quark created at a point $(\mathbf{x}_0,t_0)$:

$$G(\mathbf{x},t+a) = \left(1-\frac{a\delta H}{2}\right)\left(1-\frac{aH_0}{2n}\right)^n U_t^\dagger(x)\left(1-\frac{aH_0}{2n}\right)^n\left(1-\frac{a\delta H}{2}\right)G(\mathbf{x},t), \quad (2.108)$$

with initial condition:

$$G(\mathbf{x},t_0;\mathbf{x}_0,t_0) = \delta_{\mathbf{x},\mathbf{x}_0}. \quad (2.109)$$

The kinetic energy operator, H_0, is given by equations 2.87 and 2.88. The correction operator δH consists of the relativistic and discretization corrections:

$$\begin{aligned}\delta H &= -\frac{(\mathbf{\Delta}^{(2)})^2}{8M^3} + \frac{ig}{8M^2}(\mathbf{\Delta}^{(\pm)}\cdot\mathbf{E} - \mathbf{E}\cdot\mathbf{\Delta}^{(\pm)}, \quad (2.110)\\ &- \frac{g}{8M^2}\sigma\cdot(\tilde{\mathbf{\Delta}}^{(\pm)}\times\tilde{\mathbf{E}} - \tilde{\mathbf{E}}\times\tilde{\mathbf{\Delta}}^{(\pm)}) - \frac{g}{2M}\sigma\cdot\tilde{\mathbf{B}},\\ &+ \frac{a^2\Delta^{(4)}}{24M} - \frac{a(\Delta^{(2)})^2}{16nM^2},\\ \Delta^{(4)} &= \sum_j(\mathbf{\Delta}_j^{(+)}\mathbf{\Delta}_j^{(-)})^2. \quad (2.111)\end{aligned}$$

All that is required to extend this evolution equation to $\mathcal{O}(Mv^6)$ is the inclusion of the terms with coefficients f_1, f_2, f_3 of equation 2.74. Additionally the term $\mathbf{\Delta}^{(\pm)}\cdot\mathbf{E}$ differs from the naïve version of equation 2.86, in that for gauge invariance it has to be:

$$\Delta^{(\pm)}\cdot\mathbf{E} = \frac{1}{2a}\sum_j\left(U_j(x)E^j(x+a\hat{j})U_j^\dagger(x) - U_j^\dagger(x-a\hat{j})E^j(x-a\hat{j})U_j(x-a\hat{j})\right). \quad (2.112)$$

2.4.5 Radiative Corrections to the NRQCD Coupling Constants

In coupling NRQCD to QCD the calculations in $1/M$ expanded, full QCD were only carried out from the tree level amplitudes of type shown in equations 2.77 and 2.82. The accuracy of the coupling constants will thus break down when radiative corrections to the tree level amplitudes are considered. On the lattice these improved couplings should be calculable as the radiative corrections are dominated by momenta of $\mathcal{O}(\pi/a)$ or larger. With π/a typically several GeV, lattice perturbation theory in the weak coupling region ought to give a useful method of computing the improved values of $c_1,\cdots,c_4, f_1,\cdots,f_3$.

Unfortunately, when Monte Carlo estimates of suitably short distance quantities are compared to their lattice perturbatively calculated values, large discrepancies often

occur. Thus, the expectation value of $\langle 1 - 1/3\mathrm{Tr}U_\mu \rangle$ (the lattice equivalent of $\left\langle A_\mu^2 \right\rangle$ [52]), with U_μ a lattice gauge link calculated in lattice perturbation theory gives:

$$\left\langle 1 - \frac{1}{3}\mathrm{Tr}U_\mu \right\rangle_{\text{P.T.}} = 0.078, \tag{2.113}$$

which is almost half of the nonperturbative result:

$$\left\langle 1 - \frac{1}{3}\mathrm{Tr}U_\mu \right\rangle_{\text{M.C.}} = 0.139. \tag{2.114}$$

These results were obtained on a lattice with a small coupling constant ($\alpha_{\text{lat}} = 0.08$) and at a large loop momenta scale $\pi/a \equiv 6\text{GeV}$, *i.e.* where perturbation theory should have worked fairly well. The problem was that the expansion parameter, α_{lat}, was a poor choice of perturbative expansion parameter, a renormalised coupling scheme should have been used. As an example of the problem, consider the assumed interrelation between the continuum QCD gauge degrees of freedom and the lattice version:

$$U_\mu = \mathrm{e}^{igaA_\mu} \to 1 + igaA_\mu. \tag{2.115}$$

Explicitly letting the lattice spacing tend to zero should reproduce the continuum gauge field. However, in a fixed gauge terms such as $\left\langle A_\mu^2 \right\rangle$ quadratically diverge (leading to the expectation that it is dominated by high momenta of $\mathcal{O}(\pi/a)$) like $1/a^2$, so:

$$g^2a^2 \left\langle A_\mu^2 \right\rangle \to \mathcal{O}(g^2). \tag{2.116}$$

This effectively destroys the convergence between the continuum and the lattice in the continuum limit and necessitates a large renormalisation in order to make these agree. Such higher order terms ($\overline{\psi}A^2\psi$) are known as *tadpole contributions.* The method adopted here to increase the lattice-continuum convergence is to split the gauge fields into infra-red and ultraviolet modes, then to integrate out the offending ultraviolet modes, *i.e*:

$$U_\mu \to u_0^{\text{U.V.}} \mathrm{e}^{igaA_\mu^{\text{I.R.}}}, \tag{2.117}$$

where u_0 contains the integrated U.V. contribution. Following the convention in [52], the u_0 used in this thesis is defined as:

$$u_0^{(P)} = \left\langle \frac{1}{3}\mathrm{Tr}U_P \right\rangle^{1/4}. \tag{2.118}$$

A common alternative to this definition is to choose u_0 to be the mean value of the link variable:

$$u_0^{(L)} = \left\langle \frac{1}{3}\mathrm{Tr}U_\mu \right\rangle. \tag{2.119}$$

It should be noted the choice between using tadpole improvement from equation 2.118 or equation 2.119 does effect some results. In particular the lattice hyperfine

splitting ($1^3S_1 - 1^1S_0$) shows a significant discrepancy between results using the link and those using the plaquette versions of improvement. Both Shakespeare [53] and the SESAM [54] lattice collaboration indicate that the hyperfine splitting is larger under the link scheme.

Under this improvement, lattice gauge links are changed through:

$$U_\mu \rightarrow \frac{U_\mu}{u_0}, \tag{2.120}$$

with the important subsidiary consequence for cloverleaf NRQCD derived fields:

$$\begin{aligned} \mathbf{E}^{(c)} &\rightarrow \frac{\mathbf{E}}{u_0^4}, \\ \mathbf{B}^{(c)} &\rightarrow \frac{\mathbf{B}}{u_0^4}. \end{aligned} \tag{2.121}$$

Renormalising the lattice coupling g to give $\tilde{g}$, defined by $\tilde{g}^2 = g^2_{\rm lat}/u_0^4$, allows a much more continuum like lattice perturbative series to be constructed in the tadpole improved expansion parameter $\tilde{\alpha}_{\rm lat}$.

Morningstar [55] found that the corrections to the tree level couplings between QCD and NRQCD was $\approx 10\%$, and so they should only become significant at the $\mathcal{O}(Mv^6)$ for NRQCD. Consequently they have not been included here.

2.4.6 Tadpole Improvement of Lattice Cloverleaf Fields

In the light of equations 2.120 and 2.121 it is trivial to tadpole improve the lattice NRQCD operators except for the case of the improved cloverleaf tensor $\tilde{F}^{(c)}_{\mu\nu}$ of equation 2.105. Consider the term:

$$U_\mu(x)F^{(c)}_{\mu\nu}(x + a\hat{\mu})U^\dagger_\mu(x). \tag{2.122}$$

Substituting in the expression 1.57 gives four terms, one of which has the form:

$$U_\mu(x)U_\nu(x + a\hat{\mu})U^\dagger_\mu(x + a\hat{\mu} + a\hat{\nu})U^\dagger_\nu(x + a\hat{\nu})U_\mu(x)U^\dagger_\mu(x). \tag{2.123}$$

Since $U_\mu(x)U^\dagger_\mu(x) = 1$, this superficially six term expression has, in fact, only four terms. There is a similar cancellation down to four terms (this time occuring from the left) on the piece of $F^{(c)}_{\mu\nu}(x + a\hat{\mu})$ with structure $U^\dagger_\mu(x)\cdots$. The other two terms in the equation 2.122 have no cancellation. Thus, overall equation 2.122 evaluates to four terms, two with six gauge links and two with four gauge links.

In the code, gauge links are tadpole improved prior to this particular calculation via equation 2.120, so the terms which reduce to four gauge links will be over tadpole improved by a factor $1/u_0^2$. Overall, in order to correct for this problem, the following term needs to be added to equation 2.105 [56]:

$$+\frac{1}{3}\left(\frac{1}{u_0^2} - 1\right) F^{(c)}_{\mu\nu}(x). \tag{2.124}$$

2.5 Lattice Correlation Functions

The knowledge of how the Green's functions evolve has to be connected to the allowed channels (*i.e.* states with the appropriate quantum numbers) which undergo that evolution. The correlation function of these Green's functions behaves as a series of decaying exponentials parameterised by the energy eigenvalues of the evolution. Through the use of smearing functions the various eigenvalues can be extracted on smaller lattices.

The heavy quark action can be written as:

$$S_Q = \sum_{x,y} \psi^\dagger(x) K_Q(x,y) \psi(y). \tag{2.125}$$

The quark is created at x by $\psi^\dagger$ and destroyed at y by ψ. Here K is the inverse of the heavy quark Green's function. The antiquark action is:

$$S_A = \sum_{x,y} \chi^\dagger(x) K_A(x,y) \chi(y), \tag{2.126}$$

where $\chi^\dagger$ now creates an antiquark. The heavy quark annihilation operators transform as $\psi(x) \to G(x)\psi(x)$ under $SU(3)$ colour. $G(x)$ is an $SU(3)$ matrix. The quark creation operator will then transform as $\psi^\dagger \to \psi^\dagger G^\dagger$. Gauge invariance requires that the inverse Green's function transforms as $K_Q \to G K_Q G^\dagger$. The antiquark operators transform as the complex conjugate of the quark transform, $\chi \to G^* \chi$. This leads to the conclusion that the transformation property of K_A is $K_A \to G^* K_A G^{\mathrm{T}}$, suggesting that $K_A^* = K_Q$ [3]. This relation gives an important simplification, it is only necessary to calculate the quark Green's function, the antiquark function is then simply the complex conjugate.

Combining the heavy quark and antiquark creation operators creates a heavy meson. Projecting these operators to create a heavy meson with definite momentum, (carrying out the evolution is computationally faster in momentum space), we have:

$$M^\dagger(\mathbf{p},t) = \sum_{\mathbf{x_1},\mathbf{x_2}} \psi^\dagger_{i;\alpha}(\mathbf{x}_1,t) \Gamma_{i,j}(\mathbf{x}_1 - \mathbf{x}_2) \chi^\dagger_{j;\alpha}(\mathbf{x}_2,t) \mathrm{e}^{\frac{\mathrm{i}\mathbf{p}}{2}\cdot(\mathbf{x}_1+\mathbf{x}_2)}. \tag{2.127}$$

The subscripts i,j are colour indices and α the spin index for the quarks. The rôle of the Γ matrix is to increase the overlap of the meson with channels of appropriate quantum numbers. For example Γ differs for the ${}^3S_1$ channel and for the ${}^1S_0$. For ${}^3S_1$ there are 3 spin states (corresponding to the spin eigenvalues, in the z direction, say, of $S_z = 0, \pm 1$) and consequently part of its Γ is a Pauli spin matrix σ_k. The three such matrices give the three components of ${}^3S_1$. The corresponding part of $\Gamma_{{}^1S_0}$ is simply the identity which reproduces the single spin component of ${}^1S_0$.

A meson propagating with momentum $\mathbf{p}$ from time t_0 to time t in the is represented by the correlation:

$$\left\langle 0 | M(\mathbf{p},t) M^\dagger(\mathbf{p},t_0) | 0 \right\rangle. \tag{2.128}$$

[3] Unlike the full QCD case there are no γ_5 matrices involved in this relation. This is because γ_5 relates upper and lower components of Dirac spinors. The FWT [45] transformation which decouples upper and lower Dirac components also removes γ_5 matrices from the theory.

The correlation evaluates to:

$$\left\langle 0 \left| \sum_{\mathbf{y}_1,\mathbf{y}_2} \chi(\mathbf{y}_2,t)\chi^\dagger(\mathbf{0},t_0)\Gamma^\dagger_{(\mathrm{sk})}(\mathbf{y}_1-\mathbf{y}_2)\mathrm{e}^{-\frac{i\mathbf{p}}{2}\cdot(\mathbf{y}_1+\mathbf{y}_2)} \sum_{\mathbf{x}} \psi(\mathbf{y}_1,t)\psi^\dagger(\mathbf{x},t_0)\Gamma_{(\mathrm{sc})}(\mathbf{x})\mathrm{e}^{\frac{i\mathbf{p}}{2}\cdot\mathbf{x}} \right| 0 \right\rangle . \tag{2.129}$$

There is only one spatial point summed over $\mathbf{x}$ at the source time, t_0, as the second spatial point suggested in equation 2.127 has been eliminated thanks to translational invariance. There is no change of sign in the rearrangement of the Grassmann quark creation/annihilation operators as they only move across even numbers of like operators.

The quark and antiquark propagators are:

$$G_{i,j;\alpha,\beta}(\mathbf{y},t;\mathbf{x},t_0) = \left\langle 0,t|\psi_{i;\alpha}(\mathbf{y},t)\psi^\dagger_{j;\beta}(\mathbf{x},t_0)|0,t_0\right\rangle , \tag{2.130}$$

$$G^A_{i,j;\alpha,\beta}(\mathbf{y},t;\mathbf{x},t_0) = \left\langle 0,t|\chi_{i;\alpha}(\mathbf{y},t)\chi^\dagger_{j;\beta}(\mathbf{x},t_0)|0,t_0\right\rangle . \tag{2.131}$$

As $G^A = G^*$, equation 2.129 becomes:

$$\sum_{\mathbf{y}_1,\mathbf{y}_2} G^*(\mathbf{y}_2,t;\mathbf{0},t_0)\Gamma^\dagger_{(\mathrm{sk})}(\mathbf{y}_1-\mathbf{y}_2)\mathrm{e}^{-\frac{i\mathbf{p}}{2}\cdot(\mathbf{y}_1+\mathbf{y}_2)} \sum_{\mathbf{x}} G(\mathbf{y}_1,t;\mathbf{x},t_0)\Gamma_{\mathrm{sc}}(\mathbf{x})\mathrm{e}^{\frac{i\mathbf{p}}{2}\cdot\mathbf{x}}. \tag{2.132}$$

The sum over $\mathbf{x}$ propagates source terms $\Gamma_{(\mathrm{sc})}(\mathbf{x})\mathrm{e}^{\frac{i\mathbf{p}}{2}\cdot\mathbf{x}}$ to $\mathbf{y}_1$ at time t. Using this to rewrite $\sum_{\mathbf{x}}\cdots$ as $\tilde{G}(\mathbf{y}_1,t;\mathbf{x},t_0)$, and explicitly writing the colour and spin indices, the correlation function becomes:

$$\sum_{\mathbf{y}_1,\mathbf{y}_2} G^*_{k,j;\beta,\alpha}(\mathbf{y}_2,t;\mathbf{0},t_0)\Gamma^{(\mathrm{sk})\dagger}_{k,l}(\mathbf{y}_1-\mathbf{y}_2)\mathrm{e}^{-\frac{i\mathbf{p}}{2}\cdot(\mathbf{y}_1+\mathbf{y}_2)}\tilde{G}_{l,j;\beta,\alpha}(\mathbf{y}_1,t;\mathbf{x},t_0). \tag{2.133}$$

Inspection of the colour and spin indices shows that this expression is equal to:

$$\sum_{\mathbf{y}_1,\mathbf{y}_2} \mathrm{Tr}\left[G^\dagger(\mathbf{y}_2,t;\mathbf{0},t_0)\Gamma^\dagger_{(\mathrm{sk})}(\mathbf{y}_1-\mathbf{y}_2)\tilde{G}(\mathbf{y}_1,t;\mathbf{x},t_0)\right]\mathrm{e}^{-\frac{i\mathbf{p}}{2}\cdot(\mathbf{y}_1+\mathbf{y}_2)}. \tag{2.134}$$

For the calculation the correlator shown above is evaluated for each different gauge configuration and then averaged over to give the average meson correlation. Source terms are propagated from 4 maximally spaced points on the initial timeslice *i.e.* $t_0 = 0$, with another 4 from the middle timeslice $t_0 = T/2$. T is the temporal dimension of the lattice. In practice it took too long to propagate through the entire temporal extent of the lattice. Starting from $T/2$ increases the statistics..

2.5.1 Measurements from Correlation Functions

The calculation of the correlation function of the last section allows the measurement of the energies of lattice states in the large time limit. Consider the expression (in the Heisenberg representation [57]):

$$_H\left\langle 0|M_H(t)M^\dagger_H(t_0)|0\right\rangle_H . \tag{2.135}$$

The time evolution of the system occurs through the Heisenberg operators, and not through the state vectors, as in equation 2.128. Now this expression is transformed into the Schrödinger representation. In the Schrödinger representation the state vectors carry time dependence (*c.f.* the Schrödinger equation) as $|k,t\rangle_S = U(t,t_0)\,|k,t_0\rangle_S$, with the lattice (Euclidean space) evolution operator generically:

$$U(t,t_0) \equiv \mathrm{e}^{-aH(t-t_0)}. \tag{2.136}$$

The following transformation properties are defined for going between the two pictures:

$$|k\rangle_H = U^\dagger\,|k,t\rangle_S = |k,t_0\rangle_S\,, \tag{2.137}$$

$$M^H(t) = U^\dagger M^S U. \tag{2.138}$$

Thus equation 2.135 becomes:

$$\begin{aligned} &\to {}_S\left\langle 0,t_0\left|U^\dagger M_S U M_S^\dagger\right|0,t_0\right\rangle_S\,, \\ &= {}_S\left\langle 0,t\left|M_S U M_S^\dagger\right|0,t_0\right\rangle. \end{aligned} \tag{2.139}$$

Inserting a complete set of energy eigenstates, with:

$$\sum_{\text{states}} |m\rangle\,\langle m| = 1. \tag{2.140}$$

Equation 2.139 becomes:

$$\begin{aligned} &\sum_{\text{states}} {}_S\,\langle 0,t|\,M_S U\,|m\rangle\,\langle m|\,M_S^\dagger\,|0,t_0\rangle_S, \\ &= \sum_{\text{states}} {}_S\,\langle 0,t|\,M_S \mathrm{e}^{-aE_m t}\,|m\rangle\,\langle m|\,M_S^\dagger\,|0,t_0\rangle_S, \\ &= \sum_{\text{states}} |\langle\,0\,|M_S|\,m\,\rangle|^2\,\mathrm{e}^{-aE_m(t-t_0)}, \end{aligned} \tag{2.141}$$

where E_m is the energy of the state $|m\rangle$. Thus, the overlap of the meson annihilation operator in the Schrödinger equation, with the ground state and the mth state, gives the coefficient of the exponential decay of the mth state with time. In effect, there is a series of decaying exponentials, and so, in the limit, $t \to \infty$, all states decay with the last to do so being the lowest energy (ground) state, $|0\rangle$. this motivates the definition of the effective mass:

$$am_{\text{eff}}(t+1/2) = -\ln\left(\frac{C(t+1)}{C(t)}\right). \tag{2.142}$$

If this expression is plotted against time for large time values it should give a plateau at the mass of the ground state. In practice, lattices with large temporal extents are computationally very expensive. The extraction of energies can be made easier via the use of *smearing functions*, intended to increase the overlap of states and operators in equation 2.141 for the desired state. Smearing functions are dealt with in the next section.

$^{2S+1}L_J(J^{PC})$	Lattice Representation	Ω
$^1S_0(0^{-+})$	A_1^{-+}	I
$^3S_1(1^{--})$	$T_{1(i)}^{--}$	σ_i
$^1P_1(1^{+-})$	$T_{1(i)}^{+-}$	Δ_i
$^3P_0(0^{++})$	A_1^{++}	$\sum_j \Delta_j\sigma_j$
$^3P_1(1^{++})$	$T_{1(k)}^{++}$	$\Delta_i\sigma_j - \Delta_j\sigma_i$
$^3P_2(2^{++})$	$E_{(k)}^{++}$	$\Delta_i\sigma_i - \Delta_j\sigma_j$
	$T_{2(ij,i\neq j)}^{++}$	$\Delta_i\sigma_j + \Delta_j\sigma_i$

Table 2.3: The states analysed in this thesis for the $b\bar{b}$ system.

2.5.2 Lattice Meson Operators

In this section the structure of the operators $\Gamma^{(sk,sc)}$ is considered. These consist of two parts:

$$\Gamma(\mathbf{x}) = \Omega\phi(|\mathbf{x}|). \tag{2.143}$$

The operator Ω plays the rôle of differentiating between the allowed J^{PC} quantum numbers of lattice bottomonium states. States of the same J^{PC} (or $^{2S+1}L_J$) have the same Ω and so there will be mixing between the states $1^1S_0, 2^1S_0$ and 3^1S_0. The rôle of the smearing function ϕ is to differentiate such states, *i.e.* it extracts the principal quantum number n.

Choice of Ω

The operator Ω selects lattice states with the appropriate J^{PC} quantum numbers. These matrices are non-relativistic, 2×2 matrices, chosen so that mesonic operators (such as that shown in equation 2.127, exhibit the correct J^{PC}). For example, for the $^1S_0(0^{-+})$ correlator, $\Omega = I_2$, the 2×2 identity matrix, for the $^3S_1(1^{--})$ correlator, the three values of S (or J) correspond to the three Pauli spin matrices σ_i. It has been shown [30] that these values of Ω do indeed reproduce the hoped for J^{PC} numbers. All the values of Ω for the states used in this thesis are shown in table 2.3.

The lattice representation entries of table 2.3 are shown. They arise as a consequence of the discretisation. The orbital angular momentum quantum numbers in the continuum arise through the identification of the appropriate operators as proportional to the generators of the continuous group $SO(3)$. On the lattice, rotations must be discrete and so the angular momentum representations differ from the physical case. For most of the states shown in table 2.3 there is a 1-1 correspondence between the continuum and lattice angular momentum states, the major difference is that the continuum $^3P_2$ state splits into two lattice channels: $^3P_{2E}$ and $^3P_{2T}$.

Smearing Functions

The Ω operators of the previous section maximise overlap with correlators possessing the desired J^{PC} quantum numbers. However, each such channel consists of a series of radially different states, which vary in the principal quantum number. Thus, the use of $\Omega = \sigma_i$ makes the correlation function overlap with not just the 1^3S_1 channel, but with $2^3S_1, 3^3S_1 \cdots$. To do this, it is necessary to vary the function $\phi(|\mathbf{x}|)$ in equation 2.143, in such a way that $|\langle 0 | M_S(\phi_m) | m \rangle|$ of equation 2.141 is maximised, whilst terms such as $|\langle 0 | M_S(\phi_m) | n(\neq m) \rangle|$ are minimised. This process is known as *smearing*, and the functions, ϕ, are called *smearing functions.*

The smearing function for S states could be an operator with zero separation between the quark and antiquark operators, however, all radial S state excitations have a non-zero wavefunction at the origin, and so such an operator would overlap with all the states $1S, 2S, \cdots$. Instead, the operator is chosen to have a non-zero quark-antiquark separation, *i.e.* it is "smeared" across the lattice 3-space.

The form of the final correlation function of equation 2.134 isn't gauge invariant. Such a quantity will vanish when the ensemble average is taken. There are two possible ways around this problem. One is to connect the (spatially separated) quark and antiquark operators in the correlation function by a series of gauge field links, thereby making the correlation function gauge invariant. Such a method has been successfully applied by Manke *et al.* [49], and Lacock *et al.* [58]. The latter found that by varying the shape of the gauge link path between the quark and antiquark they could change the overlap with the desired channel. for example a "U" shaped chain of links overlapped well with lattice hybrid mesons, and a straighter chain overlapped with the P and D waves. The overlap with particular radial states could then be improved by varying the quark antiquark separation [18]. The second way to solve this difficulty, (and the method adopted here) is to use *gauge fixing*[4]. By fixing an overall lattice gauge the non gauge-invariant correlation function doesn't vanish when the ensemble average is taken. The chosen gauge was the *Coulomb Gauge*, defined as the gauge in which:

$$\nabla \cdot \mathbf{A} = 0. \tag{2.144}$$

This gauge was used as it is the natural gauge for non-relativistic systems. As an example, consider the power counting arguments of section 2.3.3. Calculating the field equations in the Coulomb gauge led to a form of the covariant spatial derivative with a suppressed $\mathbf{A}$ field, and a lowest order "Schrödinger type" evolution equation, 2.65.

Choice of Smearing Functions

The smearing function $\phi(|\mathbf{x}|(\neq 0))$ are chosen purely to have different overlaps with appropriate orbital excitations. The exact form of the ϕ is not important, what matters is that they possess the qualitative properties of the appropriate wavefunction. Thus, it

[4]Gauge fixing was implemented using a Fourier accelerated steepest descents mehtod

is only important for S state ϕs that they are symmetric and non-zero at the origin, in mimicry of physical S states. The ϕs could then be, for example, Gaussian functions. Other methods involved using wavefunctions obtained from potential models [59]. The method adopted here was to use radial *hydrogenic* wavefunctions.

Hydrogenic wavefunctions for the wavefunction of the hydrogen state $n^{2S+1}L_{L+S}$ are obtained via separating the wavefunction $\psi_{n,L,S}$ into a radial function and a spherical harmonic:

$$\psi_{n,L,S} = R_{n,L}(r)Y_{L,S}(\theta,\phi), \tag{2.145}$$

where r, θ and ϕ are spherical coordinates. For this thesis, the S smearing functions are taken as $R_{1,0}, R_{2,0}$ and $R_{3,0}$, (without the usual atomic number dependence) [60]:

$$\begin{aligned}
\phi_g^S(r, r_0^S) &= \exp(-r/r_0^S), & (2.146)\\
\phi_e^S(r, r_0^S) &= (2r_0^S - r)\exp(-r/2r_0^S), & (2.147)\\
\phi_d^S(r, r_0^S) &= (27(r_0^S)^2 - 18r_0^S r + 2r^2)\exp(-r/3r_0^S), & (2.148)
\end{aligned}$$

where the labels g, e, d (ground, excited, doubly excited) refer to the radial hydrogenic functions $R_{1,0}, R_{2,0}$ and $R_{3,0}$ respectively.

P Waves differ from S waves in that they have vanishing wavefunction at the origin. They were constructed from the S state smearing functions by:

$$\begin{aligned}
(\phi_{g,e}^P(r))_x &= |x|\phi_{g,e}^S(r, r_0^P), & (2.149)\\
(\phi_{g,e}^P(r))_y &= |y|\phi_{g,e}^S(r, r_0^P), & (2.150)\\
(\phi_{g,e}^P(r))_z &= |z|\phi_{g,e}^S(r, r_0^P), & (2.151)
\end{aligned}$$

where $()_{x,y,z}$ pick out the x, y and z direction P state smearing functions. The "Bohr radius", r_0, has separate values for P and S smearing since the value $r_0^P = (1/2)r_0^S$ gives better results than straightforward equality. Thus, r_0^S and r_0^P are varied independently, neither should be confused with a lattice version of the Bohr radius; they are simply adjusted to give the best results[5]. The d subscript is dropped for the P state smearing since the only radial states considered are the $1P$ and $2P$ states.

These smearing functions enter the Γ matrices of equation 2.143, and from there into equation 2.134. Inspection of equation 2.134 shows that Γ is applied at both the source (sc) and the sink (sk). Whilst all sources are smeared, some of the sinks are only multiplied by delta functions, a process known as local smearing.

[5] "Best" results were achieved by optimising the smearing. This involves varying r_0 until the effective mass plots for radially different correlators have as little overlap as possible.

2.6 Fitting

2.6.1 Expected Functional Form of the Lattice Smeared Correlation Functions

Analysis of smeared meson correlation functions should allow for the calculation of lattice state energies via equation 2.141. The simplest way to do this is to calculate the effective mass as shown in equation 2.142. In practice, however, the smeared correlators decay quickly to the ground state, and the effective mass is only really reliable for the lattice ground state (see section 3.4).

The method used to extract the ground state *and* radial excitations is to fit several correlators simultaneously to the expected functional form for a correlator [61] [62]. There are two possible forms considered here. A *matrix fit* fits the complete set of correlators, with the source and sink smearing taking all possible values. It has the form:

$$C_{\text{fit}}(n_{\text{sc}}, n_{\text{sk}}; t) = \sum_{m=1}^{N_{\text{exp}}} a(n_{\text{sc}}, m) a^*(n_{\text{sk}}, m) \mathrm{e}^{-aE_m(t-t_0)}. \tag{2.152}$$

Here, the number of different lattice states under consideration is given by N_{exp}. For S states this is 3, whereas for P states, only 2. Thus, for S states the smearing combinations $(n_{\text{sc}}, n_{\text{sk}})$ have the values (g,g), (g,e), (g,d), (e,g), (e,e), (e,d), (d,g), (d,e) and (d,d). For the P states, only those combinations involving e and g were used. The second functional form is a *vector (or row) fit.* For this thesis vector fits were carried out on those correlators with local (delta function) smearing at the sink. The functional form is:

$$C_{\text{fit}}(n_{\text{sc}}, \text{loc}; t) = \sum_{m=1}^{N_{\text{exp}}} b(n_{\text{sc}}, m) \mathrm{e}^{-aE_m(t-t_0)}. \tag{2.153}$$

Thus, for S states the combinations utilised are (g,loc), (e,loc) and (d,loc)[6], and the P states again only those for g and e.

Comparing equation 2.152 with equation 2.141 gives the identities:

$$a(n_{\text{sc}}, m) = \langle m | M^\dagger_{\text{sc}} | 0 \rangle, \tag{2.154}$$

$$a(n_{\text{sk}}, m) = \langle m | M^\dagger_{\text{sk}} | 0 \rangle. \tag{2.155}$$

Making the substitution $n_{\text{sk}} = \text{loc}$ in equation 2.152, gives the further identity:

$$b(n_{\text{sc}}, m) = a(n_{\text{sc}}, m) a^*(\text{loc}, m). \tag{2.156}$$

The fitting parameters may also be used to give information about the wavefunction at the origin (see section 3.7).

[6]The sink smearing doesn't have to be loc in order to do a vector fit, a vector fit could be carried out on (g,g), (e,g) and (d,g), for instance. In that case, however, the functional form of equation 2.153 would have to be different. Such fits were not necessary in this thesis.

2.6.2 Analysing Fit Quality

The quality of the fit can be improved by seeking to minimise the χ^2 value of the fit [61], [11]. To do this, the correlation functions were first averaged over all runs (N_{runs}). This is equal to the product of the number of configurations and the number of origins per configuration (results of tests for autocorrelations between configurations and origins on the same configuration are shown in the next chapter). The average correlator is given by:

$$\overline{C_\alpha(t)} = \sum_{i=1}^{N_{\text{runs}}} (C_\alpha(t))_i. \tag{2.157}$$

where Greek indices label the different types of correlators. The *covariance matrix* is then defined as:

$$\sigma^2_{\alpha\beta}(t,t') = \frac{1}{N_{\text{runs}}} \sum_{j=1}^{N_{\text{runs}}} (C_\alpha(t) - \overline{C_\alpha(t)})(C_\beta(t') - \overline{C_\beta(t')}). \tag{2.158}$$

Thus, $\sigma_{\alpha\alpha}(t,t)$ simply gives the usual variance in any one correlator (*i.e.* the variance in the absence of correlations between different correlators). In the case with $\alpha \neq \beta$ simultaneity enters into the results as different correlators (fitting to the same energies by equations 2.152 and 2.153) are analysed together.

Calling the theoretical formula to be fitted to C_{fit}, the χ^2 function is given by:

$$\chi^2 = \sum_{1<(\alpha,\beta)<N_{\text{corr}}} \sum_{t_{\min}<(t,t')<t_{\max}} \left(C^\alpha_{\text{fit}}(t;\lambda_i) - \overline{C^\alpha(t)}\right) (\sigma^2)^{-1}_{\alpha,\beta}(t,t') \left(C^\beta_{\text{fit}}(t';\lambda_i) - \overline{C^\beta(t')}\right). \tag{2.159}$$

Here, the parameters λ_i represent the fit parameters: the amplitudes and energies appearing in equations 2.153 and 2.152. The best fit of the form C_{fit} to the data will occur for the minimum value of χ^2, *i.e.* where $\lambda_i = \overline{\lambda_i}$. Knowing these best fit parameters it only remains to work out the error on such parameters, or what range of λ_i give good fits. To do this χ^2 is shifted by 1 from its minimum. Defining the values of λ_i at the minimium of χ^2 as λ_i^{fit}, then Taylor expanding around a minima yields [59]:

$$\begin{aligned} \delta\chi^2 &= \chi^2(\lambda_i^{\text{fit}}) + \delta\lambda_j \frac{\partial\chi^2}{\partial\lambda_j}\bigg|_{\lambda_i^{\text{fit}}} + \frac{1}{2}\delta\lambda_j\delta\lambda_k \frac{\partial^2\chi^2}{\partial\lambda_j\partial\lambda_k}\bigg|_{\lambda_i^{\text{fit}}} - \chi^2(\lambda_i^{\text{fit}}), \\ &= \frac{1}{2}\delta\lambda_j\delta\lambda_k \frac{\partial^2\chi^2}{\partial\lambda_j\partial\lambda_k}\bigg|_{\lambda_i^{\text{fit}}}. \end{aligned} \tag{2.160}$$

Thus, a parameter can be changed infinitesimally by $\delta\lambda_i$ ($i \neq j,k$) and $\delta\chi^2$ remains 1. Whereas changing λ_j shifts $\delta\chi^2$ from 1. From these values the error on λ_j is taken as being $\sigma_j \equiv \delta\lambda_j$.

Knowing χ^2 it is possible to assess the quality of the fit. Defining the number of degrees of freedom as $\nu = N_{\text{runs}} - N_{\text{params}}$, with N_{params} the total number of parameters,

i.e. for λ_i, $i = 1 \cdots N_{\text{params}}$, a measure of the quality of the fit is given by [61]:

$$Q\left(\frac{\nu}{2}, \frac{\chi^2}{2}\right) \equiv \frac{1}{\Gamma\left(\frac{\nu}{2}\right)} \int_{\frac{\chi^2}{2}}^{\infty} \mathrm{e}^{-t} t^{\frac{\nu}{2}-1} dt. \tag{2.161}$$

Here, $\Gamma()$ is the familiar *Gamma function*, defined as:

$$\Gamma(a) = \int_0^{\infty} t^{a-1} \mathrm{e}^{-t} dt. \tag{2.162}$$

It is easy to see that Q possesses the limiting values:

$$Q\left(\frac{\nu}{2}, 0\right) = 1 \quad \text{and} \quad Q\left(\frac{\nu}{2}, \infty\right) = 0. \tag{2.163}$$

Thus, the smaller the χ^2 of the fit the closer Q comes to unity. The function $Q\left(\frac{\nu}{2}, \frac{\chi^2}{2}\right)$ is the probability that the observed value of the chi-square will exceed χ^2 by chance even for a correct model. Thus, the higher the value of Q the higher the quality of the fit. Generally $Q > 0.1$ is considered sufficient for an acceptable fit. Poor fits tend to be characterised by extremely small values of Q, although occasionally models with small Qs such as $Q \sim 10^{-3}$ may be acceptable, Conversely $Q = 1$ should be treated with suspicion as being perhaps too good [61].

Chapter 3

Upsilon Spectroscopy on the Lattice

3.1 Introduction

The calculation was carried out on four sets of configurations. Three of these were "matched" dynamical configurations, i.e. they had the same lattice volume and spacing but different sea quark masses. This was achieved by varying κ (and hence by equation 1.45 m_{sea}) and adjusting β and C_{SW} accordingly. The remaining set was a quenched set on the same lattice volume. However, when this calculation was done no quenched configurations were available with the same lattice spacing as the dynamical. Thus the calculation used the quenched configurations with lattice spacing nearest to the dynamical ensembles.

The dynamical configurations suffer from autocorrelations. To combat this the configurations chosen for the calculation were thought to have had a greater separation in Monte Carlo step space than the measured length of the autocorrelations [26]. Checks were then carried out to see if the maximally spaced configurations were indeed decorrelated. No evidence for the existence of autocorrelations was found. In figure 3.1 plots are shown for the jackknife error on a secondary quantity, the effective mass (see equation 3.10). The presence of autocorrelations amongst such an ordered (in terms of Monte carlo step number) ensemble would manifest itself as an increase in the jackknife error with an increase in the length of bins used (see section 1.6.2). The bin length beyond which no clear increase in error can be found would be the length of the autocorrelated region in Monte Carlo space. It is clear from those results that there is no consistent autocorrelation amongst the data. No evidence of residual autocorrelations was found for the effective masses in this thesis. For the quenched case more configurations were used as they were decorrelated anyway.

For each configuration 8 origins were chosen, 4 with maximum spatial separation on the first timeslice and the same at the middle timeslice. With time constraints the heavy quark evolution equation was only carried out for 16 timeslices from each origin, hence starting from the middle timeslice ensured that the entire temporal extent of the lattice was utilised. The parameters for these configurations are listed in table 3.1.

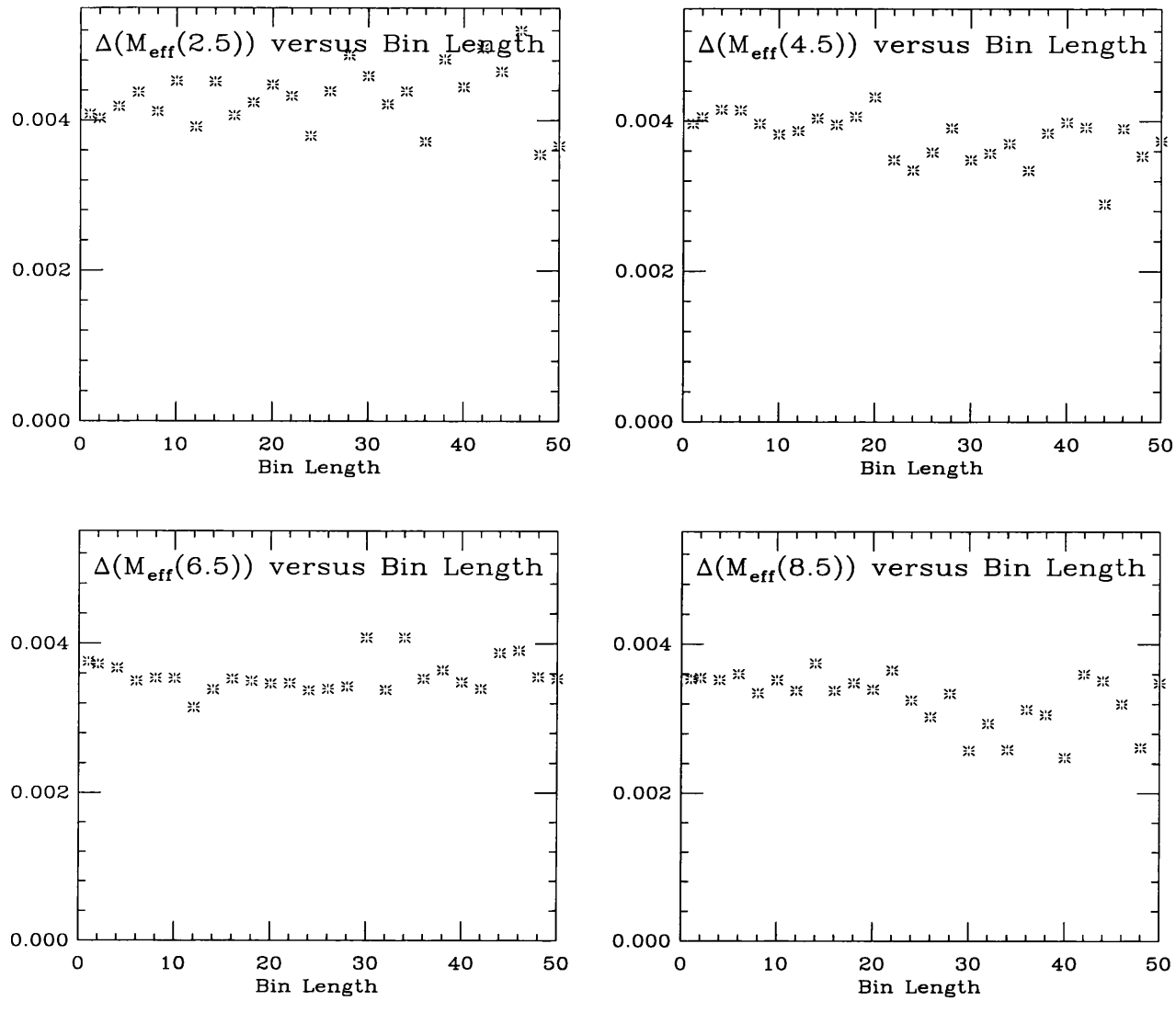

Figure 3.1: Plots of the jackknife errors on the effective masses for the ${}^3S_1$ propagator, with n_{sc}=n_{sk}=g. The argument of M_{eff} is the timeslice. Data from the dynamical run with β=5.29, κ=0.134, C_{SW}=1.92, and aM_b=1.8.

Volume(L^3T)	β	κ	C_{SW}	u_0	# of cfgs.	aM_b^0
$16^3 32$	5.2	0.135	2.02	0.855	99,103	1.8,2.1
$16^3 32$	5.26	0.1345	1.95	0.857	106,112	1.8,2.1
$16^3 32$	5.29	0.134	1.92	0.858	100,100	1.8,2.1
$16^3 48$	6.0	*	*	0.878	162,163	1.55,1.8

Table 3.1: Parameters for the lattice calculations used in this thesis. *Quenched. For the dynamical configurations the definition of β is equation 1.53, κ is equation 1.45 and for C_{SW} equation 1.65.

There are several different numbers of configurations listed for each different lattice, as the calculations were carried out for different quark masses in order to yield two values of the Υ kinetic mass.

3.2 Calculating the Lattice Spacing

A lattice used for Upsilon spectroscopy must have suitable dimensions relative to some of the scales associated with the Upsilon. It should have a lattice spacing small enough to resolve the length scale of a typical b quark momentum inside the Υ. It should also have enough lattice sites to make the overall lattice length big enough to cover the length scale for the quark kinetic energy. Following section 2.3.3, these scales are, $\mathcal{O}(1/Mv)$, or $\sim 0.2fm$, for the quark momentum, and $\mathcal{O}(1/Mv^2)$, or $\sim 0.5fm$ for the quark kinetic energy. Beyond these criteria it is desirable to make the lattice spacing as small as possible. A small a gives smaller discretisation errors, and prevents the perturbative expansion of the lattice coupling constant from diverging. However, the smaller a is made the more computationally expensive is the Monte Carlo. Indeed, for the dynamical configurations used in this thesis, the relationship is [27]:

$$\frac{\text{Tflophrs}}{\text{configuration}} = 13\left(\frac{L}{3\text{fm}}\right)^5\left(\frac{0.1\text{fm}}{a}\right)^{8.25}\left(\frac{m_s/2}{m_{\text{dyn}}}\right)^{3.25}, \tag{3.1}$$

where L is the number of sites on a side of the lattice, m_s the strange quark mass and m_{dyn} the dynamical quark mass. Thus, there is a trade-off between the accuracy of the calculation, and its feasibility.

The actual method used to calculate the lattice spacing was to measure the lattice splitting $a(E(1^1P_1) - E(1^3S_1))$ and then comparing this to the experimental value of the $\overline{\chi_b} - \Upsilon$ splitting. $\overline{\chi_b}$ is defined (dropping the flavour subscript and replacing it with the notation χ_J, where J is the angular momentum quantum no.) as:

$$\overline{\chi} = \frac{\chi_0 + 3\chi_1 + 5\chi_2}{9}. \tag{3.2}$$

The lattice $^1P_1$ state is used rather than $\overline{^3P}$ as it is directly calculated in the code, it is expected to have the same mass[1]. The truth of this assertion was tested for my data. The results indicate that there was no significant difference in mass between the $^1P_1$ and $\overline{^3P}$ states (see tables 3.21 and 3.22).

Using this method, the lattice spacings for the various ensembles were measured and found to have values around 0.07fm (quenched) and 0.09fm (dynamical). All had spatial extents of 16 lattice sites, making the overall lattice dimensions 1.1fm (quenched) and 1.4fm (dynamical). So they satisfy the momentum-energy scale criteria mentioned previously. The individual results are shown in tables 3.23, and 3.24.

[1]Any splitting between these states would come from V_{SS} (equation 2.29). However, V_{SS} doesn't affect P states.

3.3 Interpolating to the Meson Kinetic Mass

For NRQCD theory to match experiment, the bare quark mass M_b^0 used in the NRQCD evolution equation has to be chosen to reproduce an experimental result. Whilst spin independent splittings don't have much M_b^0 dependence, spin dependent splittings do. Indeed, the hyperfine splitting ($^3S_1 - ^1S_0$) is thought to vary inversely with M_b^0 (see section 2.2.4).

For a wholly non-relativistic Υ particle the energy at a non-zero momentum, $E(\mathbf{p} \neq \mathbf{0})$ should differ from the Υ energy at zero momentum according to the formula:

$$E_\Upsilon(\mathbf{p}) - E_\Upsilon(\mathbf{0}) = \frac{\mathbf{p}^2}{2M_{kin}}. \tag{3.3}$$

This ansatz was used previously [59] to test the suitability of the choice of aM_b. The parameter M_{kin} is known as the kinetic mass. This should match the experimental Υ mass of 9.46GeV. This formula comes from the Lorentz invariant energy-momentum dispersion relation:

$$E^2(\mathbf{p}) = \mathbf{p}^2 + M^2. \tag{3.4}$$

where M is the rest mass of the particle. However, for NRQCD, the momentum of the Υ is small relative to the mass and so $E(\mathbf{p})$ may be expanded as:

$$E(\mathbf{p}) = M_0 + \frac{\mathbf{p}^2}{2M_1} - \frac{\mathbf{p}^4}{8M_2^3} + \cdots. \tag{3.5}$$

Here the parameter, M_0, looks like the rest mass for the meson. However, just as with full QCD, NRQCD uses the bare quark mass as an arbitrary input parameter. This lattice "rest mass", M_0, is adjusted to reproduce experimental results, it is not something that should be regarded as a lattice observable. The quantity that was initially measured for this thesis was the kinetic mass of eqn. 3.3, or M_1 in eqn. 3.5. Similarly, M_1 differs from M_2 because there are other terms (higher order in $\mathbf{p}$) in the expansion. All of these additional terms would need to be included before the condition $M_1 = M_2$ is met.

An alternative way of accounting for these higher order corrections is to use the "more correct" version of equation 3.3. This involves no expansion in $\mathbf{p}$, and is given by:

$$E_\Upsilon(\mathbf{p}) - E_\Upsilon(\mathbf{0}) = \left(\mathbf{p}^2 + M_{kin}^2\right)^{1/2} - M_{kin}. \tag{3.6}$$

Thus, the kinetic mass is:

$$M_{kin} = \frac{\mathbf{p}^2 - (\Delta E(\mathbf{p}))^2}{2\Delta E(\mathbf{p})}, \tag{3.7}$$

where ΔE is defined as:

$$\Delta E(\mathbf{p}) = E(\mathbf{p}) - E(\mathbf{0}). \tag{3.8}$$

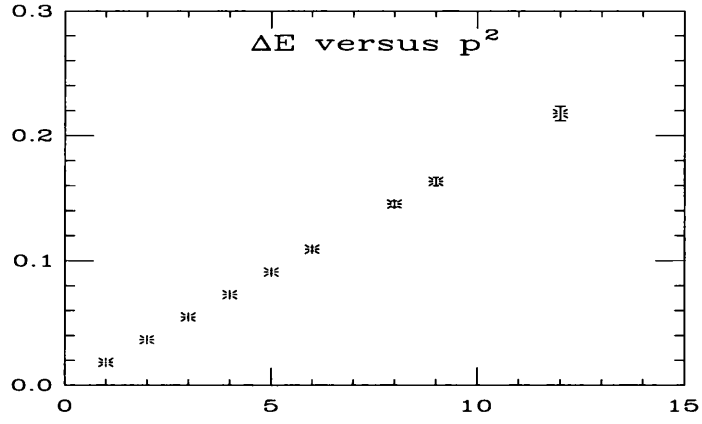

Figure 3.2: The energy difference of small momenta upsilon correlators from zero momenta correlators plotted against the squared lattice momenta. Data from the dynamical run with β=5.2, κ=0.135, C_{SW}=2.02 and aM_b^0=1.8

So, in order to set the bare quark mass accurately, the difference between the meson energies at small momenta, and this arbitrary lattice "rest mass" was calculated, and an estimate of the meson kinetic mass could be made from the ansatz forms of equations 3.3 and 3.7. The inputted bare quark mass, aM_b^0 was varied until the measured meson kinetic mass nearly reproduced the experimental value.

The method adopted to find this point was to use two different values of M_b^0. They were chosen to yield one M_{kin} above, and one below the experimental value for the Υ. Then the results could be interpolated to the experimental result giving a tighter constraint on the final answer, and providing information on the variation of lattice masses and splittings with the bare mass.

For the calculation, ${}^3S_1$ propagators with a smeared source and a local sink were used. There were propagators for small $\mathbf{p}$ up to (p_x, p_y, p_z) of $(\pm 2, \pm 2, \pm 2)$, in units of $2\pi/La$, where L is the size of the spatial dimensions of the lattice (16 in all cases), and a is the lattice spacing. Thus, overall, there were propagators with squared lattice momenta taking values throughout the set of Miller indices up to and including 12, i.e. $p^2 = 1, 2, 3, 4, 5, 6, 8, 9, 12$. There were no values for $p^2 = 7, 10, 11$. This is because there are no integers n_x, n_y, n_z with, $n_{x,y,z} \leq 2$, such that:

$$n_x^2 + n_y^2 + n_z^2 = 7, 10, 11. \tag{3.9}$$

Figure 3.2 shows a plot of $\Delta E(\mathbf{p}^2)$ against $\mathbf{p}^2$.

Values of M_{kin} were generated using both eqn. 3.3 and eqn. 3.7. The results are shown in table 3.2.

Clearly more statistics are required to make these methods distinguishable. Nevertheless the results from eqn. 3.7 indicate that the relativistic method gives a more

Table 3.2: Relativistic and non-relativistic calculations of aM_{kin} for the dynamical run at β=5.2, κ=0.135, C_{SW}=2.02 and aM_b^0=1.8.

$\mathbf{p}_i^2$	$\mathbf{p}_i^4$	Relativistic	Non-relativistic
1	1	4.188(48)	4.197(48)
2	2	4.187(51)	4.205(51)
3	3	4.186(55)	4.214(55)
4	16	4.199(59)	4.236(59)
5	17	4.190(63)	4.235(63)
6	18	4.182(66)	4.237(66)
8	32	4.173(76)	4.245(76)
9	33	4.165(86)	4.247(86)
12	48	4.141(113)	4.250(113)

stable value of M_{kin} for low momenta. This is as expected since the value of M_{kin} calculated from equation 3.3 has to increase with $\mathbf{p}$ in order to compensate for the missing relativistic $\mathbf{p}^4$ correction.

3.4 Fitting results

The procedure for extracting lattice state masses was to use the multi-correlation fitting procedures (outlined in section 2.6) to the data. For S states three different smearing functions were used; with $n_{sc} = g, e, d$, and for the P states, only g and e.

Initially, simple effective mass plots were used on only one file (one (source,sink) combination) to give initial guesses about energies which could then be input into the multi-correlation fitting routines. The procedure was to jackknife the individual correlators (C_t) of different configurations together to get the appropriate average value, $\overline{C_{t,J}}$. Then the effective mass could be taken using:

$$M_{eff,t+1/2} = -\log\frac{\overline{C_{t+1,J}}}{\overline{C_{t,J}}}. \tag{3.10}$$

Figure 3.3 shows effective mass plots for (n_{sc},n_{sk}) combinations (g,loc), (e,loc) and (d,loc).

The difficulty with effective mass plots is that, for channels with the same J^{PC} quantum numbers, the only way to differentiate between different radial excitations in one channel is through the smearing functions, and these are dominated by the lowest radial level (the lattice equivalent of the physical radial ground state).

The (g,loc) plot gives a good plateau (region of constant M_{eff}), indicating that the ground state radial smearing function gives a good overlap with the 1^3S_1 channel. The

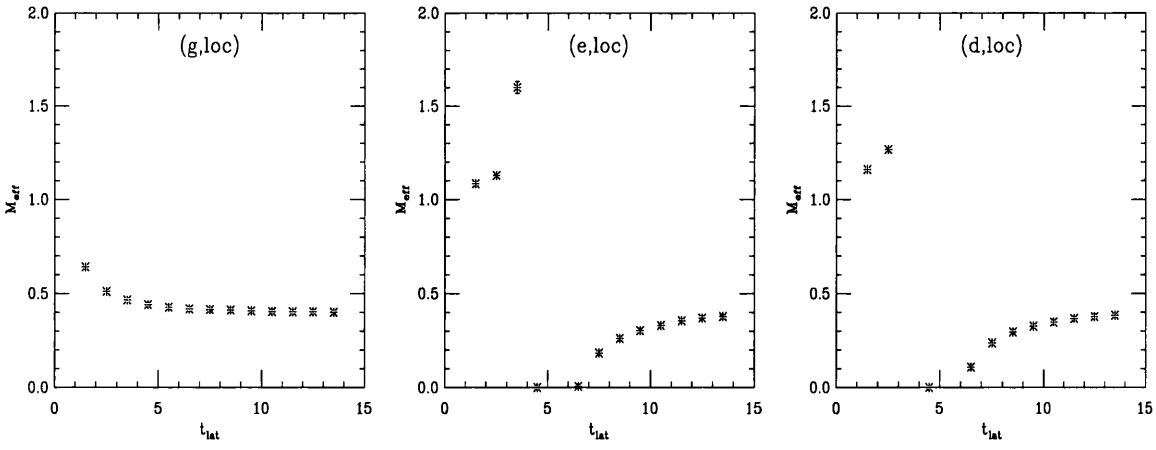

Figure 3.3: Effective mass plots for the ${}^3S_1$ channel, taken from the dynamical run with β=5.2, κ_{sea}=0.135, C_{SW}=2.02 and aM_b^0=1.8. M_{eff} was set to 0 when the ratio of C_{t+1} to C_t became less than 0.

(e,loc) and (d,loc) effective masses rise sharply before reappearing at M_{eff}=0 and then rising to reach the ground state plateau.

Following [18] this behaviour can be explained. The correlator C_t contains the lowest energy (E_1) part of the channel, but also contains a higher energy (E_2) contamination. For simplicity higher energies may be ignored. Thus C_t has the form:

$$C_t = A_1 e^{-E_1 t} + A_2 e^{-E_2 t}. \tag{3.11}$$

The effective mass of this correlator approximates as:

$$M_{eff,t} \approx -\frac{d}{dt}\log C_t = \frac{E_1 + \frac{A_2}{A_1}E_2 e^{-(E_2-E_1)t}}{1 + \frac{A_2}{A_1}e^{-(E_2-E_1)t}}. \tag{3.12}$$

Thus, as t grows there are two qualitatively different ways to approach the plateau. If $A_2/A_1 > 0$ for C_t, the approach is from above. If $A_2/A_1 < 0$ then the approach is from below with a vertical asymptote at a time, t, when:

$$t = \frac{\log\left|\frac{A_2}{A_1}\right|}{E_2 - E_1}. \tag{3.13}$$

Either way, the essential point is that as $t \to \infty$ the lowest energy level with the particular J^{PC} of C_t comes to dominate. To recover the different E_i in a channel, taking effective masses is not enough. Instead, multi-correlation fitting routines are required.

Effective mass plots for correlators with n_{sc}, n_{sk} taking values other than *loc* are shown in fig. 3.4.

In the cases where the same smearing function was used at both the source and the sink ((g,g), (e,e), (d,d) here), the correlator is positive definite and A_2/A_1 is always positive. Hence the approach to the plateau is non-asymptotic and from above.

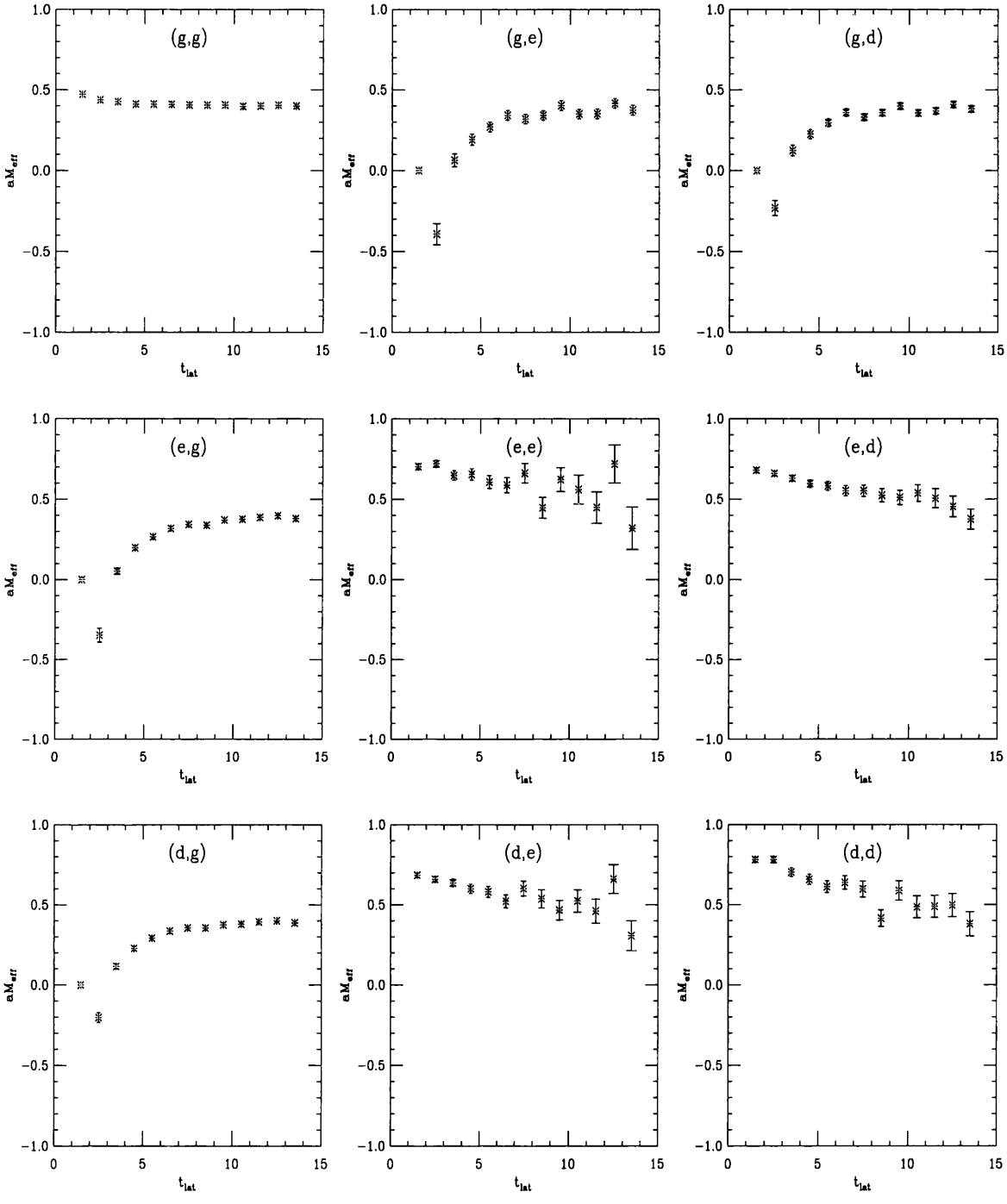

Figure 3.4: Effective mass plots for the $^3S_1$ channel, taken from the dynamical run with β=5.2, κ_{sea}=0.135, C_{SW}=2.02 and aM_b^0=1.8. M_{eff} was set to 0 when the ratio of C_{t+1} to C_t became less than 0.

Type	n_{sc}	n_{sk}	# of corrs.	# of amps.	Energies
2e2s	g,e	loc	2	4	E_1, E_2
2e2s(Kinetic Ratio)	g,e	loc	4	4	E_1, E_2
3e3s	g,e,d	loc	3	9	E_1, E_2, E_3
2e2s	g,e	g,e	4	4	E_1, E_2
3e3s	g,e,d	g,e,d	9	9	E_1, E_2, E_3

Table 3.3: Parameters for the multi-correlation fits used in this thesis.

Despite the failure of this "naïve" effective mass method it is still a useful exercise, in that it gives an indication of where the excited sub-channels in a channel should be. For example, one can visually extrapolate the curves for the (e,loc) and (d,loc) plots of Figure 3.3, as if their asymptote didn't occur, and those curves remained parallel to the (g,loc) curve. This provides a rough guess at the energies of the excited sub-channels. These rough guesses can then be used as input to "tell" multi-correlation fitting routines where to "look" for excited energies.

In this thesis three smearing functions were used for the S channels, and two for the P channels. Fits were carried out to the level of fits to three exponentials with three smearings for S states (henceforth $3e3s$ fits), and two for P states, giving $2e2s$ fits. The $2e2s$ fits can also be done for the S states, but the evidence from the results (see *e.g.* table 3.4 is that a $3e3s$ fit is better than a $2e2s$, if more difficult. Following the convention introduced in section 2.5.2, the fits have the properties listed in table 3.3. Thus, for a $3e3s$ fit with $n_{sc}, n_{sk} = g, e, d$, *i.e.* a matrix fit, there are 9 correlators used for the same J^{PC} numbers. These are all the combinations (n_{sc}, n_{sk}). These are simultaneously fitted to the functional form of equation 2.152. Thus, there are nine amplitudes ($a(n_{sc}, k)$, or $a^*(n_{sk}, k)$ with $n_{sc,sk}$=g,e,d, and k=1,2,3) in the fit, and three energies, $E_{1,2,3}$. Whereas for the vector $3e3s$ fit, n_{sk}=loc. So only three correlators are utilised ($(g, loc), (e, loc)$, and (d, loc)), but the number of amplitudes are still nine ($b(n_{sc}, k)$, with n_{sc}=g,e,d and k=0,1,2). Similarly, the fit also has three energies.

Notice from table 3.3 that there were a different number of correlators utilised in the $2e2s$ vector fits for the "normal" correlators, compared to those for the calculations of the kinetic mass. This is because the kinetic fits actually fit to jackknifed ratios of correlators, such as $E(\mathbf{p})/E(\mathbf{0})$, for the kinetic mass at momentum $\mathbf{p}$. Thus they utilise 4 correlators ((g,loc) and (e,loc) for $\mathbf{p}$=0, and two again for $\mathbf{p} \neq \mathbf{0}$).

The fitting procedure was a multi-step process. Initially, the effective mass plots were used to provide rough guesses at state energies. Then individual correlators were fitted to $1e1s$ fit forms. Like the M_{eff} plots these gave energies around the ground state. The best fit was chosen and used as a guess for input to the next stage in the fitting process. For a $2e2s$ fit the next stage is a $1e2s$ fit, again giving a ground state energy, followed by a $2e2s$ fit with the parameters shown in table 3.3.

Alternative routes were available for the $3e3s$ fit. These were:

$$1e1s \rightarrow 1e3s \rightarrow 2e3s \rightarrow 3e3s, \tag{3.14}$$

Type	t_{min}/t_{max}	aE_1	aE_2	aE_3	Q
3e3s	2/13	0.4007(9)	0.6809(77)	0.8047(195)	2.2×10^{-2}
	3/13	0.3996(10)	0.6817(88)	0.8465(354)	0.14
	4/13	0.3995(10)	0.6691(153)	0.7828(504)	0.18
	5/13	0.3991(11)	0.6733(151)	0.8507(1073)	0.17
	6/13	0.3990(11)	0.6848(223)	0.7548(1204)	0.16
	7/13	0.3987(12)	0.6824(252)	0.8473(2016)	0.30
	8/13	0.3994(13)	0.7334(322)	1.633(755)	0.50
	9/13	0.3990(14)	0.6914(638)	2.760(4406)	0.48
	10/13	0.3941(299)	0.4908(3505)	1.455(1878)	0.53
	11/13*				
2e2s	2/13	0.4004(11)	0.6828(67)		0.18
	3/13	0.3995(12)	0.6804(89)		0.47
	4/13	0.3993(12)	0.6736(117)		0.35
	5/13	0.3992(12)	0.6726(160)		0.22
	6/13	0.3996(13)	0.7009(231)		0.23
	7/13	0.3989(14)	0.6967(323)		0.30
	8/13	0.3995(14)	0.7457(484)		0.56
	9/13	0.3997(15)	0.7504(734)		0.29
	10/13	0.4006(18)	0.7107(1108)		0.46
	11/13	0.3997(20)	0.8721(2073)		0.63

Table 3.4: Matrix fits to the $^3S_1$ channel. From the dynamical ensemble with β=5.2, κ=0.135, C_{SW}=2.02 and aM_b=1.8. *Mass becoming negative in the fit.

and:

$$1e1s \rightarrow 1e2s \rightarrow 2e2s \rightarrow 2e3s \rightarrow 3e3s. \tag{3.15}$$

Table 3.4 shows the results for a $3e3s$ matrix fit to the $^3S_1$ channel. The parameters t_{min} and t_{max} are the minimum and maximum lattice times used in the fit. For the matrix fits, the results were obtained up to lattice timeslice t_{max}-2. However, for the vector fits more timeslices have to be dropped to ensure that results are selected after the plateau is reached. A $2e2s$ vector fit gives results up to and including t_{max}-3, whilst for the $3e3s$ case, only until t_{max}-4. The quality of fit, Q, should ideally be greater than 0.1 [61]. However, a caveat should be borne in mind regarding the use of Q. It grows as the error on the result grows because it is easier to find a fit to data with large error bars. Thus, earlier results with worse Q values are preferred to later results with better Qs.

Including the extra states in the $3e3s$ fit clearly reduces the measured mass of the lowest two radial states relative to the $2e2s$ fit. This is because the inclusion of $n_{sc,sk}$=d smeared correlators into the fit removes some of the lattice 3^3S_1 channel contamination of the $1, 2^3S_1$ lattice states. However, the difference made by the use of the third smearing is typically only a fraction of a standard deviation, which isn't statistically significant. Thus, a $2e2s$ fit is also acceptable. The increase in the number of correlators used from

4 to 9 also reduces the errors in the fit results. This explains why the $3e3s$ fit exhibits worse Q values than the $2e2s$.

One time slice has to be chosen as giving the best fit to the data, and its energies chosen as the measurement result. The value chosen should be one within one sigma of any plateau in the fit results. It should ideally have a central value very close to the plateau central value too. Similarly, the fit should have a good Q value ($\geq$0.1) at that particular timeslice. However, as the noise grows in the correlators over time, they become "easier" to fit and the value of Q will increase, even if the central value for the fit is clearly wrong. Thus, there is a premium in choosing fit results at earlier timeslices. The different sorts of correlators and fits behave differently as the smearing constraints and statistics differ. However, they should all be deriving the same lattice energy levels. It is thus important that the different fits give results which overlap well with each other. There is an algorithm which satisfies these criteria and helps to impose some regularity on the choice of fit time. Counting from the first time slice with $Q \geq$0.1, a number of time slices were dropped. The number dropped was given by the ratio of the number of parameters used in the fit ansatz, to the number of different correlators used in the fit. Thus, for a $3e3s$ matrix fit, there are 9 fit amplitudes, and 3 fit energies, which give 12 fit parameters. There are 9 correlators. So, 12/9, with 1 as the nearest integer, gives a drop of 1 more timeslice. Thus for table 3.4 the first time slice with $Q \geq$0.1 is at t_{min}=3. Dropping 1 extra time slice rules out t_{min}=4, so the fit may be chosen from 5 onwards. Inspection of table 3.4 shows that the times which have been ruled out gave higher energies than all the following and a bit higher than the central value of the plateau. Thus, the algorithm "picked" a good time. For the $2e2s$ case, inspection of table 3.3, gives the number of fit parameters as 6 and the number of correlators as 4, so 2 (*i.e.* more than for the higher statistics $3e3s$ case) time slices should be dropped. In this case they are t_{min}=2,3, anything from then onwards is a good choice.

The results of vector fits to the $^3S_1$ channel are shown in table 3.5. It is clear that the fit is noisier than the matrix fit and has a higher error also. The increased noise is because the (n_{sc}, loc) correlators are less constrained than the matrix fit correlators, with smearing implemented at the origin only. The error increases because there are fewer less constrained correlators used in the vector fit. The algorithm for dropping initial timeslices says drop 4 timeslices from the first good Q in this case. This procedure compensates for the reduced number of correlators (relative to matrix fits), by forcing the timeslice chosen to be later, and so noisier.

Once again, the lattice ground state has a higher energy for the $2e2s$ vector fit than for the $3e3s$. Implementing the algorithm for dropping time slices suggests dropping 4 time slices. It doesn't work for the $3e3s$ fit as it only has 2 "good" Q values. In this case, time slice 8 would be chosen as the final good Q. However, due to the poor Qs, the $3e3s$ fit here is not regarded as a good enough measurement. For the $2e2s$ case, the algorithm says drop 3 time slices, *i.e.* 3,4,5 and 6 are ruled out. This takes the choice to the lowest energy value for the ground state before increasing noise drives the result upwards again.

The main purpose of the dropping algorithm is to ensure agreement between

Type	t_{min}/t_{max}	aE_1	aE_2	aE_3	Q
3e3s	2/13	0.4007(17)	0.7686(1920)	0.7849(1920)	2.0×10^{-10}
	3/13	0.3988(20)	0.7399(2443)	0.7558(2462)	5.1×10^{-3}
	4/13	0.3985(24)	0.7417(2409)	0.7633(2504)	1.5×10^{-2}
	5/13	0.3957(26)	0.7596(2365)	0.7932(2708)	6.4×10^{-2}
	6/13	0.3963(25)	0.7906(1643)	0.8938(2843)	0.13
	7/13	0.3976(27)	0.8361(5439)	0.9208(8860)	7.8×10^{-2}
	8/13	0.3989(23)	0.8260(881)	1.702(1123)	0.10
	9/13	0.3954(79)	0.8159(23622)	0.8416(29811)	5.2×10^{-2}
2e2s	2/13	0.3980(13)	0.7368(56)		1.7×10^{-9}
	3/13	0.3985(14)	0.7080(65)		0.11
	4/13	0.3985(15)	0.6973(78)		0.22
	5/13	0.3990(16)	0.6889(97)		0.28
	6/13	0.3981(18)	0.6810(120)		0.30
	7/13	0.3971(20)	0.6887(167)		0.26
	8/13	0.3976(22)	0.7081(237)		0.21
	9/13	0.3992(22)	0.7630(355)		0.82
	10/13	0.3981(28)	0.7433(551)		0.63

Table 3.5: Vector fits to the $^3S_1$ channel using (n_{sc}, loc) correlators. From the dynamical ensemble with β=5.2, κ=0.135, C_{SW}=2.02 and aM_b=1.8.

Type	Vector	Matrix
2e2s	0.3971(20)	0.3993(12)
3e3s	0.3989(23)	0.3991(11)

Table 3.6: Comparison of vector and matrix fits to the $^3S_1$ channel. From the dynamical ensemble with β=5.2, κ=0.135, C_{SW}=2.02 and aM_b=1.8.

results obtained from the vector and matrix fits. A choice of lattice ground state from each type is shown in table 3.6. Notice that despite poor Q values the $3e3s$ vector fit agrees better with both matrix fits. Similarly the agreement between the types of matrix fit is better than between the vector types.

The conclusion drawn was that the best fits were the $3e3s$ matrix fits, as a $3e3s$ fit is better than a $2e2s$, and a matrix fit is better than a vector fit, because the matrix fit is more constrained. However, fits with suitably good Q values were not always obtainable. Inspection of table 3.6 reveals that taking results from worse types of fit is still acceptable and gives results which are not significantly different, although the accuracy of the result is, of course, reduced.

For P states there was no third smearing function and so the choice was between $2e2s$ vector and matrix fits; with the matrix fits preferred. Table 3.7 shows the matrix and vector fit to the lattice $^1P_1$ channel. Owing to a coding error no valid (n_{sc}, n_{sk})

Type	t_{min}/t_{max}	aE_1	aE_2	Q
Matrix	2/13	0.6098(45)	0.8427(100)	0.68
	3/13	0.6075(52)	0.8373(140)	0.74
	4/13	0.6049(62)	0.8249(193)	0.75
	5/13	0.6068(70)	0.8442(312)	0.62
	6/13	0.6087(74)	0.8757(504)	0.71
	7/13	0.6075(103)	0.8264(747)	0.59
	8/13	0.6191(94)	0.9833(1391)	0.74
	9/13	0.6186(117)	1.001(258)	0.47
	10/13	0.6189(246)	0.8616(3996)	0.28
	11/13	0.6136(215)	2.007(1565)	0.95
Vector	2/13	0.6049(55)	0.9247(116)	6.0×10^{-2}
	3/13	0.6072(72)	0.8746(157)	0.90
	4/13	0.6058(89)	0.8722(222)	0.81
	5/13	0.6051(110)	0.8690(337)	0.68
	6/13	0.6148(136)	0.8959(587)	0.70
	7/13	0.6343(208)	0.8861(1058)	0.87
	8/13	0.6268(179)	1.078(203)	0.92
	9/13	0.6271(170)	1.539(687)	0.89
	10/13	0.6152(2535)	0.6904(9510)	0.86

Table 3.7: Comparison of vector and matrix fits to the $^1P_1$ channel. From the dynamical ensemble with β=5.2, κ=0.135, C_{SW}=2.02 and aM_b=1.8.

$^3P_{1,2T}$ states were available.

In the event of the fits having poor Q values, the time, t_{max}, can be reduced. This procedure was followed with the data shown in table 3.8. Clearly the Q values are dramatically improved. This is understandable because with less data to fit to there is more flexibility in fitting. However, this should also mean that the fit is less accurate. Indeed, the fitted values are noticeably higher for the smaller t_{max} with more dominance of higher energies at low t_{min} in the reduced data set.

The biggest problem encountered in the fitting process, was with the dynamical run with β=5.29, κ=0.134 and C_{SW}=1.92 for both masses. Results for the (usually easy) $2e2s$ matrix fit to the $^3S_1$ channel are shown in table 3.9.

Whilst the vector fits to the (n_{sc}, loc) correlators worked well for this ensemble, the matrix fits gave values of $Q \leq 0.1$. Various procedures were attempted. Initially reduction of the data used in the fit was tried. Both t_{min} and t_{max} were varied, but the results were disappointing. The data sets were then split into two parts in order to check if there was a problem with a subset of the data which could then be ignored. Similarly, this yielded no success. Nevertheless the matrix fits gave better spin splitting (see section 3.5) and radial-orbital ratio results (see section 3.6). Furthermore, although the Q values were low, Q values which are ≥ 0.0001 are acceptable (see reference [61]), provided they are

t_{min}/t_{max}	aE_1	aE_2	aE_3	Q
2/13	0.3937(21)	0.6068(131)	0.8389(146)	1.6×10^{-2}
3/13	0.3920(23)	0.6341(239)	0.7893(265)	8.7×10^{-2}
4/13	0.3913(26)	0.6538(366)	0.7820(451)	4.8×10^{-2}
5/13	0.3893(28)	0.6874(667)	0.7813(911)	5.9×10^{-2}
6/13	0.3884(29)	0.7137(782)	0.8517(1587)	6.3×10^{-2}
7/13	0.3917(54)	0.6587(2372)	0.7144(2577)	2.0×10^{-2}
8/13	0.3956(84)	0.6577(4554)	0.7040(4480)	7.3×10^{-3}
9/13	0.3245(25)	0.4298(1553)	0.6533(1391)	7.2×10^{-3}
2/12	0.3956(25)	0.5970(130)	0.8464(142)	0.24
3/12	0.3936(27)	0.6203(210)	0.8109(243)	0.46
4/12	0.3927(32)	0.6253(261)	0.8300(371)	0.33
5/12	0.3904(34)	0.6525(351)	0.8525(659)	0.36
6/12	0.3894(37)	0.7209(1067)	0.8382(1891)	0.43
7/12	0.3923(49)	0.6992(1326)	0.8346(2793)	0.23
8/12	0.3945(37)	0.7496(662)	1.580(796)	0.88

Table 3.8: Comparison of (n_{sc}, loc) vector fits to the ${}^3S_1$ channel for different t_{max}. From the dynamical ensemble with β=5.2, κ=0.135, C_{SW}=2.02 and aM_b=2.4.

t_{min}/t_{max}	aE_1	aE_2	Q
2/13	0.3888(11)	0.6704(62)	9.5×10^{-4}
3/13	0.3881(11)	0.6650(83)	4.7×10^{-3}
4/13	0.3878(11)	0.6656(108)	6.6×10^{-3}
5/13	0.3875(12)	0.6471(143)	8.2×10^{-3}
6/13	0.3867(12)	0.6351(184)	1.2×10^{-2}
7/13	0.3870(13)	0.6531(254)	2.3×10^{-2}
8/13	0.3869(14)	0.6682(375)	6.9×10^{-2}
9/13	0.3854(16)	0.6457(538)	0.17
10/13	0.3862(16)	0.6807(830)	6.8×10^{-2}
11/13	0.3833(48)	0.5719(1309)	0.52

Table 3.9: Matrix fit to the ${}^3S_1$ channel for the dynamical run with β=5.29, κ=0.134, C_{SW}=1.92 and aM_b=1.8.

the exception overall. To accept the vector fits instead would make comparisons with different κs less meaningful.

3.5 Fitting Results for Spin Splittings

The terms in the NRQCD Lagrangian (equation 2.71) which give rise to spin splittings are, unsurprisingly, those which include the Pauli spin matrices, σ, *viz.*

$$-c_3\frac{g}{8(M_b^0)^2}\sigma\cdot(\mathbf{\Delta}\times\mathbf{E}-\mathbf{E}\times\mathbf{\Delta}), \tag{3.16}$$

and

$$-c_4\frac{g}{2M_b^0}\sigma\cdot\mathbf{B}. \tag{3.17}$$

From examination of table 2.1, it is apparent that the first term gives rise to the P state fine-structure whilst the second gives the hyperfine S state splitting. Using the power counting arguments of section 2.3.3 the order of magnitude for these terms can be predicted. With tree-level values for the couplings, c_3 and c_4 both set to 1, and with $\sigma{=}\frac{1}{2}$, we get

$$-c_3\frac{g}{8(M_b^0)^2}\sigma\cdot(\mathbf{\Delta}\times\mathbf{E}-\mathbf{E}\times\mathbf{\Delta})\sim\frac{1}{8M^2}\cdot\frac{1}{2}\cdot(Mv)(M^2v^3)\sim\mathcal{O}(Mv^4), \tag{3.18}$$

and

$$-c_4\frac{g}{2M_b^0}\sigma\cdot\mathbf{B}\sim\frac{1}{2M}\cdot\frac{1}{2}\cdot(M^2v^4)\sim\mathcal{O}(Mv^4). \tag{3.19}$$

Thus both sets of splittings should be of the same order.

In order to get sufficiently accurate spin-splittings the fitting results have to be jackknifed (see section: 1.6.2). The process greatly reduces the error on the splittings via the jacknifing but also because the data is correlated, even between correlators of different J^{PC}. For instance, some of the error in the $^3S_1$ and $^1S_0$ fits is due to fluctuations of fit values around the plateau across different time slices. However, due to the correlations between different types of correlator on the same lattice, when the $^3S_1$ state has a fit value above its plateau, then the $^1S_0$ has a high value too. Thus, provided the jackknife averaging is done between correlated data sets at the same time slice much of the error in the individual fits is greatly reduced in the final splitting results. Table 3.10 shows fitting results used in the S state hyperfine calculation. Calculations of the hyperfine splitting $(n^3S_1 - n^1S_0)$ would carry too large an error if the best fit value were taken from each and simply subtracted.

Results using the jackknifed difference method are shown for matrix results for the S state hyperfine splitting in table 3.11. The corresponding splittings for vector fits are shown in table 3.12.

Channel	t_{min}/t_{max}	aE_1	aE_2	aE_3	Q
$^1S_0$	2/13	0.3769(10)	0.6673(63)	0.8159(207)	4.4×10^{-3}
	3/13	0.3758(10)	0.6661(79)	0.8332(358)	2.4×10^{-2}
	4/13	0.3760(10)	0.6528(140)	0.7574(511)	4.2×10^{-2}
	5/13	0.3758(11)	0.6529(162)	0.7683(851)	2.7×10^{-2}
	6/13	0.3762(11)	0.6728(219)	0.7525(1059)	0.15
	7/13	0.3749(14)	0.6527(282)	0.9051(1739)	0.26
	8/13	0.3757(12)	0.7104(284)	1.421(571)	0.52
	9/13	0.3755(13)	0.6833(581)	1.819(1849)	0.38
	10/13*				
	11/13	0.3635(1236)	0.4239(4343)	3.305(21226)	0.30
$^3S_1$	2/13	0.4007(9)	0.6809(77)	0.8047(195)	2.2×10^{-2}
	3/13	0.3996(10)	0.6817(88)	0.8465(354)	0.14
	4/13	0.3995(10)	0.6691(153)	0.7828(504)	0.18
	5/13	0.3991(11)	0.6733(151)	0.8507(1073)	0.17
	6/13	0.3990(11)	0.6848(223)	0.7548(1204)	0.16
	7/13	0.3987(12)	0.6824(252)	0.8473(2016)	0.30
	8/13	0.3994(13)	0.7334(322)	1.633(755)	0.50
	9/13	0.3990(14)	0.6914(638)	2.760(4406)	0.48
	10/13	0.3941(299)	0.4908(3505)	1.455(1878)	0.53
	11/13*				

Table 3.10: $2e2s$ matrix fits to the $^1S_0$ and $^3S_1$ channels. From the dynamical run with β=5.2, κ=0.135, C_{SW}=2.02 and aM_b=1.8.

Type	t_{min}/t_{max}	$aE(1^3S_1 - 1^1S_0)$	$aE(2^3S_1 - 2^1S_0)$	$aE(3^3S_1 - 3^1S_0)$
Matrix	2/13	0.02396(35)	0.0179(19)	0.0133(55)
3e3s	3/13	0.02373(37)	0.0164(26)	0.010(10)
	4/13	0.02360(39)	0.0155(41)	0.023(14)
	5/13	0.02362(40)	0.0154(46)	0.024(22)
	6/13	0.02355(50)	0.010(36)	0.012(34)
	7/13	0.02355(52)	0.0132(78)	0.054(65)
	8/13	0.02367(44)	0.0223(92)	0.23(31)
	9/13	0.02371(49)	0.004(26)	-0.2(12)
Matrix	2/13	0.02381(30)	0.0178(14)	
2e2s	3/13	0.02365(32)	0.0170(19)	
	4/13	0.02349(34)	0.0185(24)	
	5/13	0.02341(35)	0.0178(32)	
	6/13	0.02337(38)	0.0197(50)	
	7/13	0.02324(40)	0.0182(66)	
	8/13	0.02354(42)	0.024(11)	
	9/13	0.02366(45)	0.32(17)	
	10/13	0.02374(55)	0.019(26)	
	11/13	0.02388(61)	0.061(74)	

Table 3.11: Hyperfine splitting results for matrix fits. Results from the dynamical run with β=5.2, κ=0.135, C_{SW}=2.02 and aM_b=1.8.

Type	t_{min}/t_{max}	$aE(1^3S_1 - 1^1S_0)$	$aE(2^3S_1 - 2^1S_0)$	$aE(3^3S_1 - 3^1S_0)$
Vector	2/12	0.02247(85)	0.0179(50)	0.0424(57)
3e3s	3/12	0.02233(97)	0.0169(78)	0.0193(92)
	4/12	0.0222(10)	0.014(12)	0.021(16)
	5/12	0.0224(11)	0.031(16)	-0.008(33)
	6/12	0.0229(11)	0.062(45)	-0.08(16)
	7/12	0.023(10)	0.031(470)	0.02(66)
	8/12	0.0234(10)	0.058(32)	-0.2(44)
Vector	2/12	0.02331(44)	0.0398(19)	
2e2s	3/12	0.02304(45)	0.0300(19)	
	4/12	0.02286(50)	0.0281(24)	
	5/12	0.0226(55)	0.0222(30)	
	6/12			
	7/12	0.0225(76)	0.0260(57)	
	8/12	0.02266(87)	0.0217(84)	

Table 3.12: Hyperfine splitting results for vector fits. Results from the dynamical run with β=5.2, κ=0.135, C_{SW}=2.02 and aM_b=1.8.

Splitting
${}^1P_1 - {}^3P_0$
${}^1P_1 - {}^3P_1$
${}^3P_{2E} - {}^1P_1$
${}^3P_{2T} - {}^1P_1$
$\overline{{}^3P} - {}^1P_1$

Table 3.13: P state splittings analysed in this thesis.

The hyperfine splittings calculated from the fits shown in table 3.10, are shown in table 3.11. By comparing the two we can see how much better the jackknifed difference technique is. For example, when t_{min}=2, simply subtracting the results in table 3.10, gives a value for the lattice $(1^3S_0 - 1^3S_1)$ splitting as 0.0238(21). From table 3.11, the jackknifed difference is 0.02381(30). Thus, jackknifing correlated fit results together reduces the uncertainty in the result by an order of magnitude.

Tables 3.12 and 3.11 indicate once again that the matrix fits give better results than vectors. A comparison of the lattice ground and first excited state splittings indicates that the matrix version is more stable. Curiously, however, the $2e2s$ matrix fit to the first excited state splitting is more stable than the $3e3s$ version. This effect does not show up in the vector splittings, though, and may just be a peculiarity of these particular fits.

The same procedure was applied to the P state splittings. These presented more problems, since by equations 3.18 and 3.19 they are smaller than the S state hyperfines. The fits to individual lattice P states also carry a greater uncertainty than is the case with the S states.

The P state splittings which were analysed are shown in table 3.13. The $\overline{{}^3P}$ state is defined in eqn. 3.20.

$$\overline{{}^3P} = \frac{{}^3P_0 + 3{}^3P_1 + 2{}^3P_{2E} + 3{}^3P_{2T}}{9} \tag{3.20}$$

In eqn. 3.20 the lattice representation of the physical ${}^3P_2$ state is split into two parts: ${}^3P_{2E}$ and ${}^3P_{2T}$. This splitting is a discretisation error which results from the discretisation of rotation on the lattice. In the continuum there are no separate $2E$ and $2T$ states.

Results for the ${}^1P_1 - {}^3P_0$ splitting for both vector and scalar fits are shown in table 3.14. It is clear that the results aren't as good as with the S state hyperfines, for the reasons mentioned above. Once again the matrix fit is better than the vector fit.

Unfortunately, at this stage in the analysis, it became apparent that there was a problem. The lattice ${}^3P_1$ and ${}^3P_{2T}$ matrix correlators couldn't be fitted in the conventional manner. Further investigation revealed the source of the problem to be a bug in the code. Thus, for the dynamical ${}^3P_1$ and ${}^3P_{2T}$ lattice states there are only vector fits.

Type	t_{min}/t_{max}	$aE(1^1P_1 - 1^3P_0)$	$aE(2^1P_1 - 2^3P_0)$
Matrix	2/13	0.0141(16)	0.0171(29)
	3/13	0.0139(19)	0.0154(46)
	4/13	0.0134(23)	0.0125(62)
	5/13	0.0145(27)	0.019(11)
	6/13	0.0153(31)	0.006(17)
	7/13	0.0151(42)	-0.002(24)
	8/13	0.0209(49)	0.041(48)
	9/13	0.0252(63)	0.053(87)
	10/13	0.032(16)	0.12(11)
	11/13	0.027(13)	0.5(12)
Vector	2/13	0.0137(30)	0.0366(60)
	3/13	0.0138(41)	0.0386(91)
	4/13	0.0157(51)	0.034(14)
	5/13	0.0176(65)	0.041(20)
	6/13	0.0257(82)	0.036(35)
	7/13	0.037(13)	-0.042(58)
	8/13	0.028(12)	0.005(120)
	9/13	0.0279(96)	-1.25(99)

Table 3.14: $^1P_1 - ^3P_0$ splittings. Taken from the dynamical results with β=5.2, κ=0.135, C_{SW}=2.02, with aM_b=1.8.

Type	t_{min}/t_{max}	$\frac{2^3S_1-1^3S_1}{1^1P_1-1^3S_1}$
Matrix	2/13	1.348(28)
	3/13	1.350(35)
	4/13	1.334(43)
	5/13	1.316(58)
	6/13	1.439(95)
	7/13	1.42(12)
	8/13	1.57(20)
	9/13	1.60(31)
	10/13	1.42(41)
	11/13	2.2(11)
Vector	2/13	1.638(48)
	3/13	1.483(55)
	4/13	1.442(64)
	5/13	1.406(76)
	6/13	1.304(88)
	7/13	1.23(12)
	8/13	1.36(13)
	9/13	1.60(17)
	10/13	1.6(70)

Table 3.15: R_{radorb} for both matrix and vector fits. Results taken from the dynamical run with β=5.2, κ=0.135, C_{SW}=2.02 and aM_b=1.8.

3.6 The Ratio of Radial to Orbital Splittings

The splitting $2^3S_1 - 1^3S_1$ is a radial splitting because the only difference in the split states is with the radial quantum number, n, in the notation $n^{2S+1}L_J$. The splitting $1^1P_1 - 1^3S_1$ is an orbital splitting because the two states differ in their orbital quantum number, L. The ratio of these splittings, R_{radorb}, is defined in eqn. 3.21. R_{radorb} is dimensionless, both physically, and on the lattice. So it is a number with no a dependence and the lattice result may be compared to the experimental result without worrying about a.

$$R_{radorb} = \frac{2^3S_1 - 1^3S_1}{1^1P_1 - 1^3S_1} \tag{3.21}$$

The usual jackknife procedure for obtaining splittings was followed and then the results were jackknifed together again for the ratio calculation. Some results for this calculation are shown in table 3.15. The experimental result is 1.28(3) [29].

One possible source of error is any difference between the lattice $^1P_1$ and $\overline{^3P}$ state masses. This is because the experimental $1P$ states used are the $\chi_{b0,1,2}$. These are combined to give $\overline{\chi_b}$ as in eqn. 3.2. The experimental $\overline{\chi_b}$ is the equivalent of the lattice state $\overline{^3P}$. Hence, any difference in the masses of the lattice $^1P_1$ and $\overline{^3P}$ states will cause

a corresponding error in the lattice R_{radorb} result.

A second ratio of splittings was analysed in the same way. This ratio involves P states and is given by:

$$R_P = \frac{1^3P_{2E} - 1^1P_1}{1^1P_1 - 1^3P_0}. \tag{3.22}$$

Had the $^3P_{1,2T}$ matrix fits worked properly, the lattice calculation should have been for the ratio:

$$R = \frac{1\overline{^3P_2} - 1^3P_1}{1^3P_1 - 1^3P_0}. \tag{3.23}$$

This is the lattice version of the Peskin ratio [37] of equation 2.37. Due to the discretisation error which splits the continuum $^3P_2$ state into the $^3P_{2E}$ and $^3P_{2T}$ states on the lattice, the latter ought to be combined to give the lattice state $\overline{^3P_2}$. It is defined as:

$$\overline{^3P_2} = \frac{2^3P_{2E} + 3^3P_{2T}}{5}. \tag{3.24}$$

In that case the physical state, χ_{b0}, could be identified as the equivalent of the lattice state $^3P_0$, and similarly for the other J values. However, given the failure with the lattice $^3P_{1,2T}$ states a direct comparison with experiment is not possible. Using $^3P_{2E}$ in eqn. 3.22 instead of $\overline{^3P_2}$ adds an additional error to any possible comparison.

3.7 Wavefunctions at the Origin

The amplitudes in the fit ansatzes (equations 2.152 and 2.153) may be used to calculate the mesonic wavefunction at the origin. Here, "at the origin" means there is zero separation between the quark and the antiquark. From equation 2.127, the operator, $\sum_{\mathbf{x}} \psi^\dagger(\mathbf{x})\chi^\dagger(\mathbf{x})$, operating on the vacuum state, $|0\rangle$, creates a meson with zero quark-antiquark separation and zero momentum in the $^1S_0$ state, $|loc\rangle$.

$$|loc\rangle = \sum_{\mathbf{x}} \psi^\dagger(\mathbf{x})\chi^\dagger(\mathbf{x})\,|0\rangle \tag{3.25}$$

Next, consider $|m\rangle$ as the state vector for an η_b meson with radial excitation, m. Then the wavefunction at the origin for the η_b with excitation, m, is given by $\Psi_m(0)$, a quantity which is simply the overlap of the $|m\rangle$ and $|0\rangle$ state vectors.

$$\Psi_m(0) = \langle m|loc\rangle \tag{3.26}$$

Consider an operator $M_H^\dagger(t)$, in the Heisenberg picture [57]. This creates a $^1S_0$ meson at time, t. Then the correlator,

$$_H\langle 0, t = t|M_H(t)M_H^\dagger(t_0)|0, t_0\rangle_H, \tag{3.27}$$

Type	t_{min}/t_{max}	$\psi_1(0)$	Type	$\psi_2(0)$	Type	$\psi_3(0)$
(g,1)	2/12	0.1550(50)	(g,2)	0.030(35)	(g,3)	0.478(79)
	3/12	0.1514(55)		0.078(51)		0.34(13)
	4/12	0.1505(63)		0.112(83)		0.21(19)
	5/12	0.1443(62)		0.29(15)		-0.36(42)
	6/12	0.1464(62)		0.61(60)		-0.70(87)
	7/12	0.153(28)		2(19)		-2(24)
	8/12	0.1553(58)		0.17(18)		$4(190) \times 10^{10}$
(e,1)	2/12	0.1666(84)	(e,2)	0.0793(32)	(e,3)	-0.9(11)
	3/12	0.1600(83)		0.0814(70)		-0.34(29)
	4/12	0.1574(89)		0.092(14)		0.8(97)
	5/12	0.1486(82)		0.110(26)		1(440)
	6/12	0.1480(82)		0.22(12)		-0.7(28)
	7/12	0.152(46)		3(29)		17(370)
	8/12	0.1564(78)		0.174(83)		$5(240) \times 10^9$
(d,1)	2/12	0.1650(76)	(d,2)	0.0924(76)	(d,3)	0.1432(86)
	3/12	0.1580(76)		0.082(10)		0.153(14)
	4/12	0.1562(83)		0.101(26)		0.140(31)
	5/12	0.1486(78)		0.119(41)		0.143(72)
	6/12	0.1484(78)		0.26(17)		-0.12(20)
	7/12	0.154(36)		3(31)		-5(54)
	8/12	0.1577(73)		0.195(91)		$-5(230) \times 10^9$

Table 3.16: Wavefunction at the orgin results for the $^3S_1$ channel. The "Type" column is labelled by the (n_{sc}, m) fit amplitudes. Results come from the dynamical run with β=5.2, κ=0.135, C_{SW}=2.02, and aM_b^0=1.8.

represents the meson propagating from time t_0 to t. By the argument of equations 2.135 to 2.141, in the Schrödinger picture this becomes:

$$\sum_{\text{states}} \langle loc|m\rangle\langle m|loc\rangle e^{-aE_m(t-t_0)}. \tag{3.28}$$

If we put $(n_{sc}, n_{sk}) = (loc, loc)$ in equation 2.152, and consider a limit of an infinite number of exponentials, $\langle m|loc\rangle$ equals $a(loc, m)$. Using eqn. 3.26 this is also equal to $\Psi_m(0)$. From equation 2.156 the dimensionless lattice wavefunction at the origin is given by:

$$a^{3/2}\Psi_m(0) = a^{3/2}\frac{b(n_{sc}, m)}{a(n_{sc}, m)} = \frac{a^3 b(n_{sc}, m)}{a^{3/2}a(n_{sc}, m)}. \tag{3.29}$$

For this thesis, amplitudes from both row ($a^3b(n_{sc}, m)$) and matrix ($a^{3/2}a(n_{sc}, m)$) fits were analysed for both the $^1S_0$ and $^3S_1$ states. Typical results for $\Psi_m(0)$ for the $^3S_1$ channel are shown in Table 3.16.

Inspection of Table 3.16 indicates that the lattice ground state wavefunction

($\psi_1(0)$) is more stable across lattice timeslices. Generally, this ground state dominance held across all results. The results are generally better for $\psi_1(0)$ than for $\psi_2(0)$. As expected the results for (n_{sc}, m) with $m{=}n_{sc}$ give better results too. This is as expected given that the imposition of the same smearing function at both the sink and the source ought to give a better overlap with the particular lattice state being studied. The results also sound a cautionary warning about the choice of the best timeslice in a fit. At t_{min}=8, the anomalously high results for (g,3), (e,3) and (d,3) all clearly indicate that the fits become unstable at those noisier timeslices.

These results also indicate the usefulness of the smearing functions. The smallesst errors are for the wavefunctions at the origin of type (g,1), (e,2) and (d,3). This is because the amplitudes calculated from $a(\mathrm{g},1), b(\mathrm{g},1), \cdots$ were larger numbers. From equations 2.154 and 2.156 being larger is the same as having a higher weight in the fit, or, alternatively, more overlap with the desired lattice energy level. Thus, the most "smeared" correlators most closely resemble the desired lattice state.

3.8 Lattice Results

Tables 3.17 and 3.18 contain the values of the lattice state energies. Tables 3.19 and 3.20 contain the lattice kinetic state energies. Tables 3.21 and 3.22 contain the values of lattice splittings and lattice wavefunctions at the origin. They were selected using the dropping algorithm outlined in section 3.4. It ought to be pointed out that, although unused in this thesis, there was clearly a problem with the ${}^1P_1(x,y,z)$ states. The results are shown in tables 3.17 and 3.18. These states were included as a test to ensure that no particular spatial direction was different from any other. They were analysed late on in the analysis when it became clear that they had, in fact, been averaged in the past and not subsequently "un-averaged".

	Quenched		κ=0.135	
	aM_b			
	1.55	1.8	1.8	2.1
Lattice State	aE			
1^3S_1	0.3348(8)	0.3573(8)	0.3990(11)	0.3835(12)
2^3S_1	0.5683(101)	0.5838(95)	0.6848(223)	0.6671(206)
3^3S_1	0.7098(247)	0.7086(235)	0.7548(1204)	0.7606(1016)
1^1S_0	0.3176(7)	0.3419(7)	0.3762(11)	0.3616(11)
2^1S_0	0.5582(88)	0.5750(85)	0.6728(219)	0.6518(165)
3^1S_0	0.7031(268)	0.7018(252)	0.7525(1059)	0.7439(1022)
1^1P_1	0.5048(40)	0.5253(39)	0.6049(62)	0.5877(59)
2^1P_1	0.7233(114)	0.7396(113)	0.8249(193)	0.7920(192)
$1^1P_1(x)$	0.5048(40)	0.5253(39)	0.6050(62)	*
$2^1P_1(x)$	0.7233(114)	0.7296(113)	0.8249(193)	*
$1^1P_1(y)$	0.5048(40)	0.5253(39)	0.6049(62)	*
$2^1P_1(y)$	0.7233(114)	0.7296(113)	0.8249(193)	*
$1^1P_1(z)$	0.5048(40)	0.5253(39)	0.6049(62)	*
$2^1P_1(z)$	0.7233(114)	0.7296(113)	0.8249(193)	*
1^3P_0	0.4911(41)	0.5132(41)	0.5915(57)	0.5766(55)
2^3P_0	0.7041(123)	0.7131(123)	0.8124(197)	0.7835(196)
1^3P_{2E}	0.5059(46)	0.5261(46)	0.6105(65)	0.5930(62)
2^3P_{2E}	0.7330(131)	0.7377(128)	0.8325(197)	0.7980(195)
$1^3P_{2E}(xy)$	0.5067(50)	0.5273(49)	0.6152(74)	0.5956(70)
$2^3P_{2E}(xy)$	0.7309(138)	0.7372(135)	0.8446(235)	0.8105(230)
$1^3P_{2E}(xz)$	0.5062(52)	0.5261(52)	0.6074(71)	0.5933(75)
$2^3P_{2E}(xz)$	0.7326(141)	0.7357(136)	0.8215(203)	0.8248(330)
$1^3P_{2E}(yz)$	0.5047(52)	0.5244(51)	0.6106(73)	0.5939(71)
$2^3P_{2E}(yz)$	0.7332(141)	0.7367(138)	0.8263(203)	0.7941(201)

Table 3.17: Final lattice state energies for the quenched run and the dynamical run with κ=0.135. * Fits were unsuccessful.

	κ=0.1345		κ=0.134	
	aM_b			
	1.8	2.1	1.8	2.1
Lattice State	aE			
1^3S_1	0.3896(12)	0.4043(14)	0.3860(15)	0.4021(15)
2^3S_1	0.6203(403)	0.6816(215)	0.6700(369)	0.6746(377)
3^3S_1	0.8434(1091)	0.9498(1562)	0.9476(454)	0.9315(4177)
1^1S_0	0.3672(10)	0.3843(12)	0.3649(13)	0.3831(13)
2^1S_0	0.6205(333)	0.6732(177)	0.6478(327)	0.6555(344)
3^1S_0	0.8592(1377)	0.9459(1691)	0.8919(4018)	0.8881(4039)
1^1P_1	0.5924(55)	0.6095(43)	0.5817(192)	0.6077(55)
2^1P_1	0.8561(211)	0.8706(205)	0.8085(3066)	0.8184(201)
$1^1P_1(x)$	0.5924(55)	0.6090(53)	0.5598(3381)	*
$2^1P_1(x)$	0.8561(211)	0.8664(218)	0.6024(4229)	*
$1^1P_1(y)$	0.5924(55)	0.6090(53)	0.5622(3436)	*
$2^1P_1(y)$	0.8561(211)	0.8664(218)	0.6036(4419)	*
$1^1P_1(z)$	0.5924(55)	0.6090(53)	0.5622(3436)	*
$2^1P_1(z)$	0.8561(211)	0.8664(218)	0.6036(4419)	*
1^3P_0	0.5783(49)	0.5968(48)	0.5566(172)	0.5416(589)
2^3P_0	0.8418(210)	0.8538(215)	0.7349(404)	0.6544(699)
1^3P_{2E}	0.5985(58)	0.6142(56)	0.5815(128)	0.5991(128)
2^3P_{2E}	0.8645(215)	0.8738(221)	2.262(1995)	2.438(2233)
$1^3P_{2E}(xy)$	0.6072(63)	0.6226(60)	0.6004(100)	0.6123(66)
$2^3P_{2E}(xy)$	0.8718(235)	0.8806(240)	1.047(178)	0.8211(211)
$1^3P_{2E}(xz)$	0.5964(63)	0.6130(60)	0.5722(157)	0.5899(156)
$2^3P_{2E}(xz)$	0.8732(240)	0.8843(247)	0.7580(2605)	0.8359(2797)
$1^3P_{2E}(yz)$	0.5912(67)	0.6065(63)	0.5336(2975)	0.6028(160)
$2^3P_{2E}(yz)$	0.8485(217)	0.8574(222)	0.7483(7594)	2.878(3344)

Table 3.18: Final lattice state energies for the dynamical runs with κ=0.1345 and 0.134. * Fits were unsuccessful.

	Quenched		κ=0.135	
	aM_b			
	1.55	1.8	1.8	2.1
Lattice State	aE			
Kinetic States				
$(a\mathbf{p})^2$	$aE(1^3S_1)$			
1	0.02155(17)	0.01901(15)	0.01829(24)	0.01620(19)
2	0.04295(37)	0.03793(32)	0.03652(51)	0.03238(40)
3	0.06421(62)	0.05675(53)	0.05470(83)	0.04854(64)
4	0.08555(84)	0.07564(73)	0.07240(123)	0.06436(92)
5	0.1066(12)	0.09433(99)	0.09063(160)	*
6	0.1275(15)	0.1130(13)	0.1088(21)	0.09681(155)
8	0.1694(24)	0.1503(20)	0.1452(31)	0.1293(24)
9	0.1907(28)	0.1692(24)	0.1635(38)	0.1456(29)
12	0.2545(41)	0.2257(39)	0.2195(66)	0.1948(48)

Table 3.19: Final lattice kinetic masses for the quenched run and the dynamical run with κ=0.135. * Fit was unsuccessful.

	κ=0.1345		κ=0.134	
	aM_b			
	1.8	2.1	1.8	2.1
$(a\mathbf{p})^2$	$aE(1^3S_1)$			
1	0.01908(32)	0.01659(23)	0.01811(25)	0.01586(22)
2	0.03814(65)	0.03319(48)	0.03639(38)	0.03158(48)
3	0.05718(100)	0.04978(77)	0.05443(61)	0.04716(79)
4	0.07594(151)	0.06595(110)	0.07210(87)	0.06259(114)
5	0.09495(191)	0.08254(146)	0.09002(115)	0.07785(156)
6	0.1139(23)	0.09910(185)	0.1079(15)	0.09295(208)
8	0.1515(35)	0.1318(28)	0.1433(22)	0.1225(34)
9	0.1700(40)	0.1482(34)	0.1609(27)	0.1369(43)
12	0.2242(60)	0.1963(56)	0.2126(47)	0.1774(88)

Table 3.20: Final lattice kinetic masses for the dynamical runs with κ=0.1345 and 0.134.

	Quenched		κ=0.135	
	aM_b			
	1.55	1.8	1.8	2.1
S States	$a^{3/2}\psi(0)$			
1^1S_0	0.1407(40)	0.1539(48)	0.1772(59)	0.1961(71)
1^3S_1	0.1157(38)	0.1314(46)	0.1445(51)	0.1646(62)
Lattice Splitting	aE(Splitting)			
$1^3S_1 - 1^1S_0$	0.01721(22)	0.01540(19)	0.02355(50)	0.02187(39)
$2^3S_1 - 2^1S_0$	0.0102(24)	0.0089(20)	0.0132(78)	0.0152(85)
$3^3S_1 - 3^1S_0$	0.0068(70)	0.0068(59)	0.012(34)	0.016(21)
$1^1P_1 - 1^3P_0$	0.0105(15)	0.0091(13)	0.0134(23)	0.0111(20)
$2^1P_1 - 2^3P_0$	0.0186(43)	0.0158(36)	0.0125(62)	0.0086(55)
$1^3P_{2E} - 1^1P_1$	0.0043(10)	0.00378(87)	0.0058(16)	0.0053(14)
$2^3P_{2E} - 2^1P_1$	0.0102(29)	0.0088(24)	0.0052(43)	0.0060(35)
$1^3\overline{P} - 1^1P_1$	0.00064(67)	0.00054(56)	0.0013(22)	0.0013(19)
$2^3\overline{P} - 2^1P_1$	0.0023(20)	0.0020(16)	-0.0055(53)	-0.0039(47)
$(2^3S_1 - 1^3S_1)/(1^1P_1 - 1^3S_1)$	1.374(50)	1.349(46)	1.439(95)	1.443(93)
$(1^3P_{2E} - 1^1P_1)/(1^1P_1 - 1^3P_0)$	0.41(10)	0.42(10)	0.44(13)	0.48(14)

Table 3.21: Final lattice wavefunction at the origin and splitting results for the quenched runs and the dynamical runs at κ=0.135.

	κ=0.1345		κ=0.134	
	aM_b			
	1.8	2.1	1.8	2.1
S States	$a^{3/2}\psi(0)$			
1^1S_0	0.203(12)	0.237(28)	0.211(61)	0.229(58)
1^3S_1	0.175(14)	0.231(52)	0.178(54)	0.207(76)
Lattice Splitting	aE(Splitting)			
$1^3S_1 - 1^1S_0$	0.02243(42)	0.01998(40)	0.02112(49)	0.01898(43)
$2^3S_1 - 2^1S_0$	0.0003(200)	0.0084(69)	0.022(10)	0.0175(95)
$3^3S_1 - 3^1S_0$	-0.015(78)	0.004(45)	0.06(16)	0.03(14)
$1^1P_1 - 1^3P_0$	0.0141(22)	0.0127(36)	0.20(50)	0.15(64)
$2^1P_1 - 2^3P_0$	0.0144(72)	0.017(16)	0.2(14)	2.0(12)
$1^3P_{2E} - 1^1P_1$	0.0061(15)	0.0048(40)	0.0004(630)	-0.0110(48)
$2^3P_{2E} - 2^1P_1$	0.0084(48)	0.003(16)	2.0(16)	0.5(10)
$1^3\overline{P} - 1^1P_1$	0.0032(18)	0.0027(16)	-0.0025(96)	-0.007(13)
$2^3\overline{P} - 2^1P_1$	-0.0040(51)	-0.0022(42)	0.20(19)	0.13(12)
$(2^3S_1 - 1^3S_1)/(1^1P_1 - 1^3S_1)$	1.311(78)	1.318(93)	1.38(23)	1.38(23)
$(1^3P_{2E} - 1^1P_1)/(1^1P_1 - 1^3P_0)$	0.43(11)	0.38(41)	0.005(300)	-0.07(29)

Table 3.22: Final lattice wavefunction at the origin and splittings for the dynamical results with κ=0.1345 and 0.134.

	Quenched		κ=0.135		
	aM_b				
	1.55	1.8	1.8	2.1	2.4
a^{-1}(GeV)	2.59(6)	2.62(6)	2.14(7)	2.15(6)	2.15(6)
a(fm)	0.076(2)	0.075(2)	0.092(3)	0.092(3)	0.092(3)

Table 3.23: Inverse lattice spacing calculated from the $1^1P_1 - 1^3S_1$ splitting.

	κ=0.1345		κ=0.134	
	aM_b			
	1.8	2.1	1.8	2.1
a^{-1}(GeV)	2.17(6)	2.14(5)	2.14(6)	2.14(6)
a(fm)	0.091(3)	0.092(2)	0.092(3)	0.092(3)

Table 3.24: Inverse lattice spacing calculated from the $1^1P_1 - 1^3S_1$ splitting.

Chapter 4

Physical Results

4.1 Introduction

In this chapter the results at different lattice bare heavy quark masses are combined, and (if required) interpolated to yield values at the physical Υ mass of 9.460 GeV. Most quantities of interest have sufficiently slight bare mass dependence that there is no significant difference between the results at either bare quark mass. However, the potential model expectation (see equation 2.42) that the hyperfine splitting has a strong dependence on the bare mass is confirmed. It also displays sea quark mass dependence, so the results were interpolated to a physical light pseudoscalar meson mass[1]. A significant signal for unquenching was also seen for the hyperfine splitting. This difference allowed an extrapolation to be made to the expected "real world" case where there are three flavours of sea quark in the bottomonium system. This gives a prediction of a mass of 9.517(4) GeV for the η_b particle.

4.2 Interpolation to the Upsilon Mass

The calculations of the previous chapter were carried out at two different lattice bare quark masses, chosen to give physical kinetic mass values either side of the actual upsilon mass. The results then have to be interpolated to the upsilon scale.

The results for the upsilon mass at small non-zero momenta for any one bare mass showed no significant discrepancy from each other (for example see table 3.2). Thus the fitted results chosen were those for the smallest momentum, since they had the smallest errors.

Calculations with different bare masses gave slight (non-significant) discrepancies in the values of the lattice spacing (see tables 3.23 and 3.24). In order to reduce this

[1]Chiral perturbation theory suggests that the square of the pseudoscalar mass varies with the sea quark mass, so this quantity is chosen for the extrapolation.

a^{-1}				
	Quenched	κ=0.135	κ=0.1345	κ=0.134
In GeV	2.61(6)	2.15(6)	2.16(6)	2.14(6)
In fm	0.076(2)	0.092(3)	0.091(3)	0.092(3)

Table 4.1: The inverse lattice spacing values used for the calculations in this chapter.

M_{kin}(GeV)				
Quenched		κ=0.135		
aM_b				
1.55	1.8	1.8	2.1	2.4
9.31(23)	10.56(26)	9.04(28)	10.22(31)	11.43(34)

Table 4.2: Upsilon kinetic masses (in GeV) for the quenched data and the dynamical data with the lightest dynamical quarks.

slight uncertainty an "average" for both bare masses was taken, with the errors remaining the same. The inverse lattice spacing values adopted via this procedure are shown in table 4.1. The resulting kinetic mass results are shown in tables 4.2 and 4.3.

In the absence of further information on the variation of the physical kinetic mass with the lattice bare mass linear regression was used to obtain the line between kinetic masses at the different values of the bare mass. From this line the lattice bare mass which would have resulted in a physical kinetic mass equal to the upsilon rest mass was calculated. The results from this calculation are shown in table 4.4.

4.3 Dependence of Results on Dynamical Quark Masses

In order to measure the variations of lattice observables with dynamical quark mass, it was necessary to use a measurement of the lattice dynamical quark mass in terms of some physically observable quantity. Chiral perturbation theory suggests that for most quantities the dependence on dynamical quark mass is linear. The quantity chosen was

M_{kin}(GeV)			
κ=0.1345		κ=0.134	
aM_b			
1.8	2.1	1.8	2.1
8.71(28)	10.02(31)	9.09(28)	10.39(33)

Table 4.3: Upsilon kinetic masses (in GeV) for the two dynamical data sets with the heavier dynamical quarks.

aM_b interpolated to $M_{\rm kin} = M(\Upsilon)$			
Quenched	κ=0.135	κ=0.1345	κ=0.134
1.58(3)	1.91(4)	1.97(4)	1.89(4)

Table 4.4: Lattice bare b quark mass interpolated to give $M_{\rm kin} = M(\Upsilon)$.

Pseudoscalar masses				
	Quenched	κ=0.135	κ=0.1345	κ=0.134
am_{PS}	∞	0.408^{+4}_{-4}	0.512^{+4}_{-3}	0.578^{+3}_{-2}
m_{PS} (GeV)	∞	0.8772(260)	1.1059(319)	1.2369(353)
m^2_{PS} (GeV^2)	∞	0.7695(456)	1.2230(706)	1.5299(873)

Table 4.5: Pseudoscalar masses used in this thesis. It should be noted that although taken from [63], the physical results differ from those shown there as different values of the lattice spacing were used in this case.

the pseudoscalar mass squared. Accordingly, lattice pseudoscalar mass measurements from light hadron spectroscopy on these configurations were chosen [63]. These pseudoscalar meson masses were calculated by other members of the UKQCD collaboration using the clover and non-perturbatively improved Wilson fermion action outlined in sections 1.5.1, 1.5.4 and 1.5.5. They were measured on the lattice using the light quark action of those sections instead of the NRQCD action used here for heavy bottomonium spectroscopy. Of course, light quark actions are also included through the Hybrid Monte Carlo algorithm, generated with a fixed, unique κ value (called the *sea* κ). For the light spectroscopy carried out on those dynamical configurations the value of κ (called this time the *valence* κ) was varied in the spectroscopic action. This allowed measurements of light quark results on configurations with one $\kappa_{\rm sea}$ and various values of $\kappa_{\rm valence}$. For the Υ system such light quarks are regarded as sea quarks, hence the value chosen for the light pseudoscalar mass was the one calculated with $\kappa_{\rm valence} = \kappa_{\rm sea}$.

The lattice spacing values used to convert these results to dimensionful units were taken from table 4.1, and not from the lattice spacing values calculated from the light spectroscopy results in [63]. Otherwise the extrapolation of the hyperfine splitting (calculated using $a^{-1}_{\rm heavy}$) would then be interpolated to a point calculated using $a^{-1}_{\rm light}$. The pseudoscalar masses used are shown in table 4.5.

In choosing which lattice state measurements to use in the interpolation, care was taken to avoid introducing systematic errors from fitting. As an example, for the configurations with κ=0.135 and 0.1345 the S states were adjudged to have their best value at $t_{\rm min}/t_{\rm max} = 6/13$, whereas, for κ=0.134, it was considered safer to take the best results (owing to the poor Q values at early timeslices) from $t_{\rm min}/t_{\rm max} = 9/13$. Thus, to choose on the grounds of the best results for an individual state could introduce a systematic error owing to the different timeslices chosen. Furthermore, the final results for splittings *etc.* didn't appear to be qualitatively any worse at earlier timeslices for

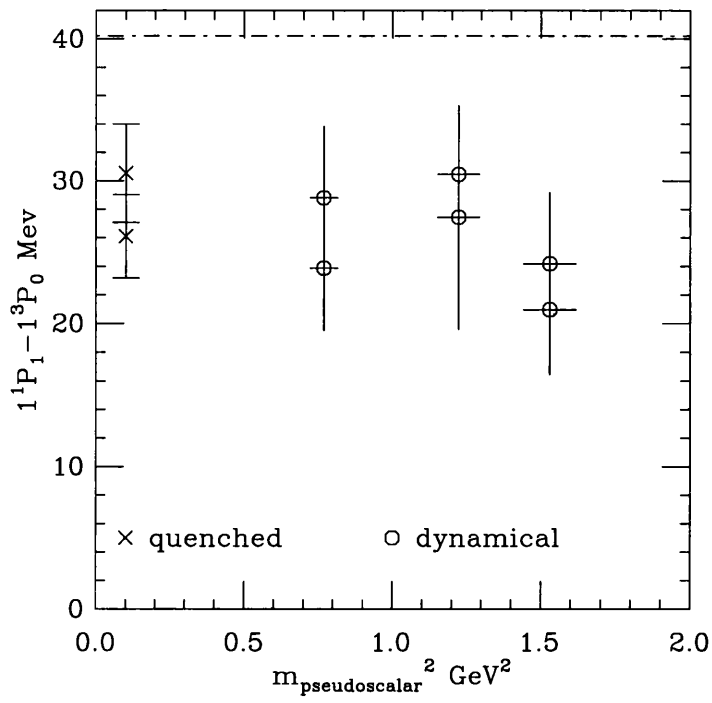

Figure 4.1: $1^1P_1 - 1^3P_0$ splitting versus pseudoscalar mass. Note that the quenched result should have $m_{\text{Pseudoscalar}} = \infty$. The dashed line is the experimental result for $\overline{\chi_b} - \chi_{b0}$. For a definition of $\overline{\chi_b}$, see equation 3.2.

κ=0.134, than in the other configurations. Therefore the quantities used in this part of the analysis were chosen at the same timeslice in all cases, for the S states the value chosen was t_{min}=6, and for P states, t_{min}=4.

Given the knowledge of the lattice bare quark masses at the physical Upsilon rest mass shown in table 4.4, lattice results at the differing bare quark masses could be interpolated to this "physical" lattice bare mass. However, in many cases the errors on quantities of interest were too large to show a significant difference in the results for different lattice bare masses. This was the case for the results for the $1^1P_1 - 1^3P_0$ and $1^3P_{2E} - 1^1P_1$ splittings, shown in figures 4.1 and 4.2 respectively. It should be noted that for these graphs (and the others to follow), the quenched value is plotted at M_{PS}^2=0.1 MeV^2 for visibility, there is no physical significance to its position. Of course, it is also possible to plot the results against $1/M_{PS}^2$, but chiral perturbation theory suggests that M_{PS}^2 has a linear dependence on the dynamical quark mass, making M_{PS}^2 the natural choice for the linear extrapolations which were carried out.

Unsurprisingly, the ratio of the previous splittings (*i.e.* $(1^3P_{2E} - 1^1P_1)/(1^1P_1 - 1^3P_0)$) suffers from the same problem. That result is shown in figure 4.3. The ratio of the radial to the orbital splitting, taken from the lattice results as $(2^3S_1 - 1^3S_1)/(1^1P_1 - 1^3S_1)$ is shown in figure 4.4. Its behaviour was as expected, indicating that at the physical value of M_{PS}^2 the dynamical radial-orbital splitting would be higher then the quenched

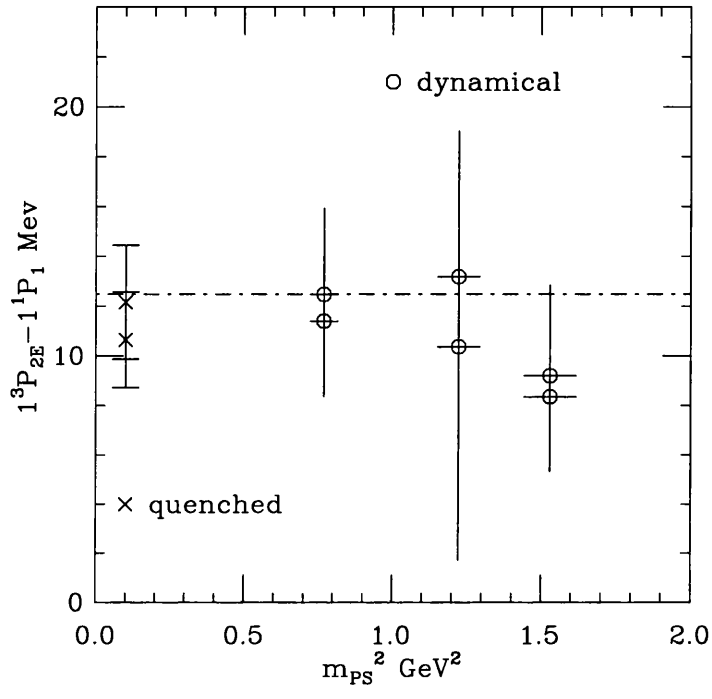

Figure 4.2: $1^3P_{2E} - 1^1P_1$ splitting versus pseudoscalar mass. Note that the quenched result should have $m_{PS} = \infty$. The dashed line is the experimental result for $\chi_{b2} - \overline{\chi_b}$. For a definition of $\overline{\chi_b}$, see equation 3.2.

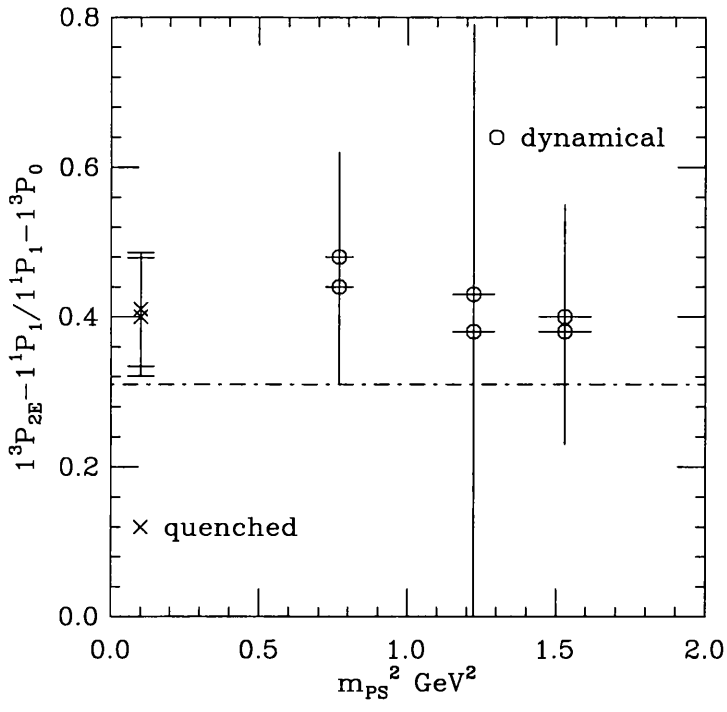

Figure 4.3: $(1^3P_{2E} - 1^1P_1)/(1^1P_1 - 1^3P_0)$ ratio versus pseudoscalar mass. The dashed line is the experimental result for $(\chi_{b2} - \overline{\chi_b})/(\overline{\chi_b} - \chi_{b0})$. For the definition of $\overline{\chi_b}$, see equation 3.2.

value, although the trend is not very statistically significant. This was as expected, since a larger n_f should give a larger α_s by equation 2.14, and indeed does in figure 5.3. A larger value of α_s in turn should decrease the value of the $^3S_1$ channel mass relative to the masses of the $^1P_1$. However, it is clear that the trend would give a dynamical value which has less agreement with experiment than the quenched.

The results for the wavefunction at the origin, for both 1^1S_0 and 1^3S_1, don't show any significant difference either. They are shown in figures 4.5 and 4.6 respectively. It is clear from both figures that the results on the dynamical configurations with κ=0.1345 have large errors. Unfortunately, there is no discernible trend. The potential model expectation of equation 2.54 suggests that an increase in α_s (as expected from unquenching, by equation 2.14), should increase the wavefunction at the origin. Equation 2.54 also indicates that the wavefunction at the origin should have heavy quark mass dependence, an effect which was only really seen for the results with lower errors. Thus, overall, there is little which can be said with certainty regarding the results for the wavefunction at the origin.

In the case of the hyperfine splitting, $1^3S_1 - 1^1S_0$, there was a significant difference between the results on different bare quark masses. The results are shown in figure 4.7. Such relatively strong bare quark mass dependence is as expected from potential model predictions, such as 2.54. There is a clear trend in figure 4.7: the hyperfine

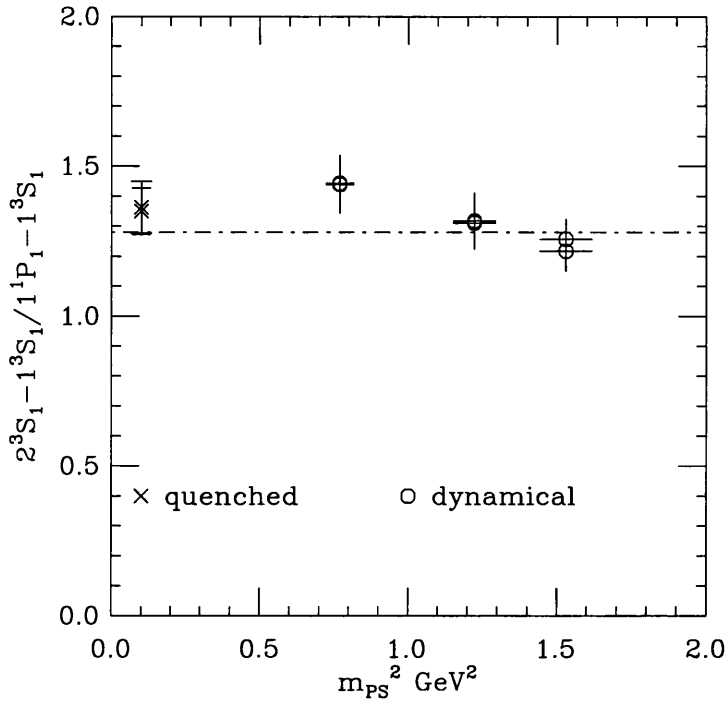

Figure 4.4: $(2^3S_1 - 1^3S_1)/(1^1P_1 - 1^3S_1)$ ratio versus pseudoscalar mass. The dashed line is the experimental result for $(\Upsilon' - \Upsilon)/(\overline{\chi_b} - \Upsilon)$. For the definition of $\overline{\chi_b}$, see equation 3.2.

Results at $M_{\rm kin} = M(\Upsilon)$				
	Quenched	κ=0.135	κ=0.1345	κ=0.134
$aE(1^3S_1 - 1^1S_0)$	0.01699(26)	0.02293(51)	0.02104(42)	0.02080(41)
$1^3S_1 - 1^1S_0$ (MeV)	44.3(12)	49.3(18)	45.5(16)	44.5(15)

Table 4.6: Values for the hyperfine splitting interpolated to the point where the lattice kinetic mass, $M_{\rm kin} = M_\Upsilon$, the experimental mass.

splitting is larger at $n_f = 2$ than at $n_f = 0$ (at a physical value of M_{PS}^2). Essentially the same argument used previously in this section with the results for the wavefunction at the origin applies in reverse. A larger value of α from the effect of unquenching on the running coupling (equation 2.14) should increase the hyperfine splitting for $n_f = 2$ (equation 2.41).

In order to obtain the result at the physical Υ kinetic mass, linear interpolation between the hyperfines was used and the results obtained at the "physical" bare quark masses of table 4.4. The final interpolated values are given in table 4.6, and displayed in figure 4.8.

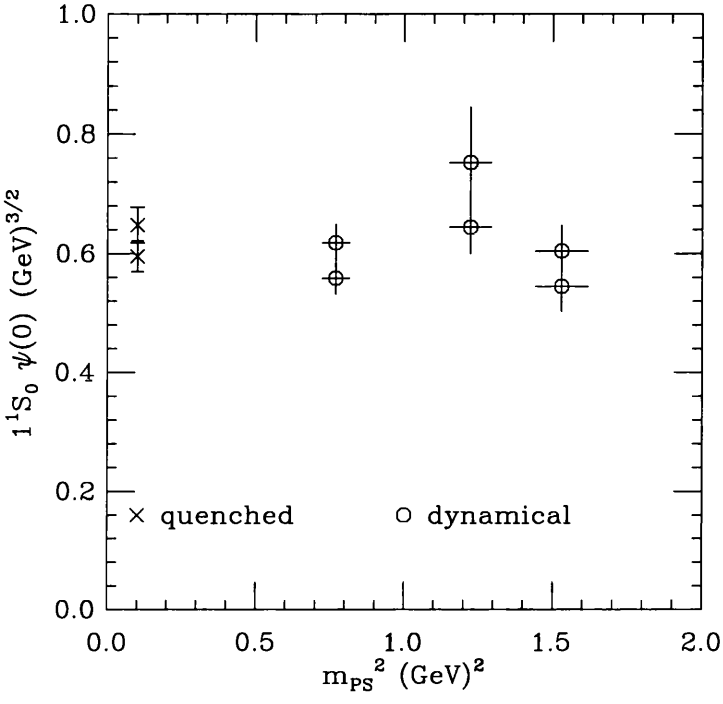

Figure 4.5: Results for the wavefunction at the origin, $\psi(0)$, for the 1^1S_0 lattice state, versus pseudoscalar mass. The method used to calculate the wavefunction at the origin is described in section 3.7.

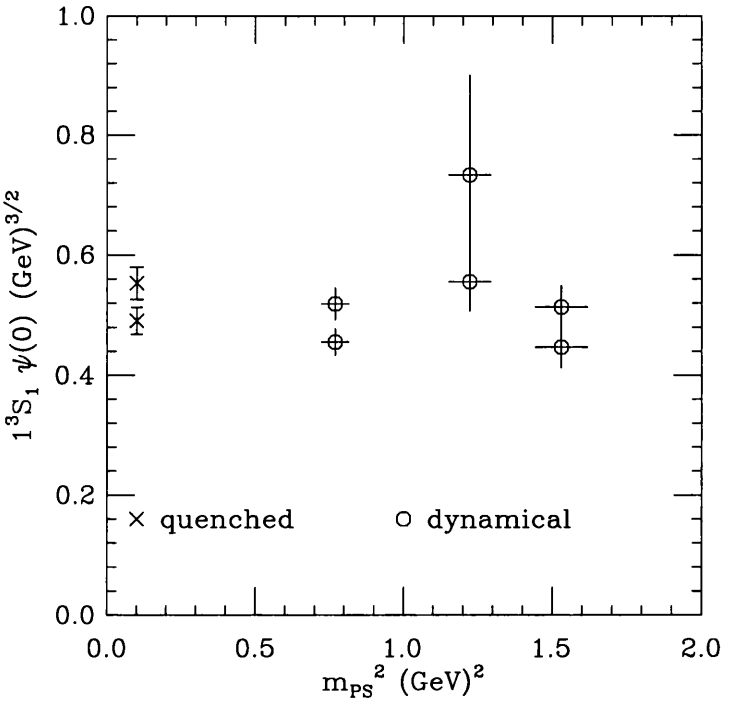

Figure 4.6: Results for the wavefunction at the origin, $\psi(0)$, for the 1^3S_1 lattice state, versus pseudoscalar mass. The method used to calculate the wavefunction at the origin is described in section 3.7.

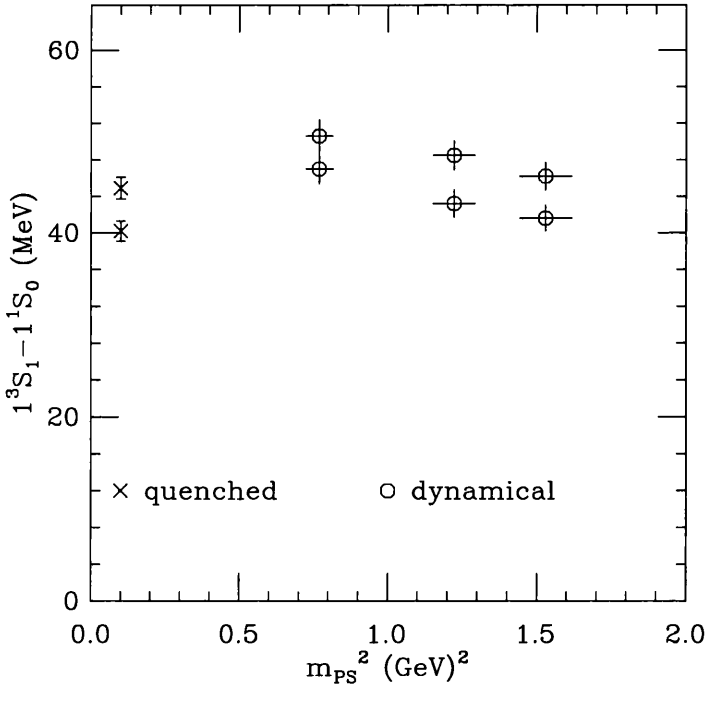

Figure 4.7: Results for the hyperfine splitting, $1^3S_1 - 1^1S_0$, versus pseudoscalar mass.

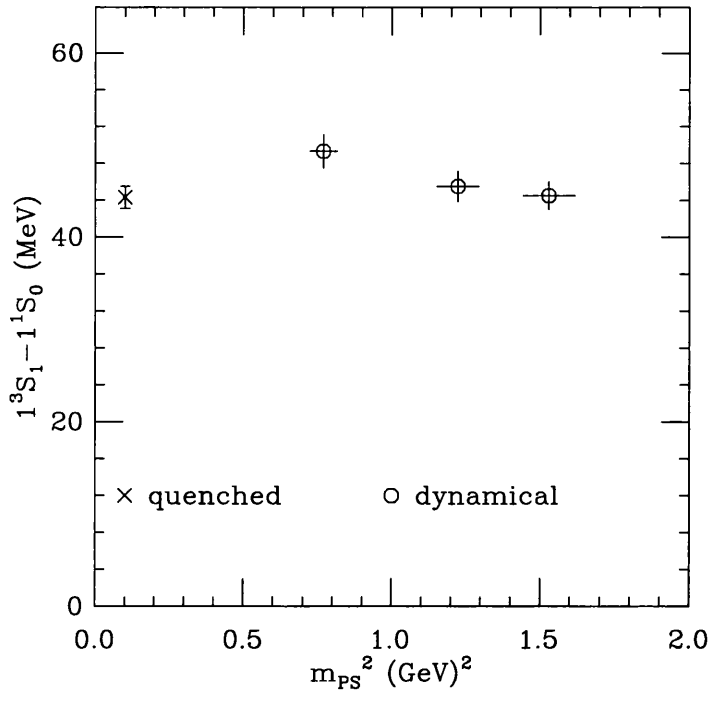

Figure 4.8: Results for the hyperfine splitting at the physical scale where $M_{\rm kin} = M_\Upsilon$, versus pseudoscalar mass.

4.4 Extrapolation to Experimental Light Quark Masses

The pseudoscalar masses of the previous section have been derived from the lattice measurements of light pseudoscalar meson masses in [63]. It is important to extrapolate from those masses to some sort of physical value for M_{PS}^2.

The typical momentum inside bottomonium is $\sim$1 GeV($\gg m_{u,d,s}$). Thus, the dynamical quarks of importance in the sea for the $b\bar{b}$ system are the three lightest quarks, u, d, and s. This suggests that an appropriate value for the dynamical quark mass, $m_{\rm dyn}$ (for degenerate lattice sea quarks), with all three physical sea quarks active is:

$$m_{\rm dyn} = \frac{m_u + m_d + m_s}{3}. \tag{4.1}$$

Equation 4.1 is the simplest expression for the dynamical quark mass in the absence of more information. Translating into observable meson masses, using chiral perturbation theory, the pseudoscalar meson mass should be taken as [65]:

$$m^2_{\rm pseudoscalar} = \frac{2m_K^2 + m_\pi^2}{3}. \tag{4.2}$$

The mass taken for the K and π was the average of both the neutral and

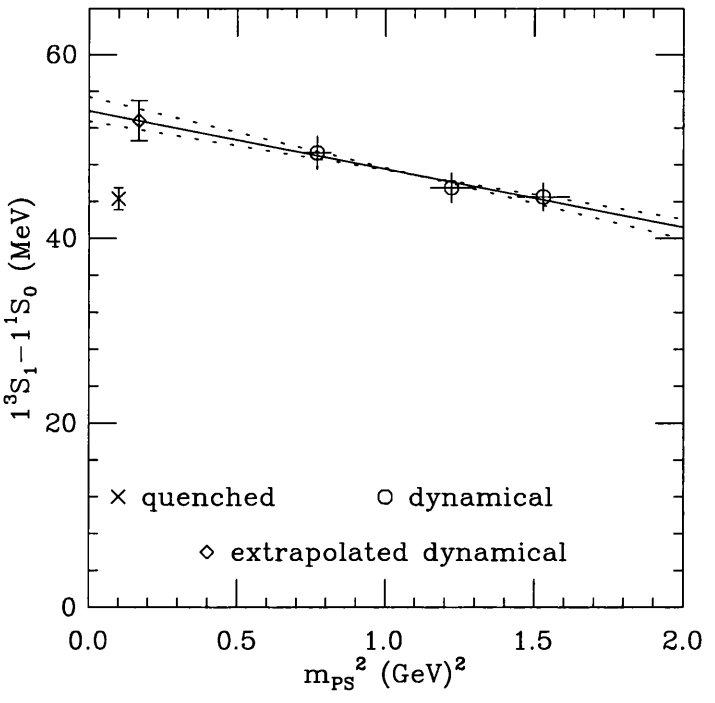

Figure 4.9: Results for the hyperfine splitting at the physical scale where M_{PS} is as defined in equations 4.2 and 4.3, versus pseudoscalar mass. The solid line is the best linear fit to the three dynamical hyperfines with the dashed lines due to the uncertainties in lattice pseudoscalar masses.

charged particles in either case:

$$\begin{aligned} m_\pi &= \frac{m_{\pi^0} + m_{\pi^\pm}}{2}, \\ m_K &= \frac{m_{K^0} + m_{K^\pm}}{2}. \end{aligned} \tag{4.3}$$

This averaging is required as we take the u and d quark masses to be degenerate. From table A.2, $m_{\text{pseudoscalar}} = 412.4$ MeV, slightly lighter than the K^0. The results for the extrapolation are shown in figure 4.9. The solid line in figure 4.9 is the best linear fit to the data. The dashed lines were obtained via the errors on the pseudoscalar masses. They were calculated by refitting, taking the outermost values of the lightest (m_{PS}^l) and heaviest (m_{PS}^h) pseudoscalars. Thus, the first fit came from the masses $m_{PS}^l - \Delta(m_{PS}^l)$ and $m_{PS}^h + \Delta(m_{PS}^h)$, and vice versa for the second. The value obtained for the hyperfine splitting was $52.8(22)\left(^{+13}_{-10}\right)$ MeV^2.

[2]The first (symmetric) error comes from the extrapolation and the original errors on the hyperfine splitting. The second (unsymmetric) errors come from the uncertainties in the pseudoscalar masses and are simply the difference between the best and worst fit lines at the physical pseudoscalar mass.

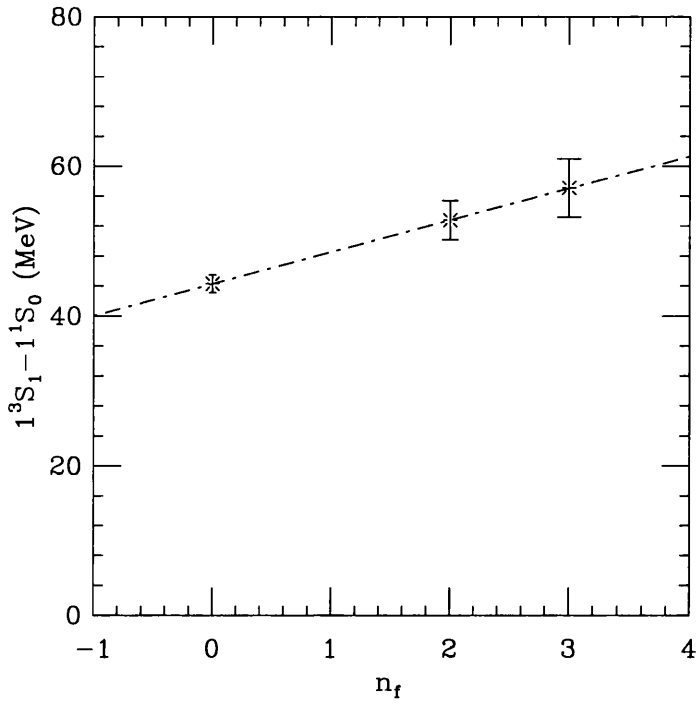

Figure 4.10: Extrapolation of the hyperfine splitting to n_f=3.

4.5 Extrapolation to $n_f = 3$

Following the extrapolation to the physical pseudoscalar mass of the preceding section, it was necessary to extrapolate again from this result for two flavours of dynamical quarks to the real world case where three flavours would be reasonable. The quenched result has $n_f = 0$ and so provides the other point. The extrapolation result is shown in figure 4.10.

The error on the dynamical (n_f=2) hyperfine was calculated by adding its symmetric and unsymmetric errors in quadrature. The final value obtained for the hyperfine splittings was 57.1(35) MeV, leading to a prediction for the η_b mass of 9.517(4) GeV.

4.6 Comparison of Lattice Spacings from Different Scales

In lattice calculations the lattice spacing, a, is determined by comparing a lattice measurement of some quantity to its physical value. For the spectroscopy presented thus far in this thesis, the quantity chosen was the physical $\chi_b - \Upsilon$ splitting; with lattice equivalent, the splitting $aE(1^1P_1 - 1^3S_1)$. The spacing is then determined by equating both results.

Another way of determining a is via lattice potential models, by comparing the

Lattice Spacing (fm)			
Quenched, β=6.0	κ=0.135	κ=0.1345	κ=0.134
$0.0913(9)\binom{+4}{-0}$	$0.1030(10)\binom{+20}{-1}$	$0.1038(11)\binom{+11}{-10}$	$0.1018(10)\binom{+20}{-7}$

Table 4.7: Values of the lattice spacing from [67] determined at the Sommer scale.

lattice potential model fit with the dimensionful "real world" case. One such method is to evaluate the interquark force at the *Sommer Scale* [66]. For the dynamical configurations used in this calculation such an analysis has been carried out [67]. The results are shown in table 4.7. The two types of error quoted were combined in quadrature, taking the largest of the unsymmetric errors in that case. Thus there may be a slight overestimate of errors in the subsequent results. The quenched result was taken from the formula [68]:

$$\ln(a/r_0) = -1.6805 - 1.7139(\beta - 6) + 0.8155(\beta - 6)^2 - 0.6667(\beta - 6)^3. \quad (4.4)$$

For the quenched results used here the value of r_o used was $\approx$0.49fm. In order to derive an error on this value it was compared to the result for r_0=0.495fm and 0.485fm.

The ratios of the values of a calculated in this thesis to those from [67] are shown in figure 4.11. As the lattice spacing shouldn't vary with the calculation being performed on the same lattice, the ratios ought to equal one in all cases. Unfortunately this wasn't the case. However, the dynamical results were certainly significantly closer to unity than the quenched.

4.7 Hyperfine Splitting results obtained by other Collaborations

Other collaborations have completed calculations similar to that done in this thesis. This section compares my results for the hyperfine splitting with those of the SESAM [54] and CP-PACS [64] collaborations. The hyperfine splitting is used as it is the most precisely determined quantity in the calculation. The hyperfine splitting should be larger for $n_f = 2$ than for $n_f = 0$. Unquenching should increase the value of the running coupling by equation 2.14, and potential models suggest that the larger running coupling should increase the hyperfine splitting (see equation 2.41). Overall, it is a quantity which is expected to give a good signal for unquenching effects if there are any.

The SESAM collaboration used dynamical configurations with a fixed value of β and varied the sea quark mass (κ). Thus, the lattice spacing varies across their dynamical configurations. It was thus difficult for them to differentiate physical effects from finite lattice spacing effects. They kept the lattice bare quark mass (aM_b^0) constant. Overall, their calculation had an accuracy of $\mathcal{O}(M_b v^6, a^2)$.

SESAM kept the lattice bare quark mass (aM_b^0) constant. From figure 4.7 of this thesis, however, there is an indication that the hyperfine splitting is quite sensitive to

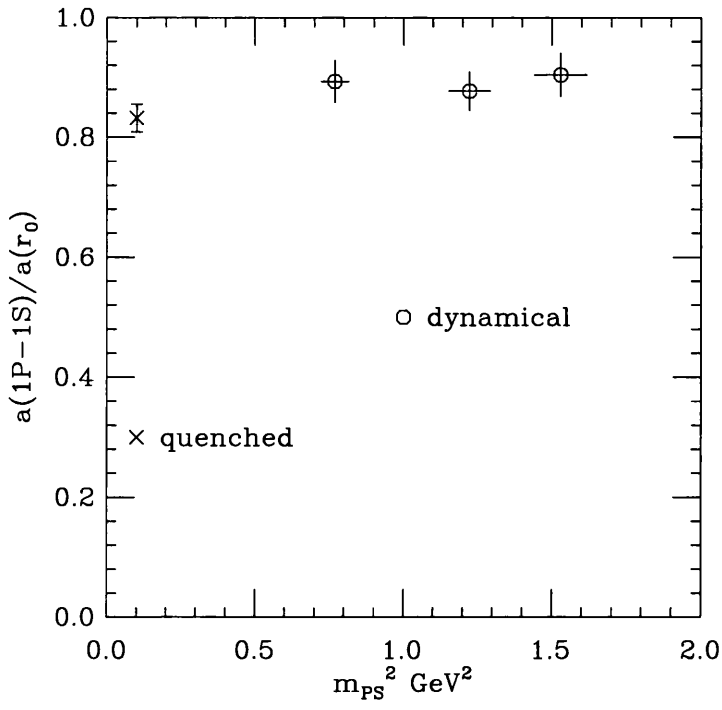

Figure 4.11: Ratio of the lattice spacing from mesonic and gluonic fits.

the bare heavy quark mass. Equation 2.42 makes the same prediction from the standpoint of potential models. Subsequently, in their interpolation of the sea quark mass to $m_s/3$, they find that the hyperfine splitting falls linearly with dynamical quark mass. This contrasts with the extrapolation shown in figure 4.9 of this thesis, where the hyperfine grows as the sea quark mass falls.

The final SESAM result for the hyperfine splitting is also lower than my result, it is ~30 MeV. However, they included the extra terms of $\mathcal{O}(M_b v^6)$, shown in equation 2.74, and compared this with the $\mathcal{O}(M_b v^4)$ action used in this thesis. They found that the inclusion of their additional terms suppressed the hyperfine, by an amount (~10%) consistent with the potential model predictions that $v^2 \approx 0.1$ for bottomonium. Such an effect was also observed by Manke *et al.* [49]. They also found that the hyperfine splitting is sensitive to the tadpole improvement scheme used, an effect they did not see for spin-independent splittings. They used a "link" tadpole improvement scheme (see equation 2.119), as opposed to the plaquette scheme (equation 2.118) which I used. The effect seen by SESAM was that the "plaquette" scheme suppressed the hyperfine splitting relative to the "link" scheme. Such suppression was also found by Shakespeare and Trottier [53]. If their conclusions are correct, then the inclusion of the $\mathcal{O}(M_b v^6)$ terms of equation 2.74 and the use of the link tadpole improvement, $u_0^{(L)}$, should reduce my value for the hyperfine splitting. Unfortunately SESAM over-corrected when tadpole improving by failing to implement the equation 2.124 so their correction of $\mathcal{O}(a^2)$ in the NRQCD action was incorrect.

The CP-PACS Collaboration calculation used the same $\mathcal{O}(M_b v^6)$ heavy quark action as the SESAM group, and the standard (clover improved) light quark action following the Symanzik improvement program. Similarly to the SESAM group they didn't implement the important correction of equation 2.124. As they were working on coarser lattices they used a non-standard gluon action selected by a RG-analysis of the pure gauge theory as an alternative to the gluonic action used in this thesis. Like the SESAM group they fixed β and varied κ, so their lattice spacing wasn't matched across different dynamical quark masses. Their accuracy was $\mathcal{O}(M_b v^6, a^2)$.

Unlike the SESAM group, CP-PACS varied the bare heavy quark mass. As with this thesis (see figure 4.7) they found strong heavy quark mass-dependence for the hyperfine. Again, unlike SESAM and like the results shown here (see figure 4.9), they discovered that the hyperfine increased with decreasing sea quark mass. However, they found a linear plus quadratic interpolation yielded a closer fit to their data. Similarly to this thesis (see figure 4.10) they found that the dynamical hyperfine splitting was significantly larger than their quenched value. Their ratio for the splitting at $n_f = 2$ to that at $n_f = 0$ was 1.3(1), which compares reasonably well with my value of 1.2(1). However, their individual values were ~24 Mev ($n_f = 0$) and ~30 MeV ($n_f = 2$), lower than the corresponding values of 44.3(12) MeV (see table 4.6) and $52.8(22)\binom{+13}{-10}$ (see section 4.4).

CP-PACS also discovered scaling violations for the hyperfine splitting. It is thus difficult to tell whether or not their trends for the hyperfine were scaling artefacts or unquenching effects. As their calculation had the same size of discretisation errors ($\mathcal{O}(a^2)$) as mine, scaling could also hold true for my results. However, they used coarser lattices, and their differing gluon action could also have had an effect. They noticed a signal for unquenching amongst the scaling results as well, finding that results for ($n_f = 0$) and ($n_f = 2$) lay on different scaling lines. Like the SESAM group their values for the hyperfine were smaller than mine, as discussed above. However, CP-PACS' scaling analysis revealed that the hyperfine increased with declining lattice spacing, and so my results, on finer lattices, were closer to theirs than is the case at first sight.

Overall, given the presence of the scaling errors found by the CP-PACS collaboration, the strategy followed by UKQCD of using "matched" dynamical configurations with the same lattice spacings, was a successful policy. The trend seen in figure 4.9 of an increasing hyperfine splitting with decreasing sea quark mass, can be distinguished as an actual trend and not an effect of lattice spacing. Neither the CP-PACS nor SESAM groups included the corrections (equation 2.124) which avoid doing too much tadpole improvement on the $\tilde{\mathbf{E}}$ and $\tilde{\mathbf{B}}$ fields. This makes their $\mathcal{O}(a^2)$ corrections slightly incorrect. As Shakespeare and Trottier have shown [53] this does make a difference to the hyperfine results.

Chapter 5

Determination of α_s and m_b

5.1 Introduction

Lattice QCD can also be used to determine parameters of the standard model. In this chapter two are determined, the strong coupling constant, α_s and the b quark mass, m_b.

In measuring α_s there are various steps. Initially the plaquette expectation value and its scale are determined. Then $\mathcal{O}(a^2)$ errors in the lattice 1^3S_1 channel are accounted for, yielding new values for the channel mass and ultimately a slightly different value for the lattice spacing. With these results a perturbative expansion of the plaquette expectation value is used to measure the plaquette scheme strong coupling constant, α_P. The scale at which the values of α_P are measured is a function of the lattice spacing, so the results are then evolved to a common scale using a three loop beta function. From this result, the dynamical values of $\alpha_P^{(2)}$[1] are evolved to a physical pseudoscalar mass in the same way as in chapter 4. From there, an extrapolation using the quenched and dynamical measures of α_P gives a value of $\alpha_P^{(3)}$. This value is then converted into the common $\overline{\rm MS}$ renormalisation scheme. By employing suitable matching conditions at the c and b quark thresholds the result is run to $\alpha_{\overline{\rm MS}}^{(5)}(M_Z)$, a conventional scale at which to express α_s.

The measurement of m_b is carried out in two ways, the so-called E_0 and Z_m methods. The E_0 method applies a meson "binding energy" correction to the trivial ansatz that $m_b = \frac{1}{2}M_\Upsilon$ yielding a pole mass, $M_{\rm pole}$ for the b quark. This result is then renormalised to give a value for the $\overline{\rm MS}$ b quark mass. The Z_m method has the same renormalisation into the $\overline{\rm MS}$ scheme, but differs from the E_0 method in taking a different measure of $M_{\rm pole}$. The value of $M_{\rm pole}$ is instead derived directly from the lattice bare quark mass. Both methods yield comparable results.

[1] The conventional notation used in this chapter is $\alpha^{(n_f)}$, where n_f is the number of sea quarks included in the calculation.

Results used in calculating $a\Delta M_g$.				
	Quenched		κ=0.135	
aM_b	1.55	1.8	1.8	2.1
α_P(5GeV)	0.19	0.19	0.194	0.194
$a^{3/2}\psi_0(0)$	0.1164(42)	0.1312(52)	0.1445(51)	0.1646(62)
$a^3\psi_0^2(0)$	0.01355(98)	0.01721(136)	0.02088(147)	0.02709(204)
$a\Delta M_g$	0.0022	0.0027	0.0034	0.0044
	κ=0.1345		κ=0.134	
aM_b	1.8	2.1	1.8	2.1
α_P(5GeV)	0.194	0.194	0.194	0.194
$a^{3/2}\psi_0(0)$	0.175(14)	0.231(52)	0.1427(97)	0.164(10)
$a^3\psi_0^2(0)$	0.0306(49)	0.0534(240)	0.02036(277)	0.0269(33)
$a\Delta M_g$	0.0050	0.0087(39)	0.0033	0.0044

Table 5.1: Lattice results used to calculate the gluonic mass shift, $a\Delta M_g$.

5.2 Lattice Spacing and the Gluonic Mass Shift

The (inverse) lattice spacings used in this thesis were derived from the formula:

$$a^{-1}(GeV) = \frac{m(\overline{\chi_b}) - m(\Upsilon)}{aE(1^1P_1 - 1^3S_1)}. \tag{5.1}$$

where $\overline{\chi_b}$ is defined in equation 3.2, and $m()$ signifies the experimentally measured masses. This led to the values chosen in table 4.1. However the gluon action of the theory (see equations 1.52 and 1.54) is only accurate to $\mathcal{O}(a^2)$. These discretisation errors are short distance quantities and so may be estimated using perturbation theory. Perturbation theory [69] gives a *gluonic mass shift* of:

$$a\Delta M_g = \frac{4\pi\alpha_P(q_\delta)}{15} a^3 \left|\psi(0)\right|^2. \tag{5.2}$$

Here, the momentum scale $q_\delta \approx 5GeV$ is the typical momentum transferred through the interaction. The dependence on the mesonic wavefunction at the origin, $\psi(0)$, means that $\Delta M_g = 0$ for P-wave mesons.

The value of α_P(5GeV)=0.19 used for the quenched results at $\beta = 6.0$ was taken from [59]. As the dynamical results don't vary much over κ, one value was taken for them, it was α_P(5GeV)=0.194 [70]. The values used for the wavefunction at the origin were interpolated to the "physical" lattice bare mass values where $M_{\text{kin}} = M_\Upsilon$ (see section 4.2, and in particular table 4.4). The resulting values of the lattice wavefunction at the origin and ultimately $a\Delta M_g$ are shown in table 5.1.

Examination of table 5.1 reveals that the dynamical values of $a\Delta M_g$ are about double the standard value for κ=0.1345. Further examination of figure 4.5 reveals that

	Quenched		κ=0.135	
aM_b	1.55	1.8	1.8	2.1
$aE(1^1P_1 - 1^3S_1)$ Uncorrected	0.1700(41)	0.1680(40)	0.2060(63)	0.2042(60)
$aE(1^1P_1 - 1^3S_1)$ Corrected	0.1678(41)	0.1653(40)	0.2026(63)	0.1998(60)
Corrected a^{-1} (GeV)	2.62(6)	2.66(6)	2.17(7)	2.20(7)
New mean a^{-1} (GeV)	2.64(6)		2.19(7)	
	κ=0.1345		κ=0.134	
aM_b	1.8	2.1	1.8	2.1
$aE(1^1P_1 - 1^3S_1)$ Uncorrected	0.2028(56)	0.2052(45)	0.2058(57)	0.2056(57)
$aE(1^1P_1 - 1^3S_1)$ Corrected	0.1994(56)	0.2008(45)	0.2025(57)	0.2012(57)
Corrected a^{-1}(GeV)	2.21(6)	2.19(5)	2.17(6)	2.19(6)
New mean a^{-1} (GeV)	2.20(6)		2.18(6)	

Table 5.2: Gluonic mass shift corrections and the subsequent corrected lattice spacing values.

$\psi_0(0)$ for κ=0.1345 has much larger errors. Comparison of the data from tables B.171 and B.207 with the other dynamical results indicates that the fit results for κ=0.1345 become noisy sooner than the others. It was thus decided to use an average of the values from the other two κs and use those instead at κ=0.1345. For example, for a lattice bare mass of 1.8, κ=0.135 gave $a\Delta M_g$=0.0034, and 0.0033 for κ=0.134, so the (rounded) average of 0.0034 was used.

Given these results for the gluonic mass shift, the values of the inverse lattice spacing shown in table 4.1 were shifted. In order to make these corrections the lattice $1P-1S$ splittings were calculated as previously, yielding uncorrected splitting values then re-averaged to give a corrected version of table 4.1. The formula used for the correction is:

$$\left(aE(1^1P_1) - aE(1^3S_1)\right)_{\text{corrected}} = \left(aE(1^1P_1) - aE(1^3S_1)\right)_{\text{uncorrected}} - a\Delta M_g. \qquad (5.3)$$

The resulting values are shown in table 5.2.

As with the uncorrected results shown in table 4.1 a mean value was taken for the corrected inverse lattice spacing, with the errors not averaged. The corrected values of a^{-1} are slightly larger than the uncorrected versions (see equation 5.3), but the shift is only $\sim$ 2% and well within the statistical errors.

5.3 The Plaquette Coupling, α_P

The plaquette, introduced in section 1.5.2 and illustrated in figure 1.6, is a small (hence perturbative) gauge invariant quantity in lattice QCD. As it has no explicit fermionic dependence it can be easily computed non-perturbatively. Hence, it is an ideal object

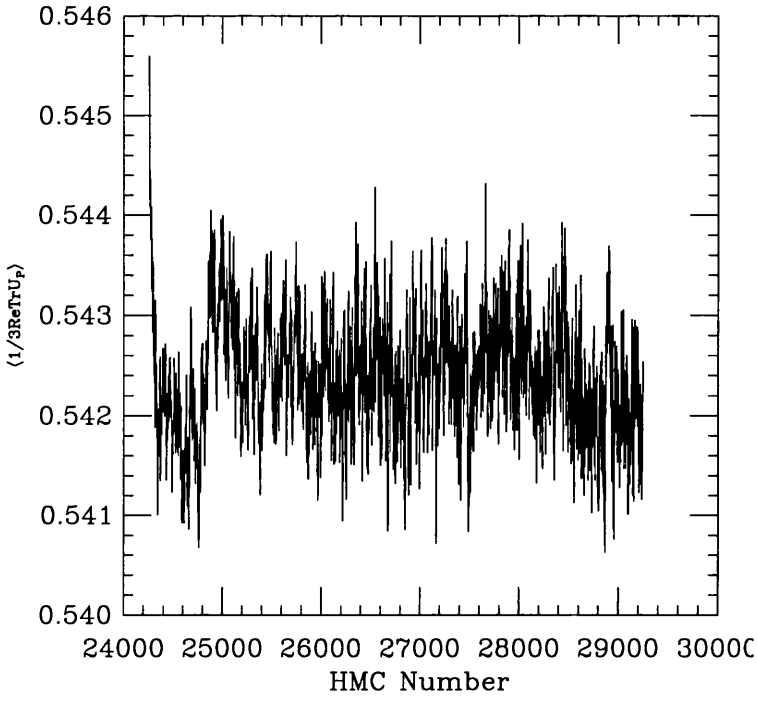

Figure 5.1: $\left\langle \frac{1}{n_c} \mathrm{ReTrU_P} \right\rangle$ versus Hybrid Monte Carlo step number for the dynamical configurations with κ=0.134.

to use in order to make a comparison of its non-perturbative value with a perturbative expansion. The comparison yields values of the plaquette coupling, α_P.

5.3.1 Measuring the Average Plaquette

The UKQCD configuration have an archive of values of the average plaquette, or more precisely of $\left\langle \frac{1}{n_c} \mathrm{ReTrU_P} \right\rangle$, with n_c the number of colour degrees of freedom and U_P is the plaquette of section 1.5.2. This quantity is plotted against the (Hybrid) Monte Carlo step number in figure 5.1. Notice that the initial few values (below ~25000 Monte Carlo steps) differ from the latter plateau, and hence ought to be dropped in any averaging.

Using the data shown in figure 5.1 an average for the whole run was obtained. The average was a jackknife average as there are correlations along the HMC steps. In order to remove the non-thermalised initial data, some of this was skipped. Results for κ=0.134 are shown in table 5.3. From this table it is clear that the value which should be taken is 0.5424. By increasing the size of the bins in which the jackknifing was carried out, the size of the true errors was measured (see section 1.6.2). The value of the error is taken as the error at the point when increasing the bin length produced no corresponding increase in the error. A typical result is shown in figure 5.2, the autocorrelation length of between 100 and 1000 Monte Carlo steps is also fairly typical. It ought to be noted however, that in these calculations there is an ambiguity as to whether the effect of the

Initial HMC Steps Skipped	$\langle\langle 1/3\mathrm{ReTrU_P}\rangle\rangle$
0	0.54242
50	0.54240
100	0.54240
500	0.54245
1000	0.54241

Table 5.3: Average values of $\langle 1/3\mathrm{ReTrU_P}\rangle$ for various different numbers of initial Monte Carlo steps skipped.

	Quenched	κ=0.135	κ=0.1345	κ=0.134
$\langle\langle 1/3\mathrm{ReTrU_P}\rangle\rangle$	0.5937(0)	0.53366(2)(4)	0.53978(2)(5)	0.54242(2)(5)
$-\ln\langle\langle 1/3\mathrm{ReTrU_P}\rangle\rangle$	0.5214(0)	$0.62800(^{+9}_{-10})$	$0.61659(^{+10}_{-9})$	$0.61172(^{+9}_{-10})$

Table 5.4: Results for plaquette expectation values over the whole (Hybrid) Monte Carlo run. The quenched result is taken from [69].

error reaching a plateau is due to the bin length having reached the same size as the autocorrelation length or simply that the bin length is so long that the total number of bins becomes small. With large bins relative to the total number of results it is also possible that many of the later results are discarded as they aren't sufficient to fill a bin. The larger the bin size the greater the number of results missed from the calculation in this way. Nevertheless, the results shown in table 5.4 do indicate that the jackknife error was fairly constant for the different matched dynamical runs, in spite of their differing total statistics. This hints that autocorrelations due to the algorithm are being measured, as opposed to meaningless effects from overly large bin sizes.

The final results obtained for $\langle\langle 1/3\mathrm{ReTrU_P}\rangle\rangle$ are shown in table 5.4. The quenched result was taken from [69]. The first error on the dynamical results arises from the statistical scatter of the results (as in table 5.3), and the second from the jackknife error, owing to autocorrelations. The perturbative expansion of these results is made with reference to $-\ln\langle\langle 1/3\mathrm{ReTrU_P}\rangle\rangle$, hence the second row of results in table 5.3. For those results the two different types of error on the previous row were combined in quadrature.

5.3.2 Plaquette Coupling Results

The perturbative expansion of the negative logarithm of the plaquette is given by the formula [71]:

$$\begin{aligned} -\ln\langle\langle 1/3\mathrm{ReTrU_P}\rangle\rangle &= \frac{4\pi}{3}\alpha_P(1-b\alpha_P), \\ \alpha_P &\equiv \alpha_P(3.40/a), \\ b &= b_1 n_c + b_2 n_f, \\ b_1 &= 0.39687, \end{aligned} \tag{5.4}$$

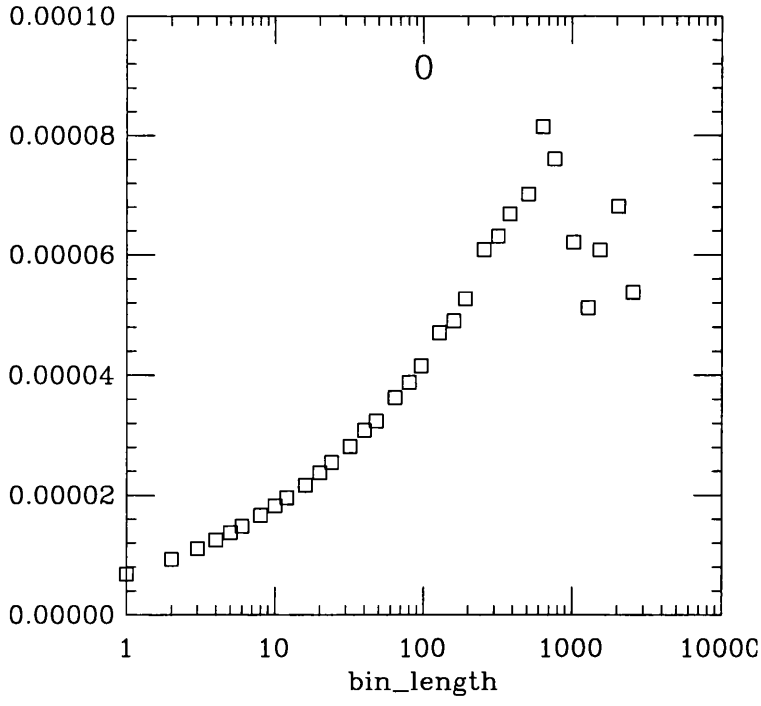

Figure 5.2: Jackknife errors versus the bin length, for the configurations with κ=0.135.

	Quenched	κ=0.135	κ=0.1345	κ=0.134
$3.40/a$ (GeV)	8.98(20)	7.45(24)	7.48(20)	7.41(20)
$\alpha_P(3.40/a)$	0.1520(0)	0.17164(3)	0.16801(3)	0.16646(3)
α_P(8.2 GeV)	0.1563(11)(0)	$0.16691(^{+153}_{-155})(3)$	$0.16367(^{+122}_{-123})(3)$	$0.16178(^{+120}_{-122})(3)$

Table 5.5: Results for the scale at which α_P was measured and its value at a scale of 8.2 GeV.

$$
\begin{aligned}
b_2 &= \frac{12\ln 3.40 - 10}{36\pi}, \\
&- 4\pi P_4 + 32\pi x_2, \\
P_4 &= 0.006696001 - 0.0050467 C_{SW}, \\
&+ 0.029843 C_{SW}^2, \\
x_2 &= 0.00069292 - 0.0000202 C_{SW}, \\
&+ 0.00059624 C_{SW}^2.
\end{aligned}
$$

This definition of α_P is chosen to coincide to $\mathcal{O}(\alpha_P^{n_f})^2$ with the coupling α_V, as defined in [52]. The arbitrary momentum scale at which α_P is obtained, $3.40/a$, comes from [52] too. Note that this scale comes out in the range 7-9 GeV, confirming that the plaquette is quite ultraviolet. It is important to note that the lattice perturbation theory performed in the derivation of equation 5.4 assumed massless quarks.

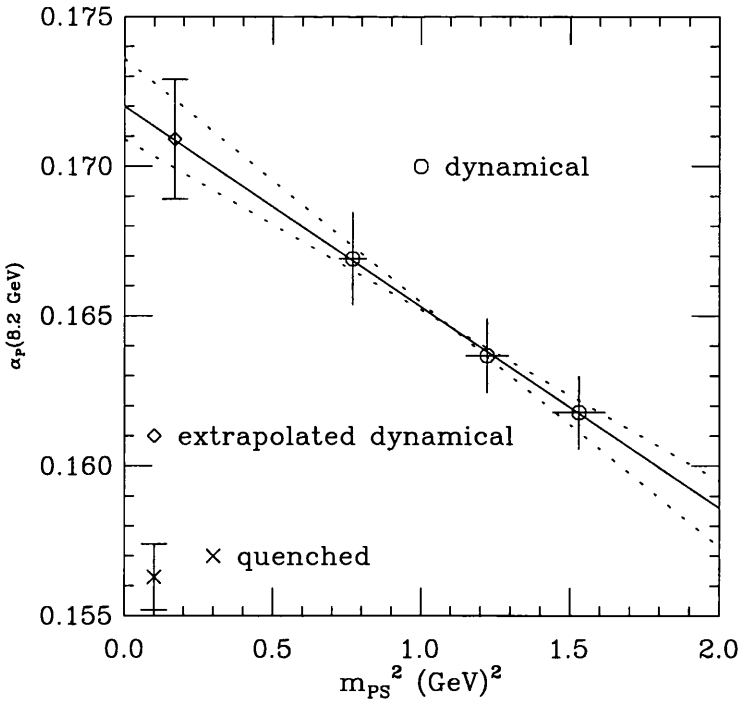

Figure 5.3: Extrapolation of $\alpha_P^{(2)}(8.2\text{ GeV})$ to the physical dynamical pseudoscalar mass defined in equations 4.2 and 4.3. The error bar on the extrapolated point comes from the fit (assuming no uncertainty on simulation pseudoscalar masses). The error lines come from the errors on the non-physical pseudoscalar masses.

The couplings were then evolved to a common scale (8.2 GeV) using the three loop beta function for the plaquette coupling scheme. For this purpose, the scale error (from the lattice spacing in $3.40/a$) was transferred into an error on the plaquette coupling itself. In table 5.5 the scale error in $\alpha_P(8.2\text{ GeV})$ is the (larger) unsymmetric error, whilst the second comes from the the error in $\alpha_P(3.40/a)$. Clearly the scale error is the only one which need be taken into account.

5.3.3 Evolution of $\alpha_P(8.2\text{ GeV})$ to a Physical Pseudoscalar Mass

The results shown in table 5.5 were surprising as they showed an unexpected dependence of $\alpha_P^{(2)}$ on the sea quark mass. This calls into question the usefulness of equation 5.4 for these results. It was derived for massless quarks, *i.e* assuming no sea quark mass dependence for $\alpha_P^{(2)}$.

Given these results for $\alpha_P(8.2\text{ GeV})$, it was clearly necessary to extrapolate the result to the physical dynamical quark mass as in section 4.4. The dynamical mass chosen was again that defined in equations 4.2 and 4.3. For simplicity a linear extrapolation was carried out. The extrapolation is illustrated in figure 5.3.

The error bar on the extrapolated point in figure 5.3 comes from the fit and errors on the individual values of $\alpha_P(8.2\text{ GeV})$. The fit assumed no errors on the unphysical pseudoscalar masses. The errors on these unphysical masses were accounted for by adding the mass error to one outlying point and subtracting the error on the other outlying point, and vice versa. This gives the two dotted lines around the fit line of figure 5.3.

An attempt was made to account for the discrepancy between the massless quark value of $\alpha_P^{(2)}$ from equation 5.4, and the clear dependence on sea quark masses seen in table 5.5, and shown in figure 5.3. In order to do this the gap between the extrapolated value of α_P at a physical pseudoscalar mass, and its value at the lightest of the unphysical pseudoscalar masses was added as an error.

The value obtained for for $\alpha_P^{(2)}(8.2\text{ GeV})$ at the physical pseudoscalar mass was $0.1709(20)\binom{+13}{-10}$. The symmetric error came from the fit (assuming no dynamical mass errors), and the unsymmetric errors from the dynamical mass error. With this value the additional error discussed in the preceding paragraph (concerning the unexpected sea quark mass dependence of the $\alpha_P^{(2)}$) values was evaluated. It was 0.1709-0.16691(from table 5.5)=0.0040.

5.3.4 Extrapolation of $\alpha_P(8.2\text{ GeV})$ to $n_f = 3$.

After the extrapolation to the physical pseudoscalar mass for the dynamical results for $\alpha_P(8.2\text{ GeV})$, the results had to be extrapolated to $n_f = 3$, as with the hyperfine splitting in section 4.5. For this purpose the symmetric, unsymmetric and unexpected mass dependence errors on $\alpha_P^{(2)}(8.2\text{ GeV})$ were combined, the first two in quadrature. The error from the unexpected mass dependence was not added in quadrature with the others as it wasn't independent of them. The largest of the unsymmetric limits were taken as representative of both unsymmetric errors. Hence, it is possible that a slight overestimation of the errors occurs at this stage. The extrapolation to $n_f = 3$ is shown in figure 5.4. It should be noted that it was $1/\alpha_P$ which was extrapolated. This is because perturbation theory suggests that $1/\alpha_P^{(n_f)}$ is more linear against n_f than $\alpha_P^{(n_f)}$ itself. The result obtained for $\alpha_P^{(3)}(8.2\text{ GeV})$ was 0.1793(79).

5.4 Investigation of α_P results

Generally, values of α_s are quoted in the $\overline{\text{MS}}$ scheme. The results shown previously are in the plaquette scheme, and may be translated into the $\overline{\text{MS}}$ scheme, using the formula [72]:

$$\alpha_{\overline{\text{MS}}}^{(n_f)}(Q) = \alpha_P^{(n_f)}(\mathrm{e}^{5/6}Q)\left\{1 + \frac{2}{\pi}\alpha_P^{(n_f)} + \mathcal{O}((\alpha_P^{(n_f)})^2)\right\}, \tag{5.5}$$

where the $\mathrm{e}^{5/6}$ factor is chosen to remove the n_f dependence of the $(\alpha_P^{(n_f)})^2$ coefficient [69]. The coefficient of the $\mathcal{O}((\alpha_P^{(n_f)})^3)$ term is not known at the time of writing [73]. Previous

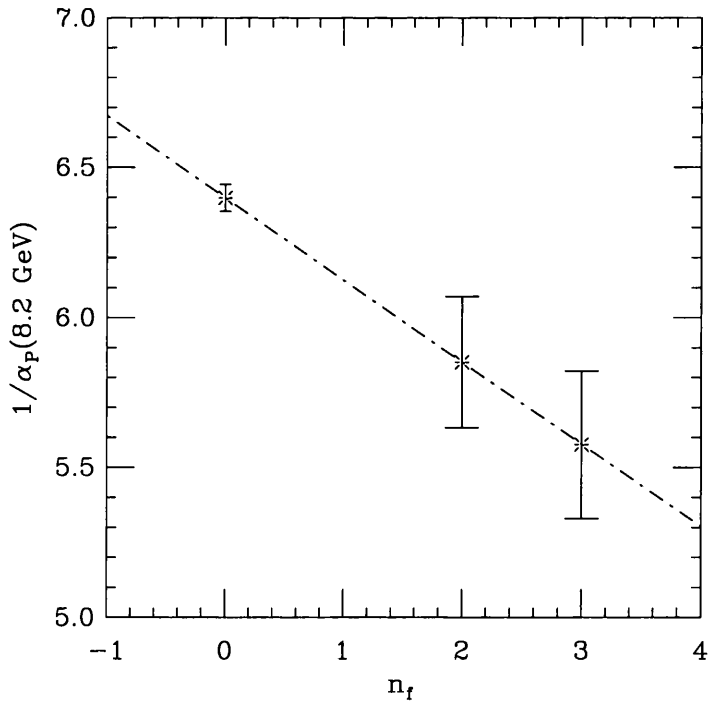

Figure 5.4: Extrapolation of $1/\alpha_P(8.2\ \mathrm{GeV})$ to $n_f = 3$.

lattice calculations [59] [69] did take a (quenched) value of ≈ 0.95, however a mistake has since been found in the calculation which derived that result [73]. The error on $\alpha^{(3)}_{\overline{\mathrm{MS}}}(\mathrm{e}^{-5/6} \times 8.2\mathrm{GeV})$ was obtained by taking the error on $\alpha^{(3)}_P(8.2\ \mathrm{GeV})$ combined in quadrature with the value of $(\alpha^{(3)}_P)^3$, which assumes the coefficient of the leading truncated term to be 1. The result obtained was:

$$\alpha^{(3)}_{\overline{\mathrm{MS}}}(3.56\mathrm{GeV}) = 0.1998(119). \tag{5.6}$$

The third order perturbative beta function for $\alpha^{(n_f)}_{\overline{\mathrm{MS}}}$ was then numerically integrated. Matching conditions [74] were applied at quark thresholds with a view to obtaining a result for $\alpha^{(5)}_{\overline{\mathrm{MS}}}(M_Z)$. Here M_Z is the mass of the Z boson, a conventional scale at which to express α results. The value chosen for the $\overline{\mathrm{MS}}$ c quark mass was 1.3 GeV, following [59][2]. The value chosen for m_b was 4.3 GeV following the determination of this value in section 5.5.1. The values obtained are:

$$\alpha^{(3)}_{\overline{\mathrm{MS}}}(1.3\mathrm{GeV}) = 0.301(30), \tag{5.7}$$

$$\alpha^{(4)}_{\overline{\mathrm{MS}}}(1.3\mathrm{GeV}) = 0.301(30), \tag{5.8}$$

$$\alpha^{(4)}_{\overline{\mathrm{MS}}}(4.3\mathrm{GeV}) = 0.195(11), \tag{5.9}$$

[2] In [59] the dependence of the results on the particular values chosen for m_c and m_b was investigated thoroughly. The conclusion was that the results for $\alpha^{(4)}$ and $\alpha^{(5)}$ are very insensitive to changes in m_c and m_b around these values.

$$\alpha_{\overline{\rm MS}}^{(5)}(4.3{\rm GeV}) = 0.195(11), \quad (5.10)$$

$$\alpha_{\overline{\rm MS}}^{(5)}(91.2{\rm GeV}) = 0.110(4). \quad (5.11)$$

The current world average for this value is [29] 0.118(2). Compared to previous UKQCD lattice determinations [59] [69] the value is also lower. The discrepancy with the older lattice results partially comes from the more truncated form of equation 5.5.

However, the most challenging aspect of this result is the unexpected sea quark mass dependence shown by $\alpha_P^{(2)}(8.2\ {\rm GeV})$, shown in figure 5.3. Such dependence was a new feature and wasn't accounted for in the derivation of eqaution 5.4. Further investigation is clearly required on this issue.

5.5 Determination of the b quark mass

The value of the $\overline{\rm MS}$ bottom quark mass ($\overline{m}_b$) can be determined by combining results from the Υ spectroscopy part of this thesis with the measurements of the plaquette coupling, α_P. There are two ways of doing this calculation, the so-called E_0 and Z_m methods. Both are outlined in [75].

5.5.1 The E_0 method

The E_0 method involves implementing the formulae[3]:

$$M_{\rm pole} = \frac{1}{2}\left(M_\Upsilon - E_{\rm sim} + 2E_0\right), \quad (5.12)$$

$$\overline{m}_b(\overline{m}_b) = Z_{\rm cont} M_{\rm pole}, \quad (5.13)$$

$$Z_{\rm cont} = 1 - 0.4244\alpha_P(0.63M_{\rm pole}) + \mathcal{O}(\alpha_P^2(0.63M_{\rm pole})). \quad (5.14)$$

Here, $M_{\rm pole}$ is the b quark pole mass, a sort of infra-red quark mass required here purely for calculational purposes. The value of M_Υ is 9.460 GeV, the mass of the physical Υ particle (see table A.1). The variable $E_{\rm sim}$ is simply the lattice mass of the 1^3S_1 channel converted to physical units using the lattice spacing values shown in table 4.1 (*i.e.* derived from the lattice measurement of the splitting $1^1P_1 - 1^3S_1$). The variables E_0 and $Z_{\rm cont}$ are the heavy quark self-energy constant and the continuum renormalisation between $M_{\rm pole}$ and $\overline{m}_b(\mu)$ respectively. Morningstar [76] has calculated some of these variables and his results are used to calculate E_0 and $Z_{\rm cont}$ [77]. The value of E_0 is calculated from the equation:

$$aE_0 = \alpha_P(q^*)A + \mathcal{O}(\alpha_P^2(q^*)). \quad (5.15)$$

[3]The calculation is carried out to $\mathcal{O}(\alpha)$. To this order $\overline{m}_b(\overline{m}_b) = \overline{m}_b(M_{\rm pole})$. For a higher order calculation the result would be $\overline{m}_b(\mu)$ and would then require to be run to $\mu = \overline{m}_b$.

aM_b	aA	aq^*
2.00	0.7312(12)	0.4837(16)
1.70	0.6442(13)	0.7950(59)
1.60	0.6056(13)	0.8460(65)
1.50	0.5641(14)	0.9020(73)

Table 5.6: Values used in calculation of E_0, taken from [76]. It should be noted that these results are tadpole improved.

	Quenched	κ=0.135	κ=0.1345	κ=0.134
aA	0.5973	0.7051	0.7225	0.6993
aq^*	0.8572	0.5771	0.5148	0.5978
$\alpha_P(q^*)$	0.2691	0.3909	0.4039	0.3522
aE_0	0.161(72)	0.276(153)	0.292(163)	0.246(124)
$aE_{\rm sim}$	0.3376(33)	0.3933(41)	0.3979(39)	0.3920(43)
$-aE_{\rm sim}+2aE_0$	-0.016(144)	0.159(306)	0.186(362)	0.100(248)
$-E_{\rm sim}+2E_0$ (GeV)	-0.042(378)	0.342(658)	0.402(782)	0.214(531)
$M_{\rm pole}$	4.71(19)	4.90(33)	4.93(39)	4.84(27)
$\alpha_P(0.63M_{\rm pole})$	0.2313	0.2338	0.2266	0.2245
$Z_{\rm cont}$	0.902(26)	0.901(26)	0.904(25)	0.905(24)
$\overline{m}_b(\overline{m}_b)$ (GeV)	4.25(21)	4.42(33)	4.46(37)	4.38(27)

Table 5.7: Results for A and aq^* of table 5.6 interpolated to the aM_b values shown in table 4.4. The lattice measurement of the 1^3S_1 channel mass was similarly interpolated.

Here A is a function of aM_b. Both A and the plaquette coupling, α_P[4] are taken at the scale q^*. These results were taken from [76] and are shown in table 5.6. Notice that the values of the lattice bare quark masses in this table differ from the values obtained for the real bare b quark masses on my lattice (see table 4.4). Thus, the data of table 5.6 was interpolated to the aM_b values of table 4.4, and those interpolated values chosen for A and q^*. These values are shown in table 5.7. The values of $\alpha_P(8.2\text{ GeV})$ in table 5.5 were run to this q^* and this value used in the calculation.

Table 5.7 contains no error values excepting those shown for E_0. The error for E_0 was calculated by considering the $\mathcal{O}(\alpha^2)$ errors of equation 5.15. In the absence of other information the coefficient was taken as unity. This truncation error is the dominant error so the others were ignored in the calculation.

The values of $E_{\rm sim}$ used for the results in table 5.7, were selected from a $t_{\rm min}$ value of 6 for the 1^3S_1 channel fit. The same timeslice was used for all results to avoid introducing systematic errors when comparing the results. The errors in $Z_{\rm cont}$ came only from the $\mathcal{O}(\alpha_P^2)$ round up errors. The inverse lattice spacings used in converting to

[4]The value chosen for the plaquette coupling was $\alpha_P^{(0)}$ for the quenched data and $\alpha_P^{(2)}$ for the dynamical data.

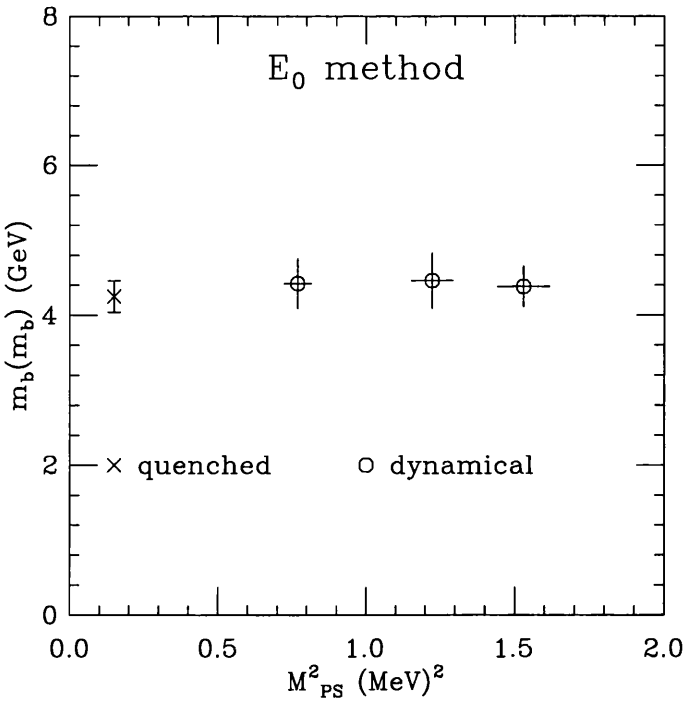

Figure 5.5: Results from the E_0 method of calculating $\overline{m}_b(\overline{m}_b)$.

physical units come from the familiar $1P - 1S$ derived spacings of table 4.1. With errors at this order in the E_0 calculation (see equation 5.15), the coefficient was chosen as unity. However, in the case of $Z_{\rm cont}$ there is a perturbative determination of the coefficient of the α^2 piece [77], the value being -0.4771. Thus, the error on $Z_{\rm cont}$ was taken as $0.4771\alpha_P^2(0.63M_{\rm pole})$.

Finally, there are two sources of errors on the value of $\overline{m}_b$. The first comes from the pole mass errors and the second from the $Z_{\rm cont}$ errors. These two sources of errors were combined in quadrature to give the final values of $\overline{m}_b(\overline{m}_b)$ shown in table 5.7 and in figure 5.5.

The value of $\overline{m}_b$ from the quenched results is smaller than the dynamical results, but not significantly. No such difference had been anticipated, in fact it was expected that the dynamical results would be smaller, given the larger α in the $Z_{\rm cont}$ calculation. Part of the difference was caused by the quenched $M_{\rm pole}$ result being slightly smaller. It had been anticipated that $M_{\rm pole}$ would be the same across both quenched and dynamical results, since M_Υ is an order of magnitude larger than either E_0 or $E_{\rm sim}$. The major reason for expecting the quenched result to be larger was that $Z_{\rm cont}$(quenched) might have been larger as $\alpha_{\rm quenched}$ would be smaller, and indeed was at 8.2 GeV. However, the scale at which $Z_{\rm cont}$ is calculated, $0.63M_{\rm pole}$ is $\approx$3 GeV, where $\alpha_{\rm quenched}$ and $\alpha_{\rm dynamical}$ are very similar. Thus, the $Z_{\rm cont}$ results are practically the same.

aM_b	aB	$a\tilde{q}^*$
2.50	0.3180(23)	0.5988(74)
2.00	0.4183(22)	0.5783(57)
1.70	0.4899(24)	0.57(12)
1.60	0.5131(24)	0.723(23)
1.50	0.5376(22)	0.835(17)
2.10	0.3982(22)	0.5824(64)
1.80	0.4660(20)	0.5728(62)
1.55	0.5254(21)	0.779(21)

Table 5.8: Values used in calculation of Z_m, taken from [76]. It should be noted that these results are tadpole improved.

5.5.2 The Z_m method

The Z_m method involves the use of equation 5.13 again, except that there is a new definition of $M_{\rm pole}$, called $\tilde{M}_{\rm pole}$ for clarity:

$$\tilde{M}_{\rm pole} = Z_m M_b^0, \tag{5.16}$$

where M_b^0 is the bare heavy quark mass and Z_m is the lattice NRQCD renormalisation calculated to $\mathcal{O}(\alpha_s)$ by Morningstar [76] as:

$$Z_m = 1 + \alpha_P(\tilde{q}^*)B + \mathcal{O}(\alpha_P^2(\tilde{q}^*)). \tag{5.17}$$

It is important to note that the values taken for aM_b^0 were not those shown in table 4.4. Here, instead of interpolating to the real bare b quark mass, the actual bare b quark masses used in the simulations were chosen. Any difference in the real bare b quark mass is then corrected for by using an a^{-1} defined by:

$$a^{-1}(\text{GeV}) = \frac{\text{M}_\Upsilon(= 9.460\text{GeV})}{\text{aM}_{\rm kin}}, \tag{5.18}$$

where the values used for $aM_{\rm kin}$ were taken from tables 3.19 and 3.20. Thus, the interpolated values for aM_b are replaced by non-interpolated values at two separate lattice bare quark masses. The values of B and $a\tilde{q}^*$ from [76] shown in table 5.8 then have to be interpolated to give the points at which aM_b was used as an input in the calculation *i.e.* 1.55, 1.8 and 2.1. The interpolated values are shown in the lower part of table 5.8.

The new lattice spacing results are shown in tables 5.9 and 5.10. Also shown are the calculations of Z_m. From equation 5.17 the error in Z_m was taken by assuming a coefficient of unity for the $\mathcal{O}((\alpha_P(\tilde{q}^*))^2)$ unknown term. The new values of $Z_{\rm cont}$ were calculated using equation 5.14 with the $M_{\rm pole}$ values of tables 5.9 and 5.10. As with the E_0 method the errors on the $Z_{\rm cont}$ values were taken as $0.4771\alpha_P^2(0.63M_{\rm pole})$. The final result for $\overline{m}_b$ was then derived using equation 5.14. As with the E_0 method, the scale

	Quenched		κ=0.135	
aM_b	1.55	1.8	1.8	2.1
a^{-1} (GeV)	2.65(3)	2.34(3)	2.25(4)	1.99(3)
$\alpha_P(\tilde{q}^*)$	0.2637	0.3534	0.3874	0.3825
Z_m	1.139(70)	1.165(125)	1.181(150)	1.152(146)
$aM_{\rm pole}$	1.77(11)	2.10(23)	2.13(27)	2.42(31)
$M_{\rm pole}$ (GeV)	4.69(30)	4.91(54)	4.79(61)	4.82(62)
$\alpha_P(0.63M_{\rm pole})$	0.2321	0.2143	0.2388	0.2262
$Z_{\rm cont}$	0.902(26)	0.909(22)	0.899(27)	0.904(24)
$\overline{m}_b(\overline{m}_b)$ (GeV)	4.23(30)	4.46(50)	4.31(56)	4.36(57)

Table 5.9: Results for the calculation of $\overline{m}_b(\overline{m}_b)$ for the quenched run and the dynamical run with κ=0.135.

	κ=0.1345		κ=0.134	
aM_b	1.8	2.1	1.8	2.1
a^{-1} (GeV)	2.35(6)	2.04(4)	2.23(4)	1.95(4)
$\alpha_P(\tilde{q}^*)$	0.3667	0.3623	0.3583	0.3542
Z_m	1.171(135)	1.144(131)	1.167(128)	1.141(126)
$aM_{\rm pole}$	2.11(24)	2.40(28)	2.10(23)	2.40(27)
$M_{\rm pole}$ (GeV)	4.96(58)	4.90(58)	4.68(52)	4.68(54)
$\alpha_P(0.63M_{\rm pole})$	0.2323	0.2204	0.2298	0.2175
$Z_{\rm cont}$	0.901(26)	0.907(23)	0.903(25)	0.908(23)
$\overline{m}_b(\overline{m}_b)$ (GeV)	4.47(54)	4.44(54)	4.23(48)	4.25(50)

Table 5.10: Results for the calculation of $\overline{m}_b(\overline{m}_b)$ for the dynamical results with κ=0.1345 and 0.134.

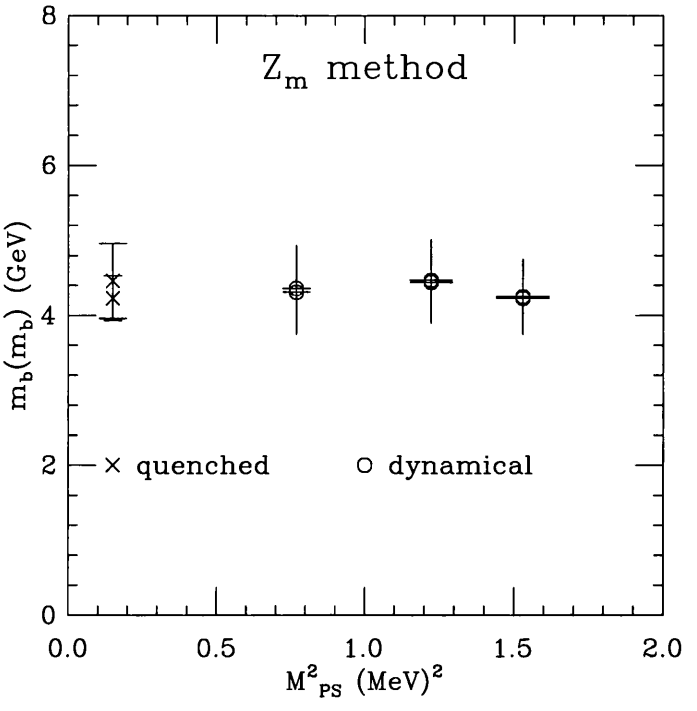

Figure 5.6: Results from the Z_m method of calculating $\overline{m}_b(\overline{m}_b)$.

at which $\overline{m}_b$ is determined is arbitrary to the level of accuracy (in α) available in the perturbative renormalisations used here.

From the final results for $\overline{m}_b$ of tables 5.9 and 5.10 it is clear that, whilst there is slightly less spread in the results, there is a larger error then with the E_0 method due entirely to the $M_{\rm pole}$ values. The result is illustrated in figure 5.6. Indeed, the dynamical result for κ=0.134 is lower than the quenched result.

5.5.3 Conclusion for the $\overline{m}_b(\overline{m}_b)$ Results

To conclude, there was no significant difference between the quenched and dynamical results for $\overline{m}_b(\overline{m}_b)$. Taking the most precise result (from the E_0 method), on the lightest dynamical quark mass configurations, the value obtained is:

$$\overline{m}_b(\overline{m}_b) = 4.42(33)\text{GeV}. \tag{5.19}$$

In terms of other results the central value compares fairly well with another UKQCD determination from lattice $B\overline{B}$ studies [78]:

$$\overline{m}_b(\overline{m}_b) = 4.32(8)\text{GeV}. \tag{5.20}$$

The $B\overline{B}$ studies have better perturbation theory results using infinite mass quarks, which gives them a smaller error for $\overline{m}_b$. The best way of improving $\overline{m}_b$ results

from the finite mass Υ calculation would be through improved perturbative results for finite mass quarks.

Chapter 6

Conclusions

The upsilon system has been considered for a while to be an ideal place to study the effect of introducing dynamical quarks into lattice QCD. Several mass splittings are sensitive to such short distance physics, even if at present the sea quarks are relatively heavy ($m_{\rm sea}$ varies from $\sim m_s$ to $\sim 2m_s$).

The results were generated using an $\mathcal{O}(v_b^4, a^2)$ NRQCD heavy quark action on gauge configurations with two flavours of dynamical quarks. These configurations were generated by the UKQCD collaboration using a Hybrid Monte Carlo algorithm. An important feature of the dynamical configurations used was that they were generated with matched lattice spacings by allowing β to vary to compensate for the sea quark mass variation. This allowed systematic effects due to different dynamical quark masses to be isolated from lattice spacing effects. In order to try and study unquenching effects the calculation was repeated on a quenched configuration at β=6.0. Unfortunately, this lattice was slightly finer than the dynamical lattices as there were no matched, quenched configurations available when the calculation was carried out.

Another new feature in this calculation was the inclusion of discretisation corrections to the lattice $F_{\mu\nu}$ cloverleaf fields. Two bare b quark masses were used on each configuration to give one kinetic mass larger and one smaller than the physical upsilon mass. Where required, results were then interpolated to the physical upsilon mass.

Multicorrelation fitting routines were used to extract lattice state energies and amplitudes. Two types of fit were tried: matrix and vector. The matrix fits gave more accurate results and stabler plateaux. For the S waves three different radial smearing functions were used, for the P waves only two. For the former, there was thus a choice between fits with two smearing functions and those with three. The fits with three smearings gave more stable ground and first excited state results, although, the $2P$ and $3S$ results were still very noisy. Most of the fits were of good quality, unfortunately, for the dynamical run with κ=0.134 the fits had quite poor Q values. Some results from the dynamical run with κ=0.1345 also seemed suspect giving large errors on the wavefunction at the origin (via fit amplitudes) and for lattice P channel splittings. An error in the code prevented matrix fits being carried out on the lattice $^3P_1$ and $^3P_{2T}$ channels, vector fits

were fine though.

The lattice spacing values used for the upsilon spectroscopy were calculated by comparing the lattice $1^1P_1 - 1^3S_1$ splittings with the physical $\overline{\chi}_b - \Upsilon$ splitting. The lattice 1^1P_1 channel was used rather than the $1\overline{^3P}$ channel due to the difficulties with the matrix $^3P_{1,2T}$ channel fits. Vector fits to the 1^1P_1 and $1\overline{^3P}$ channels could resolve no difference in their masses. The results confirmed that the three dynamical ensembles had the same spacing within error. These lattice spacing values were compared with those determined using the gluonic Sommer scale. There was better agreement between the dynamical results, indicating that physics at different scales is more consistent on the dynamical lattices.

The splitting between the zero-momentum lattice 1^3S_1 channel, and several small, non-zero momenta versions was used in evaluating the lattice kinetic masses. Two types of ansatz for the kinetic mass were applied, one non-relativistic and one with a small relativistic correction. The relativistic version gave a more stable kinetic mass value, but the errors were too large to make a definitive choice between them.

In making comparisons between results on dynamical configurations with different sea quark masses, the same initial time slice was chosen for the best fit values, even where a better choice could be made on individual fits. This was done in order to avoid introducing additional sources of systematic error. For all quantities except the hyperfine splitting the results on the different bare quark masses overlapped. The significant differences between the hyperfines were as expected from potential model studies. Unfortunately, the related effect for the wavefunction at the origin of the S waves wasn't observed due to the larger errors on the values for κ=0.1345. The trend of the wavefunction at the origin also seemed to be in an unexpected direction, growing as the sea quark mass fell, like the hyperfine, when it should have gone the opposite way to the hyperfine. The ratio of radial to orbital splittings gave evidence of unquenching and sea quark mass dependence, but, once again, in the opposite direction from the expected change. The trend wasn't very significant though. The hyperfine splitting results showed a clear unquenching signal.

The hyperfines were interpolated to the physical upsilon kinetic mass and then extrapolated to a physical light pseudoscalar meson mass (by chiral perturbation theory the same thing as a physical sea quark mass). The dynamical hyperfine was larger than that obtained in the quenched approximation. The quenched and dynamical hyperfine results were extrapolated to the physically appropriate $n_f = 3$ case. This procedure gave a prediction for the η_b mass of 9.517(4) GeV. Comparison of this result with that obtained by other collaborations indicated that it was larger than other measurements. However, the other groups didn't use matched lattice spacings, so there is an ambiguity as to whether their trends in sea quark mass were spacing effects or sea quark effects. They also used incorrect $\mathcal{O}(a^2)$ corrections to the NRQCD action.

Plaquette expectation values for the various configurations used were measured. These gave clear unquenching signals with the running coupling larger for dynamical results, as expected. One unexpected feature was the dependence of the dynamical

coupling results on the sea quark mass. This effect introduced addititonal errors, since the perturbation theory used to calculate the lattice couplings had assumed no such dependence. The same extrapolation to a physical sea quark mass as used for the hyperfine splittings was repeated for the couplings. The dynamical and quenched coupling results were used to give a value at $n_f = 3$. This value was converted into the $\overline{\rm MS}$ scheme. Using a three loop beta function and matching conditions at the c and b quark thresholds the result was run to $n_f = 5$ and a scale equal to the Z boson mass. The eventual best result obtained for the strong coupling constant was $\alpha^{(5)}_{\overline{\rm MS}}(M_Z)$=0.110(4). This was slightly lower than the current world average of 0.118(2). The discrepancy and, in particular, the sea quark mass dependence of the coupling clearly require further study.

Two methods were used to calculate the $\overline{\rm MS}$ bar b quark mass. Neither set of results showed significant unquenching effects. One method gave results for both lattice bare masses on one set of configurations. These results indicated insensitivity to the lattice bare quark mass, although it should be noted that the perturbation theory used was only accurate to first order in the lattice coupling. The best result obtained from the dynamical configurations was $\overline{m}_b(\overline{m}_b)$=4.42(33) GeV. More accurate perturbation theory is required before the upsilon result has the same degree of accuracy as those from lattice B meson studies.

Appendix A

Experimental Masses

A.1 Experimental Meson Masses

A.1.1 Experimental Masses of Bottomium Mesons

State	Rest Mass (GeV)
1^1S_0, or η_b	*
1^3S_1, or Υ, $\Upsilon(1S)$	9.460
2^3S_1, or Υ', $\Upsilon(2S)$	10.023
3^3S_1, or Υ'', $\Upsilon(3S)$	10.355
4^3S_1, or $\Upsilon(4S)$	$10.580(4)^\dagger$
5^3S_1, or $\Upsilon(5S)$	$10.865(8)^\dagger$
6^3S_1, or $\Upsilon(6S)$	$11.019(8)^\dagger$
1^1P_1, or h_b	*
1^3P_0, or $\chi_{b0}(1P)$	9.860(1)
2^3P_0, or $\chi_{b0}(2P)$	10.232
1^3P_1, or $\chi_{b1}(1P)$	9.893
2^3P_1, or $\chi_{b1}(2P)$	10.255
1^3P_2, or $\chi_{b2}(1P)$	9.913
2^3P_2, or $\chi_{b2}(2P)$	10.269

Table A.1: Experimental bottomium spectrum. * State not found. † Masses above the $B\overline{B}$ threshold. Data taken from [29].

A.1.2 Experimental Masses of Light Mesons

Meson	Rest Mass (MeV)
π^0	134.98
$\pi^\pm$	139.57
K^0	497.67(3)
$K^\pm$	493.68(2)

Table A.2: Experimental Masses of the light mesons needed for this thesis. Data taken from [29].

Appendix B

Best Lattice Fits

B.1 Lattice Results for the Quenched Calculations

B.1.1 Lattice State Fits for aM_b=1.55

t_{min}/t_{max}	aE_1	aE_2	aE_3	Q
2/13	0.3371(7)	0.5848(48)	0.7217(66)	1.1×10^{-7}
3/13	0.3362(7)	0.5774(65)	0.7136(99)	1.3×10^{-2}
4/13	0.3356(8)	0.5769(80)	0.7158(163)	0.13
5/13	0.3348(8)	0.5683(101)	0.7098(247)	0.50
6/13	0.3349(8)	0.5653(163)	0.6790(333)	0.51
7/13	0.3350(9)	0.5740(201)	0.6704(497)	0.50
8/13	0.3351(9)	0.5698(342)	0.6664(685)	0.27
9/13	0.3350(10)	0.5643(507)	0.6327(920)	0.29
10/13	0.3340(11)	0.5831(231)	1.004(293)	0.89
11/13	0.3341(24)	0.3850(3319)	0.6004(374)	0.82

Table B.1: Matrix fit to the $^3S_1$ channel.

t_{min}/t_{max}	aE_1	aE_2	aE_3	Q
2/13	0.3192(6)	0.5705(45)	0.7027(72)	1.2×10^{-5}
3/13	0.3185(7)	0.5644(60)	0.6955(106)	4.2×10^{-2}
4/13	0.3181(7)	0.5654(72)	0.7044(178)	0.21
5/13	0.3176(7)	0.5582(88)	0.7031(268)	0.46
6/13	0.3176(7)	0.5547(142)	0.6632(354)	0.46
7/13	0.3177(8)	0.5627(170)	0.6515(516)	0.44
8/13	0.3177(8)	0.5593(288)	0.6457(713)	0.21
9/13	0.3176(9)	0.5480(461)	0.6070(909)	0.31
10/13	0.3166(9)	0.5596(203)	0.9204(2588)	0.88
11/13	0.3168(11)	0.4424(3152)	0.5786(382)	0.77

Table B.2: Matrix fit to the $^1S_0$ channel.

t_{min}/t_{max}	aE_1	aE_2	Q
2/13	0.5188(25)	0.7659(46)	1.6×10^{-4}
3/13	0.5131(29)	0.7480(63)	7.5×10^{-2}
4/13	0.5114(33)	0.7439(86)	0.11
5/13	0.5048(40)	0.7233(114)	0.38
6/13	0.5041(46)	0.7092(157)	0.64
7/13	0.5070(51)	0.7227(227)	0.56
8/13	0.5062(61)	0.6976(324)	0.67
9/13	0.5049(75)	0.6861(475)	0.60
10/13	0.5028(72)	0.7634(820)	0.81
11/13	0.5021(168)	0.6326(1171)	0.75

Table B.3: Matrix fit to the ${}^1P_1$ channel.

t_{min}/t_{max}	aE_1	aE_2	Q
2/13	0.5188(25)	0.7659(46)	1.6×10^{-4}
3/13	0.5131(29)	0.7480(63)	7.5×10^{-2}
4/13	0.5114(33)	0.7439(86)	0.11
5/13	0.5048(40)	0.7233(114)	0.38
6/13	0.5041(46)	0.7092(157)	0.64
7/13	0.5070(51)	0.7227(227)	0.56
8/13	0.5062(61)	0.6976(324)	0.67
9/13	0.5049(75)	0.6861(475)	0.60
10/13	0.5028(72)	0.7634(820)	0.81
11/13	0.5021(168)	0.6326(1171)	0.75

Table B.4: Matrix fit to the ${}^1P_1$ channel in the x direction.

t_{min}/t_{max}	aE_1	aE_2	Q
2/13	0.5188(25)	0.7659(46)	1.6×10^{-4}
3/13	0.5131(29)	0.7480(63)	7.5×10^{-2}
4/13	0.5114(33)	0.7439(86)	0.11
5/13	0.5048(40)	0.7233(114)	0.38
6/13	0.5041(46)	0.7092(157)	0.64
7/13	0.5070(51)	0.7227(227)	0.56
8/13	0.5062(61)	0.6976(324)	0.67
9/13	0.5049(75)	0.6861(475)	0.60
10/13	0.5028(72)	0.7634(820)	0.81
11/13	0.5021(168)	0.6326(1171)	0.75

Table B.5: Matrix fit to the ${}^1P_1$ channel in the y direction.

t_{min}/t_{max}	aE_1	aE_2	Q
2/13	0.5188(25)	0.7659(46)	1.6×10^{-4}
3/13	0.5131(29)	0.7480(63)	7.5×10^{-2}
4/13	0.5114(33)	0.7439(86)	0.11
5/13	0.5048(40)	0.7233(114)	0.38
6/13	0.5041(46)	0.7092(157)	0.64
7/13	0.5070(51)	0.7227(227)	0.56
8/13	0.5062(61)	0.6976(324)	0.67
9/13	0.5049(75)	0.6861(475)	0.60
10/13	0.5028(72)	0.7634(820)	0.81
11/13	0.5021(168)	0.6326(1171)	0.75

Table B.6: Matrix fit to the ${}^1P_1$ channel in the z direction.

t_{min}/t_{max}	aE_1	aE_2	Q
2/13	0.5048(27)	0.7462(53)	5.8×10^{-3}
3/13	0.5002(30)	0.7312(70)	0.18
4/13	0.4982(34)	0.7240(93)	0.13
5/13	0.4911(41)	0.7041(123)	0.48
6/13	0.4897(48)	0.6987(172)	0.67
7/13	0.4937(53)	0.7157(246)	0.61
8/13	0.4932(65)	0.6840(354)	0.70
9/13	0.4974(74)	0.6955(532)	0.57
10/13	0.4936(74)	0.7526(908)	0.81
11/13	0.4982(97)	0.7517(1462)	0.53

Table B.7: Matrix fit to the $^3P_0$ channel.

t_{min}/t_{max}	aE_1	aE_2	Q
2/13	0.5150(28)	0.7627(52)	2.3×10^{-3}
3/13	0.5096(32)	0.7465(71)	0.12
4/13	0.5071(36)	0.7392(94)	9.2×10^{-2}
5/13	0.4994(44)	0.7187(124)	0.42
6/13	0.4979(51)	0.7138(175)	0.69
7/13	0.5011(55)	0.7323(257)	0.62
8/13	0.5001(68)	0.6948(371)	0.71
9/13	0.5029(75)	0.7041(563)	0.56
10/13	0.4991(74)	0.7560(931)	0.85
11/13	0.5045(95)	0.7656(1530)	0.60

Table B.8: Matrix fit to the $^3P_1$ channel.

t_{min}/t_{max}	aE_1	aE_2	Q
2/13	0.5163(31)	0.7634(56)	5.5×10^{-2}
3/13	0.5119(35)	0.7510(77)	0.31
4/13	0.5097(40)	0.7489(105)	0.23
5/13	0.5012(49)	0.7243(142)	0.68
6/13	0.4994(58)	0.7152(203)	0.82
7/13	0.5014(64)	0.7304(294)	0.73
8/13	0.5031(76)	0.7112(431)	0.62
9/13	0.5057(79)	0.7279(669)	0.56
10/13	0.4977(83)	0.7542(1102)	0.87
11/13	0.5021(109)	0.8466(1989)	0.61

Table B.9: Matrix fit to the $^3P_1$ channel in the x direction.

t_{min}/t_{max}	aE_1	aE_2	Q
2/13	0.5156(31)	0.7630(56)	1.8×10^{-3}
3/13	0.5095(35)	0.7428(76)	0.14
4/13	0.5054(40)	0.7318(98)	0.14
5/13	0.4981(49)	0.7139(131)	0.29
6/13	0.4950(57)	0.6994(178)	0.60
7/13	0.4995(64)	0.7274(267)	0.54
8/13	0.4978(75)	0.6901(378)	0.80
9/13	0.5036(87)	0.7179(594)	0.81
10/13	0.5041(92)	0.8065(1043)	0.76
11/13	0.5091(120)	0.8534(1846)	0.41

Table B.10: Matrix fit to the ${}^3P_1$ channel in the y direction.

t_{min}/t_{max}	aE_1	aE_2	Q
2/13	0.5144(31)	0.7607(54)	1.2×10^{-2}
3/13	0.5091(35)	0.7477(73)	0.11
4/13	0.5069(39)	0.7374(99)	0.12
5/13	0.4975(48)	0.7122(127)	0.55
6/13	0.4963(55)	0.7110(181)	0.75
7/13	0.4978(63)	0.7131(262)	0.71
8/13	0.4959(81)	0.6685(374)	0.82
9/13	0.4973(97)	0.6544(535)	0.69
10/13	0.4945(90)	0.6974(868)	0.93
11/13	0.5019(127)	0.6409(1309)	0.88

Table B.11: Matrix fit to the ${}^3P_1$ channel in the z direction.

t_{min}/t_{max}	aE_1	aE_2	Q
2/13	0.5230(30)	0.7770(53)	2.5×10^{-3}
3/13	0.5170(34)	0.7600(73)	9.3×10^{-2}
4/13	0.5145(38)	0.7551(99)	6.9×10^{-2}
5/13	0.5059(46)	0.7330(131)	0.52
6/13	0.5029(55)	0.7152(183)	0.90
7/13	0.5049(61)	0.7246(265)	0.86
8/13	0.5045(77)	0.6979(386)	0.82
9/13	0.5082(84)	0.7055(585)	0.67
10/13	0.5060(80)	0.7981(1034)	0.90
11/13	0.5104(104)	0.8172(1745)	0.62

Table B.12: Matrix fit to the ${}^3P_{2E}$ channel.

t_{min}/t_{max}	aE_1	aE_2	Q
2/13	0.5224(32)	0.7750(54)	1.1×10^{-2}
3/13	0.5168(36)	0.7613(76)	0.13
4/13	0.5164(41)	0.7591(106)	7.0×10^{-2}
5/13	0.5067(50)	0.7309(138)	0.49
6/13	0.5031(60)	0.7118(192)	0.92
7/13	0.5027(74)	0.7035(266)	0.88
8/13	0.5028(100)	0.6882(387)	0.84
9/13	0.5074(122)	0.6874(572)	0.69
10/13	0.5086(101)	0.7539(1010)	0.90
11/13	0.5125(144)	0.7584(1614)	0.61

Table B.13: Matrix fit to the ${}^3P_{2E}$ channel, xy component.

t_{min}/t_{max}	aE_1	aE_2	Q
2/13	0.5243(32)	0.7777(57)	1.1×10^{-2}
3/13	0.5181(37)	0.7582(78)	0.24
4/13	0.5137(43)	0.7482(104)	0.24
5/13	0.5062(52)	0.7326(141)	0.45
6/13	0.5020(63)	0.7112(188)	0.75
7/13	0.5050(67)	0.7203(278)	0.75
8/13	0.5026(83)	0.6968(405)	0.66
9/13	0.5064(92)	0.6989(621)	0.52
10/13	0.5056(92)	0.8094(1097)	0.58
11/13	0.5128(123)	0.8030(1850)	0.28

Table B.14: Matrix fit to the ${}^3P_{2E}$ channel, xz component.

t_{min}/t_{max}	aE_1	aE_2	Q
2/13	0.5248(33)	0.7789(58)	8.3×10^{-4}
3/13	0.5189(38)	0.7632(80)	1.1×10^{-2}
4/13	0.5151(43)	0.7586(107)	1.1×10^{-2}
5/13	0.5047(52)	0.7332(141)	0.24
6/13	0.5023(63)	0.7148(205)	0.43
7/13	0.5046(67)	0.7370(306)	0.37
8/13	0.5057(79)	0.7028(443)	0.57
9/13	0.5095(81)	0.7277(683)	0.45
10/13	0.5034(90)	0.8262(1243)	0.61
11/13	0.5030(115)	0.8836(2260)	0.31

Table B.15: Matrix fit to the ${}^3P_{2E}$ channel, yz component.

t_{min}/t_{max}	aE_1	aE_2	Q
2/13	0.5233(30)	0.7772(53)	1.9×10^{-3}
3/13	0.5175(34)	0.7603(73)	0.10
4/13	0.5150(38)	0.7548(98)	7.6×10^{-2}
5/13	0.5065(46)	0.7333(131)	0.58
6/13	0.5034(54)	0.7185(182)	0.94
7/13	0.5058(60)	0.7295(268)	0.91
8/13	0.5063(74)	0.7075(395)	0.87
9/13	0.5095(83)	0.7032(588)	0.80
10/13	0.5082(81)	0.7861(1024)	0.90
11/13	0.5121(105)	0.7788(1686)	0.63

Table B.16: Matrix fit to the ${}^3P_{2T}$ channel.

t_{min}/t_{max}	aE_1	aE_2	Q
2/13	0.5234(32)	0.7763(55)	5.3×10^{-3}
3/13	0.5181(36)	0.7631(77)	8.8×10^{-2}
4/13	0.5180(41)	0.7609(107)	4.8×10^{-2}
5/13	0.5082(50)	0.7315(139)	0.45
6/13	0.5048(59)	0.7135(195)	0.86
7/13	0.5063(71)	0.7145(276)	0.80
8/13	0.5081(96)	0.7040(408)	0.79
9/13	0.5117(123)	0.6817(584)	0.71
10/13	0.5137(103)	0.7478(1028)	0.82
11/13	0.5176(161)	0.7324(1617)	0.53

Table B.17: Matrix fit to the ${}^3P_{2T}$ channel, xy component.

t_{min}/t_{max}	aE_1	aE_2	Q
2/13	0.5245(32)	0.7774(56)	9.9×10^{-3}
3/13	0.5188(37)	0.7580(78)	0.21
4/13	0.5141(43)	0.7471(104)	0.22
5/13	0.5066(52)	0.7305(140)	0.42
6/13	0.5031(62)	0.7089(188)	0.75
7/13	0.5065(66)	0.7230(280)	0.70
8/13	0.5048(82)	0.6972(404)	0.62
9/13	0.5086(87)	0.7010(619)	0.57
10/13	0.5078(92)	0.7857(1061)	0.57
11/13	0.5147(117)	0.7869(1756)	0.35

Table B.18: Matrix fit to the ${}^3P_{2T}$ channel, xz component.

t_{min}/t_{max}	aE_1	aE_2	Q
2/13	0.5243(33)	0.7779(57)	7.7×10^{-4}
3/13	0.5181(37)	0.7617(78)	2.0×10^{-2}
4/13	0.5144(42)	0.7561(105)	2.1×10^{-2}
5/13	0.5043(51)	0.7337(140)	0.33
6/13	0.5013(62)	0.7141(203)	0.59
7/13	0.5027(67)	0.7351(303)	0.51
8/13	0.5042(77)	0.7110(447)	0.74
9/13	0.5079(83)	0.7232(677)	0.60
10/13	0.5034(92)	0.8220(1239)	0.67
11/13	0.5021(119)	0.8330(2183)	0.32

Table B.19: Matrix fit to the ${}^3P_{2T}$ channel, yz component.

t_{min}/t_{max}	aE_1	aE_2	Q
2/13	0.02319(5)	3.090(52)	0.00
3/13	0.02231(6)	1.077(17)	7.7×10^{-158}
4/13	0.02202(7)	0.9619(109)	2.6×10^{-21}
5/13	0.02181(9)	0.7451(196)	1.2×10^{-3}
6/13	0.02166(11)	0.6372(324)	5.3×10^{-2}
7/13	0.02161(14)	0.4975(503)	0.24
8/13	0.02155(17)	0.4779(802)	0.13
9/13	0.02121(31)	0.3567(1186)	0.37
10/13	0.02134(25)	0.6272(2371)	0.88

Table B.20: Vector fit to the kinetic $^3S_1$ mass, with $(a\mathbf{p})^2$=1.

t_{min}/t_{max}	aE_1	aE_2	Q
2/13	0.04646(11)	3.095(51)	0.00
3/13	0.04453(13)	1.077(17)	1.9×10^{-159}
4/13	0.04399(15)	0.9764(106)	1.1×10^{-23}
5/13	0.04353(19)	0.7558(187)	4.2×10^{-4}
6/13	0.04321(23)	0.6421(307)	3.3×10^{-2}
7/13	0.04308(30)	0.4975(465)	0.29
8/13	0.04295(37)	0.4802(739)	0.15
9/13	0.04218(71)	0.3581(1068)	0.41
10/13	0.04242(60)	0.5744(2001)	0.83

Table B.21: Vector fit to the kinetic $^3S_1$ mass, with $(a\mathbf{p})^2$=2.

t_{min}/t_{max}	aE_1	aE_2	Q
2/13	0.06983(16)	3.105(50)	0.00
3/13	0.06670(21)	1.081(17)	1.6×10^{-160}
4/13	0.06592(24)	0.9913(104)	1.2×10^{-25}
5/13*			
6/13	0.06465(37)	0.6495(297)	2.8×10^{-2}
7/13	0.06441(49)	0.5034(445)	0.35
8/13	0.06421(62)	0.4886(716)	0.20
9/13	0.06288(123)	0.3604(1010)	0.49
10/13	0.06312(113)	0.5278(1813)	0.81

Table B.22: Vector fit to the kinetic $^3S_1$ mass, with $(a\mathbf{p})^2$=3. *Mass becoming negative.

t_{min}/t_{max}	aE_1	aE_2	Q
2/13*			
3/13	0.08870(29)	1.086(17)	1.0×10^{-161}
4/13	0.08765(34)	1.005(10)	3.6×10^{-26}
5/13	0.08666(43)	0.7846(177)	6.8×10^{-5}
6/13	0.08586(53)	0.6503(285)	5.0×10^{-2}
7/13	0.08570(69)	0.5432(455)	0.18
8/13	0.08555(84)	0.5390(764)	7.9×10^{-2}
9/13	0.08275(233)	0.3377(1033)	0.49
10/13	0.08387(169)	0.5344(1845)	0.81

Table B.23: Vector fit to the kinetic $^3S_1$ mass, with $(a\mathbf{p})^2$=4. *Mass becoming negative.

t_{min}/t_{max}	aE_1	aE_2	Q
2/13*			
3/13	0.1108(4)	1.090(16)	8.3×10^{-164}
4/13	0.1096(4)	1.022(10)	1.8×10^{-29}
5/13	0.1083(6)	0.7995(169)	1.5×10^{-5}
6/13	0.1072(7)	0.6652(273)	2.0×10^{-2}
7/13	0.1068(9)	0.5437(422)	0.20
8/13	0.1066(12)	0.5448(711)	9.0×10^{-2}
9/13	0.1029(31)	0.3530(951)	0.44
10/13	0.1040(26)	0.5196(1671)	0.82

Table B.24: Vector fit to the kinetic $^3S_1$ mass, with $(a\mathbf{p})^2$=5. *Mass becoming negative.

t_{min}/t_{max}	aE_1	aE_2	Q
2/13*			
3/13	0.1329(5)	1.103(16)	4.4×10^{-164}
4/13	0.1316(6)	1.040(10)	1.8×10^{-30}
5/13	0.1298(7)	0.8151(166)	2.8×10^{-5}
6/13	0.1284(9)	0.6811(277)	2.1×10^{-2}
7/13	0.1277(13)	0.5531(424)	0.28
8/13	0.1275(15)	0.5624(738)	0.14
9/13	0.1225(45)	0.3589(953)	0.55
10/13	0.1230(45)	0.4720(1657)	0.81

Table B.25: Vector fit to the kinetic $^3S_1$ mass, with $(a\mathbf{p})^2$=6. *Mass becoming negative.

t_{min}/t_{max}	aE_1	aE_2	Q
2/13*			
3/13	0.1770(7)	1.145(16)	2.8×10^{-164}
4/13	0.1754(8)	1.082(10)	1.9×10^{-29}
5/13	0.1726(10)	0.8593(170)	3.0×10^{-5}
6/13	0.1706(14)	0.7212(296)	1.2×10^{-2}
7/13	0.1693(20)	0.5833(466)	0.17
8/13	0.1694(24)	0.6154(870)	8.1×10^{-2}
9/13	0.1596(100)	0.3575(1048)	0.31
10/13	0.1628(71)	0.5405(2048)	0.76

Table B.26: Vector fit to the kinetic $^3S_1$ mass, with $(a\mathbf{p})^2$=8. *Mass becoming negative.

t_{min}/t_{max}	aE_1	aE_2	Q
2/13*			
3/13	0.1992(8)	1.170(16)	9.9×10^{-162}
4/13	0.1974(9)	1.102(10)	4.5×10^{-27}
5/13	0.1938(12)	0.8755(177)	3.5×10^{-4}
6/13	0.1915(16)	0.7392(324)	2.9×10^{-2}
7/13	0.1900(24)	0.6025(511)	0.25
8/13	0.1907(28)	0.6767(1047)	0.15
9/13	0.1756(170)	0.3442(1103)	0.44
10/13	0.1706(276)	0.3736(1903)	0.55

Table B.27: Vector fit to the kinetic $^3S_1$ mass, with $(a\mathbf{p})^2$=9. *Mass becoming negative.

t_{min}/t_{max}	aE_1	aE_2	Q
2/13*			
3/13	0.2666(12)	1.306(18)	2.0×10^{-151}
4/13	0.2620(14)	1.164(11)	3.2×10^{-17}
5/13	0.2560(20)	0.9321(224)	8.4×10^{-3}
6/13	0.2530(29)	0.7905(452)	5.9×10^{-2}
7/13	0.2517(45)	0.6633(766)	0.12
8/13	0.2545(41)	0.9331(2126)	0.10
9/13	0.1322(1485)	0.2856(316)	0.14
10/13*			

Table B.28: Vector fit to the kinetic $^3S_1$ mass, with $(a\mathbf{p})^2$=12. *Mass becoming negative.

B.1.2 Wavefunction at the Origin for aM_b=1.55

t_{min}/t_{max}	$\psi_0(0)$
2/13	0.1426(24)
3/13	0.1411(28)
4/13	0.1420(35)
5/13	0.1407(40)
6/13	0.1412(47)
7/13	0.1393(56)
8/13	0.1330(62)
9/13	0.133(11)

Table B.29: Wavefunction at the origin for the lattice 1^1S_0 channel.

t_{min}/t_{max}	$\psi_0(0)$
2/13	0.1153(21)
3/13	0.1153(24)
4/13	0.1161(31)
5/13	0.1157(38)
6/13	0.1164(42)
7/13	0.1144(51)
8/13	0.1099(53)
9/13	0.1165(82)

Table B.30: Wavefunction at the origin for the lattice 1^3S_1 channel.

B.1.3 Lattice Splittings for aM_b=1.55

t_{min}/t_{max}	$aE(1^3S_1 - 1^1S_0)$	$aE(2^3S_1 - 2^1S_0)$	$aE(3^3S_1 - 3^1S_0)$
2/13	0.01789(20)	0.0144(12)	0.0190(19)
3/13	0.01767(20)	0.0130(15)	0.0182(26)
4/13	0.01750(20)	0.0115(19)	0.0114(43)
5/13	0.01721(22)	0.0102(24)	0.0068(70)
6/13	0.01724(23)	0.0106(42)	0.016(10)
7/13	0.01729(25)	0.0113(57)	0.019(14)
8/13	0.01738(28)	0.0105(98)	0.021(20)
9/13	0.01741(30)	0.016(19)	0.026(26)
10/13	0.01741(33)	0.0235(69)	0.08(14)
11/13	0.0167(36)	-0.08(31)	0.021(21)

Table B.31: Results from the $3e3s$ matrix fit.

t_{min}/t_{max}	$aE(1^1P_1 - 1^3P_0)$	$aE(2^1P_1 - 2^3P_0)$
2/13	0.01314(96)	0.0217(18)
3/13	0.0122(11)	0.0205(23)
4/13	0.0117(13)	0.0217(32)
5/13	0.0105(15)	0.0186(43)
6/13	0.0094(17)	0.0095(59)
7/13	0.0081(20)	0.0050(90)
8/13	0.0086(24)	0.009(12)
9/13	0.0076(29)	0.001(17)
10/13	0.0075(34)	0.005(33)
11/13	0.0090(48)	-0.013(55)

Table B.32: Results from the matrix fit.

t_{min}/t_{max}	$aE(1^3P_{2E} - 1^1P_1)$	$aE(2^3P_{2E} - 2^1P_1)$
2/13	0.00506(65)	0.0091(11)
3/13	0.00464(74)	0.0083(15)
4/13	0.00466(87)	0.0094(21)
5/13	0.0043(10)	0.0102(29)
6/13	0.0039(12)	0.0071(42)
7/13	0.0031(14)	0.0039(66)
8/13	0.0027(18)	0.0049(84)
9/13	0.0032(21)	0.009(12)
10/13	0.0050(24)	0.041(26)
11/13	0.0032(34)	0.078(61)

Table B.33: Results from the matrix fit.

t_{min}/t_{max}	$aE(1^3\overline{P} - 1^1P_1)$	$aE(2^3\overline{P} - 2^1P_1)$
2/13	0.00045(43)	0.00096(75)
3/13	0.00046(49)	0.0007(11)
4/13	0.00054(56)	0.0005(14)
5/13	0.00064(67)	0.0023(20)
6/13	0.00090(76)	0.0047(28)
7/13	0.00088(90)	0.0072(45)
8/13	0.0005(11)	0.0055(60)
9/13	0.0007(13)	0.0063(90)
10/13	0.0020(14)	0.018(17)
11/13	0.0004(20)	0.041(36)

Table B.34: Results from the matrix fit.

t_{min}/t_{max}	$\frac{2^3S_1 - 1^3S_1}{1^1P_1 - 1^3S_1}$
2/13	1.364(27)
3/13	1.365(34)
4/13	1.374(40)
5/13	1.374(50)
6/13	1.363(86)
7/13	1.39(11)
8/13	1.37(19)
9/13	1.34(25)
10/13	1.48(13)
11/13	0.26(47)

Table B.35: Results from the matrix fit.

t_{min}/t_{max}	$\frac{1^3P_{2E}-1^1P_1}{1^1P_1-1^3P_0}$
2/13	0.386(52)
3/13	0.383(65)
4/13	0.400(79)
5/13	0.41(10)
6/13	0.42(14)
7/13	0.38(18)
8/13	0.31(21)
9/13	0.43(29)
10/13	0.67(38)
11/13	0.35(38)

Table B.36: Results from the matrix fit.

B.1.4 Lattice State Fits for aM_b=1.8

t_{min}/t_{max}	aE_1	aE_2	aE_3	Q
2/13	0.3594(7)	0.6003(45)	0.7207(68)	5.0×10^{-6}
3/13	0.3586(7)	0.5943(61)	0.7144(100)	3.8×10^{-2}
4/13	0.3581(8)	0.5926(75)	0.7148(160)	0.20
5/13	0.3573(8)	0.5838(95)	0.7086(235)	0.55
6/13	0.3574(8)	0.5837(148)	0.6826(316)	0.65
7/13	0.3575(9)	0.5919(183)	0.6765(468)	0.62
8/13	0.3577(9)	0.5942(265)	0.6853(712)	0.44
9/13	0.3576(10)	0.5872(367)	0.6598(1018)	0.45
10/13	0.3566(11)	0.5978(231)	0.9424(2532)	0.95
11/13	0.3569(13)	0.4565(3402)	0.6147(405)	0.82

Table B.37: Matrix fit to the $^3S_1$ channel.

t_{min}/t_{max}	aE_1	aE_2	aE_3	Q
2/13	0.3434(6)	0.5881(42)	0.7064(73)	1.4×10^{-4}
3/13	0.3428(7)	0.5833(57)	0.7006(107)	9.0×10^{-2}
4/13	0.3424(7)	0.5828(68)	0.7059(173)	0.28
5/13	0.3419(7)	0.5750(85)	0.7018(252)	0.51
6/13	0.3420(7)	0.5745(132)	0.6698(335)	0.60
7/13	0.3421(8)	0.5827(154)	0.6637(495)	0.57
8/13	0.3421(8)	0.5848(216)	0.6735(757)	0.37
9/13	0.3421(9)	0.5743(309)	0.6440(1055)	0.44
10/13	0.3412(9)	0.5810(205)	0.9321(2460)	0.94
11/13	0.3413(11)	0.4938(3228)	0.5968(456)	0.76

Table B.38: Matrix fit to the $^1S_0$ channel.

t_{min}/t_{max}	aE_1	aE_2	Q
2/13	0.5378(25)	0.7662(48)	2.8×10^{-3}
3/13	0.5330(29)	0.7512(64)	0.15
4/13	0.5316(33)	0.7480(86)	0.15
5/13	0.5253(39)	0.7396(113)	0.42
6/13	0.5252(45)	0.7190(156)	0.73
7/13	0.5281(50)	0.7321(222)	0.66
8/13	0.5275(59)	0.7128(316)	0.72
9/13	0.5265(73)	0.6994(462)	0.68
10/13	0.5238(73)	0.7621(772)	0.87
11/13	0.5240(137)	0.6744(1161)	0.71

Table B.39: Matrix fit to the ${}^1P_1$ channel.

t_{min}/t_{max}	aE_1	aE_2	Q
2/13	0.5378(25)	0.7662(48)	2.8×10^{-3}
3/13	0.5330(29)	0.7512(64)	0.15
4/13	0.5316(33)	0.7480(86)	0.15
5/13	0.5253(39)	0.7296(113)	0.42
6/13	0.5252(45)	0.7190(156)	0.73
7/13	0.5281(50)	0.7321(222)	0.66
8/13	0.5275(59)	0.7128(316)	0.72
9/13	0.5265(73)	0.6994(462)	0.68
10/13	0.5238(73)	0.7621(772)	0.87
11/13	0.5240(137)	0.6744(1161)	0.71

Table B.40: Matrix fit to the ${}^1P_1$ channel in the x direction.

t_{min}/t_{max}	aE_1	aE_2	Q
2/13	0.5378(25)	0.7662(48)	2.8×10^{-3}
3/13	0.5330(29)	0.7512(64)	0.15
4/13	0.5316(33)	0.7480(86)	0.15
5/13	0.5253(39)	0.7296(113)	0.42
6/13	0.5252(45)	0.7190(156)	0.73
7/13	0.5281(50)	0.7321(222)	0.66
8/13	0.5275(59)	0.7128(316)	0.72
9/13	0.5265(73)	0.6994(462)	0.68
10/13	0.5238(73)	0.7621(772)	0.87
11/13	0.5240(137)	0.6744(1161)	0.71

Table B.41: Matrix fit to the ${}^1P_1$ channel in the y direction.

t_{min}/t_{max}	aE_1	aE_2	Q
2/13	0.5378(25)	0.7662(48)	2.8×10^{-3}
3/13	0.5330(29)	0.7512(64)	0.15
4/13	0.5316(33)	0.7480(86)	0.15
5/13	0.5253(39)	0.7296(113)	0.42
6/13	0.5252(45)	0.7190(156)	0.73
7/13	0.5281(50)	0.7321(222)	0.66
8/13	0.5275(59)	0.7128(316)	0.72
9/13	0.5265(73)	0.6994(462)	0.68
10/13	0.5238(73)	0.7621(772)	0.87
11/13	0.5240(137)	0.6744(1161)	0.71

Table B.42: Matrix fit to the ${}^1P_1$ channel in the z direction.

t_{min}/t_{max}	aE_1	aE_2	Q
2/13	0.5259(27)	0.7503(54)	2.5×10^{-2}
3/13	0.5218(30)	0.7377(72)	0.21
4/13	0.5201(34)	0.7315(94)	0.14
5/13	0.5132(41)	0.7131(123)	0.48
6/13	0.5124(48)	0.7098(169)	0.69
7/13	0.5163(53)	0.7259(240)	0.64
8/13	0.5161(64)	0.7003(344)	0.67
9/13	0.5203(73)	0.7080(513)	0.55
10/13	0.5158(73)	0.7647(870)	0.86
11/13	0.5196(94)	0.8141(1449)	0.60

Table B.43: Matrix fit to the ${}^3P_0$ channel.

t_{min}/t_{max}	aE_1	aE_2	Q
2/13	0.5345(28)	0.7635(54)	1.5×10^{-2}
3/13	0.5299(32)	0.7504(72)	0.17
4/13	0.5277(36)	0.7439(95)	0.11
5/13	0.5203(44)	0.7252(124)	0.46
6/13	0.5192(50)	0.7221(173)	0.76
7/13	0.5223(55)	0.7382(248)	0.69
8/13	0.5218(67)	0.7085(357)	0.74
9/13	0.5249(74)	0.7165(538)	0.60
10/13	0.5207(74)	0.7671(887)	0.91
11/13	0.5249(93)	0.8215(1496)	0.66

Table B.44: Matrix fit to the ${}^3P_1$ channel.

t_{min}/t_{max}	aE_1	aE_2	Q
2/13	0.5355(31)	0.7643(58)	0.13
3/13	0.5317(35)	0.7547(78)	0.34
4/13	0.5296(40)	0.7521(104)	0.25
5/13	0.5211(49)	0.7291(138)	0.72
6/13	0.5199(57)	0.7216(196)	0.87
7/13	0.5220(63)	0.7360(278)	0.79
8/13	0.5240(75)	0.7195(402)	0.70
9/13	0.5269(78)	0.7346(622)	0.63
10/13	0.5190(84)	0.7599(1018)	0.91
11/13	0.5208(106)	0.8800(1851)	0.74

Table B.45: Matrix fit to the $^3P_1$ channel in the x direction.

t_{min}/t_{max}	aE_1	aE_2	Q
2/13	0.5351(31)	0.7641(58)	8.3×10^{-3}
3/13	0.5298(35)	0.7469(77)	0.16
4/13	0.5261(40)	0.7368(99)	0.14
5/13	0.5191(49)	0.7199(130)	0.28
6/13	0.5166(56)	0.7091(174)	0.57
7/13	0.5210(63)	0.7335(256)	0.48
8/13	0.5194(73)	0.7055(363)	0.69
9/13	0.5253(85)	0.7307(565)	0.72
10/13	0.5248(90)	0.8119(981)	0.69
11/13	0.5300(117)	0.9069(1805)	0.35

Table B.46: Matrix fit to the $^3P_1$ channel in the y direction.

t_{min}/t_{max}	aE_1	aE_2	Q
2/13	0.5342(30)	0.7618(55)	4.1×10^{-2}
3/13	0.5297(34)	0.7511(74)	0.15
4/13	0.5280(39)	0.7432(100)	0.13
5/13	0.5190(48)	0.7203(127)	0.56
6/13	0.5184(54)	0.7211(180)	0.82
7/13	0.5197(62)	0.7219(255)	0.78
8/13	0.5186(79)	0.6866(366)	0.83
9/13	0.5209(93)	0.6732(520)	0.73
10/13	0.5176(87)	0.7204(848)	0.98
11/13	0.5240(116)	0.7107(1315)	0.89

Table B.47: Matrix fit to the $^3P_1$ channel in the z direction.

t_{min}/t_{max}	aE_1	aE_2	Q
2/13	0.5413(30)	0.7752(54)	1.6×10^{-2}
3/13	0.5364(33)	0.7616(73)	0.15
4/13	0.5342(38)	0.7568(98)	9.4×10^{-2}
5/13	0.5261(46)	0.7377(128)	0.53
6/13	0.5239(53)	0.7245(178)	0.92
7/13	0.5259(60)	0.7333(255)	0.88
8/13	0.5261(73)	0.7111(368)	0.84
9/13	0.5299(81)	0.7193(558)	0.71
10/13	0.5273(79)	0.7946(958)	0.92
11/13	0.5308(99)	0.8577(1657)	0.66

Table B.48: Matrix fit to the ${}^3P_{2E}$ channel.

t_{min}/t_{max}	aE_1	aE_2	Q
2/13	0.5413(32)	0.7739(55)	2.6×10^{-2}
3/13	0.5366(36)	0.7630(76)	0.12
4/13	0.5363(40)	0.7614(104)	6.0×10^{-2}
5/13	0.5273(49)	0.7372(135)	0.38
6/13	0.5248(58)	0.7243(189)	0.88
7/13	0.5244(71)	0.7149(259)	0.83
8/13	0.5254(95)	0.7005(374)	0.79
9/13	0.5304(116)	0.6990(546)	0.65
10/13	0.5309(98)	0.7612(951)	0.87
11/13	0.5346(131)	0.8039(1552)	0.55

Table B.49: Matrix fit to the ${}^3P_{2E}$ channel, xy component.

t_{min}/t_{max}	aE_1	aE_2	Q
2/13	0.5424(32)	0.7757(58)	3.9×10^{-2}
3/13	0.5371(36)	0.7595(78)	0.30
4/13	0.5331(43)	0.7501(103)	0.27
5/13	0.5261(52)	0.7357(136)	0.45
6/13	0.5226(61)	0.7180(180)	0.78
7/13	0.5255(66)	0.7279(264)	0.74
8/13	0.5236(80)	0.7096(381)	0.65
9/13	0.5277(89)	0.7136(581)	0.53
10/13	0.5267(90)	0.8057(1002)	0.57
11/13	0.5343(118)	0.8653(1797)	0.26

Table B.50: Matrix fit to the ${}^3P_{2E}$ channel, xz component.

t_{min}/t_{max}	aE_1	aE_2	Q
2/13	0.5428(32)	0.7772(59)	6.0×10^{-3}
3/13	0.5379(37)	0.7649(80)	2.9×10^{-2}
4/13	0.5344(42)	0.7598(106)	2.3×10^{-2}
5/13	0.5244(51)	0.7367(138)	0.34
6/13	0.5230(60)	0.7236(198)	0.59
7/13	0.5252(65)	0.7436(290)	0.50
8/13	0.5264(76)	0.7164(417)	0.68
9/13	0.5301(79)	0.7426(645)	0.57
10/13	0.5234(89)	0.8120(1127)	0.74
11/13	0.5217(110)	0.9030(2052)	0.50

Table B.51: Matrix fit to the ${}^3P_{2E}$ channel, yz component.

t_{min}/t_{max}	aE_1	aE_2	Q
2/13	0.5415(30)	0.7754(54)	1.2×10^{-2}
3/13	0.5368(33)	0.7620(73)	0.14
4/13	0.5345(38)	0.7568(98)	8.7×10^{-2}
5/13	0.5265(45)	0.7380(129)	0.55
6/13	0.5242(53)	0.7244(179)	0.94
7/13	0.5264(58)	0.7371(257)	0.90
8/13	0.5273(71)	0.7189(377)	0.86
9/13	0.5306(79)	0.7186(563)	0.78
10/13	0.5284(79)	0.7847(954)	0.92
11/13	0.5316(99)	0.8262(1615)	0.65

Table B.52: Matrix fit to the ${}^3P_{2T}$ channel.

t_{min}/t_{max}	aE_1	aE_2	Q
2/13	0.5420(32)	0.7751(56)	1.5×10^{-2}
3/13	0.5376(36)	0.7646(77)	8.1×10^{-2}
4/13	0.5376(40)	0.7632(106)	4.0×10^{-2}
5/13	0.5283(49)	0.7374(137)	0.35
6/13	0.5259(57)	0.7253(192)	0.80
7/13	0.5270(69)	0.7230(267)	0.74
8/13	0.5293(92)	0.7120(390)	0.72
9/13	0.5337(114)	0.6950(559)	0.64
10/13	0.5340(98)	0.7536(965)	0.80
11/13	0.5384(137)	0.7803(1559)	0.49

Table B.53: Matrix fit to the ${}^3P_{2T}$ channel, xy component.

t_{min}/t_{max}	aE_1	aE_2	Q
2/13	0.5424(32)	0.7754(58)	2.7×10^{-2}
3/13	0.5375(36)	0.7595(78)	0.23
4/13	0.5333(42)	0.7494(103)	0.21
5/13	0.5263(52)	0.7344(136)	0.37
6/13	0.5232(59)	0.7167(181)	0.73
7/13	0.5264(65)	0.7299(266)	0.66
8/13	0.5252(78)	0.7109(383)	0.57
9/13	0.5293(84)	0.7165(584)	0.52
10/13	0.5279(89)	0.7895(984)	0.54
11/13	0.5345(114)	0.8492(1719)	0.27

Table B.54: Matrix fit to the ${}^3P_{2T}$ channel, xz component.

t_{min}/t_{max}	aE_1	aE_2	Q
2/13	0.5423(32)	0.7763(58)	7.0×10^{-3}
3/13	0.5372(36)	0.7635(78)	5.0×10^{-2}
4/13	0.5337(42)	0.7579(105)	4.1×10^{-2}
5/13	0.5240(50)	0.7371(136)	0.45
6/13	0.5220(60)	0.7232(196)	0.72
7/13	0.5235(65)	0.7422(286)	0.64
8/13	0.5249(74)	0.7229(420)	0.82
9/13	0.5286(81)	0.7386(640)	0.69
10/13	0.5231(91)	0.8064(1122)	0.78
11/13	0.5207(113)	0.8579(1988)	0.49

Table B.55: Matrix fit to the ${}^3P_{2T}$ channel, yz component.

t_{min}/t_{max}	aE_1	aE_2	Q
2/13*			
3/13	0.01977(6)	1.112(7)	2.4×10^{-115}
4/13	0.01955(6)	1.051(12)	2.0×10^{-94}
5/13	0.01932(8)	0.7848(124)	2.0×10^{-17}
6/13	0.01914(9)	0.6221(185)	8.7×10^{-5}
7/13	0.01907(12)	0.4865(278)	0.11
8/13	0.01901(15)	0.4488(425)	6.6×10^{-2}
9/13	0.01870(23)	0.3582(613)	0.40
10/13	0.01871(24)	0.4861(1062)	0.90

Table B.56: Vector fit to the kinetic ${}^3S_1$ mass, with $(a\mathbf{p})^2$=1. *Mass becoming negative.

t_{min}/t_{max}	aE_1	aE_2	Q
2/13*	0.04479(9)	4.369(3469)	0.00
3/13	0.03955(11)	1.129(7)	2.2×10^{-121}
4/13	0.03908(13)	1.057(13)	3.2×10^{-99}
5/13	0.03862(16)	0.7969(120)	9.2×10^{-19}
6/13	0.03822(20)	0.6330(179)	2.9×10^{-5}
7/13	0.03805(26)	0.4951(266)	0.13
8/13	0.03793(32)	0.4589(407)	7.9×10^{-2}
9/13	0.03725(50)	0.3674(579)	0.42
10/13	0.03722(55)	0.4735(977)	0.88

Table B.57: Vector fit to the kinetic $^3S_1$ mass, with $(a\mathbf{p})^2$=2. *Bad fit.

t_{min}/t_{max}	aE_1	aE_2	Q
2/13	0.06807(15)	4.387(3120)	0.00
3/13	0.05935(18)	1.146(7)	3.7×10^{-126}
4/13	0.05864(21)	1.064(13)	4.8×10^{-103}
5/13	0.05792(26)	0.8100(117)	2.2×10^{-19}
6/13	0.05726(32)	0.6451(176)	1.7×10^{-5}
7/13	0.05695(42)	0.5061(259)	0.16
8/13	0.05675(53)	0.4712(401)	9.8×10^{-2}
9/13	0.05563(85)	0.3756(562)	0.48
10/13	0.05541(99)	0.4573(930)	0.87

Table B.58: Vector fit to the kinetic $^3S_1$ mass, with $(a\mathbf{p})^2$=3.

t_{min}/t_{max}	aE_1	aE_2	Q
2/13*			
3/13	0.07904(24)	1.163(7)	2.5×10^{-126}
4/13	0.07807(29)	1.077(13)	6.1×10^{-104}
5/13	0.07715(36)	0.8277(116)	2.1×10^{-21}
6/13	0.07616(45)	0.6535(170)	7.4×10^{-5}
7/13	0.07582(58)	0.5338(261)	7.6×10^{-2}
8/13	0.07564(73)	0.5033(416)	3.5×10^{-2}
9/13	0.07356(136)	0.3717(581)	0.48
10/13	0.07369(145)	0.4724(968)	0.86

Table B.59: Vector fit to the kinetic $^3S_1$ mass, with $(a\mathbf{p})^2$=4. *Mass becoming negative.

t_{min}/t_{max}	aE_1	aE_2	Q
2/13*			
3/13	0.09900(32)	1.180(7)	3.3×10^{-135}
4/13	0.09773(38)	1.081(13)	1.1×10^{-109}
5/13	0.09656(47)	0.8419(112)	6.8×10^{-23}
6/13	0.09521(59)	0.6695(165)	1.0×10^{-5}
7/13	0.09460(78)	0.5424(249)	8.8×10^{-2}
8/13	0.09433(99)	0.5148(397)	4.1×10^{-2}
9/13	0.09164(183)	0.3868(547)	0.44
10/13	0.09140(211)	0.4681(902)	0.86

Table B.60: Vector fit to the kinetic $^3S_1$ mass, with $(a\mathbf{p})^2$=5. *Mass becoming negative.

t_{min}/t_{max}	aE_1	aE_2	Q
2/13*	0.1429(4)	4.574(2725)	0.00
3/13	0.1190(4)	1.199(7)	3.0×10^{-138}
4/13	0.1175(5)	1.093(13)	6.3×10^{-112}
5/13	0.1160(6)	0.8578(110)	4.0×10^{-22}
6/13	0.1142(8)	0.6864(167)	8.1×10^{-6}
7/13	0.1133(10)	0.5554(250)	0.13
8/13	0.1130(13)	0.5307(410)	5.9×10^{-2}
9/13	0.1095(25)	0.3964(552)	0.49
10/13	0.1083(33)	0.4445(898)	0.86

Table B.61: Vector fit to the kinetic $^3S_1$ mass, with $(a\mathbf{p})^2$=6. *Bad fit.

t_{min}/t_{max}	aE_1	aE_2	Q
2/13*	0.1979(6)	4.664(2428)	0.00
3/13	0.1591(6)	1.240(7)	1.9×10^{-135}
4/13	0.1570(7)	1.132(13)	9.3×10^{-112}
5/13	0.1548(9)	0.8987(110)	5.8×10^{-21}
6/13	0.1522(11)	0.7254(175)	9.8×10^{-6}
7/13	0.1507(15)	0.5903(270)	0.10
8/13	0.1503(20)	0.5758(466)	3.9×10^{-2}
9/13	0.1444(44)	0.4119(613)	0.32
10/13	0.1428(56)	0.4782(1046)	0.81

Table B.62: Vector fit to the kinetic $^3S_1$ mass, with $(a\mathbf{p})^2$=8. *Bad fit.

t_{min}/t_{max}	aE_1	aE_2	Q
2/13*	0.2276(7)	4.661(2163)	0.00
3/13	0.1793(7)	1.259(7)	1.3×10^{-129}
4/13	0.1771(8)	1.155(13)	1.7×10^{-108}
5/13	0.1742(10)	0.9163(112)	7.3×10^{-18}
6/13	0.1712(13)	0.7435(188)	4.8×10^{-5}
7/13	0.1693(19)	0.6078(290)	0.16
8/13	0.1692(24)	0.6055(528)	6.4×10^{-2}
9/13	0.1615(60)	0.4142(670)	0.37
10/13	0.1541(118)	0.3999(1054)	0.67

Table B.63: Vector fit to the kinetic $^3S_1$ mass, with $(a\mathbf{p})^2$=9. *Bad fit.

t_{min}/t_{max}	aE_1	aE_2	Q
2/13*	0.3254(11)	4.646(1639)	0.00
3/13	0.2392(10)	1.320(8)	2.8×10^{-96}
4/13**			
5/13	0.2311(16)	0.9753(130)	7.6×10^{-11}
6/13	0.2271(22)	0.7971(245)	2.3×10^{-3}
7/13	0.2248(33)	0.6638(402)	0.13
8/13	0.2257(39)	0.7139(850)	6.0×10^{-2}
9/13	0.2095(163)	0.4071(943)	0.11
10/13	0.09627(12714)	0.2782(414)	0.45

Table B.64: Vector fit to the kinetic $^3S_1$ mass, with $(a\mathbf{p})^2$=12. *Bad fit, **mass becoming negative.

B.1.5 Wavefunction at the Origin for aM_b=1.8

t_{min}/t_{max}	$\psi_0(0)$
2/13	0.1567(30)
3/13	0.1546(34)
4/13	0.1555(41)
5/13	0.1539(48)
6/13	0.1537(56)
7/13	0.1512(67)
8/13	0.1434(71)
9/13	0.145(11)

Table B.65: Wavefunction at the origin for the lattice 1^1S_0 channel.

t_{min}/t_{max}	$\psi_0(0)$
2/13	0.1315(27)
3/13	0.1309(31)
4/13	0.1319(39)
5/13	0.1314(46)
6/13	0.1312(52)
7/13	0.1289(63)
8/13	0.1225(60)
9/13	0.132(11)

Table B.66: Wavefunction at the origin for the lattice 1^3S_1 channel.

B.1.6 Lattice Splittings for aM_b=1.8

t_{min}/t_{max}	$aE(1^3S_1 - 1^1S_0)$	$aE(2^3S_1 - 2^1S_0)$	$aE(3^3S_1 - 3^1S_0)$
2/13	0.01599(17)	0.0123(10)	0.0144(18)
3/13	0.01580(17)	0.0110(13)	0.0138(23)
4/13	0.01566(18)	0.0098(16)	0.0089(37)
5/13	0.01540(19)	0.0089(20)	0.0068(59)
6/13	0.01543(20)	0.0092(33)	0.0128(81)
7/13	0.01546(22)	0.0093(48)	0.013(11)
8/13	0.01553(24)	0.0094(74)	0.012(18)
9/13	0.01552(27)	0.012(12)	0.015(29)
10/13	0.01550(29)	0.0178(52)	0.037(71)
11/13	0.01559(44)	-0.06(20)	0.017(17)

Table B.67: Results from the $3e3s$ matrix fit.

t_{min}/t_{max}	$aE(1^1P_1 - 1^3P_0)$	$aE(2^1P_1 - 2^3P_0)$
2/13	0.01106(83)	0.0173(15)
3/13	0.01051(95)	0.0170(20)
4/13	0.0100(11)	0.0177(27)
5/13	0.0091(13)	0.0158(36)
6/13	0.0080(15)	0.0080(49)
7/13	0.0067(17)	0.0028(73)
8/13	0.0073(21)	0.0056(95)
9/13	0.0064(26)	0.002(14)
10/13	0.0067(31)	-0.001(25)
11/13	0.0077(42)	-0.025(46)

Table B.68: Results from the matrix fit.

t_{min}/t_{max}	$aE(1^3P_{2E} - 1^1P_1)$	$aE(2^3P_{2E} - 2^1P_1)$
2/13	0.00439(54)	0.00754(94)
3/13	0.00409(62)	0.0070(13)
4/13	0.00408(73)	0.0076(18)
5/13	0.00378(87)	0.0088(24)
6/13	0.0035(10)	0.0067(34)
7/13	0.0029(12)	0.0045(53)
8/13	0.0028(15)	0.0052(67)
9/13	0.0033(18)	0.0093(95)
10/13	0.0048(20)	0.031(19)
11/13	0.0036(29)	0.069(48)

Table B.69: Results from the matrix fit.

t_{min}/t_{max}	$aE(\overline{^3P} - {}^1P_1)$	$aE(\overline{2^3P} - 2^1P_1)$
2/13	0.00043(35)	0.00095(62)
3/13	0.00040(40)	0.00064(88)
4/13	0.00047(46)	0.0005(12)
5/13	0.00054(56)	0.0020(16)
6/13	0.00076(63)	0.0043(23)
7/13	0.00078(75)	0.0066(36)
8/13	0.00058(93)	0.0057(48)
9/13	0.0008(11)	0.0068(71)
10/13	0.0018(12)	0.015(13)
11/13	0.0006(17)	0.041(30)

Table B.70: Results from the matrix fit.

t_{min}/t_{max}	$\frac{2^3S_1-1^3S_1}{1^1P_1-1^3S_1}$
2/13	1.351(25)
3/13	1.353(32)
4/13	1.353(37)
5/13	1.349(46)
6/13	1.350(77)
7/13	1.376(99)
8/13	1.39(14)
9/13	1.36(18)
10/13	1.45(12)
11/13	0.6(21)

Table B.71: Results from the matrix fit. S states taken from $3e3s$ matrix fits.

$tmin/t_{max}$	$\frac{1^3P_{2E}-1^1P_1}{1^1P_1-1^3P_0}$
2/13	0.398(51)
3/13	0.391(62)
4/13	0.410(76)
5/13	0.42(10)
6/13	0.45(13)
7/13	0.44(19)
8/13	0.38(21)
9/13	0.52(30)
10/13	0.73(38)
11/13	0.47(38)

Table B.72: Results from the matrix fit.

B.2 Lattice Results for the Dynamical Calculations with κ=0.135

B.2.1 Lattice State Fits for aM_b=1.8

t_{min}/t_{max}	aE_1	aE_2	aE_3	Q
2/13	0.4007(9)	0.6809(77)	0.8047(195)	2.2×10^{-2}
3/13	0.3996(10)	0.6817(88)	0.8465(354)	0.14
4/13	0.3995(10)	0.6691(153)	0.7828(504)	0.18
5/13	0.3991(11)	0.6733(151)	0.8507(1073)	0.17
6/13	0.3990(11)	0.6848(223)	0.7548(1204)	0.16
7/13	0.3987(12)	0.6824(252)	0.8473(2016)	0.30
8/13	0.3994(13)	0.7334(322)	1.633(755)	0.50
9/13	0.3990(14)	0.6914(638)	2.760(4406)	0.48
10/13	0.3941(299)	0.4908(3505)	1.455(1878)	0.53
11/13*				

Table B.73: Matrix fit to the $^3S_1$ channel. *Fitted lattice state energy becoming negative.

t_{min}/t_{max}	aE_1	aE_2	aE_3	Q
2/13	0.3769(10)	0.6673(63)	0.8159(207)	4.4×10^{-3}
3/13	0.3758(10)	0.6661(79)	0.8332(358)	2.4×10^{-2}
4/13	0.3760(10)	0.6528(140)	0.7574(511)	4.2×10^{-2}
5/13	0.3758(11)	0.6529(162)	0.7683(851)	2.7×10^{-2}
6/13	0.3762(11)	0.6728(219)	0.7525(1059)	0.15
7/13	0.3749(14)	0.6527(282)	0.9051(1739)	0.26
8/13	0.3757(12)	0.7104(284)	1.421(571)	0.52
9/13	0.3755(13)	0.6833(581)	1.819(1849)	0.38
10/13*				
11/13	0.3635(1236)	0.4239(4343)	3.305(21226)	0.30

Table B.74: Matrix fit to the $^1S_0$ channel. *Fitted lattice state energy becoi ng negative.

t_{min}/t_{max}	aE_1	aE_2	Q
2/13	0.6098(45)	0.8427(100)	0.68
3/13	0.6075(52)	0.8373(140)	0.74
4/13	0.6049(62)	0.8249(193)	0.75
5/13	0.6068(70)	0.8442(312)	0.62
6/13	0.6087(74)	0.8757(504)	0.71
7/13	0.6075(103)	0.8264(747)	0.59
8/13	0.6191(94)	0.9833(1391)	0.74
9/13	0.6186(117)	1.001(258)	0.47
10/13	0.6189(246)	0.8616(3996)	0.28
11/13	0.6136(215)	2.007(1565)	0.95

Table B.75: Matrix fit to the $^1P_1$ channel.

t_{min}/t_{max}	aE_1	aE_2	Q
2/13	0.6098(45)	0.8427(100)	0.68
3/13	0.6075(52)	0.8373(140)	0.74
4/13	0.6050(62)	0.8249(193)	0.75
5/13	0.6068(70)	0.8441(312)	0.62
6/13	0.6087(74)	0.8757(504)	0.71
7/13	0.6075(103)	0.8262(747)	0.59
8/13	0.6191(94)	0.9833(1390)	0.74
9/13	0.6186(117)	1.000(257)	0.47
10/13	0.6189(245)	0.8627(4002)	0.28
11/13	0.6136(215)	2.007(1565)	0.95

Table B.76: Matrix fit to the $^1P_1$ channel in the x direction.

t_{min}/t_{max}	aE_1	aE_2	Q
2/13	0.6100(45)	0.8427(100)	0.68
3/13	0.6075(52)	0.8373(140)	0.74
4/13	0.6049(62)	0.8249(193)	0.75
5/13	0.6068(70)	0.8442(312)	0.62
6/13	0.6087(74)	0.8757(504)	0.71
7/13	0.6075(103)	0.8264(747)	0.59
8/13	0.6191(94)	0.9833(1391)	0.74
9/13	0.6186(117)	1.001(258)	0.47
10/13	0.6189(246)	0.8616(3996)	0.28
11/13	0.6136(215)	2.007(1565)	0.95

Table B.77: Matrix fit to the $^1P_1$ channel in the y direction.

t_{min}/t_{max}	aE_1	aE_2	Q
2/13	0.6098(45)	0.8427(100)	0.68
3/13	0.6075(52)	0.8373(140)	0.74
4/13	0.6049(62)	0.8249(193)	0.75
5/13	0.6068(70)	0.8442(312)	0.62
6/13	0.6087(74)	0.8757(504)	0.71
7/13	0.6075(103)	0.8264(747)	0.59
8/13	0.6191(94)	0.9833(1391)	0.74
9/13	0.6186(117)	1.001(258)	0.47
10/13	0.6189(246)	0.8616(3996)	0.28
11/13	0.6136(215)	2.007(1565)	0.95

Table B.78: Matrix fit to the $^1P_1$ channel in the z direction.

t_{min}/t_{max}	aE_1	aE_2	Q
2/13	0.5956(41)	0.8257(100)	0.87
3/13	0.5937(47)	0.8218(141)	0.86
4/13	0.5915(57)	0.8124(197)	0.90
5/13	0.5922(64)	0.8256(306)	0.81
6/13	0.5934(69)	0.8701(491)	0.79
7/13	0.5924(92)	0.8279(731)	0.66
8/13	0.5982(88)	0.9423(1352)	0.58
9/13	0.5934(110)	0.9475(2335)	0.36
10/13	0.5875(295)	0.7454(3296)	0.16
11/13	0.5866(204)	1.705(1062)	0.76

Table B.79: Matrix fit to the $^3P_0$ channel.

t_{min}/t_{max}	aE_1	aE_2	Q
2/13	0.6013(57)	0.9171(118)	3.7×10^{-3}
3/13	0.6050(75)	0.8574(160)	0.63
4/13	0.6025(90)	0.8587(221)	0.50
5/13	0.6016(117)	0.8425(335)	0.38
6/13	0.6105(144)	0.8644(582)	0.35
7/13	0.6321(236)	0.8596(1031)	0.45
8/13	0.6205(182)	1.065(190)	0.53
9/13	0.6202(139)	2.150(1149)	0.88
10/13	0.6067(2213)	0.7160(14517)	0.70

Table B.80: Vector fit to the $^3P_1$ channel.

t_{min}/t_{max}	aE_1	aE_2	Q
2/13	0.6033(68)	0.9062(132)	1.1×10^{-3}
3/13	0.6114(94)	0.8409(188)	0.24
4/13	0.6017(108)	0.8509(258)	0.24
5/13	0.5995(134)	0.8591(395)	0.14
6/13	0.6198(218)	0.8347(702)	0.14
7/13	0.6536(361)	0.8708(1360)	0.46
8/13	0.6275(230)	1.070(233)	0.46
9/13	0.6221(184)	1.997(1156)	0.52
10/13	0.6500(1856)	1.105(3168)	0.26

Table B.81: Vector fit to the $^3P_1$ channel, x component.

t_{min}/t_{max}	aE_1	aE_2	Q
2/13	0.5988(62)	0.9285(132)	7.6×10^{-3}
3/13	0.6020(86)	0.8604(188)	0.51
4/13	0.6006(110)	0.8526(269)	0.38
5/13	0.6051(161)	0.8083(407)	0.38
6/13	0.6104(178)	0.8605(669)	0.38
7/13	0.6665(693)	0.7903(1570)	0.83
8/13	0.6389(306)	0.9936(2092)	0.90
9/13	0.6360(252)	1.477(638)	0.93
10/13	0.6691(3713)	0.8252(16154)	0.81

Table B.82: Vector fit to the $^3P_1$ channel, y component.

t_{min}/t_{max}	aE_1	aE_2	Q
2/13	0.6014(69)	0.9156(138)	0.38
3/13	0.5998(88)	0.8800(189)	0.73
4/13	0.5997(104)	0.8855(275)	0.60
5/13	0.5949(124)	0.8852(426)	0.48
6/13	0.6008(152)	0.9086(760)	0.35
7/13	0.5944(182)	0.9550(1343)	0.22
8/13	0.6021(183)	1.209(310)	0.20
9/13	0.6109(161)	3.082(4120)	0.32
10/13	0.5201(4908)	1.004(2387)	0.34

Table B.83: Vector fit to the $^3P_1$ channel, z component.

t_{min}/t_{max}	aE_1	aE_2	Q
2/13	0.6163(47)	0.8513(100)	0.85
3/13	0.6138(54)	0.8472(143)	0.83
4/13	0.6105(65)	0.8325(197)	0.83
5/13	0.6125(74)	0.8502(319)	0.71
6/13	0.6122(79)	0.8801(529)	0.75
7/13	0.6117(108)	0.8303(784)	0.63
8/13	0.6245(108)	1.009(145)	0.80
9/13	0.6267(135)	1.039(281)	0.55
10/13	0.6225(265)	0.9233(4564)	0.38
11/13	0.6305(266)	2.525(2726)	0.89

Table B.84: Matrix fit to the $^3P_{2E}$ channel.

t_{min}/t_{max}	aE_1	aE_2	Q
2/13	0.6194(54)	0.8578(114)	0.53
3/13	0.6169(62)	0.8550(164)	0.53
4/13	0.6152(74)	0.8446(235)	0.52
5/13	0.6167(91)	0.8424(358)	0.36
6/13	0.6152(97)	0.8496(549)	0.38
7/13	0.6153(148)	0.7811(775)	0.38
8/13	0.6249(126)	1.004(157)	0.60
9/13	0.6211(176)	1.004(269)	0.41
10/13	0.6183(353)	0.9176(4723)	0.18
11/13	0.6148(332)	1.783(1381)	0.58

Table B.85: Matrix fit to the $^3P_{2E}$ channel, xy component.

t_{min}/t_{max}	aE_1	aE_2	Q
2/13	0.6161(50)	0.8518(104)	0.40
3/13	0.6118(59)	0.8386(147)	0.55
4/13	0.6074(71)	0.8215(203)	0.60
5/13	0.6108(81)	0.8495(328)	0.49
6/13	0.6143(87)	0.8827(550)	0.56
7/13	0.6146(117)	0.8310(818)	0.41
8/13	0.6276(125)	0.9418(1461)	0.36
9/13	0.6370(149)	0.9793(2616)	0.21
10/13	0.6380(301)	0.9317(4135)	0.12
11/13	0.6591(304)	3.065(4262)	0.43

Table B.86: Matrix fit to the $^3P_{2E}$ channel, xz component.

t_{min}/t_{max}	aE_1	aE_2	Q
2/13	0.6158(52)	0.8515(105)	0.46
3/13	0.6141(60)	0.8481(153)	0.47
4/13	0.6106(73)	0.8263(203)	0.49
5/13	0.6125(84)	0.8423(329)	0.34
6/13	0.6114(91)	0.8838(546)	0.40
7/13	0.6082(132)	0.8267(800)	0.25
8/13	0.6258(128)	1.022(156)	0.69
9/13	0.6358(163)	1.050(308)	0.51
10/13	0.6235(481)	0.9391(5097)	0.61
11/13	0.6276(285)	2.126(2202)	0.72

Table B.87: Matrix fit to the $^3P_{2E}$ channel, yz component.

t_{min}/t_{max}	aE_1	aE_2	Q
2/13	0.6094(60)	0.9427(121)	2.2×10^{-2}
3/13	0.6156(78)	0.8871(170)	0.72
4/13	0.6160(98)	0.8735(256)	0.62
5/13	0.6133(117)	0.8839(392)	0.48
6/13	0.6243(145)	0.9145(763)	0.55
7/13	0.6685(557)	0.8002(1503)	0.97
8/13	0.6503(290)	1.000(233)	1.00
9/13	0.6532(406)	1.052(500)	0.96
10/13	0.6377(570)	1.029(1080)	0.79

Table B.88: Vector fit to the $^3P_{2T}$ channel.

t_{min}/t_{max}	aE_1	aE_2	Q
2/13	0.6109(70)	0.9329(134)	0.20
3/13	0.6149(97)	0.8820(194)	0.81
4/13	0.6199(123)	0.8788(298)	0.73
5/13	0.6106(135)	0.9275(468)	0.82
6/13	0.6202(180)	0.9217(845)	0.74
7/13	0.6244(310)	0.8354(1374)	0.64
8/13	0.6166(254)	1.035(256)	0.61
9/13	0.6240(242)	1.489(785)	0.48
10/13	0.5988(426)	2.737(6255)	0.50

Table B.89: Vector fit to the ${}^3P_{2T}$ channel, xy component.

t_{min}/t_{max}	aE_1	aE_2	Q
2/13	0.6050(65)	0.9577(137)	0.18
3/13	0.6063(85)	0.9047(199)	0.73
4/13	0.6064(117)	0.8693(288)	0.79
5/13	0.6058(146)	0.8734(434)	0.65
6/13	0.6164(166)	0.9379(823)	0.75
7/13	0.6393(304)	0.8930(1491)	0.77
8/13	0.6547(405)	1.017(297)	0.85
9/13	0.7197(5018)	0.8234(10359)	0.76
10/13*			

Table B.90: Vector fit to the ${}^3P_{2T}$ channel, xz component.

t_{min}/t_{max}	aE_1	aE_2	Q
2/13	0.6112(72)	0.9354(136)	3.0×10^{-3}
3/13	0.6186(95)	0.8734(201)	0.14
4/13	0.6101(115)	0.8782(286)	0.11
5/13	0.6074(146)	0.8714(444)	5.9×10^{-2}
6/13	0.6224(193)	0.9078(814)	6.0×10^{-2}
7/13	0.7002(1267)	0.7978(2416)	0.94
8/13	0.6599(395)	0.9922(2643)	0.98
9/13	0.6593(730)	0.9183(5011)	0.88
10/13	0.6270(574)	1.157(1014)	0.70

Table B.91: Vector fit to the ${}^3P_{2T}$ channel, yz component.

t_{min}/t_{max}	aE_1	aE_2	Q
2/13*			
3/13*			
4/13	0.01873(12)	0.7917(191)	4.6×10^{-17}
5/13	0.01877(13)	0.8137(250)	9.3×10^{-18}
6/13	0.01868(16)	0.6322(228)	1.6×10^{-3}
7/13	0.01837(21)	0.4927(340)	0.55
8/13	0.01829(24)	0.4703(534)	0.39
9/13	0.01819(27)	0.5568(937)	0.64
10/13	0.01808(34)	0.5614(1722)	0.33

Table B.92: Vector fit to the kinetic $^3S_1$ mass, with $(a\mathbf{p})^2$=1. *Mass becoming negative.

t_{min}/t_{max}	aE_1	aE_2	Q
2/13*			
3/13	0.04035(18)	3.319(977)	0.00
4/13	0.03744(25)	0.8128(189)	2.2×10^{-17}
5/13	0.03754(28)	0.8312(250)	4.2×10^{-18}
6/13	0.03734(33)	0.6498(226)	$2.2\times^{-3}$
7/13	0.03667(44)	0.5117(338)	0.61
8/13	0.03652(51)	0.4946(530)	0.43
9/13	0.03631(57)	0.5796(948)	0.68
10/13	0.03604(75)	0.5661(1713)	0.38

Table B.93: Vector fit to the kinetic $^3S_1$ mass, with $(a\mathbf{p})^2$=2. *Mass becoming negative.

t_{min}/t_{max}	aE_1	aE_2	Q
2/13*			
3/13	0.06090(28)	3.342(977)	0.00
4/13	0.05615(39)	0.8354(188)	1.2×10^{-17}
5/13	0.05634(44)	0.8507(251)	2.3×10^{-18}
6/13	0.05601(53)	0.6669(226)	3.2×10^{-3}
7/13	0.05490(71)	0.5281(338)	0.70
8/13	0.05470(83)	0.5149(528)	0.51
9/13	0.05437(93)	0.5954(963)	0.74
10/13	0.05389(127)	0.5612(1700)	0.45

Table B.94: Vector fit to the kinetic $^3S_1$ mass, with $(a\mathbf{p})^2$=3. *Mass becoming negative.

t_{min}/t_{max}	aE_1	aE_2	Q
2/13*			
3/13	0.08129(39)	3.369(1000)	0.00
4/13	0.07449(54)	0.8387(185)	1.4×10^{-17}
5/13	0.07480(62)	0.8526(247)	2.8×10^{-18}
6/13	0.07445(74)	0.6810(221)	2.0×10^{-3}
7/13	0.07282(101)	0.5373(338)	0.65
8/13	0.07240(123)	0.5012(508)	0.54
9/13	0.07157(151)	0.5277(830)	0.59
10/13	0.07082(204)	0.5257(1445)	0.30

Table B.95: Vector fit to the kinetic $^3S_1$ mass, with $(a\mathbf{p})^2$=4. *Mass becoming negative.

t_{min}/t_{max}	aE_1	aE_2	Q
2/13*			
3/13	0.1026(5)	3.394(997)	0.00
4/13	0.09324(71)	0.8645(182)	6.8×10^{-18}
5/13	0.09375(81)	0.8741(247)	1.6×10^{-18}
6/13	0.09321(98)	0.7017(220)	4.4×10^{-3}
7/13	0.09103(135)	0.5613(330)	0.78
8/13	0.09063(160)	0.5381(511)	0.62
9/13	0.08969(195)	0.5740(883)	0.70
10/13*			

Table B.96: Vector fit to the kinetic $^3S_1$ mass, with $(a\mathbf{p})^2$=5. *Mass becoming negative.

t_{min}/t_{max}	aE_1	aE_2	Q
2/13*			
3/13	0.1244(6)	3.420(1003)	0.00
4/13	0.1121(9)	0.8920(184)	4.9×10^{-18}
5/13	0.1129(10)	0.9012(249)	1.4×10^{-18}
6/13	0.1120(13)	0.7208(224)	8.8×10^{-3}
7/13	0.1092(17)	0.5785(339)	0.88
8/13	0.1088(21)	0.5637(523)	0.73
9/13	0.1077(253)	0.6008(949)	0.81
10/13*			

Table B.97: Vector fit to the kinetic $^3S_1$ mass, with $(a\mathbf{p})^2$=6. *Mass becoming negative.

t_{min}/t_{max}	aE_1	aE_2	Q
2/13*			
3/13	0.1691(9)	3.478(1037)	0.00
4/13	0.1494(13)	0.9363(186)	5.3×10^{-17}
5/13	0.1509(15)	0.9558(244)	3.6×10^{-17}
6/13	0.1495(19)	0.7657(232)	3.7×10^{-2}
7/13	0.1453(26)	0.6253(368)	0.93
8/13	0.1452(31)	0.6214(586)	0.80
9/13	0.1438(39)	0.6632(1153)	0.84
10/13	0.1413(61)	0.6101(2046)	0.60

Table B.98: Vector fit to the kinetic $^3S_1$ mass, with $(a\mathbf{p})^2$=8. *Mass becoming negative.

t_{min}/t_{max}	aE_1	aE_2	Q
2/13*			
3/13	0.1926(11)	3.508(1057)	0.00
4/13	0.1685(15)	0.9668(193)	6.7×10^{-17}
5/13	0.1706(18)	0.9933(247)	8.1×10^{-17}
6/13	0.1686(22)	0.7832(245)	5.9×10^{-2}
7/13	0.1634(33)	0.6343(390)	0.97
8/13	0.1635(38)	0.6360(620)	0.90
9/13	0.1616(50)	0.6632(1255)	0.91
10/13*			

Table B.99: Vector fit to the kinetic $^3S_1$ mass, with $(a\mathbf{p})^2$=9. *Mass becoming negative.

t_{min}/t_{max}	aE_1	aE_2	Q
2/13*			
3/13	0.2655(16)	3.601(1176)	0.00
4/13	0.2252(24)	1.051(23)	1.8×10^{-14}
5/13	0.2298(28)	1.112(25)	7.5×10^{-13}
6/13	0.2260(37)	0.8464(307)	0.26
7/13	0.2177(58)	0.6793(514)	0.98
8/13	0.2195(66)	0.7014(885)	0.94
9/13	0.2155(99)	0.6822(1881)	0.89
10/13*			

Table B.100: Vector fit to the kinetic $^3S_1$ mass, with $(a\mathbf{p})^2$=12. *Mass becoming negative.

B.2.2 Wavefunction at the Origin for aM_b=1.8

t_{min}/t_{max}	$\psi_0(0)$
2/13	0.1869(48)
3/13	0.1840(53)
4/13	0.1829(61)
5/13	0.1758(60)
6/13	0.1772(59)
7/13	0.204(62)
8/13	0.210(73)

Table B.101: Wavefunction at the origin for the lattice 1^1S_0 channel.

t_{min}/t_{max}	$\psi_0(0)$
2/13	0.1513(42)
3/13	0.1487(58)
4/13	0.1477(68)
5/13	0.1428(67)
6/13	0.1445(51)
7/13	0.1491(53)
8/13	0.1509(43)

Table B.102: Wavefunction at the origin for the lattice 1^3S_1 channel.

B.2.3 Lattice Splittings for aM_b=1.8

t_{min}/t_{max}	$aE(1^3S_1 - 1^1S_0)$	$aE(2^3S_1 - 2^1S_0)$	$aE(3^3S_1 - 3^1S_0)$
2/13	0.02396(35)	0.0179(19)	0.0133(55)
3/13	0.02373(37)	0.0164(26)	0.010(10)
4/13	0.02360(39)	0.0155(41)	0.023(14)
5/13	0.02362(40)	0.0154(46)	0.024(22)
6/13	0.02355(50)	0.010(36)	0.012(34)
7/13	0.02355(52)	0.0132(78)	0.054(65)
8/13	0.02367(44)	0.0223(92)	0.23(31)
9/13	0.02371(49)	0.004(26)	-0.2(12)

Table B.103: Results from the $3e3s$ matrix fit.

t_{min}/t_{max}	$aE(1^1P_1 - 1^3P_0)$	$aE(2^1P_1 - 2^3P_0)$
2/13	0.0141(16)	0.0171(29)
3/13	0.0139(19)	0.0154(46)
4/13	0.0134(23)	0.0125(62)
5/13	0.0145(27)	0.019(11)
6/13	0.0153(31)	0.006(17)
7/13	0.0151(42)	-0.002(24)
8/13	0.0209(49)	0.041(48)
9/13	0.0252(63)	0.053(87)
10/13	0.032(16)	0.12(11)
11/13	0.027(13)	0.5(12)

Table B.104: Results from the matrix fit.

t_{min}/t_{max}	$aE(1^3P_{2E} - 1^1P_1)$	$aE(2^3P_{2E} - 2^1P_1)$
2/13	0.0068(12)	0.0104(21)
3/13	0.0063(14)	0.0077(31)
4/13	0.0058(16)	0.0052(43)
5/13	0.0062(21)	0.0015(78)
6/13	0.0049(23)	-0.005(13)
7/13	0.0050(33)	-0.015(16)
8/13	0.0071(39)	-0.001(34)
9/13	0.0135(50)	0.008(61)
10/13	0.006(16)	0.029(97)
11/13	0.0240(96)	1.1(46)

Table B.105: Results from the matrix fit.

t_{min}/t_{max}	$aE(1^3\overline{P} - 1^1P_1)$	$aE(2^3\overline{P} - 2^1P_1)$
2/13	0.0016(13)	0.0019(24)
3/13	0.0019(17)	-0.0026(35)
4/13	0.0013(22)	-0.0055(53)
5/13	-0.0006(27)	-0.0019(87)
6/13	0.0005(36)	-0.005(16)
7/13	0.011(11)	-0.044(35)
8/13	0.0054(66)	-0.032(57)
9/13	0.0057(91)	0.11(54)

Table B.106: Results from the vector fit.

t_{min}/t_{max}	$\frac{2^3S_1 - 1^3S_1}{1^1P_1 - 1^3S_1}$
2/13	1.348(28)
3/13	1.350(35)
4/13	1.334(43)
5/13	1.316(58)
6/13	1.439(95)
7/13	1.42(12)
8/13	1.57(20)
9/13	1.60(31)
10/13	1.42(41)
11/13	2.2(11)

Table B.107: Results from the matrix fit.

t_{min}/t_{max}	$\frac{1^3P_{2E}-1^1P_1}{1^1P_1-1^3P_0}$
2/13	0.481(92)
3/13	0.46(11)
4/13	0.44(13)
5/13	0.43(15)
6/13	0.31(15)
7/13	0.33(21)
8/13	0.34(18)
9/13	0.54(21)
10/13	0.18(53)
11/13	0.88(46)

Table B.108: Results from the matrix fit.

B.2.4 Lattice State Fits for aM_b=2.1

t_{min}/t_{max}	aE_1	aE_2	aE_3	Q
2/13	0.3843(10)	0.6598(64)	0.7973(193)	1.5×10^{-2}
3/13	0.3832(11)	0.6554(83)	0.7968(313)	6.8×10^{-2}
4/13	0.3834(11)	0.6435(148)	0.7403(417)	7.5×10^{-2}
5/13	0.3831(12)	0.6462(157)	0.7800(765)	5.5×10^{-2}
6/13	0.3835(12)	0.6671(206)	0.7606(1016)	0.17
7/13	0.3824(15)	0.6481(302)	0.9302(1737)	0.43
8/13	0.3831(13)	0.7020(301)	1.389(604)	0.64
9/13	0.3831(14)	0.6816(552)	2.254(2525)	0.54
10/13	0.3818(124)	0.6699(1506)	0.8063(23606)	0.54
11/13*				

Table B.109: Matrix fit to the $^3S_1$ channel. *Fitted lattice state energy becoming negative.

t_{min}/t_{max}	aE_1	aE_2	aE_3	Q
2/13	0.3621(9)	0.6448(60)	0.7882(206)	1.5×10^{-2}
3/13	0.3612(10)	0.6418(77)	0.7875(332)	4.7×10^{-2}
4/13	0.3615(10)	0.6301(138)	0.7177(442)	5.7×10^{-2}
5/13	0.3612(10)	0.6321(145)	0.7559(764)	3.5×10^{-2}
6/13	0.3616(11)	0.6518(165)	0.7439(1022)	0.18
7/13	0.3610(12)	0.6458(209)	0.8620(1734)	0.39
8/13	0.3611(12)	0.6835(274)	1.257(484)	0.62
9/13	0.3611(12)	0.6699(464)	2.478(3059)	0.50

Table B.110: Matrix fit to the $^1S_0$ channel.

t_{min}/t_{max}	aE_1	aE_2	Q
2/13	0.5929(44)	0.8106(102)	0.66
3/13	0.5901(50)	0.8046(141)	0.69
4/13	0.5877(59)	0.7920(192)	0.64
5/13	0.5891(66)	0.8170(309)	0.54
6/13	0.5902(69)	0.8585(503)	0.69
7/13	0.5892(93)	0.8145(748)	0.53
8/13	0.5987(91)	0.9491(1351)	0.67
9/13	0.5979(114)	0.9151(2277)	0.39
10/13	0.6043(205)	0.8561(3592)	0.29

Table B.111: Matrix fit to the $^1P_1$ channel.

t_{min}/t_{max}	aE_1	aE_2	Q
2/13	0.5810(40)	0.7973(104)	0.90
3/13	0.5787(46)	0.7924(143)	0.87
4/13	0.5766(55)	0.7835(196)	0.87
5/13	0.5771(61)	0.8053(309)	0.80
6/13	0.5776(66)	0.8575(502)	0.83
7/13	0.5767(85)	0.8265(755)	0.67
8/13	0.5811(87)	0.9244(1363)	0.59
9/13	0.5765(112)	0.8808(2185)	0.35
10/13	0.5771(224)	0.7583(3250)	0.15
11/13	0.5794(202)	1.941(1349)	0.84

Table B.112: Matrix fit to the $^3P_0$ channel.

t_{min}/t_{max}	aE_1	aE_2	Q
2/13	0.5845(57)	0.8749(115)	4.0×10^{-2}
3/13	0.5875(75)	0.8302(156)	0.63
4/13	0.5833(90)	0.8341(214)	0.54
5/13	0.5822(113)	0.8242(321)	0.40
6/13	0.5914(142)	0.8434(544)	0.36
7/13	0.6154(255)	0.8175(974)	0.46
8/13	0.6032(185)	1.025(173)	0.60
9/13	0.6066(158)	1.706(701)	0.83
10/13	0.5938(1664)	0.7059(10339)	0.63

Table B.113: Vector fit to the $^3P_1$ channel.

t_{min}/t_{max}	aE_1	aE_2	Q
2/13	0.5795(60)	0.8828(108)	3.2×10^{-3}
3/13	0.5876(78)	0.8283(151)	0.61
4/13	0.5860(91)	0.8307(221)	0.47
5/13	0.5867(115)	0.8205(339)	0.33
6/13	0.5984(151)	0.8282(572)	0.33
7/13	0.6256(320)	0.8026(1100)	0.49
8/13	0.6070(190)	1.020(186)	0.62
9/13	0.6066(152)	1.751(781)	0.86
10/13	0.5967(1403)	0.7184(11645)	0.64

Table B.114: Vector fit to the $^3P_1$ channel, x component.

t_{min}/t_{max}	aE_1	aE_2	Q
2/13	0.5845(57)	0.8749(115)	4.0×10^{-2}
3/13	0.5875(75)	0.8302(156)	0.63
4/13	0.5833(90)	0.8341(214)	0.54
5/13	0.5822(113)	0.8242(321)	0.40
6/13	0.5914(142)	0.8434(544)	0.36
7/13	0.6154(255)	0.8175(974)	0.46
8/13	0.6032(185)	1.025(173)	0.60
9/13	0.6066(158)	1.706(701)	0.83
10/13	0.5938(1664)	0.7059(10339)	0.63

Table B.115: Vector fit to the $^3P_1$ channel, y component.

t_{min}/t_{max}	aE_1	aE_2	Q
2/13	0.5831(67)	0.8781(135)	0.51
3/13	0.5815(86)	0.8493(183)	0.75
4/13	0.5808(103)	0.8540(263)	0.61
5/13	0.5750(124)	0.8547(392)	0.51
6/13	0.5828(149)	0.8866(702)	0.43
7/13	0.5770(192)	0.8974(1201)	0.27
8/13	0.5854(192)	1.119(262)	0.26
9/13	0.5950(164)	2.641(2574)	0.38

Table B.116: Vector fit to the $^3P_1$ channel, z component.

t_{min}/t_{max}	aE_1	aE_2	Q
2/13	0.5988(46)	0.8197(103)	0.56
3/13	0.5956(53)	0.8116(144)	0.62
4/13	0.5930(62)	0.7980(195)	0.54
5/13	0.5948(70)	0.8213(316)	0.42
6/13	0.5946(74)	0.8586(516)	0.59
7/13	0.5941(103)	0.8084(755)	0.43
8/13	0.6053(104)	0.9541(1377)	0.61
9/13	0.6088(129)	0.9362(2368)	0.35
10/13	0.6108(259)	0.9167(3904)	0.37
11/13	0.6224(233)	2.591(2828)	0.92

Table B.117: Matrix fit to the $^3P_{2E}$ channel.

t_{min}/t_{max}	aE_1	aE_2	Q
2/13	0.6007(52)	0.8239(116)	0.71
3/13	0.5974(59)	0.8196(163)	0.72
4/13	0.5956(70)	0.8105(230)	0.67
5/13	0.5969(83)	0.8159(353)	0.48
6/13	0.5946(88)	0.8359(552)	0.59
7/13	0.5952(123)	0.7745(790)	0.56
8/13	0.6011(117)	0.9695(1539)	0.68
9/13	0.5977(162)	0.9176(2466)	0.43
10/13	0.6033(288)	0.9108(4272)	0.26
11/13	0.6039(284)	2.331(2281)	0.91

Table B.118: Matrix fit to the $^3P_{2E}$ channel, xy component.

t_{min}/t_{max}	aE_1	aE_2	Q
2/13	0.5987(48)	0.8195(107)	0.36
3/13	0.5942(56)	0.8058(149)	0.51
4/13	0.5904(67)	0.7904(205)	0.49
5/13	0.5933(75)	0.8248(330)	0.42
6/13	0.5957(80)	0.8732(559)	0.55
7/13	0.5972(101)	0.8491(874)	0.35
8/13	0.6075(115)	0.9297(1500)	0.31
9/13	0.6124(139)	0.9345(2601)	0.17
10/13	0.6192(240)	0.9428(4283)	0.11
11/13*	0.6422(289)	3.125(4412)	0.68

Table B.119: Matrix fit to the $^3P_{2E}$ channel, xz component.

t_{min}/t_{max}	aE_1	aE_2	Q
2/13	0.5987(50)	0.8170(108)	0.38
3/13	0.5965(58)	0.8150(154)	0.36
4/13	0.5939(71)	0.7941(201)	0.35
5/13	0.5953(79)	0.8169(329)	0.28
6/13	0.5932(85)	0.8662(548)	0.39
7/13	0.5894(123)	0.8109(791)	0.23
8/13	0.6057(125)	0.9665(1467)	0.71
9/13	0.6136(158)	0.9528(2641)	0.50
10/13	0.6145(299)	0.9737(4769)	0.68
11/13	0.6149(278)	2.136(2242)	0.80

Table B.120: Matrix fit to the ${}^3P_{2E}$ channel, yz component.

t_{min}/t_{max}	aE_1	aE_2	Q
2/13	0.5906(59)	0.8982(118)	0.12
3/13	0.5943(76)	0.8562(162)	0.72
4/13	0.5918(96)	0.8533(234)	0.60
5/13	0.5890(116)	0.8594(347)	0.45
6/13	0.6003(141)	0.8985(641)	0.52
7/13	0.6390(417)	0.7850(1227)	0.93
8/13	0.6248(248)	0.9814(1940)	0.99
9/13	0.6365(398)	1.027(424)	0.98
10/13	0.6146(357)	1.301(1137)	0.96

Table B.121: Vector fit to the ${}^3P_{2T}$ channel.

t_{min}/t_{max}	aE_1	aE_2	Q
2/13	0.5893(68)	0.8936(131)	0.35
3/13	0.5931(93)	0.8533(188)	0.80
4/13	0.5973(117)	0.8539(285)	0.70
5/13	0.5875(130)	0.8978(439)	0.80
6/13	0.5959(169)	0.8981(785)	0.72
7/13	0.5995(283)	0.8176(1252)	0.62
8/13	0.5971(236)	1.018(238)	0.63
9/13	0.6083(228)	1.489(749)	0.59
10/13	0.5788(428)	2.208(3402)	0.82

Table B.122: Vector fit to the ${}^3P_{2T}$ channel, xy component.

t_{min}/t_{max}	aE_1	aE_2	Q
2/13	0.5857(65)	0.9129(131)	0.42
3/13	0.5890(84)	0.8728(191)	0.80
4/13	0.5887(114)	0.8498(279)	0.77
5/13	0.5890(146)	0.8435(420)	0.63
6/13	0.6010(162)	0.9125(795)	0.81
7/13	0.6234(321)	0.8507(1407)	0.80
8/13	0.6345(384)	0.9766(2675)	0.87
9/13	0.6925(2901)	0.8462(7913)	0.89
10/13*			

Table B.123: Vector fit to the ${}^3P_{2T}$ channel, xz component.

t_{min}/t_{max}	aE_1	aE_2	Q
2/13	0.5926(71)	0.8868(133)	5.3×10^{-3}
3/13	0.6004(96)	0.8403(191)	7.1×10^{-2}
4/13	0.5899(112)	0.8510(271)	6.7×10^{-2}
5/13	0.5879(148)	0.8373(405)	3.5×10^{-2}
6/13	0.6024(197)	0.8664(716)	2.9×10^{-2}
7/13	0.6828(1406)	0.7625(2407)	0.81
8/13	0.6391(382)	0.9426(2226)	0.91
9/13	0.6298(662)	0.8675(4092)	0.69
10/13	0.6124(426)	1.363(989)	0.68

Table B.124: Vector fit to the ${}^3P_{2T}$ channel, yz component.

t_{min}/t_{max}	aE_1	aE_2	Q
2/13*			
3/13*			
4/13	0.01762(8)	3.346(1451)	0.00
5/13	0.01651(11)	0.7781(193)	2.3×10^{-11}
6/13	0.01651(13)	0.6789(360)	1.2×10^{-10}
7/13	0.01631(16)	0.6145(242)	7.0×10^{-2}
8/13	0.01620(19)	0.5246(344)	0.72
9/13	0.01613(22)	0.5393(564)	0.54
10/13	0.01605(29)	0.5204(975)	0.24

Table B.125: Vector fit to the kinetic ${}^3S_1$ mass, with $(a\mathbf{p})^2$=1. *Mass becoming negative.

t_{min}/t_{max}	aE_1	aE_2	Q
2/13*			
3/13*			
4/13*			
5/13	0.03300(24)	0.7939(192)	2.9×10^{-11}
6/13	0.03302(28)	0.6938(359)	1.7×10^{-10}
7/13	0.03260(33)	0.6309(241)	9.1×10^{-2}
8/13	0.03238(40)	0.5436(341)	0.77
9/13	0.03225(47)	0.5564(564)	0.58
10/13	0.03207(62)	0.5280(965)	0.28

Table B.126: Vector fit to the kinetic $^3S_1$ mass, with $(a\mathbf{p})^2$=2. *Mass becoming negative.

t_{min}/t_{max}	aE_1	aE_2	Q
2/13*			
3/13*			
4/13*			
5/13	0.04951(38)	0.8098(191)	3.9×10^{-11}
6/13	0.04954(44)	0.7093(359)	2.5×10^{-10}
7/13	0.04888(53)	0.6466(240)	0.12
8/13	0.04854(64)	0.5613(339)	0.81
9/13	0.04834(75)	0.5705(567)	0.62
10/13	0.04806(102)	0.5317(956)	0.33

Table B.127: Vector fit to the kinetic $^3S_1$ mass, with $(a\mathbf{p})^2$=3. *Mass becoming negative.

t_{min}/t_{max}	aE_1	aE_2	Q
2/13*			
3/13*			
4/13**	0.07139(37)	3.420(1509)	0.00
5/13	0.06575(53)	0.8243(188)	3.4×10^{-12}
6/13	0.06584(62)	0.7133(356)	6.4×10^{-11}
7/13	0.06489(75)	0.6573(237)	4.3×10^{-2}
8/13	0.06436(92)	0.5606(331)	0.70
9/13	0.06397(111)	0.5531(527)	0.49
10/13	0.06352(151)	0.5308(892)	0.21

Table B.128: Vector fit to the kinetic $^3S_1$ mass, with $(a\mathbf{p})^2$=4. *Mass becoming negative, **bad fit.

t_{min}/t_{max}	aE_1	aE_2	Q
2/13	0.09898(50)	1.198(103)	0.00
3/13*			
4/13**	0.09001(49)	3.483(1662)	0.00
5/13	0.08231(69)	0.8413(187)	8.3×10^{-12}
6/13	0.08244(82)	0.7332(354)	1.5×10^{-10}
7/13	0.08122(100)	0.6760(236)	8.1×10^{-2}
8/13	0.08059(122)	0.5856(328)	0.80
9/13	0.08016(147)	0.5807(538)	0.60
10/13	0.07957(202)	0.5483(906)	0.29

Table B.129: Vector fit to the kinetic $^3S_1$ mass, with $(a\mathbf{p})^2$=5. *Mass becoming negative, **bad fit.

t_{min}/t_{max}	aE_1	aE_2	Q
2/13	0.1203(7)	1.165(95)	0.00
3/13*			
4/13**	0.1090(6)	3.511(1689)	0.00
5/13	0.09891(87)	0.8583(187)	2.3×10^{-11}
6/13	0.09909(104)	0.7537(356)	3.3×10^{-10}
7/13	0.09757(127)	0.6928(238)	0.13
8/13	0.09681(155)	0.6066(330)	0.87
9/13	0.09632(189)	0.5996(556)	0.68
10/13	0.09562(265)	0.5569(929)	0.39

Table B.130: Vector fit to the kinetic $^3S_1$ mass, with $(a\mathbf{p})^2$=6. *Mass becoming negative, **bad fit.

t_{min}/t_{max}	aE_1	aE_2	Q
2/13*			
3/13*			
4/13**	0.1480(9)	3.570(1765)	0.00
5/13	0.1320(13)	0.8959(190)	9.7×10^{-11}
6/13	0.1326(15)	0.8030(356)	1.1×10^{-9}
7/13	0.1303(19)	0.7309(243)	0.24
8/13	0.1293(24)	0.6477(344)	0.92
9/13	0.1288(29)	0.6433(605)	0.75
10/13	0.1276(41)	0.5979(1040)	0.45

Table B.131: Vector fit to the kinetic $^3S_1$ mass, with $(a\mathbf{p})^2$=8. *Mass becoming negative, **bad fit.

t_{min}/t_{max}	aE_1	aE_2	Q
2/13	0.1887(13)	1.049(73)	0.00
3/13*			
4/13**	0.1683(11)	3.595(1786)	0.00
5/13	0.1488(15)	0.9132(194)	3.3×10^{-10}
6/13	0.1495(18)	0.8282(362)	2.2×10^{-9}
7/13	0.1467(23)	0.7459(251)	0.33
8/13	0.1456(29)	0.6650(356)	0.94
9/13	0.1450(36)	0.6518(643)	0.81
10/13	0.1439(52)	0.6003(1105)	0.52

Table B.132: Vector fit to the kinetic $^3S_1$ mass, with $(a\mathbf{p})^2$=9. *Mass becoming negative, **bad fit.

t_{min}/t_{max}	aE_1	aE_2	Q
2/13*			
3/13*			
4/13**	0.2321(16)	3.663(1848)	0.00
5/13	0.1988(24)	0.9719(218)	2.7×10^{-8}
6/13	0.2012(29)	0.9385(368)	4.1×10^{-8}
7/13	0.1961(38)	0.7997(290)	0.61
8/13	0.1948(48)	0.7220(440)	0.94
9/13	0.1940(63)	0.6870(858)	0.81
10/13	0.1935(94)	0.6422(1597)	0.48

Table B.133: Vector fit to the kinetic $^3S_1$ mass, with $(a\mathbf{p})^2$=12. *Mass becoming negative, **bad fit.

B.2.5 Wavefunction at the Origin for aM_b=2.1

t_{min}/t_{max}	$\psi_0(0)$
2/13	0.2088(57)
3/13	0.2047(61)
4/13	0.2037(69)
5/13	0.1967(70)
6/13	0.1961(71)
7/13	0.233(96)
8/13	0.30(25)

Table B.134: Wavefunction at the origin for the lattice 1^1S_0 channel.

t_{min}/t_{max}	$\psi_0(0)$
2/13	0.1747(51)
3/13	0.1713(56)
4/13	0.1698(65)
5/13	0.1649(65)
6/13	0.1646(62)
7/13	0.216(92)
8/13	0.5(60)

Table B.135: Wavefunction at the origin for the lattice 1^3S_1 channel.

B.2.6 Lattice Splittings for aM_b=2.1

t_{min}/t_{max}	$aE(1^3S_1 - 1^1S_0)$	$aE(2^3S_1 - 2^1S_0)$	$aE(3^3S_1 - 3^1S_0)$
2/13	0.02223(31)	0.0149(16)	0.0091(52)
3/13	0.02203(33)	0.0136(22)	0.0093(90)
4/13	0.02194(35)	0.0134(32)	0.023(11)
5/13	0.02192(36)	0.0141(31)	0.024(18)
6/13	0.02187(39)	0.0152(85)	0.016(21)
7/13	0.0215(40)	0.0056(1300)	0.07(17)
8/13	0.02196(41)	0.0185(72)	0.13(17)
9/13	0.02199(49)	0.014(18)	-2(17)

Table B.136: Results from the $3e3s$ matrix fit.

t_{min}/t_{max}	$aE(1^1P_1 - 1^3P_0)$	$aE(2^1P_1 - 2^3P_0)$
2/13	0.0119(14)	0.0132(27)
3/13	0.0114(16)	0.0122(41)
4/13	0.0111(20)	0.0086(55)
5/13	0.0120(23)	0.0117(92)
6/13	0.0126(27)	0.001(15)
7/13	0.0125(36)	-0.012(23)
8/13	0.0176(44)	0.025(45)
9/13	0.0215(57)	0.034(72)
10/13	0.027(10)	0.095(94)

Table B.137: Results from the matrix fit.

t_{min}/t_{max}	$aE(1^3P_{2E} - 1^1P_1)$	$aE(2^3P_{2E} - 2^1P_1)$
2/13	0.00590(98)	0.0091(19)
3/13	0.0055(11)	0.0070(27)
4/13	0.0053(14)	0.0060(35)
5/13	0.0057(17)	0.0042(64)
6/13	0.0044(19)	0.0001(110)
7/13	0.0049(26)	-0.006(14)
8/13	0.0066(33)	0.005(30)
9/13	0.0109(42)	0.022(49)
10/13	0.0064(86)	0.059(80)

Table B.138: Results from the matrix fit.

t_{min}/t_{max}	$aE(1^3\overline{P} - 1^1P_1)$	$aE(2^3\overline{P} - 2^1P_1)$
2/13	0.0015(12)	0.0016(21)
3/13	0.0020(15)	-0.0020(31)
4/13	0.0013(19)	-0.0039(47)
5/13	-0.0003(24)	-0.0032(75)
6/13	0.0009(31)	-0.006(14)
7/13	0.0100(96)	-0.036(29)
8/13	0.0050(58)	-0.034(48)
9/13	0.0055(83)	0.08(22)

Table B.139: Results from the vector fit.

t_{min}/t_{max}	$\frac{2^3S_1-1^3S_1}{1^1P_1-1^3S_1}$
2/13	1.307(27)
3/13	1.309(34)
4/13	1.299(42)
5/13	1.298(57)
6/13	1.443(93)
7/13	1.43(12)
8/13	1.55(19)
9/13	1.61(28)
10/13	1.57(40)

Table B.140: Results from the matrix fit.

t_{min}/t_{max}	$\frac{1^3P_{2E}-1^1P_1}{1^1P_1-1^3P_0}$
2/13	0.497(95)
3/13	0.48(11)
4/13	0.48(14)
5/13	0.48(15)
6/13	0.35(16)
7/13	0.39(21)
8/13	0.37(18)
9/13	0.51(21)
10/13	0.24(33)

Table B.141: Results from the matrix fit.

B.3 Lattice Results for the Dynamical Calculations with κ=0.1345

B.3.1 Lattice State Fits for aM_b=1.8

t_{min}/t_{max}	aE_1	aE_2	aE_3	Q
2/13	0.3911(10)	0.6727(69)	0.8293(173)	3.9×10^{-4}
3/13	0.3898(11)	0.6630(98)	0.8103(278)	1.5×10^{-2}
4/13	0.3901(11)	0.6755(115)	0.8704(564)	2.9×10^{-2}
5/13	0.3896(12)	0.6140(352)	0.7803(529)	0.18
6/13	0.3896(12)	0.6203(403)	0.8434(1091)	0.23
7/13	0.3891(14)	0.4597(1125)	0.7162(543)	0.17
8/13	0.3887(51)	0.4065(1745)	0.6802(714)	9.3×10^{-2}
9/13	0.3893(17)	0.4405(2199)	0.6970(1157)	5.2×10^{-2}
10/13	0.3906(18)	0.5327(1720)	0.9684(5781)	0.20
11/13*				

Table B.142: Matrix fit to the $^3S_1$ channel. *Fitted lattice state energy becoming negative.

t_{min}/t_{max}	aE_1	aE_2	aE_3	Q
2/13	0.3683(9)	0.6543(62)	0.8186(192)	9.7×10^{-3}
3/13	0.3674(9)	0.6461(84)	0.8004(311)	7.1×10^{-2}
4/13	0.3675(9)	0.6589(97)	0.8857(631)	0.11
5/13	0.3673(10)	0.6251(284)	0.7730(679)	0.28
6/13	0.3672(10)	0.6205(333)	0.8592(1377)	0.33
7/13	0.3668(11)	0.4587(1275)	0.6802(490)	0.26
8/13	0.3465(2183)	0.3664(12)	0.6356(489)	0.20
9/13	0.3664(44)	0.3894(2690)	0.6564(887)	0.12
10/13	0.3675(40)	0.4508(3236)	0.7501(3314)	0.36
11/13	0.3680(18)	0.4393(4654)	1.251(2174)	0.39

Table B.143: Matrix fit to the $^1S_0$ channel.

t_{min}/t_{max}	aE_1	aE_2	Q
2/13	0.5943(43)	0.8382(94)	0.26
3/13	0.5875(51)	0.8333(133)	0.52
4/13	0.5924(55)	0.8561(211)	0.75
5/13	0.5934(64)	0.8540(323)	0.62
6/13	0.5916(77)	0.8225(454)	0.55
7/13	0.5835(109)	0.7995(654)	0.47
8/13	0.5807(107)	0.8653(1190)	0.53
9/13	0.5883(109)	1.070(273)	0.34
10/13*			

Table B.144: Matrix fit to the $^1P_1$ channel. *Fitted lattice state energy becoming negative.

t_{min}/t_{max}	aE_1	aE_2	Q
2/13	0.5943(43)	0.8382(94)	0.26
3/13	0.5875(51)	0.8333(133)	0.52
4/13	0.5924(55)	0.8561(211)	0.75
5/13	0.5934(64)	0.8540(323)	0.62
6/13	0.5916(77)	0.8225(454)	0.55
7/13	0.5835(109)	0.7995(654)	0.47
8/13	0.5807(107)	0.8653(1190)	0.53
9/13	0.5883(109)	1.070(273)	0.34
10/13*			
11/13	0.5731(1292)	0.6597(2429)	0.47

Table B.145: Matrix fit to the $^1P_1$ channel in the x direction. *Fitted lattice state energy becoming negative.

t_{min}/t_{max}	aE_1	aE_2	Q
2/13	0.5943(43)	0.8382(94)	0.26
3/13	0.5875(51)	0.8333(133)	0.52
4/13	0.5924(55)	0.8561(211)	0.75
5/13	0.5934(64)	0.8540(323)	0.62
6/13	0.5916(77)	0.8225(454)	0.55
7/13	0.5835(109)	0.7995(654)	0.47
8/13	0.5807(107)	0.8653(1190)	0.53
9/13	0.5883(109)	1.070(273)	0.34
10/13*			
11/13	0.5731(1292)	0.6597(2429)	0.47

Table B.146: Matrix fit to the $^1P_1$ channel in the y direction. *Fitted lattice state energy becoming negative.

t_{min}/t_{max}	aE_1	aE_2	Q
2/13	0.5943(43)	0.8382(94)	0.26
3/13	0.5875(51)	0.8333(133)	0.52
4/13	0.5924(55)	0.8561(211)	0.75
5/13	0.5934(64)	0.8540(323)	0.62
6/13	0.5916(77)	0.8225(454)	0.55
7/13	0.5835(109)	0.7995(654)	0.47
8/13	0.5807(107)	0.8653(1190)	0.53
9/13	0.5883(109)	1.070(273)	0.34
10/13*			
11/13	0.5731(1292)	0.6597(2429)	0.47

Table B.147: Matrix fit to the $^1P_1$ channel in the z direction. *Fitted lattice state energy becoming negative.

t_{min}/t_{max}	aE_1	aE_2	Q
2/13	0.5796(39)	0.8194(95)	0.25
3/13	0.5744(46)	0.8194(134)	0.47
4/13	0.5783(49)	0.8418(210)	0.80
5/13	0.5793(57)	0.8332(310)	0.70
6/13	0.5782(69)	0.8156(448)	0.54
7/13	0.5721(92)	0.8076(653)	0.51
8/13	0.5729(94)	0.9151(1244)	0.40
9/13	0.5746(96)	1.964(759)	0.41
10/13	0.3320(2497)	0.5723(117)	0.72
11/13	0.5676(814)	0.5898(3112)	0.29

Table B.148: Matrix fit to the $^3P_0$ channel.

t_{min}/t_{max}	aE_1	aE_2	Q
2/13	0.5776(50)	0.9143(103)	0.51
3/13	0.5808(61)	0.8945(147)	0.73
4/13	0.5851(76)	0.8824(229)	0.70
5/13	0.5842(92)	0.8864(354)	0.55
6/13	0.5736(122)	0.8613(529)	0.57
7/13	0.5724(149)	0.8827(832)	0.40
8/13	0.5787(235)	0.8412(1466)	0.23
9/13	0.5866(166)	1.320(388)	0.57
10/13	0.5846(306)	1.171(966)	0.24

Table B.149: Vector fit to the $^3P_1$ channel.

t_{min}/t_{max}	aE_1	aE_2	Q
2/13	0.5755(58)	0.9163(121)	0.13
3/13	0.5788(73)	0.8847(174)	0.36
4/13	0.5813(89)	0.8812(278)	0.25
5/13	0.5830(108)	0.8955(432)	0.16
6/13	0.5657(143)	0.8696(632)	0.24
7/13	0.5615(161)	0.9578(1092)	0.21
8/13	0.5718(204)	0.9754(2086)	0.12
9/13	0.5767(153)	1.929(891)	0.47
10/13*			

Table B.150: Vector fit to the $^3P_1$ channel, x component. *mass bnecoming negative.

t_{min}/t_{max}	aE_1	aE_2	Q
2/13	0.5740(58)	0.9117(112)	0.92
3/13	0.5742(72)	0.8966(162)	0.93
4/13	0.5804(89)	0.8887(263)	0.93
5/13	0.5789(104)	0.9168(427)	0.90
6/13	0.5806(136)	0.8949(711)	0.81
7/13	0.5854(202)	0.8473(1127)	0.68
8/13	0.5966(379)	0.8006(2039)	0.49
9/13	0.5931(205)	1.373(509)	0.86
10/13	0.5794(348)	1.430(1466)	0.62

Table B.151: Vector fit to the $^3P_1$ channel, y component.

t_{min}/t_{max}	aE_1	aE_2	Q
2/13	0.5809(58)	0.9144(119)	0.41
3/13	0.5889(73)	0.8997(185)	0.64
4/13	0.5943(95)	0.8752(287)	0.64
5/13	0.5905(127)	0.8444(428)	0.56
6/13	0.5739(174)	0.8170(591)	0.61
7/13	0.5770(222)	0.8248(931)	0.42
8/13	0.5758(477)	0.7322(1472)	0.29
9/13	0.5861(360)	0.9200(2780)	0.19
10/13	0.5515(690)	0.9707(5511)	6.4×10^{-2}

Table B.152: Vector fit to the $^3P_1$ channel, z component.

$tmin/tmax$	aE_1	aE_2	Q
2/13	0.6004(45)	0.8486(95)	0.34
3/13	0.5925(55)	0.8403(135)	0.64
4/13	0.5985(58)	0.8645(215)	0.80
5/13	0.5998(69)	0.8649(335)	0.69
6/13	0.5980(84)	0.8279(466)	0.64
7/13	0.5901(127)	0.7876(645)	0.55
8/13	0.5893(117)	0.8554(1193)	0.58
9/13	0.6004(115)	1.093(266)	0.46
10/13	0.3706(2422)	0.6198(166)	0.87
11/13	0.5944(1175)	0.6965(2658)	0.64

Table B.153: Matrix fit to the ${}^3P_{2E}$ channel.

t_{min}/t_{max}	aE_1	aE_2	Q
2/13	0.6055(49)	0.8539(102)	0.67
3/13	0.5994(59)	0.8417(145)	0.72
4/13	0.6072(63)	0.8718(235)	0.87
5/13	0.6101(76)	0.8649(368)	0.82
6/13	0.6113(88)	0.8463(534)	0.78
7/13	0.6070(141)	0.7968(739)	0.70
8/13	0.6066(131)	0.8901(1449)	0.66
9/13	0.6247(137)	1.434(493)	0.65
10/13	0.6336(1087)	0.6518(2371)	0.90
11/13	0.2860(3421)	0.6430(282)	0.81

Table B.154: Matrix fit to the ${}^3P_{2E}$ channel, xy component.

t_{min}/t_{max}	aE_1	aE_2	Q
2/13	0.6001(48)	0.8504(104)	0.25
3/13	0.5905(58)	0.8406(147)	0.61
4/13	0.5964(63)	0.8732(240)	0.81
5/13	0.5971(74)	0.8794(394)	0.65
6/13	0.5926(93)	0.8159(537)	0.67
7/13	0.5821(147)	0.7710(717)	0.57
8/13	0.5808(144)	0.8451(1287)	0.55
9/13	0.5927(143)	1.032(262)	0.50
10/13	0.5154(2323)	0.6341(672)	0.67
11/13	0.6212(260)	2.251(2236)	0.76

Table B.155: Matrix fit to the ${}^3P_{2E}$ channel, xz component.

t_{min}/t_{max}	aE_1	aE_2	Q
2/13	0.5967(49)	0.8439(99)	0.27
3/13	0.5867(61)	0.8340(138)	0.70
4/13	0.5912(67)	0.8485(217)	0.77
5/13	0.5934(79)	0.8583(333)	0.80
6/13	0.5923(95)	0.8406(479)	0.67
7/13	0.5844(131)	0.8148(708)	0.56
8/13	0.5802(129)	0.8412(1223)	0.67
9/13	0.5896(123)	1.557(546)	0.49
10/13*			
11/13*			

Table B.156: Matrix fit to the ${}^3P_{2E}$ channel, yz component. *Mass becoming negative.

t_{min}/t_{max}	aE_1	aE_2	Q
2/13	0.5862(52)	0.9398(108)	0.16
3/13	0.5880(65)	0.9092(155)	0.44
4/13	0.5907(78)	0.9086(239)	0.33
5/13	0.5953(90)	0.9564(421)	0.39
6/13	0.5948(122)	0.9225(716)	0.26
7/13	0.5908(151)	0.9381(1182)	0.14
8/13	0.6293(491)	0.8205(2275)	0.17
9/13	0.6217(236)	1.346(556)	0.25
10/13	0.6170(449)	1.107(1303)	7.4×10^{-2}

Table B.157: Vector fit to the ${}^3P_{2T}$ channel.

t_{min}/t_{max}	aE_1	aE_2	Q
2/13	0.5928(62)	0.9377(129)	0.38
3/13	0.6008(78)	0.9087(193)	0.80
4/13	0.6040(93)	0.9225(312)	0.75
5/13	0.6061(118)	0.9364(523)	0.62
6/13	0.6182(178)	0.8869(922)	0.60
7/13	0.6174(189)	0.9769(1635)	0.47
8/13	0.6674(752)	0.8983(3341)	0.76
9/13	0.6468(293)	1.718(1208)	0.80
10/13	0.6357(476)	1.238(2508)	0.52

Table B.158: Vector fit to the ${}^3P_{2T}$ channel, xy component.

t_{min}/t_{max}	aE_1	aE_2	Q
2/13	0.5828(59)	0.9474(120)	0.23
3/13	0.5836(74)	0.9149(181)	0.41
4/13	0.5861(91)	0.9136(281)	0.29
5/13	0.5940(101)	0.9861(546)	0.48
6/13	0.5967(145)	0.9241(928)	0.37
7/13	0.5931(218)	0.8632(1478)	0.24
8/13	0.6276(657)	0.8037(2919)	0.18
9/13	0.6155(284)	1.279(609)	0.14
10/13	0.6099(697)	0.9684(13661)	3.6×10^{-2}

Table B.159: Vector fit to the ${}^3P_{2T}$ channel, xz component.

t_{min}/t_{max}	aE_1	aE_2	Q
2/13	0.5793(60)	0.9331(121)	0.26
3/13	0.5799(76)	0.9015(176)	0.47
4/13	0.5818(93)	0.8942(269)	0.34
5/13	0.5849(106)	0.9579(467)	0.46
6/13	0.5737(138)	0.9396(786)	0.43
7/13	0.5652(179)	0.9598(1314)	0.31
8/13	0.5886(351)	0.8233(2314)	0.27
9/13	0.6016(276)	1.301(570)	0.54
10/13*			

Table B.160: Vector fit to the ${}^3P_{2T}$ channel, yz component. *Mass becoming negative.

t_{min}/t_{max}	aE_1	aE_2	Q
2/13*			
3/13**	0.02006(8)	3.057(411)	0.00
4/13	0.01868(11)	0.7896(207)	5.7×10^{-23}
5/13	0.01857(12)	0.8839(211)	4.8×10^{-18}
6/13	0.01833(14)	0.6863(239)	2.0×10^{-3}
7/13	0.01848(17)	0.5765(395)	2.5×10^{-2}
8/13	0.01871(24)	0.4135(559)	0.23
9/13	0.01908(32)	0.3666(794)	0.70
10/13	0.01905(38)	0.3964(1278)	0.35

Table B.161: Vector fit to the kinetic ${}^3S_1$ mass, with $(a\mathbf{p})^2$=1. *Mass becoming negative, **bad fit.

t_{min}/t_{max}	aE_1	aE_2	Q
2/13*			
3/13**	0.04033(18)	3.079(410)	0.00
4/13	0.03730(23)	0.8077(205)	4.7×10^{-23}
5/13	0.03710(25)	0.8971(211)	1.1×10^{-18}
6/13	0.03656(30)	0.7003(232)	1.9×10^{-3}
7/13	0.03690(37)	0.5906(383)	3.8×10^{-2}
8/13	0.03738(50)	0.4432(561)	0.25
9/13	0.03814(65)	0.4030(819)	0.72
10/13	0.03810(79)	0.4301(1327)	0.37

Table B.162: Vector fit to the kinetic $^3S_1$ mass, with $(a\mathbf{p})^2$=2. *Mass becoming negative, **bad fit.

t_{min}/t_{max}	aE_1	aE_2	Q
2/13*			
3/13**	0.06084(27)	3.102(412)	0.00
4/13	0.05586(37)	0.8273(204)	6.1×10^{-23}
5/13	0.05558(39)	0.9125(210)	4.8×10^{-19}
6/13	0.05469(48)	0.7156(228)	2.0×10^{-3}
7/13	0.05527(60)	0.6085(378)	5.7×10^{-2}
8/13	0.05600(80)	0.4760(574)	0.26
9/13	0.05718(100)	0.4428(872)	0.71
10/13	0.05716(123)	0.4667(1427)	0.36

Table B.163: Vector fit to the kinetic $^3S_1$ mass, with $(a\mathbf{p})^2$=3. *Mass becoming negative, **bad fit.

t_{min}/t_{max}	aE_1	aE_2	Q
2/13*			
3/13**	0.08146(37)	3.124(415)	0.00
4/13	0.07425(51)	0.8377(199)	4.2×10^{-23}
5/13	0.07388(54)	0.9240(209)	3.1×10^{-19}
6/13	0.07257(67)	0.7287(226)	8.2×10^{-4}
7/13	0.07322(85)	0.6244(378)	1.4×10^{-2}
8/13	0.07431(120)	0.4476(534)	0.34
9/13	0.07594(151)	0.4160(777)	0.73
10/13	0.07563(177)	0.4673(1317)	0.43

Table B.164: Vector fit to the kinetic $^3S_1$ mass, with $(a\mathbf{p})^2$=4. *Mass becoming negative, **bad fit.

t_{min}/t_{max}	aE_1	aE_2	Q
2/13*			
3/13**	0.1026(5)	3.148(414)	0.00
4/13	0.09274(67)	0.8571(197)	2.1×10^{-23}
5/13	0.09236(71)	0.9356(209)	2.2×10^{-20}
6/13	0.09055(89)	0.7418(217)	8.8×10^{-4}
7/13	0.09151(113)	0.6378(363)	3.1×10^{-2}
8/13	0.09285(155)	0.4888(540)	0.35
9/13	0.09495(191)	0.4631(822)	0.76
10/13	0.09465(225)	0.5158(1417)	0.46

Table B.165: Vector fit to the kinetic $^3S_1$ mass, with $(a\mathbf{p})^2$=5. *Mass becoming negative, **bad fit.

t_{min}/t_{max}	aE_1	aE_2	Q
2/13*			
3/13*			
4/13	0.1117(9)	0.8793(199)	4.2×10^{-23}
5/13	0.1109(9)	0.9539(209)	1.9×10^{-20}
6/13	0.1084(11)	0.7582(215)	1.6×10^{-3}
7/13	0.1098(15)	0.6603(366)	6.8×10^{-2}
8/13	0.1113(20)	0.5320(573)	0.35
9/13	0.1139(23)	0.5147(935)	0.76
10/13	0.1136(28)	0.5683(1645)	0.44

Table B.166: Vector fit to the kinetic $^3S_1$ mass, with $(a\mathbf{p})^2$=6. *Mass becoming negative.

t_{min}/t_{max}	aE_1	aE_2	Q
2/13*			
3/13**	0.1681(9)	3.227(430)	0.00
4/13	0.1480(12)	0.9161(201)	2.7×10^{-23}
5/13	0.1479(13)	0.9877(211)	4.3×10^{-21}
6/13	0.1439(17)	0.7858(215)	9.9×10^{-4}
7/13	0.1458(22)	0.6885(373)	7.5×10^{-2}
8/13	0.1478(30)	0.5637(594)	0.38
9/13	0.1515(35)	0.5588(1023)	0.72
10/13	0.1509(39)	0.6679(2022)	0.47

Table B.167: Vector fit to the kinetic $^3S_1$ mass, with $(a\mathbf{p})^2$=8. *Mass becoming negative, **bad fit.

t_{min}/t_{max}	aE_1	aE_2	Q
2/13*			
3/13**	0.1903(10)	3.254(440)	0.00
4/13	0.1662(15)	0.9430(209)	4.3×10^{-22}
5/13	0.1664(16)	1.017(21)	1.7×10^{-19}
6/13	0.1612(21)	0.8059(222)	4.2×10^{-3}
7/13	0.1638(26)	0.7246(401)	0.17
8/13	0.1670(32)	0.7072(877)	0.14
9/13	0.1700(40)	0.6271(1308)	0.76
10/13	0.1695(45)	0.7529(2768)	0.48

Table B.168: Vector fit to the kinetic $^3S_1$ mass, with $(a\mathbf{p})^2$=9. *Mass becoming negative, **bad fit.

t_{min}/t_{max}	aE_1	aE_2	Q
2/13*			
3/13*			
4/13	0.2198(22)	1.015(24)	1.9×10^{-19}
5/13	0.2214(24)	1.101(22)	1.7×10^{-14}
6/13	0.2115(33)	0.8564(266)	3.6×10^{-2}
7/13	0.2166(42)	0.8158(539)	0.41
8/13	0.2179(61)	0.6906(1028)	0.51
9/13	0.2242(60)	0.7968(2450)	0.77
10/13	0.2234(68)	1.045(670)	0.49

Table B.169: Vector fit to the kinetic $^3S_1$ mass, with $(a\mathbf{p})^2$=12. *Mass becoming negative.

B.3.2 Wavefunction at the Origin for aM_b=1.8

t_{min}/t_{max}	$\psi_0(0)$
3/13	0.1840(52)
4/13	0.1859(61)
5/13	0.1930(72)
6/13	0.203(12)
7/13	0.212(20)
8/13	16(3500)

Table B.170: Wavefunction at the origin for the lattice 1^1S_0 channel.

t_{min}/t_{max}	$\psi_0(0)$
2/13	0.1483(45)
3/13	0.1544(50)
4/13	0.1553(57)
5/13	0.1606(66)
6/13	0.175(14)
7/13	0.176(20)
8/13	0.19(10)
9/13	0.165(11)

Table B.171: Wavefunction at the origin for the lattice 1^3S_1 channel.

B.3.3 Lattice Splittings for aM_b=1.8

t_{min}/t_{max}	$aE(1^3S_1 - 1^1S_0)$	$aE(2^3S_1 - 2^1S_0)$	$aE(3^3S_1 - 3^1S_0)$
2/13	0.02283(36)	0.0185(23)	0.0107(54)
3/13	0.02247(38)	0.0170(37)	0.0099(81)
4/13	0.02254(41)	0.0167(57)	-0.015(19)
5/13	0.02238(40)	-0.011(17)	0.007(38)
6/13	0.02243(42)	0.0003(200)	-0.015(78)
7/13	0.02234(66)	0.0009(460)	0.036(22)
8/13	0.04(26)	0.030(44)	0.042(39)
9/13	0.025(23)	0.06(21)	0.045(69)
10/13	0.0235(38)	0.12(19)	0.25(42)

Table B.172: Results from the $3e3s$ matrix fit.

t_{min}/t_{max}	$aE(1^1P_1 - 1^3P_0)$	$aE(2^1P_1 - 2^3P_0)$
2/13	0.0147(15)	0.0188(29)
3/13	0.0131(18)	0.0139(42)
4/13	0.0141(22)	0.0144(72)
5/13	0.0140(27)	0.021(12)
6/13	0.0134(33)	0.007(16)
7/13	0.0113(46)	-0.008(24)
8/13	0.0078(51)	-0.050(53)
9/13	0.016(11)	-1.0(18)

Table B.173: Results from the matrix fit.

t_{min}/t_{max}	$aE(1^3P_{2E} - 1^1P_1)$	$aE(2^3P_{2E} - 2^1P_1)$
2/13	0.0062(10)	0.0104(19)
3/13	0.0051(13)	0.0070(28)
4/13	0.0061(15)	0.0084(48)
5/13	0.0065(19)	0.0110(84)
6/13	0.0064(24)	0.005(12)
7/13	0.0066(39)	-0.012(18)
8/13	0.0086(37)	-0.010(38)
9/13	0.0098(78)	-0.3(14)

Table B.174: Results from the matrix fit.

t_{min}/t_{max}	$aE(1^3\overline{P} - 1^1P_1)$	$aE(2^3\overline{P} - 2^1P_1)$
2/13	0.00068(97)	0.0005(20)
3/13	0.0021(13)	-0.0010(31)
4/13	0.0032(18)	-0.0040(51)
5/13	0.0039(22)	-0.0025(90)
6/13	0.0065(30)	-0.018(16)
7/13	0.0066(39)	-0.027(28)
8/13	0.0089(92)	-0.003(44)
9/13	0.0076(52)	-0.04(14)
10/13	0.009(12)	0.04(31)

Table B.175: Results from the vector fit.

t_{min}/t_{max}	$\frac{2^3S_1-1^3S_1}{1^1P_1-1^3S_1}$
2/13	1.403(29)
3/13	1.405(34)
4/13	1.478(51)
5/13	1.374(63)
6/13	1.311(78)
7/13	1.26(10)
8/13	1.38(17)
9/13	1.32(27)

Table B.176: Results from the matrix fit.

t_{min}/t_{max}	$\frac{1^3P_{2E}-1^1P_1}{1^1P_1-1^3P_0}$
2/13	0.418(77)
3/13	0.39(10)
4/13	0.43(11)
5/13	0.46(15)
6/13	0.48(20)
7/13	0.58(36)
8/13	1.13(80)
9/13	0.61(70)

Table B.177: Results from the matrix fit.

B.3.4 Lattice State Fits for aM_b=2.1

t_{min}/t_{max}	aE_1	aE_2	aE_3	Q
2/11	0.4063(12)	0.6793(64)	0.8293(181)	1.2×10^{-2}
3/11	0.4048(12)	0.6712(87)	0.8167(288)	9.1×10^{-2}
4/11	0.4050(13)	0.6830(101)	0.8873(577)	0.10
5/11	0.4048(13)	0.6645(230)	0.7856(735)	0.26
6/11	0.4043(14)	0.6816(215)	0.9498(1562)	0.48
7/11	0.4037(16)	0.6774(370)	0.6923(2381)	0.22
8/11	0.4040(17)	0.6527(364)	0.9134(5001)	0.13
9/11	0.3979(832)	0.4489(6190)	0.6699(1500)	3.6×10^{-2}

Table B.178: Matrix fit to the $^3S_1$ channel.

t_{min}/t_{max}	aE_1	aE_2	aE_3	Q
2/11	0.3859(10)	0.6644(60)	0.8231(197)	4.8×10^{-2}
3/11	0.3848(11)	0.6572(80)	0.8100(313)	0.15
4/11	0.3849(11)	0.6690(93)	0.8970(623)	0.18
5/11	0.3841(14)	0.6642(144)	0.8715(999)	0.16
6/11	0.3843(12)	0.6732(177)	0.9459(1691)	0.49
7/11	0.3837(14)	0.5928(2413)	0.6633(195)	0.25
8/11	0.3839(14)	0.6435(299)	1.115(671)	0.14
9/11*				

Table B.179: Matrix fit to the $^1S_0$ channel. *Fitted lattice state energy becomi ng negative.

t_{min}/t_{max}	aE_1	aE_2	Q
2/13	0.6120(34)	0.8391(88)	0.21
3/13	0.6057(40)	0.8374(127)	0.67
4/13	0.6095(43)	0.8706(205)	0.93
5/13	0.6070(51)	0.8482(301)	0.86
6/13	0.6036(63)	0.8203(446)	0.80
7/13	0.5978(91)	0.7773(618)	0.71
8/13	0.5971(94)	0.8415(1072)	0.59
9/13	0.6110(104)	1.161(253)	0.60
10/13	0.5760(1689)	0.6275(973)	0.77

Table B.180: Matrix fit to the $^1P_1$ channel.

t_{min}/t_{max}	aE_1	aE_2	Q
2/13	0.6106(42)	0.8382(97)	0.45
3/13	0.6039(50)	0.8333(136)	0.76
4/13	0.6090(53)	0.8664(218)	0.95
5/13	0.6088(63)	0.8571(329)	0.90
6/13	0.6061(76)	0.8304(461)	0.85
7/13	0.6004(108)	0.7986(652)	0.76
8/13	0.5989(113)	0.8432(1106)	0.68
9/13	0.6087(112)	1.082(248)	0.58
10/13	0.5988(988)	0.6561(1933)	0.79
11/13	0.5954(475)	0.7604(3767)	0.55

Table B.181: Matrix fit to the $^1P_1$ channel in the x direction.

t_{min}/t_{max}	aE_1	aE_2	Q
2/13	0.6106(42)	0.8382(97)	0.45
3/13	0.6039(50)	0.8333(136)	0.76
4/13	0.6090(53)	0.8664(218)	0.95
5/13	0.6088(63)	0.8571(329)	0.90
6/13	0.6061(76)	0.8304(461)	0.85
7/13	0.6004(108)	0.7986(652)	0.76
8/13	0.5989(113)	0.8432(1106)	0.68
9/13	0.6087(112)	1.082(248)	0.58
10/13	0.5988(988)	0.6561(1933)	0.79
11/13	0.5954(475)	0.7604(3767)	0.55

Table B.182: Matrix fit to the $^1P_1$ channel in the y direction.

t_{min}/t_{max}	aE_1	aE_2	Q
2/13	0.6106(42)	0.8382(97)	0.45
3/13	0.6039(50)	0.8333(136)	0.76
4/13	0.6090(53)	0.8664(218)	0.95
5/13	0.6088(63)	0.8571(329)	0.90
6/13	0.6061(76)	0.8304(461)	0.85
7/13	0.6004(108)	0.7986(652)	0.76
8/13	0.5989(113)	0.8432(1106)	0.68
9/13	0.6087(112)	1.082(248)	0.58
10/13	0.5988(988)	0.6561(1933)	0.79
11/13	0.5954(475)	0.7604(3767)	0.55

Table B.183: Matrix fit to the $^1P_1$ channel in the z direction.

t_{min}/t_{max}	aE_1	aE_2	Q
2/13	0.5979(39)	0.8228(98)	0.42
3/13	0.5924(46)	0.8209(136)	0.70
4/13	0.5968(48)	0.8538(215)	0.93
5/13	0.5966(58)	0.8387(314)	0.88
6/13	0.5949(69)	0.8240(448)	0.76
7/13	0.5906(95)	0.8017(634)	0.68
8/13	0.5925(100)	0.8761(1132)	0.50
9/13	0.5964(102)	1.435(412)	0.45
10/13*			
11/13	0.4613(3490)	0.5898(254)	0.37

Table B.184: Matrix fit to the $^3P_0$ channel.

t_{min}/t_{max}	aE_1	aE_2	Q
2/13	0.5938(51)	0.9047(100)	0.49
3/13	0.5966(63)	0.8844(140)	0.72
4/13	0.6012(79)	0.8782(216)	0.66
5/13	0.6004(95)	0.8832(329)	0.51
6/13	0.5949(125)	0.8605(496)	0.40
7/13	0.5972(151)	0.8830(786)	0.25
8/13	0.6010(249)	0.8443(1369)	0.12
9/13	0.6015(164)	1.341(354)	0.36
10/13	0.5782(415)	1.207(811)	0.20

Table B.185: Vector fit to the $^3P_1$ channel.

t_{min}/t_{max}	aE_1	aE_2	Q
2/13	0.5909(59)	0.9053(115)	0.20
3/13	0.5938(75)	0.8734(164)	0.53
4/13	0.5970(92)	0.8741(258)	0.41
5/13	0.5983(111)	0.8848(390)	0.28
6/13	0.5860(149)	0.8521(568)	0.28
7/13	0.5810(165)	0.9340(932)	0.26
8/13	0.5943(225)	0.9392(1739)	0.16
9/13	0.5946(158)	1.785(674)	0.60
10/13*			

Table B.186: Vector fit to the $^3P_1$ channel, x component. *Mass becoming negative.

t_{min}/t_{max}	aE_1	aE_2	Q
2/13	0.5899(58)	0.9053(110)	0.65
3/13	0.5893(73)	0.8866(156)	0.70
4/13	0.5950(90)	0.8846(247)	0.66
5/13	0.5948(106)	0.9104(396)	0.57
6/13	0.5989(136)	0.9020(654)	0.42
7/13	0.6077(205)	0.8614(1075)	0.30
8/13	0.6050(300)	0.8561(1878)	0.15
9/13	0.6000(191)	1.458(482)	0.49
10/13*			

Table B.187: Vector fit to the $^3P_1$ channel, y component. *Mass becoming negative.

t_{min}/t_{max}	aE_1	aE_2	Q
2/13	0.5987(61)	0.9024(117)	0.39
3/13	0.6072(77)	0.8881(178)	0.61
4/13	0.6127(100)	0.8706(271)	0.57
5/13	0.6089(131)	0.8466(402)	0.48
6/13	0.6003(183)	0.8197(575)	0.39
7/13	0.6105(230)	0.8380(938)	0.26
8/13	0.6177(731)	0.7171(1714)	0.18
9/13	0.6106(436)	0.8755(2514)	9.3×10^{-2}
10/13	0.5397(1043)	0.9231(4121)	4.7×10^{-2}

Table B.188: Vector fit to the $^3P_1$ channel, z component.

t_{min}/t_{max}	aE_1	aE_2	Q
2/13	0.6159(44)	0.8471(98)	0.55
3/13	0.6083(53)	0.8403(138)	0.84
4/13	0.6142(56)	0.8738(221)	0.97
5/13	0.6142(67)	0.8655(337)	0.93
6/13	0.6112(82)	0.8335(468)	0.92
7/13	0.6048(125)	0.7867(635)	0.86
8/13	0.6040(129)	0.8237(1076)	0.79
9/13	0.6146(132)	0.9542(1980)	0.74
10/13	0.4969(2301)	0.6440(230)	0.91
11/13	0.6118(492)	0.7924(3704)	0.67

Table B.189: Matrix fit to the ${}^3P_{2E}$ channel.

t_{min}/t_{max}	aE_1	aE_2	Q
2/13	0.6206(47)	0.8524(105)	0.80
3/13	0.6149(57)	0.8428(148)	0.84
4/13	0.6226(60)	0.8806(240)	0.96
5/13	0.6246(73)	0.8667(369)	0.94
6/13	0.6249(86)	0.8572(540)	0.90
7/13	0.6221(133)	0.8015(737)	0.83
8/13	0.6224(137)	0.8526(1302)	0.69
9/13	0.6370(164)	0.9611(2277)	0.73
10/13	0.6374(1473)	0.6838(1716)	0.88
11/13	0.4359(3535)	0.6597(326)	0.65

Table B.190: Matrix fit to the ${}^3P_{2E}$ channel, xy component.

t_{min}/t_{max}	aE_1	aE_2	Q
2/13	0.6164(47)	0.8498(108)	0.36
3/13	0.6072(57)	0.8418(152)	0.75
4/13	0.6130(60)	0.8843(247)	0.95
5/13	0.6120(73)	0.8798(395)	0.88
6/13	0.6074(90)	0.8251(543)	0.89
7/13	0.6003(137)	0.7749(725)	0.80
8/13	0.5977(157)	0.8065(1156)	0.74
9/13	0.6097(155)	0.9389(2093)	0.73
10/13	0.5923(1056)	0.6889(1844)	0.84
11/13	0.6227(251)	1.864(1355)	0.91

Table B.191: Matrix fit to the ${}^3P_{2E}$ channel, xz component.

t_{min}/t_{max}	aE_1	aE_2	Q
2/13	0.6120(47)	0.8430(102)	0.37
3/13	0.6022(59)	0.8335(140)	0.82
4/13	0.6065(63)	0.8574(222)	0.92
5/13	0.6069(77)	0.8594(333)	0.94
6/13	0.6030(94)	0.8365(471)	0.91
7/13	0.5944(139)	0.8041(665)	0.88
8/13	0.5921(141)	0.8235(1108)	0.88
9/13	0.6005(133)	1.056(256)	0.73
10/13*			

Table B.192: Matrix fit to the $^3P_{2E}$ channel, yz component.

t_{min}/t_{max}	aE_1	aE_2	Q
2/13	0.6003(53)	0.9272(103)	0.21
3/13	0.6018(66)	0.8989(146)	0.53
4/13	0.6053(80)	0.8987(222)	0.43
5/13	0.6085(94)	0.9285(371)	0.39
6/13	0.6132(131)	0.8937(617)	0.29
7/13	0.6138(166)	0.8932(989)	0.16
8/13	0.6531(605)	0.8058(2085)	0.16
9/13	0.6373(259)	1.161(384)	0.16
10/13	0.6060(442)	1.170(851)	6.7×10^{-2}

Table B.193: Vector fit to the ${}^3P_{2T}$ channel.

tmin/tmax	aE_1	aE_2	Q
2/13	0.6075(63)	0.9231(123)	0.24
3/13	0.6165(80)	0.8960(182)	0.68
4/13	0.6193(97)	0.9070(284)	0.59
5/13	0.6206(126)	0.9066(456)	0.43
6/13	0.6371(193)	0.8716(797)	0.45
7/13	0.6438(223)	0.9303(1386)	0.36
8/13	0.6923(860)	0.8851(3045)	0.50
9/13	0.6660(319)	1.449(796)	0.39
10/13	0.6330(519)	1.431(1841)	0.25

Table B.194: Vector fit to the ${}^3P_{2T}$ channel, xy component.

t_{min}/t_{max}	aE_1	aE_2	Q
2/13	0.5971(59)	0.9358(116)	0.32
3/13	0.5966(74)	0.9066(171)	0.50
4/13	0.6002(92)	0.9066(261)	0.39
5/13	0.6081(106)	0.9533(477)	0.51
6/13	0.6163(155)	0.9020(810)	0.45
7/13	0.6219(271)	0.8274(1312)	0.31
8/13	0.6580(1056)	0.7738(2909)	0.22
9/13	0.6348(328)	1.117(430)	0.15
10/13	0.5857(996)	0.9772(8037)	6.2×10^{-2}

Table B.195: Vector fit to the ${}^3P_{2T}$ channel, xz component.

t_{min}/t_{max}	aE_1	aE_2	Q
2/13	0.5917(64)	0.9255(113)	0.38
3/13	0.5932(77)	0.8956(165)	0.64
4/13	0.5976(94)	0.8839(256)	0.57
5/13	0.5966(105)	0.9326(422)	0.60
6/13	0.5905(149)	0.8842(664)	0.52
7/13	0.5836(187)	0.8936(1060)	0.37
8/13	0.6180(548)	0.7733(2090)	0.37
9/13	0.6111(258)	1.216(423)	0.59
10/13	0.5997(367)	1.265(1079)	0.26

Table B.196: Vector fit to the ${}^3P_{2T}$ channel, yz component.

t_{min}/t_{max}	aE_1	aE_2	Q
2/13*			
3/13*			
4/13**	0.01753(8)	3.329(1209)	0.00
5/13	0.01632(10)	0.7875(184)	9.3×10^{-15}
6/13	0.01611(12)	0.7527(340)	1.3×10^{-12}
7/13	0.01620(14)	0.6449(254)	5.8×10^{-4}
8/13	0 01636(18)	0.5002(342)	0.18
9/13	0.01659(23)	0.4396(491)	0.62
10/13	0.01658(29)	0.4387(794)	0.27

Table B.197: Vector fit to the kinetic $^3S_1$ mass, with $(a\mathbf{p})^2$=1. *Mass becoming negative, **bad fit.

t_{min}/t_{max}	aE_1	aE_2	Q
2/13*			
3/13*			
4/13**	0.03525(17)	3.360(1235)	0.00
5/13	0.03259(21)	0.8019(181)	5.4×10^{-15}
6/13	0.03214(25)	0.7609(338)	7.9×10^{-13}
7/13	0.03237(30)	0.6588(249)	6.9×10^{-4}
8/13	0.03270(39)	0.5198(336)	0.18
9/13	0.03319(48)	0.4621(492)	0.62
10/13	0.03316(61)	0.4644(801)	0.27

Table B.198: Vector fit to the kinetic $^3S_1$ mass, with $(a\mathbf{p})^2$=2. *Mass becoming negative, **bad fit.

t_{min}/t_{max}	aE_1	aE_2	Q
2/13*			
3/13*			
4/13**	0.05319(26)	3.390(1261)	0.00
5/13	0.04883(34)	0.8173(180)	4.7×10^{-15}
6/13*			
7/13	0.04851(48)	0.6746(245)	9.1×10^{-4}
8/13	0.04901(62)	0.5405(335)	0.19
9/13	0.04978(77)	0.4855(501)	0.61
10/13	0.04974(96)	0.4903(820)	0.26

Table B.199: Vector fit to the kinetic $^3S_1$ mass, with $(a\mathbf{p})^2$=3. *Mass becoming negative, **bad fit.

t_{min}/t_{max}	aE_1	aE_2	Q
2/13*			
3/13*			
4/13**	0.07136(36)	3.437(1347)	0.00
5/13	0.06491(47)	0.8339(179)	6.3×10^{-15}
6/13	0.06385(56)	0.7821(338)	6.1×10^{-13}
7/13	0.06433(67)	0.6901(249)	1.8×10^{-4}
8/13	0.06502(88)	0.5386(331)	0.21
9/13	0.06595(110)	0.4782(475)	0.65
10/13	0.06580(140)	0.4851(791)	0.29

Table B.200: Vector fit to the kinetic $^3S_1$ mass, with $(a\mathbf{p})^2$=4. *Mass becoming negative, **bad fit.

t_{min}/t_{max}	aE_1	aE_2	Q
2/13**	0.09298(40)	1.611(192)	0.00
3/13*			
4/13**	0.08994(47)	3.476(1391)	0.00
5/13	0.08108(62)	0.8472(175)	2.6×10^{-15}
6/13	0.07965(74)	0.7877(334)	3.2×10^{-13}
7/13	0.08042(89)	0.7033(241)	2.9×10^{-4}
8/13	0.08129(117)	0.5627(325)	0.21
9/13	0.08254(146)	0.5057(479)	0.65
10/13	0.08237(183)	0.5190(807)	0.30

Table B.201: Vector fit to the kinetic $^3S_1$ mass, with $(a\mathbf{p})^2$=5. *Mass becoming negative, **bad fit.

t_{min}/t_{max}	aE_1	aE_2	Q
2/13**	0.1126(5)	1.561(174)	0.00
3/13*			
4/13**	0.1088(6)	3.501(1393)	0.00
5/13	0.09725(78)	0.8632(174)	3.5×10^{-15}
6/13	0.09542(94)	0.8029(331)	3.4×10^{-13}
7/13	0.09653(114)	0.7208(238)	5.8×10^{-4}
8/13	0.09750(149)	0.5874(327)	0.22
9/13	0.09910(185)	0.5334(503)	0.64
10/13	0.09894(231)	0.5516(856)	0.29

Table B.202: Vector fit to the kinetic $^3S_1$ mass, with $(a\mathbf{p})^2$=6. *Mass becoming negative, **bad fit.

t_{min}/t_{max}	aE_1	aE_2	Q
2/13**	0.1535(8)	1.447(140)	0.00
3/13*			
4/13**	0.1479(9)	3.511(1277)	0.00
5/13	0.1294(11)	0.8941(173)	3.6×10^{-15}
6/13	0.1266(14)	0.8236(333)	2.2×10^{-13}
7/13	0.1285(17)	0.7505(237)	4.9×10^{-4}
8/13	0.1297(23)	0.6186(329)	0.22
9/13	0.1318(28)	0.5640(520)	0.64
10/13	0.1315(35)	0.6036(939)	0.33

Table B.203: Vector fit to the kinetic $^3S_1$ mass, with $(a\mathbf{p})^2$=8. *Mass becoming negative, **bad fit.

t_{min}/t_{max}	aE_1	aE_2	Q
2/13**	0.1748(10)	1.384(125)	0.00
3/13*			
4/13**	0.1677(10)	3.616(1550)	0.00
5/13	0.1456(14)	0.9138(176)	3.3×10^{-14}
6/13	0.1424(17)	0.8549(331)	7.2×10^{-13}
7/13	0.1446(20)	0.7754(240)	1.5×10^{-3}
8/13	0.1456(27)	0.6452(348)	0.27
9/13	0.1482(34)	0.5949(586)	0.65
10/13	0.1480(42)	0.6405(1080)	0.35

Table B.204: Vector fit to the kinetic $^3S_1$ mass, with $(a\mathbf{p})^2$=9. *Mass becoming negative, **bad fit.

t_{min}/t_{max}	aE_1	aE_2	Q
2/13*			
3/13*			
4/13**	0.2295(15)	3.642(1479)	0.00
5/13	0.1936(21)	0.9723(195)	2.4×10^{-11}
6/13	0.1897(26)	0.9573(330)	6.0×10^{-11}
7/13	0.1925(32)	0.8475(271)	1.5×10^{-2}
8/13	0.1924(46)	0.7038(442)	0.45
9/13	0.1963(56)	0.6693(852)	0.69
10/13	0.1963(67)	0.7651(1811)	0.43

Table B.205: Vector fit to the kinetic $^3S_1$ mass, with $(a\mathbf{p})^2$=12. *Mass becoming negative, **bad fit.

B.3.5 Wavefunction at the Origin for aM_b=2.1

t_{min}/t_{max}	$\psi_0(0)$
2/11	0.1894(63)
3/11	0.1940(69)
4/11	0.1951(82)
5/11	0.206(11)
6/11	0.237(28)
7/11	0.42(29)

Table B.206: Wavefunction at the origin for the lattice 1^1S_0 channel.

t_{min}/t_{max}	$\psi_0(0)$
2/11	0.1628(60)
3/11	0.1692(71)
4/11	0.1691(82)
5/11	0.178(10)
6/11	0.231(52)
7/11	0.6(21)

Table B.207: Wavefunction at the origin for the lattice 1^3S_1 channel.

B.3.6 Lattice Splittings for aM_b=2.1

t_{min}/t_{max}	$aE(1^3S_1 - 1^1S_0)$	$aE(2^3S_1 - 2^1S_0)$	$aE(3^3S_1 - 3^1S_0)$
2/11	0.02042(32)	0.0149(15)	0.0062(42)
3/11	0.02000(34)	0.0140(20)	0.0067(61)
4/11	0.02006(36)	0.0140(25)	-0.010(13)
5/11	0.0200(18)	0.007(19)	-0.002(220)
6/11	0.01998(40)	0.0084(69)	0.004(45)
7/11	0.02008(50)	-0.003(92)	0.021(42)
8/11	0.02014(78)	0.009(17)	-0.2(11)

Table B.208: Results from the $3e3s$ matrix fit.

t_{min}/t_{max}	$aE(1^1P_1 - 1^3P_0)$	$aE(2^1P_1 - 2^3P_0)$
2/13	0.0141(29)	0.0163(71)
3/13	0.0132(34)	0.0165(97)
4/13	0.0127(36)	0.017(16)
5/13	0.0104(42)	0.010(23)
6/13	0.0087(51)	-0.004(31)
7/13	0.0072(72)	-0.024(37)
8/13	0.0046(73)	-0.035(72)
9/13	0.0139(86)	-0.50(66)
10/13	0.024(16)	-0.20(34)

Table B.209: Results from the matrix fit.

t_{min}/t_{max}	$aE(1^3P_{2E} - 1^1P_1)$	$aE(2^3P_{2E} - 2^1P_1)$
2/13	0.0039(31)	0.0080(68)
3/13	0.0027(38)	0.0028(94)
4/13	0.0048(40)	0.003(16)
5/13	0.0072(48)	0.017(23)
6/13	0.0076(59)	0.013(30)
7/13	0.0070(87)	0.009(36)
8/13	0.0068(88)	-0.018(66)
9/13	0.004(10)	-0.21(36)
10/13	0.09(14)	0.033(27)

Table B.210: Results from the matrix fit.

t_{min}/t_{max}	$aE(1^3\overline{P} - 1^1P_1)$	$aE(2^3\overline{P} - 2^1S_0)$
2/13	0.00064(85)	0.0007(17)
3/13	0.0018(11)	-0.0004(26)
4/13	0.0027(16)	-0.0022(42)
5/13	0.0034(20)	-0.0006(71)
6/13	0.0060(28)	-0.012(12)
7/13	0.0065(39)	-0.022(21)
8/13	0.010(12)	-0.010(51)
9/13	0.0067(50)	-0.06(11)
10/13	0.0057(77)	0.03(19)

Table B.211: Results from the vector fit.

t_{min}/t_{max}	$\frac{2^3S_1-1^3S_1}{1^1P_1-1^3S_1}$
2/13	1.353(34)
3/13	1.349(43)
4/13	1.438(62)
5/13	1.348(75)
6/13	1.318(93)
7/13	1.24(11)
8/13	1.32(18)
9/13	1.22(25)
10/13	-56(2.9 × 10^4)

Table B.212: Results from the matrix fit.

t_{min}/t_{max}	$\frac{1^3P_{2E}-1^1P_1}{1^1P_1-1^3P_0}$
2/13	0.28(27)
3/13	0.20(34)
4/13	0.38(41)
5/13	0.70(71)
6/13	0.9(12)
7/13	1.0(21)
8/13	1.6(45)
9/13	0.29(83)

Table B.213: Results from the matrix fit.

B.4 Lattice Results for the Dynamical Calculations with κ=0.134

B.4.1 Lattice State Fits for aM_b=1.8

t_{min}/t_{max}	aE_1	aE_2	aE_3	Q
2/13	0.3878(11)	0.6651(72)	0.8028(167)	4.0×10^{-5}
3/13	0.3876(11)	0.6646(92)	0.8222(290)	2.9×10^{-4}
4/13	0.3879(11)	0.6743(118)	0.8357(494)	4.8×10^{-4}
5/13	0.3878(12)	0.6483(247)	0.7663(627)	2.0×10^{-3}
6/13	0.3872(12)	0.6367(511)	0.7015(525)	1.5×10^{-3}
7/13	0.3872(13)	0.6537(649)	0.6819(980)	3.0×10^{-3}
8/13	0.3867(15)	0.6627(341)	3.009(2941)	4.9×10^{-3}
9/13	0.3860(15)	0.6700(369)	0.9476(454)	1.8×10^{-2}
10/13	0.3873(15)	0.7512(704)	0.9608(5707)	1.2×10^{-2}
11/13	0.3829(45)	0.5409(774)	1.919(2324)	6.0×10^{-2}

Table B.214: Matrix fit to the $^3S_1$ channel.

t_{min}/t_{max}	aE_1	aE_2	aE_3	Q
2/13	0.3662(9)	0.6493(64)	0.7897(185)	8.3×10^{-5}
3/13	0.3660(10)	0.6490(82)	0.8065(307)	2.6×10^{-4}
4/13	0.3662(10)	0.6566(109)	0.7996(499)	3.5×10^{-4}
5/13	0.3661(10)	0.6293(251)	0.7303(571)	1.7×10^{-3}
6/13	0.3656(11)	0.6185(475)	0.6789(498)	8.7×10^{-4}
7/13	0.3657(11)	0.6283(484)	0.6680(1037)	2.7×10^{-3}
8/13	0.3653(13)	0.6362(303)	2.959(2606)	6.5×10^{-3}
9/13	0.3649(13)	0.6478(327)	0.8919(4018)	1.7×10^{-2}
10/13	0.3655(13)	0.6995(557)	0.9277(5268)	1.0×10^{-2}
11/13	0.3618(36)	0.5111(663)	1.977(2557)	0.10

Table B.215: Matrix fit to the $^1S_0$ channel.

t_{min}/t_{max}	aE_1	aE_2	Q
2/13	0.5921(41)	0.8310(94)	1.1×10^{-2}
3/13	0.5921(47)	0.8307(138)	7.1×10^{-3}
4/13	0.5918(55)	0.8144(194)	1.8×10^{-2}
5/13	0.5889(72)	0.7841(270)	1.8×10^{-2}
6/13	0.5843(86)	0.7695(372)	9.7×10^{-3}
7/13	0.5840(102)	0.7937(584)	8.5×10^{-3}
8/13	0.5912(82)	0.9066(1168)	2.2×10^{-2}
9/13	0.5734(142)	1.021(231)	0.22
10/13	0.5817(192)	0.8085(3066)	0.17
11/13	0.5157(1992)	0.7361(4318)	0.44

Table B.216: Matrix fit to the $^1P_1$ channel.

t_{min}/t_{max}	aE_1	aE_2	Q
2/13	0.5843(49)	0.9167(100)	1.4×10^{-2}
3/13	0.5839(60)	0.8918(145)	2.4×10^{-2}
4/13	0.5831(76)	0.8571(217)	3.2×10^{-2}
5/13	0.5746(96)	0.8383(303)	2.9×10^{-2}
6/13	0.5638(143)	0.7948(402)	2.8×10^{-2}
7/13	0.5513(163)	0.8692(642)	6.1×10^{-2}
8/13	0.5233(402)	0.7199(747)	9.3×10^{-2}
9/13	0.5757(270)	0.9083(1936)	0.16
10/13	0.5598(3381)	0.6024(4229)	0.18

Table B.217: Vector fit to the $^1P_1$ channel in the x direction.

t_{min}/t_{max}	aE_1	aE_2	Q
2/13	0.5843(49)	0.9167(100)	1.4×10^{-2}
3/13	0.5839(60)	0.8918(145)	2.4×10^{-2}
4/13	0.5831(76)	0.8570(217)	3.2×10^{-2}
5/13	0.5746(96)	0.8383(303)	2.9×10^{-2}
6/13	0.5638(143)	0.7948(402)	2.8×10^{-2}
7/13	0.5513(163)	0.8691(642)	6.1×10^{-2}
8/13	0.5233(402)	0.7199(747)	9.3×10^{-2}
9/13	0.5757(270)	0.9073(1933)	0.16
10/13	0.5622(3436)	0.6036(4419)	0.18

Table B.218: Vector fit to the ${}^1P_1$ channel in the y direction.

t_{min}/t_{max}	aE_1	aE_2	Q
2/13	0.5843(49)	0.9167(100)	1.4×10^{-2}
3/13	0.5839(60)	0.8918(145)	2.4×10^{-2}
4/13	0.5831(76)	0.8570(217)	3.2×10^{-2}
5/13	0.5746(96)	0.8383(303)	2.9×10^{-2}
6/13	0.5638(143)	0.7948(402)	2.8×10^{-2}
7/13	0.5513(163)	0.8691(642)	6.1×10^{-2}
8/13	0.5233(402)	0.7199(747)	9.3×10^{-2}
9/13	0.5757(270)	0.9073(1933)	0.16
10/13	0.5622(3436)	0.6036(4419)	0.18

Table B.219: Vector fit to the ${}^1P_1$ channel in the z direction.

t_{min}/t_{max}	aE_1	aE_2	Q
2/13	0.5722(51)	0.8803(104)	5.9×10^{-2}
3/13	0.5722(62)	0.8620(149)	5.7×10^{-2}
4/13	0.5704(80)	0.8147(217)	0.16
5/13	0.5664(105)	0.7980(305)	0.10
6/13	0.5566(172)	0.7349(404)	0.19
7/13	0.5544(202)	0.7639(620)	0.10
8/13	0.5213(534)	0.6478(695)	0.16
9/13	0.5610(422)	0.7580(1595)	0.10
10/13	0.5358(2656)	0.5993(2855)	8×10^{-2}

Table B.220: Vector fit to the $^3P_0$ channel.

t_{min}/t_{max}	aE_1	aE_2	Q
2/13	0.5830(50)	0.9064(101)	4.5×10^{-2}
3/13	0.5821(62)	0.8804(145)	8.8×10^{-2}
4/13	0.5803(78)	0.8455(217)	0.12
5/13	0.5747(98)	0.8316(306)	8.3×10^{-2}
6/13	0.5651(150)	0.7817(408)	9.4×10^{-2}
7/13	0.5524(168)	0.8464(634)	0.14
8/13	0.5205(363)	0.7459(787)	0.16
9/13	0.5663(270)	0.9092(1908)	0.20
10/13	0.2190(3241)	0.6050(515)	0.45

Table B.221: Vector fit to the $^3P_1$ channel.

$tmin/tmax$	aE_1	aE_2	Q
2/13	0.5851(60)	0.9028(120)	0.10
3/13	0.5846(76)	0.8707(172)	0.20
4/13	0.5889(101)	0.8446(265)	0.19
5/13	0.5902(140)	0.8134(383)	0.14
6/13	0.5762(196)	0.7825(523)	0.12
7/13	0.5712(196)	0.8697(852)	0.10
8/13	0.5123(559)	0.7204(886)	0.24
9/13	0.5738(289)	1.004(272)	0.40
10/13	0.4751(12300)	0.5143(8194)	0.68

Table B.222: Vector fit to the $^3P_1$ channel, x component.

t_{min}/t_{max}	aE_1	aE_2	Q
2/13	0.5831(60)	0.9068(117)	0.14
3/13	0.5807(75)	0.8819(169)	0.19
4/13	0.5786(95)	0.8425(250)	0.25
5/13	0.5727(116)	0.8494(371)	0.17
6/13	0.5679(185)	0.7740(505)	0.22
7/13	0.5339(252)	0.7954(678)	0.36
8/13	0.5255(432)	0.7391(975)	0.22
9/13	0.5702(359)	0.9114(2349)	0.19
10/13	0.4545(1888)	0.7327(2602)	0.13

Table B.223: Vector fit to the $^3P_1$ channel, y component.

t_{min}/t_{max}	aE_1	aE_2	Q
2/13	0.5791(57)	0.9058(116)	0.49
3/13	0.5794(69)	0.8824(173)	0.56
4/13	0.5767(88)	0.8512(261)	0.60
5/13	0.5676(111)	0.8435(375)	0.59
6/13	0.5601(168)	0.8013(546)	0.53
7/13	0.5568(173)	0.9004(912)	0.58
8/13	0.5320(341)	0.8200(1331)	0.52
9/13	0.5578(301)	0.9656(2964)	0.35
10/13	0.0806(5249)	0.6019(551)	0.54

Table B.224: Vector fit to the $^3P_1$ channel, z component.

t_{min}/t_{max}	aE_1	aE_2	Q
2/13	0.5963(44)	0.8388(96)	4.3×10^{-3}
3/13	0.5960(51)	0.8358(139)	2.3×10^{-3}
4/13	0.5960(59)	0.8191(194)	7.1×10^{-3}
5/13	0.5934(76)	0.7973(277)	4.2×10^{-3}
6/13	0.5889(86)	0.7885(398)	2.7×10^{-3}
7/13	0.5895(97)	0.8193(652)	1.9×10^{-3}
8/13	0.5914(82)	0.9348(1280)	2.5×10^{-2}
9/13	0.5754(110)	1.442(458)	0.22
10/13	0.5815(128)	2.262(1995)	0.45

Table B.225: Matrix fit to the ${}^3P_{2E}$ channel.

t_{min}/t_{max}	aE_1	aE_2	Q
2/13	0.5959(48)	0.8343(99)	0.15
3/13	0.5965(56)	0.8335(146)	8.8×10^{-2}
4/13	0.5966(67)	0.8170(204)	0.10
5/13	0.5953(86)	0.8081(305)	6.4×10^{-2}
6/13	0.5907(96)	0.8284(473)	8.0×10^{-2}
7/13	0.5970(102)	0.9145(829)	7.4×10^{-2}
8/13	0.6004(100)	1.047(178)	0.12
9/13	0.5872(130)	1.893(903)	0.27
10/13	0.5795(166)	2.449(3494)	0.33
11/13*			

Table B.226: Matrix fit to the ${}^3P_{2E}$ channel, xy component. *Mass becoming negative.

t_{min}/t_{max}	aE_1	aE_2	Q
2/13	0.5943(49)	0.8341(102)	5.5×10^{-3}
3/13	0.5929(57)	0.8301(144)	2.5×10^{-3}
4/13	0.5912(65)	0.8108(202)	2.1×10^{-2}
5/13	0.5852(86)	0.7847(274)	1.4×10^{-2}
6/13	0.5794(97)	0.7527(372)	2.2×10^{-2}
7/13	0.5792(107)	0.7630(581)	1.9×10^{-2}
8/13	0.5745(97)	0.8894(1115)	0.14
9/13	0.5618(139)	1.098(282)	0.34
10/13	0.5722(157)	0.7580(2605)	0.43
11/13*			

Table B.227: Matrix fit to the ${}^3P_{2E}$ channel, xz component. *Mass becoming negative.

t_{min}/t_{max}	aE_1	aE_2	Q
2/13	0.5988(47)	0.8476(105)	4.5×10^{-4}
3/13	0.6005(54)	0.8494(156)	3.3×10^{-4}
4/13	0.6028(62)	0.8387(228)	1.3×10^{-3}
5/13	0.6035(79)	0.8032(329)	1.4×10^{-3}
6/13	0.5998(96)	0.7873(459)	3.5×10^{-4}
7/13	0.5976(115)	0.8117(755)	3.7×10^{-4}
8/13	0.6029(98)	0.9762(1605)	5.0×10^{-3}
9/13	0.5760(142)	1.278(407)	0.15
10/13*	0.5860(163)	2.876(3641)	0.35
11/13	0.5336(2975)	0.7483(7594)	0.63

Table B.228: Matrix fit to the ${}^3P_{2E}$ channel, yz component. *Mass becoming negative.

t_{min}/t_{max}	aE_1	aE_2	Q
2/13	0.5891(52)	0.9317(105)	6.7×10^{-3}
3/13	0.5884(63)	0.9064(156)	9.9×10^{-3}
4/13	0.5870(79)	0.8729(236)	1.0×10^{-2}
5/13	0.5740(100)	0.8604(333)	1.8×10^{-2}
6/13	0.5679(144)	0.8270(473)	9.8×10^{-3}
7/13	0.5544(150)	0.9741(831)	0.17
8/13	0.5416(260)	0.8862(1341)	0.10
9/13	0.5790(194)	1.218(377)	0.33
10/13	0.5864(3355)	0.6436(8619)	0.22

Table B.229: Vector fit to the ${}^3P_{2T}$ channel.

t_{min}/t_{max}	aE_1	aE_2	Q
2/13	0.5933(62)	0.9176(125)	6.2×10^{-2}
3/13	0.5943(79)	0.8892(181)	9.0×10^{-2}
4/13	0.5920(100)	0.8487(266)	0.12
5/13	0.5749(130)	0.8258(365)	0.22
6/13	0.5781(197)	0.7965(549)	0.14
7/13	0.5602(196)	0.9204(852)	0.61
8/13	0.5487(261)	0.9696(1602)	0.49
9/13	0.5727(194)	1.581(655)	0.61
10/13	0.5821(3872)	0.6430(12180)	0.42

Table B.230: Vector fit to the ${}^3P_{2T}$ channel, xy component.

t_{min}/t_{max}	aE_1	aE_2	Q
2/13	0.5815(60)	0.9382(121)	4.8×10^{-2}
3/13	0.5773(72)	0.9211(179)	4.6×10^{-2}
4/13	0.5765(92)	0.8854(284)	4.3×10^{-2}
5/13	0.5654(109)	0.9023(434)	5.0×10^{-2}
6/13	0.5556(159)	0.8589(627)	3.1×10^{-2}
7/13	0.5352(184)	0.9939(1082)	0.19
8/13	0.5471(255)	0.9078(1886)	0.13
9/13	0.5708(196)	1.511(629)	0.22
10/13	0.5691(3970)	0.6230(11099)	9.2×10^{-2}

Table B.231: Vector fit to the ${}^3P_{2T}$ channel, xz component.

t_{min}/t_{max}	aE_1	aE_2	Q
2/13	0.5932(61)	0.9383(124)	2.0×10^{-2}
3/13	0.5953(75)	0.9066(191)	3.2×10^{-2}
4/13	0.5980(100)	0.8791(296)	2.3×10^{-2}
5/13	0.5855(132)	0.8475(411)	2.5×10^{-2}
6/13	0.5761(175)	0.8346(596)	1.2×10^{-2}
7/13	0.5721(155)	1.093(135)	6.7×10^{-2}
8/13	0.5199(586)	0.7822(1475)	0.15
9/13	0.6148(761)	0.8592(3938)	0.81
10/13	0.6592(5871)	0.7739(13548)	0.61

Table B.232: Vector fit to the ${}^3P_{2T}$ channel, yz component.

t_{min}/t_{max}	aE_1	aE_2	Q
2/13*			
3/13*			
4/13	0.01886(11)	0.8061(225)	4.9×10^{-21}
5/13	0.01869(12)	0.9015(219)	3.4×10^{-16}
6/13	0.01847(15)	0.6770(248)	0.16
7/13	0.01825(18)	0.5746(414)	0.71
8/13	0.01817(21)	0.5495(720)	0.61
9/13	0.01811(25)	0.5342(1197)	0.37
10/13	0.01808(38)	0.4505(1987)	0.13

Table B.233: Vector fit to the kinetic ${}^3S_1$ mass, with $(a\mathbf{p})^2$=1. *Mass becoming negative.

t_{min}/t_{max}	aE_1	aE_2	Q
2/13*			
3/13*			
4/13	0.03767(23)	0.8222(221)	3.9×10^{-21}
5/13	0.03737(26)	0.9151(218)	9.7×10^{-17}
6/13	0.03686(31)	0.6935(244)	0.12
7/13	0.03639(38)	0.5874(405)	0.61
8/13	0.03620(44)	0.5596(695)	0.50
9/13	0.03601(57)	0.5148(1104)	0.30
10/13	0.03594(93)	0.4092(1756)	9.9×10^{-2}

Table B.234: Vector fit to the kinetic $^3S_1$ mass, with $(a\mathbf{p})^2$=2. *Mass becoming negative.

t_{min}/t_{max}	aE_1	aE_2	Q
2/13*			
3/13*			
4/13	0.05645(36)	0.8400(219)	4.8×10^{-21}
5/13	0.05606(41)	0.9310(217)	5.6×10^{-17}
6/13	0.05519(48)	0.7107(242)	8.6×10^{-2}
7/13	0.05443(61)	0.6009(401)	0.52
8/13	0.05412(72)	0.5696(680)	0.40
9/13	0.05370(97)	0.5004(1042)	0.25
10/13	0.05360(168)	0.3859(1627)	8.0×10^{-2}

Table B.235: Vector fit to the kinetic $^3S_1$ mass, with $(a\mathbf{p})^2$=3. *Mass becoming negative.

t_{min}/t_{max}	aE_1	aE_2	Q
2/13*			
3/13*			
4/13	0.07504(50)	0.8441(212)	5.8×10^{-21}
5/13	0.07461(57)	0.9305(215)	1.3×10^{-17}
6/13	0.07327(68)	0.7169(234)	9.0×10^{-2}
7/13	0.07210(87)	0.6013(385)	0.68
8/13	0.07163(106)	0.5514(646)	0.61
9/13	0.07123(140)	0.5188(1033)	0.38
10/13	0.07118(216)	0.4527(1656)	0.13

Table B.236: Vector fit to the kinetic $^3S_1$ mass, with $(a\mathbf{p})^2$=4. *Mass becoming negative.

t_{min}/t_{max}	aE_1	aE_2	Q
2/13*			
3/13*			
4/13	0.09379(66)	0.8622(208)	4.0×10^{-21}
5/13	0.09339(75)	0.9461(215)	3.7×10^{-18}
6/13	0.09153(90)	0.7365(230)	5.6×10^{-2}
7/13	0.09002(115)	0.6205(379)	0.47
8/13	0.08939(141)	0.5718(629)	0.37
9/13	0.08840(205)	0.4910(941)	0.24
10/13	0.08830(351)	0.3975(1463)	7.8×10^{-2}

Table B.237: Vector fit to the kinetic $^3S_1$ mass, with $(a\mathbf{p})^2$=5. *Mass becoming negative.

t_{min}/t_{max}	aE_1	aE_2	Q
2/13*			
3/13*			
4/13	0.1126(8)	0.8836(209)	8.9×10^{-21}
5/13	0.1123(9)	0.9679(214)	8.0×10^{-18}
6/13	0.1098(11)	0.7570(233)	4.2×10^{-2}
7/13	0.1079(15)	0.6394(384)	0.34
8/13	0.1071(18)	0.5889(635)	0.24
9/13	0.1053(29)	0.4733(911)	0.18
10/13	0.1052(52)	0.3778(1432)	5.6×10^{-2}

Table B.238: Vector fit to the kinetic $^3S_1$ mass, with $(a\mathbf{p})^2$=6. *Mass becoming negative.

t_{min}/t_{max}	aE_1	aE_2	Q
2/13*			
3/13*			
4/13	0.1498(12)	0.9169(210)	5.6×10^{-20}
5/13	0.1501(14)	1.002(22)	3.7×10^{-17}
6/13	0.1458(17)	0.7913(263)	3.2×10^{-2}
7/13	0.1433(22)	0.6773(400)	0.17
8/13	0.1420(29)	0.6238(675)	9.2×10^{-2}
9/13	0.1379(54)	0.4541(931)	8.5×10^{-2}
10/13	0.1372(125)	0.3240(1412)	2.7×10^{-2}

Table B.239: Vector fit to the kinetic $^3S_1$ mass, with $(a\mathbf{p})^2$=8. *Mass becoming negative.

t_{min}/t_{max}	aE_1	aE_2	Q
2/13*			
3/13*			
4/13	0.1686(14)	0.9429(217)	7.0×10^{-19}
5/13	0.1693(16)	1.033(21)	2.1×10^{-15}
6/13	0.1639(20)	0.8149(248)	4.4×10^{-2}
7/13	0.1609(27)	0.6983(424)	0.18
8/13	0.1594(36)	0.6370(719)	0.10
9/13	0.1531(77)	0.4389(963)	0.12
10/13	0.1532(155)	0.3468(1530)	3.6×10^{-2}

Table B.240: Vector fit to the kinetic $^3S_1$ mass, with $(a\mathbf{p})^2$=9. *Mass becoming negative.

t_{min}/t_{max}	aE_1	aE_2	Q
2/13	0.3164(19)	3.841(1039)	0.00
3/13	0.2636(15)	3.332(481)	0.00
4/13	0.2243(22)	1.015(25)	1.4×10^{-15}
5/13	0.2264(25)	1.118(22)	1.2×10^{-9}
6/13	0.2173(34)	0.8811(302)	0.15
7/13	0.2126(47)	0.7573(551)	0.27
8/13	0.2095(67)	0.6771(992)	0.16
9/13	0.1900(260)	0.3937(1164)	0.21
10/13	0.1949(398)	0.3615(1937)	6.5×10^{-2}

Table B.241: Vector fit to the kinetic $^3S_1$ mass, with $(a\mathbf{p})^2$=12. **Bad fit.

B.4.2 Wavefunction at the Origin for aM_b=1.8

t_{min}/t_{max}	$\psi_0(0)$
2/13	0.1820(49)
3/13	0.1803(54)
4/13	0.1770(61)
5/13	0.1775(77)
6/13	0.174(12)
7/13	0.168(13)
8/13	0.200(39)
9/13	0.211(61)

Table B.242: Wavefunction at the origin for the lattice 1^1S_0 channel.

t_{min}/t_{max}	$\psi_0(0)$
2/13	0.1485(42)
3/13	0.1476(48)
4/13	0.1434(55)
5/13	0.1442(67)
6/13	0.1427(97)
7/13	0.142(12)
8/13	0.172(50)
9/13	0.178(54)

Table B.243: Wavefunction at the origin for the lattice 1^3S_1 channel.

B.4.3 Lattice Splittings for aM_b=1.8

t_{min}/t_{max}	$aE(1^3S_1 - 1^1S_0)$	$aE(2^3S_1 - 2^1S_0)$	$aE(3^3S_1 - 3^1S_0)$
2/13	0.02160(35)	0.0158(21)	0.0130(56)
3/13	0.02160(35)	0.0157(26)	0.0157(91)
4/13	0.02177(36)	0.0178(33)	0.036(15)
5/13	0.02169(38)	0.0190(85)	0.036(30)
6/13	0.02158(39)	0.013(24)	0.018(18)
7/13	0.02153(41)	0.012(64)	0.013(33)
8/13	0.02135(51)	0.0249(97)	-0.3(41)
9/13	0.02112(49)	0.022(10)	0.06(16)
10/13	0.02178(50)	0.052(28)	0.04(19)
11/13	0.06(16)	0.15(18)	-5(28)

Table B.244: Results from the $3e3s$ matrix fit.

t_{min}/t_{max}	$aE(1^1P_1 - 1^3P_0)$	$aE(2^1P_1 - 2^3P_0)$
2/13	0.0111(16)	0.0142(33)
3/13	0.0110(19)	0.0119(45)
4/13	0.0113(23)	0.0101(65)
5/13	0.0109(30)	0.0040(95)
6/13	0.0104(35)	0.002(13)
7/13	0.0104(44)	-0.012(23)
8/13	0.0108(46)	-0.017(60)
9/13	0.0050(81)	-0.01(19)
10/13	0.20(50)	0.2(14)

Table B.245: Results from the matrix fit.

t_{min}/t_{max}	$aE(1^3P_{2E} - 1^1P_1)$	$aE(2^3P_{2E} - 2^1P_1)$
2/13	0.0042(12)	0.0077(24)
3/13	0.0039(14)	0.0051(35)
4/13	0.0043(17)	0.0048(48)
5/13	0.0045(21)	0.0132(66)
6/13	0.0046(25)	0.019(10)
7/13	0.0055(33)	0.026(18)
8/13	0.0001(37)	0.028(37)
9/13	0.002(11)	0.44(40)
10/13	0.0004(630)	2.0(16)

Table B.246: Results from the matrix fit.

t_{min}/t_{max}	$aE(1^3\overline{P} - 1^1P_1)$	$aE(2^3\overline{P} - 2^1P_1)$
2/13	0.0006(11)	0.0014(22)
3/13	0.0005(15)	0.0024(34)
4/13	-0.0003(20)	0.0011(50)
5/13	-0.0011(25)	0.0069(74)
6/13	0.0018(36)	0.011(10)
7/13	0.0027(44)	0.041(23)
8/13	0.007(12)	0.069(36)
9/13	-0.0025(96)	0.20(19)

Table B.247: Results from the vector fit.

t_{min}/t_{max}	$\frac{2^3S_1-1^3S_1}{1^1P_1-1^3S_1}$
2/13	1.385(29)
3/13	1.357(36)
4/13	1.361(45)
5/13	1.289(54)
6/13	1.257(67)
7/13	1.352(96)
8/13	1.38(17)
9/13	1.38(23)
10/13	1.50(34)

Table B.248: Results from the matrix fit.

t_{min}/t_{max}	$\frac{1^3P_{2E}-1^1P_1}{1^1P_1-1^3P_0}$
2/13	0.38(11)
3/13	0.35(13)
4/13	0.38(15)
5/13	0.42(21)
6/13	0.44(29)
7/13	0.54(42)
8/13	0.01(35)
9/13	0.5(22)
10/13	0.005(300)

Table B.249: Results from the matrix fit.

B.4.4 Lattice State Fits for aM_b=2.1

t_{min}/t_{max}	aE_1	aE_2	aE_3	Q
2/13	0.4038(11)	0.6728(65)	0.8020(172)	9.0×10^{-5}
3/13	0.4037(11)	0.6727(84)	0.8163(287)	3.1×10^{-4}
4/13	0.4040(11)	0.6830(102)	0.8316(488)	3.7×10^{-4}
5/13	0.4039(12)	0.6575(236)	0.7530(566)	1.7×10^{-3}
6/13	0.4033(12)	0.6460(533)	0.6978(447)	1.1×10^{-3}
7/13	0.4035(13)	0.6686(393)	0.6877(1181)	2.5×10^{-3}
8/13	0.4029(15)	0.6710(347)	2.597(1767)	4.0×10^{-3}
9/13	0.4021(15)	0.6746(377)	0.9315(4177)	1.6×10^{-2}
10/13	0.4034(15)	0.7593(724)	1.028(595)	1.2×10^{-2}
11/13	0.4011(32)	0.5840(821)	1.762(2501)	3.4×10^{-2}

Table B.250: Matrix fit to the $^3S_1$ channel.

t_{min}/t_{max}	aE_1	aE_2	aE_3	Q
2/13	0.3844(9)	0.6595(59)	0.7936(187)	2.6×10^{-4}
3/13	0.3842(10)	0.6594(77)	0.8045(304)	4.2×10^{-4}
4/13	0.3844(10)	0.6677(96)	0.8019(496)	4.8×10^{-4}
5/13	0.3843(10)	0.6424(241)	0.7257(533)	2.0×10^{-3}
6/13	0.3838(11)	0.6347(476)	0.6826(481)	9.5×10^{-4}
7/13	0.3841(11)	0.6470(366)	0.6758(1137)	2.9×10^{-3}
8/13	0.3837(12)	0.6515(314)	2.736(1957)	5.9×10^{-3}
9/13	0.3831(13)	0.6555(344)	0.8881(4039)	1.5×10^{-2}
10/13	0.3838(13)	0.7183(583)	0.9970(5483)	1.0×10^{-2}
11/13	0.3811(30)	0.5369(678)	1.913(2581)	5.4×10^{-2}

Table B.251: Matrix fit to the $^1S_0$ channel.

t_{min}/t_{max}	aE_1	aE_2	Q
2/13	0.6077(41)	0.8301(99)	1.3×10^{-2}
3/13	0.6078(48)	0.8310(144)	7.4×10^{-3}
4/13	0.6077(55)	0.8184(201)	1.7×10^{-2}
5/13	0.6057(71)	0.7903(277)	1.5×10^{-2}
6/13	0.6016(84)	0.7762(377)	7.3×10^{-3}
7/13	0.6022(97)	0.8028(595)	5.9×10^{-3}
8/13	0.6082(80)	0.9531(1244)	1.9×10^{-2}
9/13	0.5902(139)	1.030(239)	0.16
10/13	0.6100(121)	2.362(2119)	0.16
11/13	0.5303(2284)	0.7406(4102)	0.37

Table B.252: Matrix fit to the $^1P_1$ channel.

t_{min}/t_{max}	aE_1	aE_2	Q
2/13	0.5886(54)	0.8766(104)	7.9×10^{-2}
3/13	0.5892(65)	0.8606(148)	6.9×10^{-2}
4/13	0.5899(84)	0.8202(217)	0.13
5/13	0.5864(108)	0.8116(306)	7.7×10^{-2}
6/13	0.5786(180)	0.7470(414)	0.13
7/13	0.5725(205)	0.7816(619)	7.0×10^{-2}
8/13	0.5416(589)	0.6544(699)	0.12
9/13	0.5872(540)	0.7422(1632)	7.3×10^{-2}
10/13	0.1178(2889)	0.5965(319)	0.26

Table B.253: Vector fit to the $^3P_0$ channel.

t_{min}/t_{max}	aE_1	aE_2	Q
2/13	0.5976(53)	0.8984(102)	6.1×10^{-2}
3/13	0.5974(65)	0.8766(145)	8.5×10^{-2}
4/13	0.5976(81)	0.8465(216)	9.7×10^{-2}
5/13	0.5925(100)	0.8436(307)	5.9×10^{-2}
6/13	0.5839(153)	0.7932(412)	6.2×10^{-2}
7/13	0.5688(171)	0.8590(630)	0.10
8/13	0.5381(390)	0.7428(752)	0.13
9/13	0.5881(313)	0.8782(1807)	0.15
10/13	0.1757(3217)	0.6099(390)	0.43

Table B.254: Vector fit to the $^3P_1$ channel.

t_{min}/t_{max}	aE_1	aE_2	Q
2/13	0.5995(62)	0.8951(120)	0.15
3/13	0.5996(78)	0.8703(170)	0.20
4/13	0.6045(103)	0.8499(261)	0.17
5/13	0.6064(139)	0.8307(382)	0.10
6/13	0.5923(197)	0.7949(516)	9.4×10^{-2}
7/13	0.5862(195)	0.8870(848)	8.9×10^{-2}
8/13	0.5304(594)	0.7168(847)	0.20
9/13	0.5971(359)	0.9260(2500)	0.30
10/13	0.4826(15495)	0.5132(11719)	0.58

Table B.255: Vector fit to the $^3P_1$ channel, x component.

t_{min}/t_{max}	aE_1	aE_2	Q
2/13	0.5972(63)	0.9000(117)	0.14
3/13	0.5955(77)	0.8793(167)	0.16
4/13	0.5958(99)	0.8450(248)	0.18
5/13	0.5891(117)	0.8622(366)	0.13
6/13	0.5863(185)	0.7885(507)	0.16
7/13	0.5473(254)	0.8079(659)	0.35
8/13	0.5444(430)	0.7486(969)	0.21
9/13	0.5889(346)	0.9451(2306)	0.22
10/13	0.4705(1949)	0.7311(2420)	0.17

Table B.256: Vector fit to the $^3P_1$ channel, y component.

t_{min}/t_{max}	aE_1	aE_2	Q
2/13	0.5948(60)	0.8973(117)	0.49
3/13	0.5960(73)	0.8776(173)	0.50
4/13	0.5957(95)	0.8478(258)	0.52
5/13	0.5866(117)	0.8463(367)	0.48
6/13	0.5805(178)	0.8042(531)	0.41
7/13	0.5753(179)	0.9034(863)	0.47
8/13	0.5471(386)	0.7959(1170)	0.43
9/13	0.5767(378)	0.8791(2488)	0.27
10/13*			

Table B.257: Vector fit to the $^3P_1$ channel, z component.

t_{min}/t_{max}	aE_1	aE_2	Q
2/13	0.6114(44)	0.8363(100)	5.7×10^{-3}
3/13	0.6112(51)	0.8346(144)	2.8×10^{-3}
4/13	0.6116(58)	0.8225(201)	7.4×10^{-3}
5/13	0.6098(74)	0.8021(284)	4.2×10^{-3}
6/13	0.6055(84)	0.7921(298)	2.5×10^{-3}
7/13	0.6064(93)	0.8242(652)	1.9×10^{-3}
8/13	0.6075(81)	0.9722(1326)	2.5×10^{-2}
9/13	0.5898(116)	1.241(367)	0.17
10/13	0.5991(128)	2.438(2233)	0.40
11/13*			

Table B.258: Matrix fit to the ${}^3P_{2E}$ channel. *Mass becoming negative

t_{min}/t_{max}	aE_1	aE_2	Q
2/13	0.6111(47)	0.8323(104)	0.20
3/13	0.6116(56)	0.8328(152)	0.12
4/13	0.6123(66)	0.8211(211)	0.12
5/13	0.6119(83)	0.8152(313)	7.6×10^{-2}
6/13	0.6071(94)	0.8310(472)	8.2×10^{-2}
7/13	0.6131(100)	0.9158(815)	8.1×10^{-2}
8/13	0.6159(99)	1.076(180)	0.14
9/13	0.6025(131)	1.752(769)	0.27
10/13	0.5978(162)	2.721(4341)	0.32
11/13*			

Table B.259: Matrix fit to the ${}^3P_{2E}$ channel, xy component. *Mass becoming negative

t_{min}/t_{max}	aE_1	aE_2	Q
2/13	0.6095(48)	0.8315(106)	5.3×10^{-3}
3/13	0.6083(57)	0.8292(150)	2.2×10^{-3}
4/13	0.6069(64)	0.8144(210)	1.6×10^{-2}
5/13	0.6019(85)	0.7876(279)	9.9×10^{-3}
6/13	0.5961(95)	0.7582(375)	1.6×10^{-2}
7/13	0.5960(103)	0.7732(588)	1.6×10^{-2}
8/13	0.5910(96)	0.9159(1141)	0.11
9/13	0.5779(142)	1.119(283)	0.32
10/13	0.5899(156)	0.8359(2797)	0.41
11/13	0.5591(2737)	0.6075(2229)	0.40

Table B.260: Matrix fit to the $^3P_{2E}$ channel, xz component.

t_{min}/t_{max}	aE_1	aE_2	Q
2/13	0.6137(46)	0.8453(110)	5.9×10^{-4}
3/13	0.6154(54)	0.8479(161)	3.8×10^{-4}
4/13	0.6176(60)	0.8410(233)	1.2×10^{-3}
5/13	0.6186(77)	0.8055(331)	1.4×10^{-3}
6/13	0.6154(93)	0.7869(450)	3.5×10^{-4}
7/13	0.6138(110)	0.8122(737)	3.8×10^{-4}
8/13	0.6176(97)	1.014(163)	5.3×10^{-3}
9/13	0.5903(146)	1.126(337)	0.10
10/13	0.6028(160)	2.878(3344)	0.29
11/13*			

Table B.261: Matrix fit to the $^3P_{2E}$ channel, yz component.

t_{min}/t_{max}	aE_1	aE_2	Q
2/13	0.6027(54)	0.9209(105)	1.2×10^{-2}
3/13	0.6030(66)	0.8998(154)	1.4×10^{-2}
4/13	0.6034(83)	0.8715(232)	1.2×10^{-2}
5/13	0.5916(101)	0.8679(329)	1.5×10^{-2}
6/13	0.5855(145)	0.8363(464)	8.0×10^{-3}
7/13	0.5694(155)	0.9699(792)	0.13
8/13	0.5548(286)	0.8610(1192)	8.5×10^{-2}
9/13	0.5981(222)	1.125(311)	0.28
10/13	0.6004(3431)	0.6517(7414)	0.20

Table B.262: Vector fit to the $^3P_{2T}$ channel.

t_{min}/t_{max}	aE_1	aE_2	Q
2/13	0.6073(66)	0.9072(124)	9.9×10^{-2}
3/13	0.6095(83)	0.8839(179)	0.11
4/13	0.6089(107)	0.8478(262)	0.14
5/13	0.5926(133)	0.8327(359)	0.21
6/13	0.5963(203)	0.8030(539)	0.14
7/13	0.5776(194)	0.9325(844)	0.60
8/13	0.5639(283)	0.9350(1459)	0.46
9/13	0.5904(215)	1.380(492)	0.53
10/13	0.6071(4223)	0.6678(11197)	0.39

Table B.263: Vector fit to the ${}^3P_{2T}$ channel, xy component.

t_{min}/t_{max}	aE_1	aE_2	Q
2/13	0.5939(63)	0.9279(120)	5.2×10^{-2}
3/13	0.5916(75)	0.9151(176)	3.6×10^{-2}
4/13	0.5932(95)	0.8808(279)	3.4×10^{-2}
5/13	0.5818(109)	0.9017(422)	4.3×10^{-2}
6/13	0.5718(160)	0.8531(594)	2.8×10^{-2}
7/13	0.5465(197)	0.9512(962)	0.15
8/13	0.5632(286)	0.8649(1603)	0.12
9/13	0.5880(212)	1.372(497)	0.23
10/13	0.5808(4677)	0.6240(9354)	0.12

Table B.264: Vector fit to the ${}^3P_{2T}$ channel, xz component.

t_{min}/t_{max}	aE_1	aE_2	Q
2/13	0.6065(63)	0.9251(123)	3.7×10^{-2}
3/13	0.6091(78)	0.8991(186)	4.5×10^{-2}
4/13	0.6134(102)	0.8787(287)	3.1×10^{-2}
5/13	0.6031(131)	0.8589(408)	2.4×10^{-2}
6/13	0.5923(172)	0.8493(582)	1.3×10^{-2}
7/13	0.5861(158)	1.082(126)	6.5×10^{-2}
8/13	0.5341(591)	0.7800(1331)	0.14
9/13	0.6399(1071)	0.8226(3924)	0.78
10/13	0.6408(2258)	0.8171(8941)	0.47

Table B.265: Vector fit to the ${}^3P_{2T}$ channel, yz component.

t_{min}/t_{max}	aE_1	aE_2	Q
2/13**	0.01843(7)	1.469(179)	0.00
3/13*			
4/13**	0.01744(8)	3.264(940)	0.00
5/13	0.01630(11)	0.7706(197)	7.1×10^{-9}
6/13	0.01628(12)	0.7531(333)	1.4×10^{-9}
7/13	0.01606(14)	0.6510(266)	3.8×10^{-2}
8/13	0.01596(17)	0.5517(401)	0.25
9/13	0.01586(22)	0.4817(606)	0.21
10/13	0.01585(34)	0.4152(961)	7.2×10^{-2}

Table B.266: Vector fit to the kinetic $^3S_1$ mass, with $(a\mathbf{p})^2$=1. *Mass becoming negative, **bad fit.

t_{min}/t_{max}	aE_1	aE_2	Q
2/13**	0.03714(14)	1.456(167)	0.00
3/13*			
4/13**	0.03502(17)	3.287(949)	0.00
5/13	0.03256(23)	0.7860(194)	3.3×10^{-9}
6/13	0.03251(26)	0.7624(334)	6.6×10^{-10}
7/13	0.03206(30)	0.6640(263)	2.3×10^{-2}
8/13	0.03184(37)	0.5635(392)	0.17
9/13	0.03158(48)	0.4840(582)	0.18
10/13	0.03155(75)	0.4130(917)	6.0×10^{-2}

Table B.267: Vector fit to the kinetic $^3S_1$ mass, with $(a\mathbf{p})^2$=2. *Mass becoming negative, **bad fit.

t_{min}/t_{max}	aE_1	aE_2	Q
2/13**	0.05618(23)	1.438(156)	0.00
3/13*			
4/13**	0.05277(26)	3.305(949)	0.00
5/13	0.04879(37)	0.8018(193)	1.8×10^{-9}
6/13	0.04870(41)	0.7740(335)	3.6×10^{-10}
7/13	0.04803(48)	0.6777(261)	1.5×10^{-2}
8/13	0.04767(59)	0.5757(385)	0.13
9/13	0.04716(79)	0.4880(565)	0.16
10/13	0.04711(124)	0.4158(891)	5.3×10^{-2}

Table B.268: Vector fit to the kinetic $^3S_1$ mass, with $(a\mathbf{p})^2$=3. *Mass becoming negative, **bad fit.

t_{min}/t_{max}	aE_1	aE_2	Q
2/13**	0.07540(32)	1.413(145)	0.00
3/13*			
4/13**	0.07066(35)	3.320(940)	0.00
5/13	0.06484(51)	0.8155(190)	2.2×10^{-9}
6/13	0.06475(57)	0.7844(332)	4.7×10^{-10}
7/13	0.06376(67)	0.6896(258)	1.8×10^{-2}
8/13	0.06324(84)	0.5797(383)	0.20
9/13	0.06259(114)	0.4979(566)	0.22
10/13	0.06256(174)	0.4405(881)	7.4×10^{-2}

Table B.269: Vector fit to the kinetic $^3S_1$ mass, with $(a\mathbf{p})^2$=4. *Mass becoming negative, **bad fit.

$tmin/tmax$	aE_1	aE_2	Q
2/13**	0.09538(43)	1.386(133)	0.00
3/13*			
4/13**	0.08890(46)	3.351(965)	0.00
5/13	0.08102(67)	0.8314(187)	7.8×10^{-10}
6/13	0.08089(75)	0.7939(332)	1.9×10^{-10}
7/13	0.07969(88)	0.7041(254)	7.3×10^{-3}
8/13	0.07898(111)	0.5944(372)	9.3×10^{-2}
9/13	0.07785(156)	0.4968(536)	0.15
10/13	0.07778(247)	0.4305(835)	5.0×10^{-2}

Table B.270: Vector fit to the kinetic $^3S_1$ mass, with $(a\mathbf{p})^2$=5. *Mass becoming negative, **bad fit.

t_{min}/t_{max}	aE_1	aE_2	Q
2/13**	0.1159(6)	1.363(123)	0.00
3/13*			
4/13**	0.1074(6)	3.372(971)	0.00
5/13	0.09721(84)	0.8482(188)	4.7×10^{-10}
6/13	0.09705(95)	0.8093(333)	1.2×10^{-10}
7/13	0.09563(112)	0.7199(255)	4.3×10^{-3}
8/13	0.09468(143)	0.6091(370)	5.6×10^{-2}
9/13	0.09295(208)	0.4996(526)	0.13
10/13	0.09287(333)	0.4322(830)	4.1×10^{-2}

Table B.271: Vector fit to the kinetic $^3S_1$ mass, with $(a\mathbf{p})^2$=6. *Mass becoming negative, **bad fit.

t_{min}/t_{max}	aE_1	aE_2	Q
2/13**	0.1587(9)	1.286(102)	0.00
3/13*			
4/13**	0.1453(8)	3.428(1019)	0.00
5/13	0.1294(12)	0.8820(188)	5.6×10^{-10}
6/13	0.1293(14)	0.8472(330)	1.3×10^{-10}
7/13	0.1274(17)	0.7548(257)	1.8×10^{-3}
8/13	0.1259(22)	0.6386(376)	2.1×10^{-2}
9/13	0.1225(34)	0.5053(531)	7.3×10^{-2}
10/13	0.1224(58)	0.4260(839)	2.4×10^{-2}

Table B.272: Vector fit to the kinetic $^3S_1$ mass, with $(a\mathbf{p})^2$=8. *Mass becoming negative, **bad fit.

t_{min}/t_{max}	aE_1	aE_2	Q
2/13*			
3/13*			
4/13**	0.1646(10)	3.448(1038)	0.00
5/13	0.1457(15)	0.9008(193)	7.7×10^{-10}
6/13	0.1456(17)	0.8720(332)	1.5×10^{-10}
7/13	0.1435(20)	0.7735(263)	2.1×10^{-3}
8/13	0.1415(27)	0.6542(387)	2.2×10^{-2}
9/13	0.1369(43)	0.5088(545)	9.7×10^{-2}
10/13	0.1370(72)	0.4397(887)	3.0×10^{-2}

Table B.273: Vector fit to the kinetic $^3S_1$ mass, with $(a\mathbf{p})^2$=9. *Mass becoming negative, **bad fit.

t_{min}/t_{max}	aE_1	aE_2	Q
2/13*			
3/13*			
4/13**	0.2255(15)	3.532(1176)	0.00
5/13	0.1943(23)	0.9619(219)	1.9×10^{-9}
6/13	0.1951(26)	0.9757(331)	3.4×10^{-9}
7/13	0.1909(33)	0.8346(298)	9.8×10^{-3}
8/13	0.1874(46)	0.7044(471)	3.8×10^{-2}
9/13	0.1774(88)	0.5121(670)	0.16
10/13	0.1782(144)	0.4560(1131)	4.7×10^{-2}

Table B.274: Vector fit to the kinetic $^3S_1$ mass, with $(a\mathbf{p})^2$=12. *Mass becoming negative, **bad fit.

B.4.5 Wavefunction at the Origin for aM_b=2.1

t_{min}/t_{max}	$\psi_0(0)$
2/13	0.1998(57)
3/13	0.1970(60)
4/13	0.1936(68)
5/13	0.1945(84)
6/13	0.193(12)
7/13	0.185(14)
8/13	0.229(58)

Table B.275: Wavefunction at the origin for the lattice 1^1S_0 channel.

t_{min}/t_{max}	$\psi_0(0)$
2/13	0.1693(51)
3/13	0.1673(54)
4/13	0.1630(64)
5/13	0.1643(76)
6/13	0.164(10)
7/13	0.162(14)
8/13	0.207(76)

Table B.276: Wavefunction at the origin for the lattice 1^3S_1 channel.

B.4.6 Lattice Splittings for aM_b=2.1

t_{min}/t_{max}	$aE(1^3S_1 - 1^1S_0)$	$aE(2^3S_1 - 2^1S_0)$	$aE(3^3S_1 - 3^1S_0)$
2/13	0.01947(31)	0.0133(16)	0.0085(48)
3/13	0.01950(31)	0.0133(21)	0.0118(79)
4/13	0.01963(32)	0.0153(26)	0.030(14)
5/13	0.01957(34)	0.0154(69)	0.028(23)
6/13	0.01946(35)	0.008(28)	0.015(13)
7/13	0.01943(37)	0.009(72)	0.011(30)
8/13	0.01923(44)	0.0183(82)	-0.3(21)
9/13	0.01898(43)	0.0175(95)	0.03(14)
10/13	0.01960(43)	0.040(28)	0.02(16)
11/13	0.0192(14)	0.023(28)	-0.10(91)

Table B.277: Results from the $3e3s$ matrix fit.

t_{min}/t_{max}	$aE(1^1P_1 - 1^3P_0)$	$aE(2^1P_1 - 2^3P_0)$
2/13	0.0096(15)	0.0108(30)
3/13	0.0095(17)	0.0091(39)
4/13	0.0098(21)	0.0063(57)
5/13	0.0096(26)	0.0032(82)
6/13	0.0091(30)	0.004(11)
7/13	0.0092(38)	-0.008(19)
8/13	0.0087(42)	-0.021(55)
9/13	0.0026(66)	-0.03(18)
10/13	0.15(64)	2.0(12)

Table B.278: Results from the matrix fit.

t_{min}/t_{max}	$aE(1^3P_{2E} - 1^1P_1)$	$aE(2^3P_{2E} - 2^1P_1)$
2/13	0.0037(10)	0.0063(21)
3/13	0.0034(12)	0.0037(31)
4/13	0.0039(14)	0.0041(43)
5/13	0.0040(18)	0.0118(58)
6/13	0.0039(21)	0.0159(87)
7/13	0.0041(28)	0.021(15)
8/13	-0.0008(31)	0.018(35)
9/13	0.0005(93)	0.33(34)
10/13	-0.0110(48)	0.5(10)

Table B.279: Results from the matrix fit.

t_{min}/t_{max}	$aE(1^3\overline{P} - 1^1P_1)$	$aE(2^3\overline{P} - 2^1P_1)$
2/13	0.0005(10)	0.0016(19)
3/13	0.0005(13)	0.0024(29)
4/13	-0.00009(180)	0.0020(43)
5/13	-0.0009(23)	0.0064(64)
6/13	0.0014(33)	0.0090(92)
7/13	0.0019(38)	0.031(20)
8/13	0.002(11)	0.056(29)
9/13	-0.007(13)	0.13(12)

Table B.280: Results from the vector fit.

t_{min}/t_{max}	$\frac{2^3S_1 - 1^3S_1}{1^1P_1 - 1^3S_1}$
2/13	1.339(29)
3/13	1.318(36)
4/13	1.330(46)
5/13	1.257(54)
6/13	1.218(67)
7/13	1.318(98)
8/13	1.39(18)
9/13	1.38(23)
10/13	1.49(47)

Table B.281: Results from the matrix fit.

t_{min}/t_{max}	$\frac{1^3P_{2E}-1^1P_1}{1^1P_1-1^3P_0}$
2/13	0.39(11)
3/13	0.36(12)
4/13	0.40(15)
5/13	0.43(20)
6/13	0.43(27)
7/13	0.46(37)
8/13	-0.08(37)
9/13	0.3(37)
10/13	-0.07(29)

Table B.282: Results from the matrix fit.

Bibliography

[1] F. Halzen and A. D. Martin, *Quarks and Leptons: An Introductory Course in Modern Particle Physics*, Wiley, U.S.A., 1984.

[2] M. Kaku, *Quantum Field Theory: A Modern Introduction*, Oxford Student Edition, New York, 1993.

[3] S.W. Herb *et al.*, *Observation of a Dimuon Resonance at 9.5GeV in 400-GeV Proton-Nucleus Collisions*, Phys. Rev. Lett. **39** (1977), 252.

[4] W.R. Innes *et al.*, *Observation of Structure in the* Υ *Region*, Phys. Rev. Lett. **39** (1977), 1240.

[5] *The Upsilon System*, CLEO Experiment Web Page: http://www.lns.cornell.edu/public/lab-info/upsilon.html.

[6] C. T. H. Davies, *The Heavy Hadron Spectrum.* Lecture course at the Computing Particle Properties School, March 1997. 36 Internationale Universitatwochen fur Kern und Teilchenphysik, Schladming, Austria. *hep-lat* **9710394**.

[7] S. Godfrey and J. L. Rosner, *Production of the* $\eta_b(nS)$ *states*, Enrico Fermi Institute preprint EFI 01-10, *ArXiv:hep-ph/***0104253**. Submitted to Physical Review D, Brief Reports.

[8] S. Godfrey and J. L. Rosner, *Production of the D-wave* $b\bar{b}$*states*, Enrico Fermi Institute preprint EFI 01-14, *ArXiv:hep-ph/***0105273**. Submitted to Physical Review D, Brief Reports.

[9] D.Bailin and A.Love, *Introduction to Gauge Field Theory*, Adam Hilger, Bristol, 1986.

[10] L.H.Ryder, *Quantum Field Theory*, Cambridge University Press, 1985.

[11] I. Montvay and G. Münster, *Quantum Fields on a Lattice*, Cambridge University Press, Cambridge, 1997.

[12] K. G. Wilson, *Confinement of Quarks*, Phys. Rev. D**10** (1974), 2445.

[13] H. J. Rothe, *Lattice Gauuge Theories*, World Scientific, Singapore, 1992.

[14] M. Creutz, *Quarks, Gluons and Lattices*, Cambridge University Press, Cambridge, 1983.

[15] K. G. Wilson, *Quarks and Strings on a Lattice* in *New Phenomena in Subnuclear Physics*, ed. A. Zichichi, Plenum Press, New York, PartA, 69.

[16] B. Sheikoleslami and R. Wohlert, *Improved Continuum Limit Lattice Action for QCD with Wilson Fermions*, Nucl. Phys. B **259** (1985), 572.

[17] K. Symanzik, *Continuum Limit and Improved Action in Lattice Theories, (I). Principles and ϕ^4 theory, (II). O(N) non-linear sigma model in perturbation theory*, Nucl. Phys. B**226** (1983), 187.

[18] P. Boyle, PhD thesis, *Heavy Meson Spectroscopy from Lattice QCD.*

[19] K. Jansen, C. Liu, M. Lüscher, H. Simma, S. Sint, R. Sommer, P. Weisz and U. Wolff, *Non-perturbative renormalization of lattice QCD at all scales*, *hep-lat/***9512009**.

[20] M. Lüscher, S. Sint, R. Sommer and P. Weisz, *Chiral symmetry and O(a) improvement in lattice QCD*, Nucl. Phys. B**478** (1996), 365.

[21] M. Lüscher, S. Sint, R. Sommer, P. Weisz, H. Wittig and U. Wolff (Check this with a German), *Some new results in O(a) improved lattice QCD*, Nucl. Phys. B(Proc. Suppl.)**53** (1997), 905; or *arXiv:hep-lat/***9604014**.

[22] M. Lüscher, S. Sint, R. Sommer, P. Weisz and U. Wolff(again check this), *Non-perturbative O(a) improvement of lattice QCD*, *hep-lat/* **9609035**.

[23] K. Jansen and R. Sommer, *O(a) improvement of lattice QCD with two flavors of Wilson quarks*, Nucl. Phys. B**530** (1998), 185; or *arXiv:hep-lat/***9803017**.

[24] B. Efron, *Computers and the Theory of Statistics: Thinking the Unthinkable*, Society for Industrial and Applied Mathematics **21** No. 4 (1979), 460.

[25] D. H. Robinson and M. C. K. Yang, *Understanding and Learning Statistics by Computer*, World Scientific Series in Computer Science Vol. 4, 1986.

[26] B. Joó, PhD thesis, *Efficient Monte Carlo Simulation of Lattice QCD.*

[27] Talk presented at the University of Glasgow by Alan Irving.

[28] W. Lucha, F. F. Schöberl and D. Gromes, *Bound States of Quarks*, Phys. Rep. **200**, 127 (1991).

[29] D. Groom *et al.*, (Particle Data Group), The European Physical Journal C, **15**(2000), 1.

[30] A. J. Lidsey, PhD thesis, *Non-Relativistic QCD on the Lattice.*

[31] H. Grosse and A. Martin, *Exact Results on Potential Models for Quarkonium Systems*, Phys. Rep. **60** C 1980, 341.

[32] E. Eichten, K. Gottfried, T. Kinoshita, J. Kogut, K. D. Lane and T.-M. Yan, *Spectrum of Charmed Quark-Anitquark Bound States*, Phys. Rev. Lett. B **34** (1975), 369.

[33] J. L. Richardson, *The Heavyq Quark Potential and the* Υ, *J/*ψ *Systems*, Phys. Lett. B, **82** (1978), 272.

[34] E. Eichten and F. Feinberg, *Spin-dependent forces in quantum chromodynamics*, Phys. Rev. D **23** (1981), 2724.

[35] G. S. Bali, K. Schilling and A. Wachter, *Complete* $\mathcal{O}(v^2)$ *corrections to the static interquark potential from SU(3) gauge theory* , Wuppertal preprint WUB 97-11, *hep-lat* **9703019**.

[36] W. Kwong and J. L. Rosner, *D-wave quarkonium levels of the* Υ *family* , Phys. Rev. D **38** (1988), 279.

[37] M. Peskin, *Dynamics and Spectroscopy at High Energy* , Proceedings of the 11th SLAC Summer Institute on Particle Physics, SLAC Report 267.

[38] W. J. Duffin, *Electricity and Magnetism* , McGraw Hill, 4th Edition, Maidenhead, 1990.

[39] SESAM Collaboration, U. Glässner, S. Güsken, H. Hoeber, Th. Lippert, G. Ritzenhöfer, K. Schilling, G. Siegert, A. Spitz and A. Wachter, *First Evidence of* N_f*-Dependence in the QCD Interquark Potential* , Phys. Lett. B **82** (1996), 98; or *arXiv:hep-lat/***9604014**.

[40] A. X. El-Khadra, G. Hockney, A. S. Kronfeld and P. B. Mackenzie, *Determination of the strong coupling constant from the charmonium spectrum*, Phys. Rev. Lett. **69** (1992), 729.

[41] A. El-Khadra *et al.* Nucl. Phys. B**30** Proc. Suppl. (1992), 449.

[42] C. Quigg and J. L. Rosner, *Quantum Mechanics with applications to Quarkonium*, Phys. Rep. C **56** (1979), 169.

[43] G. P. Lepage and B. A. Thacker, *Effective Lagrangians for Simulating of Heavy Quark Systems*, Nucl. Phys. B (Proc. Suppl.) **4** (1988), 199.

[44] B. A. Thacker and G. P. Lepage, *Heavy-quark bound states in lattice QCD*, Phys. Rev. D **43** (1991), 196.

[45] L. L. Foldy and S. A. Wouthuysen, *On the Dirac Theory of Spin 1/2 Particles and Its Non-Relativistic Limit*, Phys. Rev. **78** (1950), 29.

[46] B. Grinstein, *A Modern Introduction to Quarkonium Theory, hep-ph/***9811264**.

[47] C. Itzykson and J-B. Zuber, *Quantum Field Theory*, McGraw Hill International Editions (Physics Series), Singapore, 1985.

[48] G. P. Lepage, L. Magnea, C. Nakhleh, U. Magnea, K. Hornbostel, *Improved Nonrelativistic QCD for Heavyq Quark Physics*, Phys. Rev. D **45** (1992), 915.

[49] T. Manke, I. T. Drummond, R. R. Horgan and H. P. Shanahan, *Υ-spectrum from NRQCD with Improved Action*, *arXiv:hep-lat/***9706003**.

[50] C. T. H. Davies, K. Hornbostel, G. P. Lepage, A. Lidsey, P. McCallum, J. Shigemitsu and J.Sloan, *Scaling of the Υ spectrum in Lattice NRQCD and further determinations of m_b*, Phys. Rev. **58** (1998), 054505.

[51] C. T. H. Davies, K. Hornbostel, G. P. Lepage, A. Lidsey, J. Shigemitsu, J. Sloan, *Precision Charmonium Spectroscopy From Lattice QCD*, Phys. Rev. D **52** (1995), 6519.

[52] G. P. Lepage and P. B. Mackenzie, *On the Viability of Lattice Perturbation Theory*, Phys. Rev. D **48** (1993), 2250.

[53] N. H. Shakespeare, H. D. Trottier, *Tadpole renormalisation and relativistic corrections in lattice NRQCD*, Phys. Rev. D**58** (1998), 034502, *arXiv:hep-lat/***9802038**.

[54] SESAM Collaboration: N. Eicker, Th. Lippert, K. Schilling, A. Spitz, J. Fingberg, S. Güsken, H. Hoeber, J. Viehoff, *Improved Υ Spectrum with Dynamical Wilson Fermions*, (1997), *arXiv:hep-lat/***9709002**.

[55] C. J. Morningstar, *Radiative corrections to the kinetic couplings in nonrelativistic lattice QCD*, Phys. Rev. D **50** (1994), 5902.

[56] J. Shigemitsu, private communication.

[57] F.Mandl and G.Shaw, *Quantum Field Theory*, Wiley, Guildford and King's Lynn, 1995.

[58] P. Lacock, C. Michael, P. Boyle, P. Rowland, *Orbitally excited and hybrid mesons from the lattice*, Phys. Rev. D **54** (1996), 6997;*arXiv:hep-lat/***9605025(v2)**.

[59] P. McCallum, PhD thesis, *Upsilon Spectroscopy using Lattice QCD.*

[60] B. H. Bransden and C. J. Joachain, *Introduction to Quantum Meachanics*, Longman Scientific and Technical, Malaysia, 1992.

[61] W. H. Press, B. P. Flannery, S. A. Teukolsky and W. T. Vetterling, *Numerical Recipes*, Cambridge University Press (1986).

[62] C. T. H. Davies *et al.*, *Precision Υ Spectroscopy from Non-Relativistic Lattice QCD*, Phys. Rev. D, **50** (1994), 6963.

[63] J. Garden, PhD Thesis, *Light Hadron Spectroscopy in Lattice QCD.*

[64] CP-PACS Collaboration: T. Manke *et al.*, *Sea Quark Effects on Quarkonia*, (2000), *arXiv:hep-lat/***0005022**.

[65] C. T. H. Davies, K. Hornbostel, G. P. Lepage, P. McCallum, J. Shigemitsu, J. Sloan, *Unquenching Lattice QCD* (Unpublished).

[66] R. Sommer, *A New Way to Set the Energy Scale in Lattice Gauge Theories and its Application to the Static Force and α_s in SU(2) Yang-Mills Theory*, Nucl. Phys. B**11** (1994), 839; or *arXiv:hep-lat/***9310022**.

[67] A. Irving, Private Communication.

[68] M. Guagnelli, R. Sommer and H. Wittig, *Precision computation of a low-energy reference scale in quenched lattice QCD*, *arXiv:hep-lat/***9806005**.

[69] C. T. H. Davies, K. Hornbostel, G. P. Lepage, A. Lidsey, J. Shigemitsu, J. Sloan, *A precise determination of α_s from lattice QCD*, Phys. Lett. B**345** (1995), 42.

[70] C. T. H. Davies, Private Communication.

[71] G. Bali and P. Boyle, In preparation.

[72] S. J. Brodsky, G. P. Lepage and P. B. Mackenzie, Phys. Rev. D**28** (1983), 228.

[73] G. Bali and P. Boyle, Private Communication.

[74] G. Rodrigo and A. Santamaria, *QCD Matching Conditions at Thresholds*, Phys. Lett. B**313** (1993), 441, or *arXiv:hep-ph/***9305305**.

[75] C. T. H. Davies, K. Hornbostel, A. Langnau, G. P. Lepage, A. Lidsey, C. J. Morningstar, J. Shigemitsu and J. Sloan, *New Determination of the Pole Mass of the b Quark Using Lattice QCD*, Phys. Rev. Lett. **73** (1994), 2654.

[76] C. Morningstar, Private Communication.

[77] N. Gray, D. J. Broadhurst, W. Grafe and K. Schilcher, Z. Phys. C**48** (1990), 673.

[78] S. Collins *et al.*, *The b quark mass from lattice QCD*, In Preparation.